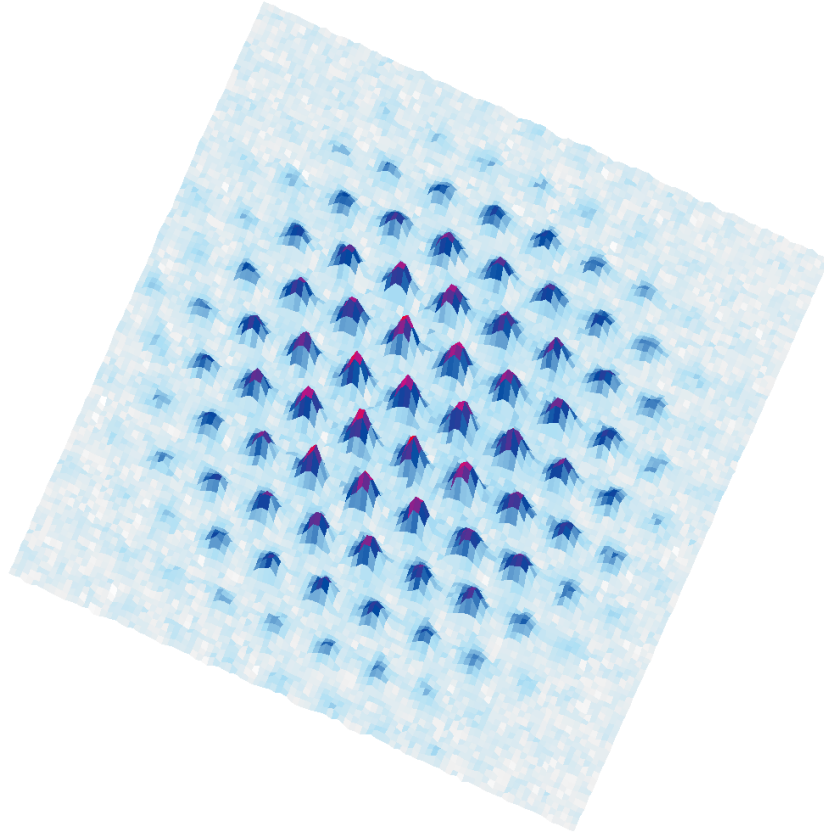


Quantum Gas Magnifier for imaging of ultracold Atoms in highly tunable optical Lattices



Dissertation zur Erlangung des Doktorgrades

an der Fakultät für Mathematik, Informatik und Naturwissenschaften

Fachbereich Physik der Universität Hamburg

vorgelegt von Luca Asteria aus Rho

Hamburg 2022

The cover image is obtained from the density distribution of a small ultracold atomic cloud in a triangular lattice, measured with quantum gas magnification.
(Luca Asteria)

Gutachter

Gutachter der Dissertation:	Prof. Dr. Klaus Sengstock Prof. Dr. Ludwig Mathey Prof. Dr. Christopher Foot
Gutachter der Disputation:	Prof. Dr. Markus Drescher Prof. Dr. Ludwig Mathey Prof. Dr. Henning Moritz Prof. Dr. Roman Schnabel Prof. Dr. Klaus Sengstock
Vorsitzende der Prüfungskommission:	Prof. Dr. Roman Schnabel
Datum der Disputation:	18.8.2022
Vorsitzender des Promotionsausschusses:	Prof. Dr. Wolfgang J. Parak
Leiter des Fachbereichs:	Prof. Dr. Günter H. W. Sigl
Dekan der Fakultät für Mathematik, Informatik und Naturwissenschaften:	Prof. Dr.-Ing. Norbert Ritter

Erklärung zur Eigenständigkeit

Ich versichere hiermit an Eides statt, dass ich die vorliegende Doktorarbeit selbstständig verfasst und nur die angegebenen Quellen und Hilfsmittel benutzt habe. Wörtlich oder dem Sinn nach aus anderen Werken entnommene Stellen sind unter Angabe der Quellen kenntlich gemacht.

Luca Asteria

Hamburg – 18.1.2022

Abstract

Ultracold gases in optical lattice are promising quantum simulation platforms: neutral atoms can be cooled down to quantum degeneracy and loaded into the lattice, thus mimicking the behaviour of electrons in "real" solid state materials. The advantage of optical lattice systems is the high degree of control over the system properties and the possibility to access a wider range of observables.

In this thesis, different experiments with ultracold atoms in optical lattices are performed, addressing both the issue of extending the measurement possibilities and the degree of control over the lattice system.

The first results reported here concern the detection of topological order in a cloud of ultracold fermionic ^{40}K atoms. Topological order can not be captured by a local order parameter as in the description of phase transitions made by Landau. Thus topological properties are often related to elusive quantities, even in a realization with cold atoms.

Following a recent theoretical proposal, we were able to demonstrate that a topological system exhibits circular dichroism, i.e. a dependence on the chirality of a rotating force perturbing the system. We showed also that the dichroic signal can be directly used to detect topological order, which will be of relevance e.g. in cases where novel topological phases are created and no suitable probes exist yet. The experimental techniques developed here also allowed to measure other quantities related to the transport properties and to the geometry of the lattice states.

With the same setup, data were taken in order to train a machine learning algorithm to recognize the topological phase transition; these results are also briefly presented.

In a set of experiments performed with ^{87}Rb , a novel technique for directly imaging the atomic density distribution in the lattice was developed and experimentally demonstrated. This technique is based on a matter-wave dynamics in which the density distribution is magnified up to almost two orders of magnitude and then directly imaged with standard methods, with a single destructive measurement and with sub-lattice resolution. Different experimental cases were studied and are presented, among them the discovery of a density wave which appears when displacing the atomic cloud with respect to the center of the confining potential. Preliminary results and considerations about the possibility of using quantum gas magnification for detecting coherence properties of the matter field with high resolution are also presented.

In the last chapter, we present a novel scheme for the realization of an optical lattice with tunable geometry. This scheme is based on the use of different frequency components controlled by radio-frequencies and we report on how this allowed the geometry of the optical lattice to be tuned fast and with high precision. This allows not only to tune our lattice to simulate different solid state systems, but also to study novel quantum phases which might emerge when changing dynamically the geometry, a scenario without a solid-state counterpart.

Zusammenfassung

Ultrakalte Quantengase bieten einzigartige Möglichkeiten für Quantensimulation: neutrale Atome können bis zur Quantenentartung gekühlt und in Gitter geladen werden; solche Systeme reproduzieren das Verhalten von Elektronen in "echten" Festkörpern. Der Vorteil von optischen Gittersystemen ist die große Kontrolle über die Eigenschaften des Systems und Zugang zu einer größeren Anzahl von Observablen.

Für diese Arbeit wurden unterschiedliche Experimente mit ultrakalten Quantengasen durchgeführt. Diese adressieren sowohl die Messungsmöglichkeiten als auch die Kontrolle über das Gittersystem.

Die ersten berichteten Ergebnisse betreffen die Detektion von topologischer Ordnung in einer Wolke von ultrakalten fermionischen ^{40}K Atomen. Die topologische Ordnung kann nicht durch einen lokalen Ordnungsparameter beschrieben werden, wie in der Theorie der Phasenübergänge von Landau. Deshalb hängen topologische Eigenschaften oft mit schwierig zu messenden Observablen zusammen, so auch in einer Implementierung mit kalten Atomen.

Einem neuen theoretischen Vorschlag folgend, konnten wir demonstrieren, dass ein topologisches System einen zirkularen Dichroismus zeigt, d.h. eine Abhängigkeit von der Chiralität einer rotierenden Kraft als Störung. Wir zeigten auch, dass das dichroische Signal direkt verwendet werden konnte, um topologische Ordnung zu detektieren. Das könnte z.B. bei der Erschaffung neuer topologischer Phasen relevant sein, wenn es noch keine geeigneten Probemethoden gibt. Die experimentellen Techniken, die hier entwickelt wurden, erlauben auch das Messen von anderen Observablen mit Bezug auf Leitungseigenschaften und zur Geometrie von Gitterzuständen.

Daten, die mit dem selben Aufbau erfasst wurden, wurden genutzt, um einen Algorithmus für maschinelles Lernen zur Erkennung von topologischen Phasenübergängen zu trainieren. Diese Ergebnisse sind auch zusammengefasst.

In mit ^{87}Rb realisierten Experimenten wurde eine neue Technik zur direkten Abbildung der Dichteverteilung im Gitter eingeführt und demonstriert. Diese Technik basiert auf einer Materienwellendynamik, welche eine Vergrößerung der ursprünglichen Dichteverteilung um bis zu fast zwei Größenordnungen realisiert. Die vergrößerte Dichteverteilung kann anschließend mit konventionellen Methoden abgebildet werden, in einer einzigen destruktiven Messung und mit sub-Gitter Auflösung.

Unterschiedliche experimentelle Situationen wurden untersucht und präsentiert, u.a. die Entdeckung einer Dichtewelle, die sich nach Verschiebung der atomaren Wolken gegenüber dem Fallenzentrum bildet. Erste Ergebnisse und Überlegungen über die Möglichkeit, den Quantumgasvergrößerer zur Detektion mit hoher Auflösung von Kohärenzeigenschaften des Materienfelds zu nutzen, werden auch präsentiert.

Zum Schluss präsentieren wir eine neue Methode zur Realisierung eines optischen Gitters mit einstellbarer Geometrie. Dieses Schema basiert auf der Anwendung von mehreren durch Radiofrequenzen kontrollierten Frequenzkomponenten. Wir berichten über die jetzt erlaubte schnelle und präzise Kontrolle der Geometrie. Das könnte nicht nur zur Simulation von unterschiedlichen Festkörper-Systemen nützlich sein, sondern auch zur Untersuchung neuer Quantenphasen in Systemen mit zeitabhängiger Geometrie, welche sich nicht in Festkörpern realisieren lassen.

Contents

1. Introduction	1
1.1. Thesis Outline	3
2. Quantum Simulation with optical lattices	5
2.1. Cold Atoms Setup	6
2.1.1. Getting ultracold: The magnetic Trap	8
2.2. Bloch Bands in optical Lattices	11
2.2.1. Band Structure Calculation	15
2.2.2. Time-of-Flight	17
2.2.3. $T/4$ Evolution in a Harmonic Trap	19
2.2.4. Band Mapping	20
2.2.5. Optical Imaging	20
2.3. Floquet Engineering of topological States	21
2.3.1. Quantum topology	21
2.3.2. Description of time-periodic Systems	23
2.3.3. Topology via Lattice Shaking	23
2.3.4. Reconstructing the Topological Phase Diagram via Machine Learning	26
3. Circular Dichroism, or "Hearing Topology"	29
3.1. Heating Rates as topological Probes	31
3.2. Experimental Implementation	35
3.2.1. Separation of Timescales	35
3.2.2. Characterization of Floquet Heating	37
3.3. Results	39
3.3.1. Chiral Spectra	39
3.3.2. Measurement of Quantized Circular Dichroism	45
3.3.3. Measurement of the Wannier Spread Functional	48
3.4. Conclusions	52
4. Quantum Gas Magnifier, or a lens for "Seeing Quantum Particles"	53
4.1. Theory	55
4.1.1. Focusing the Matter Wave Field	56
4.1.2. Deviations from the focusing Condition	59
4.1.3. Time Dependent Parameters	61
4.1.4. Imaging the Velocity Field	62
4.1.5. Other Magnification Schemes	63

4.2.	Experimental Characterization	65
4.2.1.	Results for different Lattice Geometries and Magnifications	66
4.2.2.	Focusing Condition	69
4.2.3.	Anharmonicity	72
4.2.4.	Resolution of the Quantum Gas Magnifier	73
4.3.	Precision Thermometry	76
4.4.	Sub-lattice Dynamics Measurement	78
4.4.1.	Lattice Dimerization via Beam Imbalance	78
4.4.2.	Theoretical Description of the Dynamics after a Lattice Quench	79
4.4.3.	Experimental Results	81
4.5.	Shaping of the Density Distribution with Radio-Frequencies	83
4.6.	Spontaneous Density Wave Formation	85
4.7.	Conclusions	88
5.	Microscopy of coherent phenomena	91
5.1.	Talbot Effect	92
5.1.1.	Talbot Effect in Presence of a harmonic Trap	93
5.1.2.	Talbot effect in a Honeycomb/triangular Lattice	95
5.1.3.	1D Measurement	97
5.1.4.	Mott Insulator-Superfluid Transition	98
5.1.5.	Detection of magnetic Domains and Vortices	101
5.2.	Accessing the single Particle Density-Matrix	103
5.2.1.	Realizing non-local Coupling	103
5.2.2.	Coherence between Lattice Sites	105
5.2.3.	Tuning the coupling Distance \mathbf{d}	109
5.3.	Conclusions	110
6.	Multi-Frequency Lattice	113
6.1.	Tunable Lattice Geometry via Frequency Control	114
6.2.	Implementation	119
6.2.1.	Calibration of the Geometry Phase φ_g	122
6.2.2.	Phase Drifts in Time and Space	125
6.3.	Spectroscopy via Offset Modulation	126
6.4.	Generalization to 3D	129
6.5.	Conclusions	131
7.	Conclusions	133
7.1.	Outlook	134
A.	Density of states for precision thermometry	137
B.	Quantum Gas Magnification in the Schrödinger Representation	141
B.1.	General Remarks	143
C.	Band Structure Calculation with Vector Light Shift and for the Multi-Frequency Lattice	145
C.1.	Vector light Shift	145

C.2. Multi-Frequency Lattice	147
Bibliography	151

1. Introduction

Quantum simulation ([1]) refers to the study of a quantum system through the use of another quantum system which replicates the properties of the first one.

The replicating system should have two important requirements: this concerns the possibility to set with greater precision and control the initial parameters, but also the possibility to extract a higher amount of information with a measurement. The two systems should be described by the same laws, but for the rest, they might be completely unrelated to each other.

This opens a lot of possibilities: as an example, one could try to replicate a complex system using only a small number of elements in the quantum simulation, in order to see which of them have fundamental importance in the understanding of the replicated system. Another possibility is to use a quantum simulator to study the properties of a variety of novel systems, and the parameters of the ones that are found to be of interest could be then passed to a stage for the actual realization and application of new materials and tools.

Both research direction can be investigated with ultracold atoms in optical lattices ([2]). Neutral atoms can be cooled and trapped with laser light and magnetic fields, up to temperatures a few nK above the absolute zero of the temperature and in a volume with a radius of some μm . The interference pattern of two or more laser light beams can be shined on them, and as a result of the interaction between light and matter, the atoms experience a potential which depends on the local intensity of the interference pattern. Thus neutral atoms in optical lattices can be used to reproduce the behaviour of electrons in solid state materials, in particular in crystals with a periodic spatial structure. The conduction properties of such systems can be then studied in a more controlled environment, as ultracold atoms allow for the tuning of the interparticle interactions via Feshbach resonances ([3]), and optical lattices allow for an almost defect-free control of the geometry of the system. Furthermore, detection of the momentum distribution of the atoms is possible after letting the atomic cloud freely expand for a certain time. The greater lattice spacing makes even possible in some cases to access the real space distribution of the atoms while sitting in the lattice ([4, 5]).

These systems allowed to simulate fundamental models of condensed matter, e.g. Hubbard models with both bosons and fermions, for example providing a clear realization of the Mott insulator state ([6]).

Also novel systems can be simulated: this can be useful for predicting which solid state material could exhibit particular properties, or for realization of interesting systems without solid-state counterpart. For example, some topological models could be realized for the first time in optical lattices ([7–9]).

In this thesis, several experiments are reported which deal with the access to the optical lattice system as a quantum simulator. They are related to the possibility to measure new observables, as well as to the possibility to realize systems with new properties. A novel topological effect ([10]), which relates topological order with excitation rates due to a perturbation of the system, is demonstrated in the first experiments that are presented here ([11]). Topological order is described by a non-local order parameter and as a consequence is often difficult to measure, also in a cold atoms setup.

We extended the technique of lattice shaking for the realization of topological systems to include also an additional perturbation. This allowed the measurement of topological order in the system, but also of several other quantities related to the geometry of the quantum states present in the system. This represented the first demonstration of the manifestation of topology through excitation rates, but also established this method as a way to gain insight into the topological and geometrical observables in case where these observables can not be directly measured. Data taken for the same system were also used to train a machine learning algorithm which was able to obtain the order parameter from single experimental images ([12]).

In a second series of experiments, we focused on the direct access to observables. The real space distribution of the atoms can be accessed in quantum gas microscopes, by considering a 2D optical lattice and if the number of particles in a lattice site is not bigger than one, in most cases. We developed a new technique ([13]) for the direct imaging of the density distribution, which is based on a controlled evolution of the atomic matter-wave which realizes then a magnification of the original density distribution. This allowed imaging in a single-shot with sub-lattice resolution, in particular of 3D systems with a big number of particles per lattice site.

This technique could be applied not only for the real space distribution, but also for measuring coherence properties of the lattice gas with high resolution.

Finally, we also presented in this work a new technique for the generation of a lattice of tunable geometry. The geometry could be changed continuously from a triangular lattice to a graphene-like geometry, passing through a phase where the lattice resembles a boron-nitride lattice. The geometry is tuned with radio-frequency modulation and can be precisely set. This could be useful for quantum simulation of systems of different geometry with the same experimental setup. Not only, we also demonstrated dynamical control of the lattice geometry, allowing for the realization of driven systems which are quite challenging in a solid state setup.

1.1. Thesis Outline

In chapter 2 of this thesis, the experimental setup used to perform such experiments in this thesis is presented. Also the necessary theoretical framework for describing lattice systems is introduced.

In the same chapter, topological states in lattices are also described, with focus on the technique used in our experiment to produce topological states, namely lattice shaking. Results on the individuation of the topological order parameter in such a system with the use of machine learning techniques are also summarized.

In the experiments reported in chapter 3, the topology of a system is for the first time revealed through circular dichroism i.e. a difference in the excitation rates in response to a rotating force. Also the measurements of other observables performed with the same technique are presented (optical conductivity and the Wannier spread functional).

In chapter 4, we introduced the quantum gas magnifier. A first part of the chapter is concerned with theoretical considerations about quantum gas magnification of matter waves. Successively, experimental results are presented on the direct access to the density distribution in a honeycomb and a triangular lattice geometry. In particular, it is shown how the temperature of the cloud in the lattice could be directly measured, and how the imaging resolution obtained with this technique allowed even the resolution of the dynamics of the atoms within single lattice sites. In the same chapter are also presented results on the manipulation of the density distribution with radio-frequency techniques, and on the tuning of pair tunneling as the dominant dynamical process in the lattice by introducing a constant force in the system. This effect could be identified by the observation of a density-wave pattern with about twice the lattice periodicity.

In chapter 5, the possibility of the quantum gas magnifier to image with high spatial resolution coherence properties is analyzed. In particular, preliminary results on the Talbot effect are presented, and a protocol for accessing the off-diagonal parts of the single-particle density matrix is presented.

In chapter 6, a new experimental setup for generating a tunable lattice geometry is demonstrated, including characterization and calibration of the system. Results on a new type of spectroscopy performed with periodic modulation of the offset between the two sublattices of the honeycomb lattice are presented.

Chapter 7 summarizes all the results and provides a general outlook for future research directions based on the results presented in this work.

During this thesis the following articles were published:

- [11] Luca Asteria, Duc Thanh Tran, Tomoki Ozawa, Matthias Tarnowski, Benno S. Rem, Nick Fläschner, Klaus Sengstock, Nathan Goldman and Christof Weitenberg, "*Measuring quantized circular dichroism in ultracold topological matter*", Nature Physics **15** (5), 449-454 (2019).
- [12] Benno S. Rem, Niklas Käming, Matthias Tarnowski, Luca Asteria, Nick Fläschner, Christoph Becker, Klaus Sengstock, Christof Weitenberg, "*Identifying quantum phase transitions using artificial neural networks on experimental data*", Nature Physics **15**, (9), 917-920 (2019).
- [13] Luca Asteria, Henrik P. Zahn, Marcel N. Kosch, Klaus Sengstock, Christof Weitenberg, "*Quantum gas magnifier for sub-lattice-resolved imaging of 3D quantum systems*", Nature **599** (7886), 571–575 (2021).
- [14] Henrik P. Zahn, Vijay P. Singh, Marcel N. Kosch, Luca Asteria, Lukas Freystatzky, Klaus Sengstock, Ludwig Mathey and Christof Weitenberg, "*Formation of spontaneous density-wave patterns in DC driven lattices*", arXiv:2108.11917, arXiv preprints, (2021).

2. Quantum Simulation with optical lattices

This chapter has the aim of providing an overview of the concepts and experimental techniques used in the rest of this work. In the first part, the experimental setup used for loading quantum degenerate atomic clouds in optical lattice is introduced. The second part of this chapter deals with the description of these clouds in the periodic potential provided by the lattice, and with the experimental observables accessible in such a setup.

In the third part, basic quantum topology theory elements ([15]) are presented, together with the technique of lattice shaking used in this work for engineering topological states. This part is most relevant for the results of chapter 3 ([11]), where topological phases were detected for the first time using circular dichroism. With the same setup, my PhD colleague Matthias Tarnowski and I, with Benno Rem, took the data which were used for training a machine learning algorithm to recognize such topological phases from single-shot experimental images ([12]). The algorithms were programmed by Benno Rem and Niklas Käming. These results are also briefly presented at the end of this chapter.

In the same publication time-of-flight data across the Mott-Superfluid phase transition taken by Christoph Becker were analyzed with a network which identified the phase transition with greater precision than previously existing methods. We refer to the article for a discussion on these data. The analysis and numerical simulation part was performed by all mentioned authors and Nick Fläschner, and the whole work was supervised by Christof Weitenberg and Klaus Sengstock.

2.1. Cold Atoms Setup

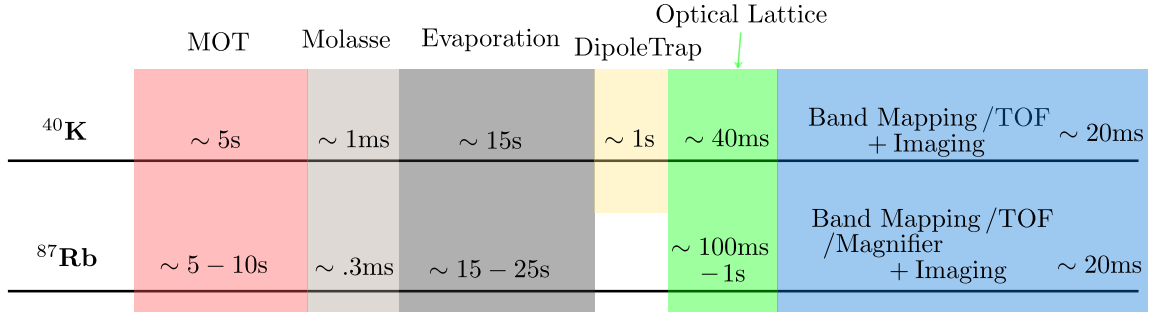


Figure 2.1.: Typical Experimental Sequences for ^{40}K and ^{87}Rb . The typical duration for the respective slots are not up to scale. After reaching quantum degeneracy with evaporative cooling, the atomic cloud is transferred to the optical lattice. In the case of ^{40}K , this happens through an intermediate passage where the cloud is solely held by an optical trap, which remains on after the lattice is ramped up. Different measurement techniques can be then applied, which will be presented later in this chapter/thesis.

In our experiment we can work with two different atomic species, namely ^{40}K and ^{87}Rb . The experiment construction is described in [16, 17] and successive developments of the machine in a number of subsequent PhD theses ([18–22]). The atomic sources are contained in a glass cell with pressure about $1 - 3 \cdot 10^{-10}\text{mbar}$. There a 2D magneto-optical trap (in short MOT) operating simultaneously for the wavelengths of ^{87}Rb and ^{40}K slows the fast thermal atoms which can be pushed down with the help of a resonant beam through a differential pumping stage to another glass cell with lower pressure ($\sim 10^{-11}\text{mbar}$), where they are trapped in a 3D MOT, also running at two wavelengths.

The experiments presented in chapter 3 were performed using ^{40}K , while the experiment presented in the rest of this work use ^{87}Rb .

In fig. 2.1 a typical experimental sequence is sketched for both situation: notice that for ^{40}K we also need ^{87}Rb for sympathetic cooling. With the MOT we reach the Doppler temperature, we go a little bit lower with the Molasses. A grey molasses for ^{40}K operates on the $D1$ transition with an additional laser source ([21, 23]). The relevant part of the level structure of the two atomic species, used for cooling and detection is illustrated in figures 2.2 and 2.3.

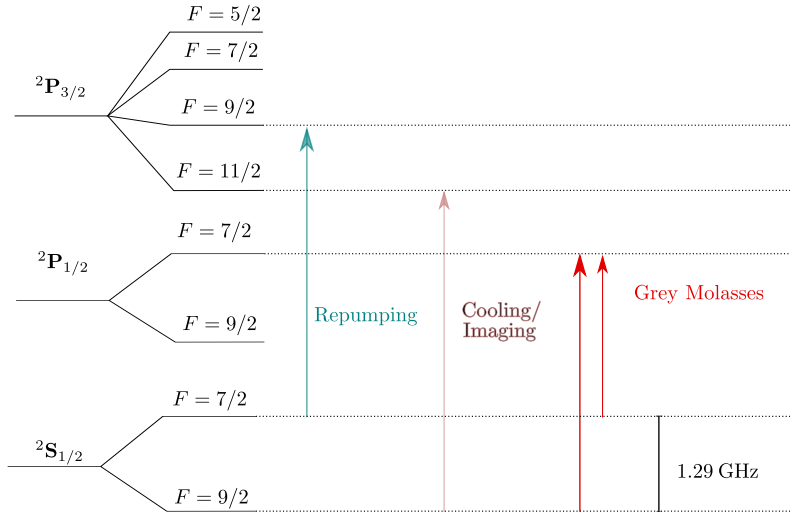


Figure 2.2.: Relevant ^{40}K Levels. The transitions used for the MOT, for the bright Molasses, for the optical pumping and imaging and for the grey Molasses are highlighted (the atomic levels are not to scale). The light operating on the cooling/imaging transition is red detuned during the MOT phase, and it also used for pushing atoms from the 2D to the 3D MOT. It is turned on resonance for optical pumping (before loading into the magnetic trap) and for absorption imaging. Different optical fibers for the different purposes bring the laser light to the atoms position. Also the repumping light is slightly detuned with respect to the shown transition in order to gain an additional cooling effect during the MOT phase. The grey molasses operates with a positive detuning on the $D1$ line and the two frequencies necessary are produced by a ~ 1.29 GHz frequency modulation with a electro-optical modulator (EOM).

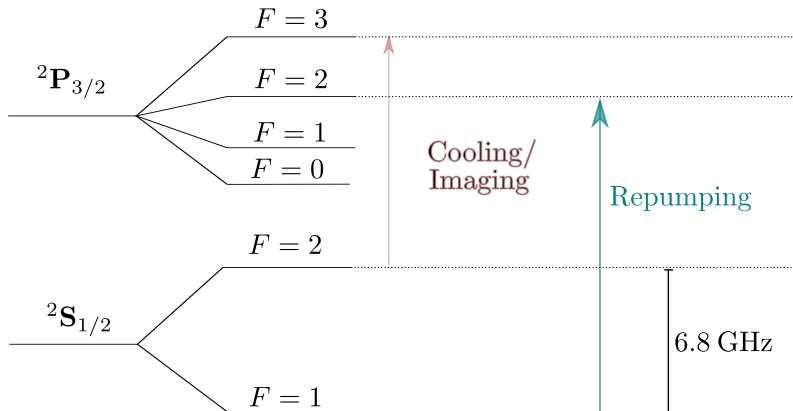


Figure 2.3.: Relevant ^{87}Rb Levels. The transitions for the MOT, for the bright Molasses, for the optical pumping and imaging are highlighted (atomic levels are not to scale). The light operating on the cooling/imaging transition is red detuned during the MOT phase, and it also used for pushing atoms from the 2D to the 3D MOT. It is turned on resonance for optical pumping (before loading into the magnetic trap) and for absorption imaging. Different optical fibers for the different purposes bring the laser light to the atoms position. Also the repumping light is kept on resonance with respect to the shown transition because the for ^{87}Rb only a smaller relative population is found in the ground state with $F = 1$.

2.1.1. Getting ultracold: The magnetic Trap

After the molasses phase, atoms are optically pumped (to the $|F = 2, m_F = 2\rangle$ state for ^{87}Rb and to the $|F = 9/2, m_F = 9/2\rangle$ state for ^{40}K) and captured without transport in a rotationally symmetric magnetic trap. A magnetic trap exploits the coupling between the magnetic moment of atoms and a magnetic field for creating a local potential minimum. A particle in the internal state $|F, m_F\rangle$, moving adiabatically in a magnetic field experiences an energy shift E_m given by:

$$E_m(\mathbf{r}) = -g_F m_F \mu_B |\mathbf{B}(\mathbf{r})| \quad (2.1)$$

where $\mathbf{B}(\mathbf{r})$ is the magnetic field vector, g_F the Landé factor, μ_B the Bohr magneton. It follows that if $g_F m_F > 0$ ("weak-field seeking states") the potential has a local minimum in correspondence of the local minima of $|\mathbf{B}(\mathbf{r})|$, where the atoms can be trapped (recall that local maxima can not be produced in a static field configuration, as enunciated in the Earnshaw theorem, and therefore atoms in "high-field seeking" states can not be trapped).

Then we change the magnetic potential to a cigar-shaped form, with tighter confinement in the xy plane, in order to get bigger collision rates during evaporative cooling. This allows, in 10 to 30 seconds, to reach quantum degeneracy ([16]).

Evaporation is performed by ramping down the frequency of a RF shield from $\sim 15\text{MHz}$ to about 1MHz (^{40}K) or $\sim 90\text{kHz}$ (^{87}Rb).

The magnetic trap is a hybrid between the cloverleaf and the $4D$ design, and can be described by the parameters B_0, B_1 and B_2 ([24, 25]):

$$\mathbf{B}(\mathbf{r}) = B_0 \begin{pmatrix} 0 \\ 0 \\ 1 \end{pmatrix} + B_1 \begin{pmatrix} x \\ -y \\ 0 \end{pmatrix} + B_2 \begin{pmatrix} -xz \\ -yz \\ z^2 + \frac{1}{2}(x^2 + y^2) \end{pmatrix} \quad (2.2)$$

Taylor expansion up to second order in the spatial coordinates yields:

$$|\mathbf{B}(\mathbf{r})| \simeq B_0 + \frac{1}{2}\rho^2(B_1^2/B_0 - B_2/2) + \frac{1}{2}z^2 B_2 \quad (2.3)$$

where $\rho = \sqrt{x^2 + y^2}$, and $B_0 > 0$ was assumed. It results that a small B_0 is desirable for high trap frequencies, useful for fast evaporation and for the experiments introduced in chapter 4. Notice that a too small B_0 might result in Majorana spin-flips and losses during evaporation, and that the range in which the Taylor expansion is a good approximation decreases for smaller values of B_0 .

The terms B_1 and B_2 are mostly due to the current flowing in the inner coils (cloverleaf/ $4D$), with currents of up to 110A , whereas the term B_0 is referred to as trap "bottom" (as it sets the energy separation between different states in the center of the trap) or as "quantization field".

The quantization field is mainly produced by a current sent through the outer Helmholtz coils for the experiments with ^{40}K , or by additional compensation coils for the experiments with ^{87}Rb , performed at a lower value of B_0 (we notice in this case a dependence of the resonance frequency between different m_F states also as a function of the current in the inner coils, and conclude that their produced magnetic field must also have a component in z direction).

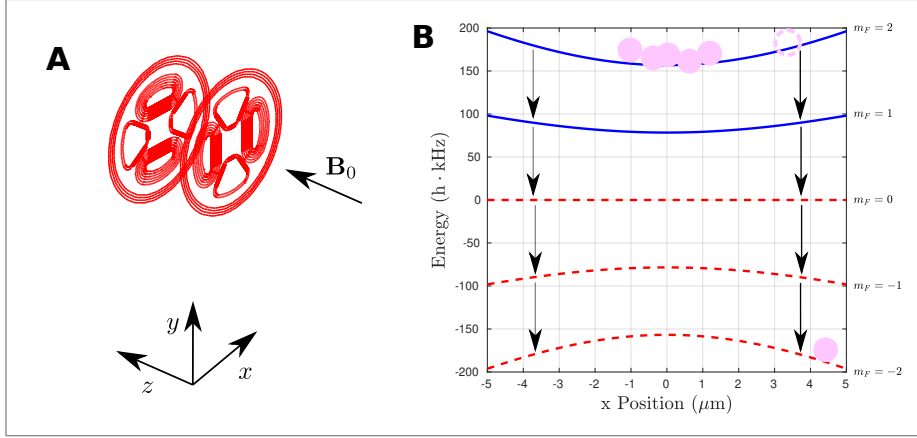


Figure 2.4.: Schematics of the Magnetic Trap and energy Levels.. In **A**, the trap coils, of the hybrid form cloverleaf-4D, are sketched (adapted from [16, 25]). The outer coils provide the gradient for the MOT (in an "anti-Helmholtz" configuration) and the quantization field \mathbf{B}_0 (in the Helmholtz configuration). Additional coils (not shown) can be used to move the center of the trap potential and to adjust the quantization field. In **B**, potential energy obtained for a current of 110A and a quantization field $B_0 = 0.11\text{G}$ for the different m_F states of ^{87}Rb in the $F = 2$ ground-state manifold. Only the states $m_F = 1$ and $m_F = 2$ can be trapped: a radio frequency, resonant only at a given distance from the trap center, can be used to remove the hotter atoms from the cloud.

The magnetic trap setup is sketched in figure 2.4, along with the resulting potential as seen by ^{87}Rb atoms in the different m_F states of the $F = 2$ manifold (we will always refer in the following to the ground state $5^2\text{S}^{1/2}$).

The in-plane trap frequency ω and along the z direction can be calculated as:

$$\begin{aligned}\omega &= \sqrt{g_F m_F \mu_B (B_1^2 / B_0 - B_2 / 2) / m} \\ \omega_z &= \sqrt{g_F m_F \mu_B B_2 / m}\end{aligned}\tag{2.4}$$

A 110A current in the inner coils produces $B_1 = 168.65\text{G/cm}$, $B_2 = 71.2 \cdot 10^4 \text{ G/cm}^2$. With an offset field of $B_0 = 0.11\text{G}$, and notating the useful relation for converting magnetic fields into energy for $F, m_F = 2, 2$ (for ^{87}Rb) $g_F m_F \mu_B = 1.4 \text{ hMHz/G}$, one gets a relatively high in-plane confinement: $\omega / (2\pi) = 640\text{Hz}$ while $\omega_z / 2\pi$ is much smaller ($\sim 11\text{Hz}$).

Similar trap frequencies can be reached by for ^{40}K in the $F = 9/2, m_F = 9/2$ ground state.

The measurements of chapter 4 are particularly sensitive on the magnetic trap form and we noticed the presence of a small ellipticity ($< 1\%$) which we attribute to the presence of gravity in y direction breaking (partially) the rotational symmetry.

We evaporate a mixture of ^{87}Rb and ^{40}K atoms in the experiments presented in chapter 3, where ^{87}Rb atoms are used for sympathetic cooling of ^{40}K atoms, with an offset field of $\simeq 1.5\text{G}$. In the experiments with ^{87}Rb (in the remaining chapters) we evaporate in a deep magnetic trap of typically $\sim 600\text{Hz}$, with an offset field of $B_0 \simeq 0.1\text{G}$, obtaining a BEC of up to $\sim 10^5$ atoms.

The experiments with ^{40}K were then performed after removing the ^{87}Rb atoms with a resonant light pulse, and loading the ^{40}K atoms in a crossed optical dipole trap. The optical lattice was ramped up while leaving on the dipole trap. The experiments with ^{87}Rb were performed after ramping down the magnetic trap to the desired depth and by ramping up directly the lattice while leaving on the magnetic trap.

2.2. Bloch Bands in optical Lattices

Quantum simulation is the idea proposed by Feynman ([1]) that a controllable quantum system can be used to replicate a more complex one, to get insight into its properties. To this end, in order to study real-solid state materials in a more controllable and accessible fashion optical lattices come in and provide an almost defect-free periodic potential for neutral cold atoms, mimicking the one that electrons see in a real crystal ([26, 27]). Importantly, with cold atoms one can also get a much richer variety of quantum statistics as one is not bound by the constraint of two internal states (electrons are fermionic particle that can appear as either spin-up or spin-down), but one could use spin-polarized fermions, or tune the relative population in the two states, as long as fermionic particles are concerned [28]. One could also use Bose-Einstein condensates ([29]) for studying bosonic excitation of electronic systems of for realizing new phases of matter impossible or very difficult in solid-state matter. Also mixtures of bosons and fermions can be studied ([17, 30, 31]).

Optical lattices can be realized by interference of two (or more) different laser beams, with intensities I_1 and I_2 and wavevectors \mathbf{k}_1 and \mathbf{k}_2 . The resulting intensity pattern can therefore be written as:

$$I = I_1 + I_2 + 2|\boldsymbol{\sigma}_1 \cdot \boldsymbol{\sigma}_2| \sqrt{I_1 I_2} \cos((\mathbf{k}_1 - \mathbf{k}_2) \cdot \mathbf{r} - \theta_{12}) \quad (2.5)$$

where $\boldsymbol{\sigma}_{1,2}$ are the complex polarization vectors, and $\theta_{12} = \arg(\boldsymbol{\sigma}_1^* \boldsymbol{\sigma}_2)$ is their relative phase.

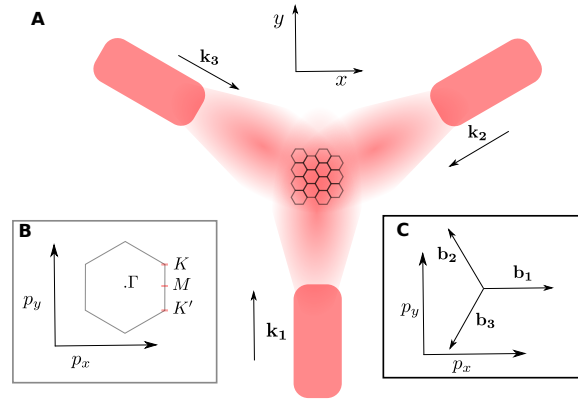


Figure 2.5.: Schematics of the optical Lattice Setup. In **A** the wavevectors of the three laser beams, lying in the xy plane and denoted as $\mathbf{k}_{1,2,3}$, are represented. Laser light is brought to the atoms position with polarization maintaining fibers. Intensity stabilization and fast turn-off are obtained via Acousto-Optical Modulators (AOMs, not shown). In the inset **B** the orientation of the Brillouin Zone and the symmetry points Γ , K , K' , M are to be seen. In the inset **C** the reciprocal lattice wavevectors $\mathbf{b}_{1,2,3}$ are represented.

In our setup we have three beams propagating in a plane aligned vertically in the lab (x - y in our coordinate system) and interfering with each other at a 120° angle. They are produced from a single laser source (Mephisto MOPA 25 NE) at wavelength

$\lambda = 1064\text{nm}$ and brought to the experiment table via three independent polarization maintaining fibers. The laser beams are focused at the position of atoms in the magnetic trap with a waist of about $160\mu\text{m}$ ([21]).

For each of the possible beam pairs an interference term of the form expressed in equation 2.5 appears, for a total of three relevant wavevectors $\mathbf{b}_{1,2,3}$ characterizing the lattice. The convention used in this work for defining the beam wavevectors and the reciprocal lattice wavevectors is presented in figure 2.5. Note that the vector triple $\mathbf{b}_{1,2,3}$ appears to be rotated 60° with respect to $\mathbf{k}_{1,2,3}$ and that $|\mathbf{b}_{1,2,3}| = \sqrt{3}|\mathbf{k}_{1,2,3}|$, where $|\mathbf{k}_{1,2,3}| = 2\pi/\lambda$.

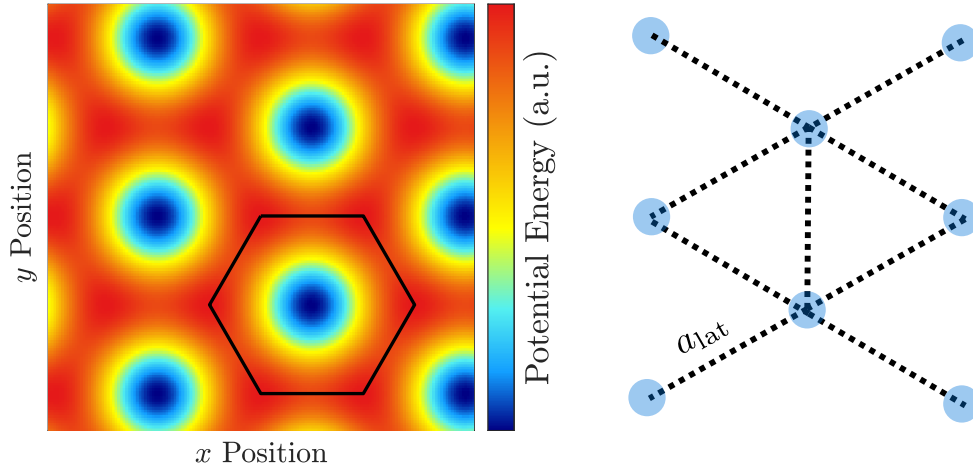


Figure 2.6.: Triangular lattice Potential. Potential obtained with the expression $V(\mathbf{r}) = E_0 - 2\sum_i V_i \cos(\mathbf{b}_i \mathbf{r})$, with $V_1 = V_2 = V_3$. The black hexagon marks (a possible choice of) the unit cell. Minima of the lattice potential are separated by a distance $a_{\text{lat}} = 2/3\lambda = 709\text{nm}$, with λ the laser light wavelength, and the area of the unit cell is $A_{\text{cell}} = \frac{2}{3\sqrt{3}}\lambda^2$.

When the beams are out of plane (the xy plane, the plane of the lattice) linearly polarized ($\boldsymbol{\sigma}_i^* \cdot \boldsymbol{\sigma}_j = 1$) the resulting potential seen by the atoms can be obtained by considering that the potential energy shift is proportional to the light intensity $V(\mathbf{r}) \propto -I(\mathbf{r})$ (with a negative constant, because the light is red-detuned).

The potential can then be written as:

$$E_{\text{pot}} = E_0 - 2\sum_i V_i \cos(\mathbf{b}_i \cdot \mathbf{r}) \quad (2.6)$$

The index i takes the values $\{1, 2, 3\}$ unless otherwise specified. $V_{1,2,3}$ are referred to as the depths of the corresponding 1D lattices. In the symmetric case, where $V_1 = V_2 = V_3 = V$, a triangular lattice, with one potential minimum per unit cell, is formed ([32]). If $V_1 = V_2 = V_3 = V$, we refer to V as the lattice depth of the 2D lattice. This potential is shown in figure 2.6.

$V_{1,2,3}$ and V are expressed in units of the recoil energy E_r which sets the typical energy scale in a lattice, and is defined as:

$$E_r \equiv \frac{(\hbar|\mathbf{k}_i|)^2}{2m} \quad (2.7)$$

where m is the mass of the particles. For ^{87}Rb , $E_r/h = 2.03$ kHz and for ^{40}K , $E_r/h = 4.41$ kHz.

When all the beams are instead in-plane linearly polarized ($\boldsymbol{\sigma}_i^* \cdot \boldsymbol{\sigma}_j = -\frac{1}{2}$ (for all $i \neq j$)) the resulting potential seen by the atoms can be written as:

$$E_{\text{pot}}(\mathbf{r}) = E_0 + 2 \sum V_i \cos(\mathbf{b}_i \mathbf{r}) \quad (2.8)$$

The potential in this case is characterized by two equivalent local minima. In the symmetric case $V_1 = V_2 = V_3$, also here a 120° rotation symmetry is present. Notice that qualitatively the difference with the triangular lattice is just in the minus sign in front of the potential. This potential is plotted in figure 2.7.

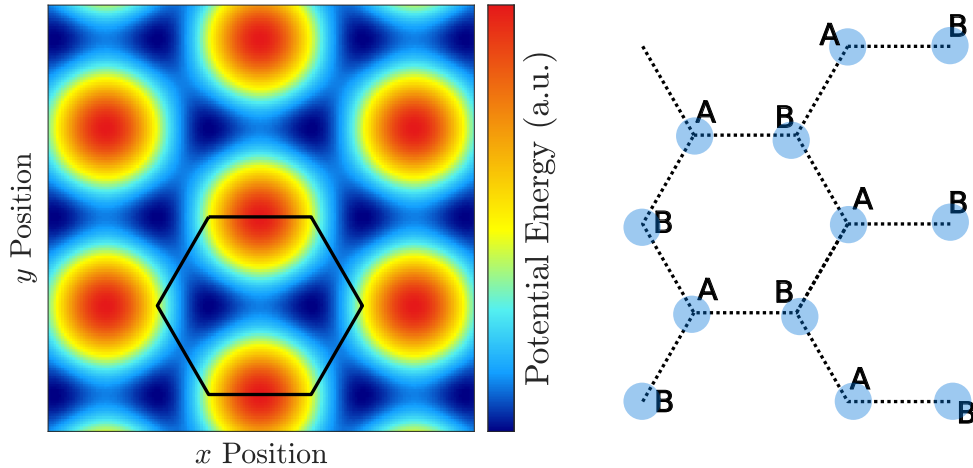


Figure 2.7.: Honeycomb optical lattice potential. Potential obtained with the expression $E_{\text{pot}}(\mathbf{r}) = E_0 + 2 \sum_i V_i \cos(\mathbf{b}_i \mathbf{r})$, with $V_1 = V_2 = V_3$. The black hexagon marks (a possible choice of) the unit cell. In it, two degenerate local minima can be found (indicated by A and B in the schematics). Nearest neighbours are spaced by a distance $\frac{2}{3\sqrt{3}}\lambda = 410\text{nm}$. Next-nearest-neighbours are spaced by $a_{\text{lat}} = 709\text{nm}$, and the area of the unit cell is $A_{\text{cell}} \frac{2}{3\sqrt{3}}\lambda^2$ as for the triangular lattice, being that the lattice periodicity is given only by the reciprocal lattice wavevectors which are fixed.

The equivalence of the two minima, and the inversion symmetry of the potential can be lifted by using elliptically polarized beams ([33]). A symmetric (under a 120° rotation) potential can be obtained by choosing elliptical polarization of at least two beams. By e.g. rotating all polarization vectors out of plane by the same angle θ and by choosing the relative phases between the in-plane and out-of-plane polarization components $\alpha_{1,2,3} = 0, 2\pi/3, 4\pi/3$ one obtains $\boldsymbol{\sigma}_i^* \cdot \boldsymbol{\sigma}_j = -\frac{1}{2} \cos(\theta)^2 + \sin(\theta)^2 e^{i2\pi/3}$ for $(i, j) = (1, 2), (2, 3), (3, 1)$ and the resulting potential seen by the atoms can be written as

$$E_{\text{pot}} = E_0 + 2 \sum V_i \cos(\mathbf{b}_i \cdot \mathbf{r} + \varphi_g/3) \quad (2.9)$$

where

$$\begin{aligned} \varphi_g/3 &\equiv \arg(-\boldsymbol{\sigma}_i^* \cdot \boldsymbol{\sigma}_j) \\ &= \arctan\left[\sin(2\pi/3) \sin(\theta)^2 / \left(\frac{1}{2} \cos(\theta)^2 - \sin(\theta)^2 \cos(2\pi/3) \right) \right] \end{aligned} \quad (2.10)$$

This potential resembles the electronic potential of boron-nitride, and an example for a particular sublattice offset is presented in figure 2.8.

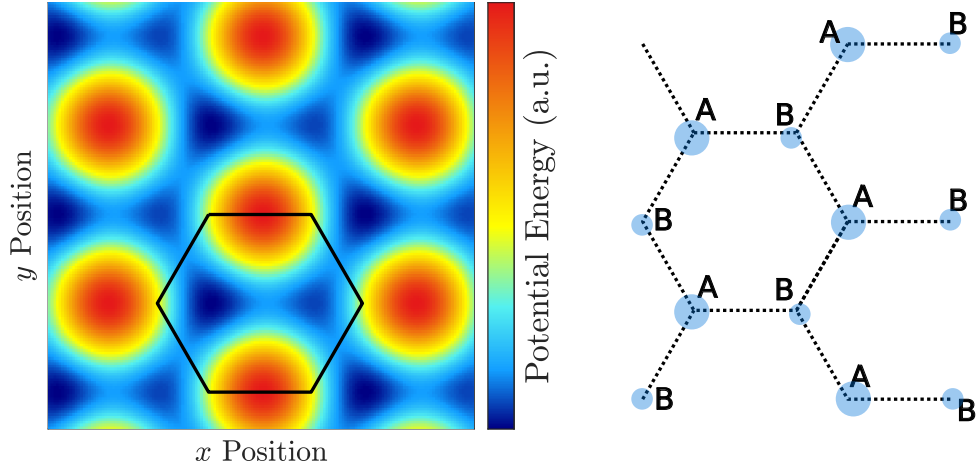


Figure 2.8.: Boron-nitride Potential. Optical lattice as described by $\sum_i \cos(\mathbf{k}_i \cdot \mathbf{r} + \varphi_g/3)$, with $\varphi_g = \frac{1}{20}\pi$. This lifts the degeneracy between the two minima in the unit cell (A and B , shown in the schematics). The black hexagon marks (a possible choice of) the unit cell. As in figure 2.7, nearest neighbours are spaced by a distance $\frac{2}{3\sqrt{3}}\lambda = 410\text{nm}$, and next-nearest-neighbours are spaced by $a_{\text{lat}} = 709\text{nm}$, and the area of the unit cell is $A_{\text{cell}} \frac{2}{3\sqrt{3}}\lambda^2$.

2.2.1. Band Structure Calculation

In a periodic potential, one can exploit the translational symmetry of the lattice and search for a solution of the Schrödinger equation that satisfies ([34]):

$$\Psi(r + a_i) = e^{iq a_i} \Psi(r) \quad (2.11)$$

where q is the quasimomentum of the wavefunction and it is a good quantum number. We notice that $e^{i(q+b)a_j} = e^{i(q)a_j + 2\pi} = e^{iqa_j}$ therefore the quasimomentum can be taken just in the unit cell of the reciprocal space, the Brillouin Zone. Therefore the spectrum of such systems is said to exhibit bands, the parts of the dispersion characterized by the same band index n . The energy difference between consecutive bands is called band gap and it determines, in real solid, important conduction properties, like being conducting or insulating materials (when electrons fill up energy bands up to a band gap, it is insulating). Bands might touch at some point in the Brillouin zone.

We get the band structure calculation for our lattice by diagonalization of the Hamiltonian in the plane-wave basis $|\mathbf{Q}\rangle = \int e^{-i\mathbf{Q}\cdot\mathbf{r}} d\mathbf{r} |\mathbf{r}\rangle$ for every q in the Brillouin zone. Only waves with wavevector $\mathbf{Q} = \mathbf{q} + n\mathbf{b}_1 + m\mathbf{b}_2$, with n, m integers, are coupled with each other. In this subspace the lattice potential can be rewritten as:

$$\begin{aligned} E_{\text{pot}}(\mathbf{r}) &= E_0 + 2 \sum_i V_i \cos(\mathbf{b}_i \cdot \mathbf{r} + \varphi_g/3) \\ &\rightarrow E_0 + \sum_{n,m} \sum_i |\mathbf{Q} + \mathbf{b}_i\rangle V_i e^{-i\varphi_g/3} \langle \mathbf{Q} | + \text{h.c.} \end{aligned} \quad (2.12)$$

The diagonal part of the lattice Hamiltonian in the plane-wave basis can be written as

$$E_{\text{kin}} = \frac{(\hbar\mathbf{Q})^2}{2m}. \quad (2.13)$$

Plotting the eigenvalues as a function of quasimomentum we get the band structure (an example is shown in figure 2.9).

In many cases the band structure can be captured by a tight-binding approximation, which can provide a more direct insight into the system. The lowest band of the triangular lattice can be well described (for $V > 0.5E_r$) by a tight-binding model of s -orbitals localized at the position of the lattice minima:

$$H_{\text{tb}}/\hbar = - \sum_{\langle i,j \rangle} J \hat{\psi}_i^\dagger \hat{\psi}_j \quad (2.14)$$

where J is the tunneling coupling between nearest-neighbours ($\langle \rangle$) lattice sites with indexes i, j , and $\hat{\psi}_i^\dagger, \hat{\psi}_j$ are creation/annihilation operators acting on sites i and j respectively.

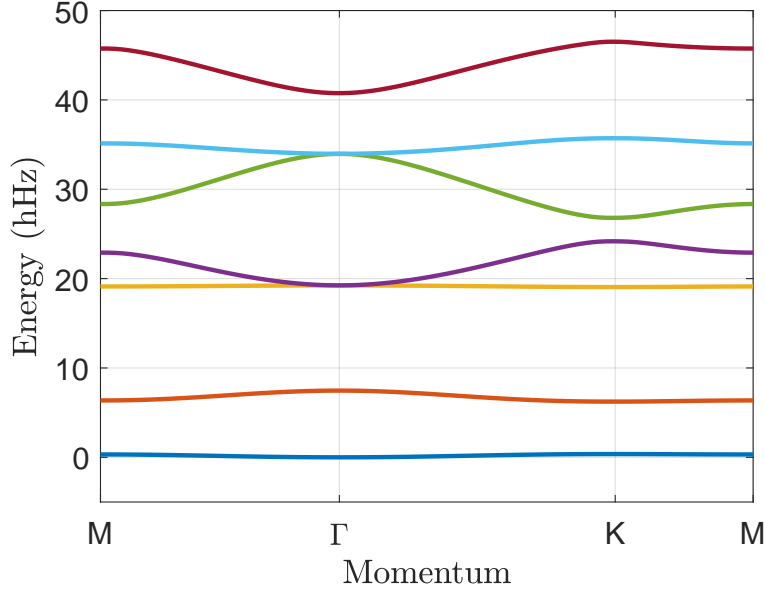


Figure 2.9.: Energy levels in a Boron Nitride Optical lattice. Energy as a function of quasimomentum along the paths $M\Gamma$, ΓK , KM . Different colors corresponds to different bands. Lattice potential obtained for $V = 8.63E_r$, and for polarization angles $\theta = 9^\circ$ and $\alpha_{1,2,3} = 0, 2\pi/3, 4\pi/3$. Notice that the first two bands are almost flat and that the energy separation corresponds roughly to the sublattice offset Δ .

For the honeycomb lattice with two local minima in the unit cell, the tight-binding approximation comprises additional terms:

$$H_{\text{tb}}/\hbar = - \sum_{\langle i,j \rangle} J \hat{\psi}_i^\dagger \hat{\psi}_j - \sum_{\langle\langle i,i \rangle\rangle} J_{AA} \hat{\psi}_i^\dagger \hat{\psi}_j - \sum_{\langle\langle j,j \rangle\rangle} J_{BB} \hat{\psi}_i^\dagger \hat{\psi}_j + \sum_i \frac{\hbar\Delta}{2} \hat{\psi}_i^\dagger \hat{\psi}_i - \sum_j \hbar \frac{\hbar\Delta}{2} \hat{\psi}_j^\dagger \hat{\psi}_j \quad (2.15)$$

where $\langle i, j \rangle$ are index pairs associated to nearest-neighbours lattice sites, corresponding to the two different sublattices A and B . $\langle\langle i, i \rangle\rangle$ ($\langle\langle j, j \rangle\rangle$) are index pairs associated to next-nearest-neighbours lattice sites, corresponding to the same sublattice A (B), and J_{AA} (J_{BB}) the corresponding tunneling coupling strength. Δ is the sublattice offset. The Honeycomb lattice with $\Delta = 0$ mimics the potential experienced by electrons in a graphene sheet ([35]).

Another important information that we get from the diagonalization are the eigenvectors, in form of a sum of plane-waves $|\mathbf{q} + n\mathbf{b}_1 + m\mathbf{b}_2\rangle$ weighted by the Bloch coefficients $c_{m,n}^B(\mathbf{q})$. (B is the band index)

We usually want to look at the eigenvectors in real space; these can be gotten by performing the transformation

$$\Psi^B(\mathbf{r}) = \sum_{m,n} c_{m,n}^B(\mathbf{q}) e^{-i(\mathbf{q} + n\mathbf{b}_1 + m\mathbf{b}_2) \cdot \mathbf{r}} \quad (2.16)$$

The ground state density distribution for the symmetric potentials we just presented is shown in figure 2.10.

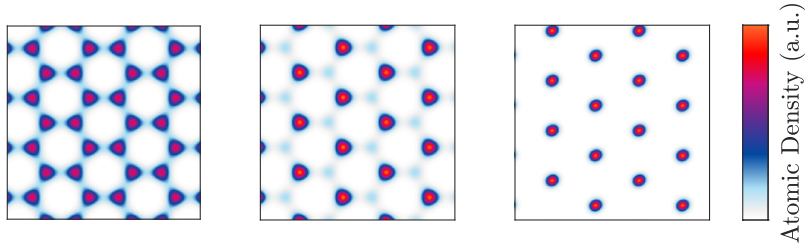


Figure 2.10.: Eigenstates in real space. Density profile of the ground-state (located at the Γ point) for the three symmetric lattice geometries: graphene-like, boron-nitride-like, and triangular lattice.

2.2.2. Time-of-Flight

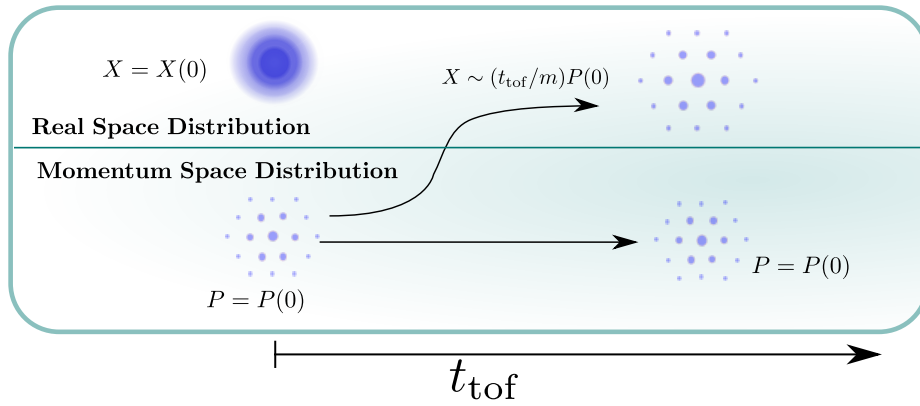


Figure 2.11.: Sketch of the time evolution of dynamical quantities during time of flight. The arrows indicate the transfer of the information about the momentum distribution: while the momentum distribution remains constant, it also gets mapped to the real space distribution.

The momentum distribution of the atoms can be measured via the so-called time-of-flight. It consists in the abrupt switch off of all optical and magnetic potentials, after which the atoms are exposed only to gravity for a time typically of the order of ~ 20 ms. We can look at the real-space distribution after time-of-flight by considering the time evolution of the position operator X , as dictated by the free-particle Hamiltonian. It is:

$$\partial_t X(t) = \frac{i}{\hbar} [H, X] = \frac{i}{\hbar} \left[\frac{P^2}{2m}, X \right] = \frac{P}{m} \quad (2.17)$$

Where P is the momentum operator of the particles of mass m . Because $[H, P] = 0$ then $P = P(0)$ at all times; one gets in the end:

$$X(t_{\text{tof}}) = X(0) + \frac{t_{\text{tof}} P(0)}{m} \quad (2.18)$$

For large enough t_{tof} , in the so-called far-field limit, $X(t_{\text{tof}}) \sim \frac{t_{\text{tof}}P(0)}{m}$; this basically says that the original momentum distribution at $t = 0$ in the lattice has been mapped to the real-space distribution, which can then be recovered via optical imaging (as sketched in figure 2.11). The presence of the $X(0)$ operator in the final expression sets a limit on the momentum space resolution δp which can be estimated by substituting $X(0)$ with the initial cloud size σ_{sys} :

$$\delta p \sim m \frac{\sigma_{\text{sys}}}{t_{\text{tof}}} \quad (2.19)$$

In the presence of gravity along the x -direction $\partial_t P = \frac{i}{\hbar}[mgX, P] = -mg$. This produces:

$$X(t_{\text{tof}}) = X(0) + \frac{t_{\text{tof}}P(0)}{m} - \frac{1}{2}gt_{\text{tof}}^2 \quad (2.20)$$

where the $\frac{1}{2}gt_{\text{tof}}^2$ term, being a real number, just shifts down the whole distribution (as compared with the case in absence gravity), without introducing any "distortion". In practice, this is often a limiting factor because it limits the maximal t_{tof} achievable (before the atoms get out of the field of view of the optical system), and hence the smallest achievable δp .

2.2.3. $T/4$ Evolution in a Harmonic Trap

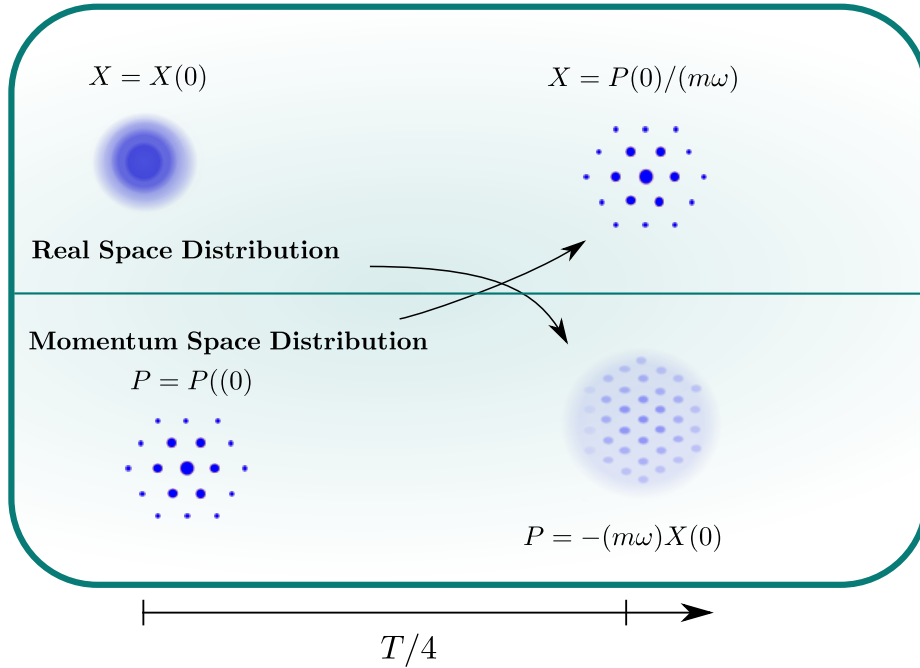


Figure 2.12.: Sketch of the time evolution of dynamical quantities during a $T/4$ hold time in a harmonic trap with period T . The arrows indicate the transfer of the information about the momentum distribution, which gets mapped to the real space distribution, and vice versa.

In presence of a high resolution imaging system, another technique is often used to image the momentum distribution ([36, 37]): that of letting the system evolve in a harmonic potential for a quarter of the trap period, denoted as $T/4$ (sketched in figure 2.12).

There the equations of motion look like:

$$\begin{aligned}\partial_t X &= P/m \\ \partial_t P &= -m\omega^2 X\end{aligned}\tag{2.21}$$

With solutions:

$$\begin{aligned}X(t) &= \cos(\omega t)X(0) + \frac{1}{m\omega} \sin(\omega t)P(0) \\ P(t) &= \cos(\omega t)P(0) - m\omega \sin(\omega t)X(0)\end{aligned}\tag{2.22}$$

At $t = T/4$, $X(t) = \frac{1}{m\omega}P(0)$, realizing perfectly the momentum distribution i.e. without the $X(0)$ term which limits the resolution in time-of-flight experiments. The finite optical resolution determines then δp and hence a good resolution imaging becomes necessary. In our experiment we don't have such a high optical resolution, but we mention this technique at this point because we are going to use it as an intermediate step for the experiments presented in chapter 4.

This technique is also at the basis of phase space manipulation techniques on an ensemble of particles [38–40] for applications like e.g. cooling to low temperatures in the kinetic degrees of freedom.

2.2.4. Band Mapping

When ramping down adiabatically the lattice depth, lattice states characterized by quasimomentum q and band index n are mapped to the momentum distribution, which can be accessed using a subsequent time-of-flight, as just explained. In practice, because often it is very difficult to remove all harmonic confinements during this procedure (especially since the lattice itself provides one), the information over the quasimomentum gets washed out and only the information about the relative population of the bands can be obtained.

2.2.5. Optical Imaging

At the end of each experimental sequence, we measure the final density distribution of the atoms in the $x - y$ plane via absorption imaging ([41]). A light beam propagating along the z -direction resonant with the $F = 2 \rightarrow F = 3$ transition is shined for $50\mu\text{s}$ on the atoms, which absorb photons from the beam and scatter them in all directions.

The light intensity at the position of the atoms is then imaged with a $4f$ imaging on a CCD camera, with an effective pixel size (taking into account an optical magnification of about 2) of $6.04\mu\text{m}$.

A second image is taken in absence of the atoms, to get the reference signal. The density of the atoms can then be recovered by usage of the Beer-Lambert law, by taking the logarithm pixelwise of the ratio between the two signals.

This measurement is destructive i.e. a new measurement can be taken anew by going through all the steps of the sequence from the beginning.

In a post-processing step, a defringing algorithm is applied to the experimental images in order to remove artifacts due to interference effects ([22, 24, 42, 43]).

2.3. Floquet Engineering of topological States

2.3.1. Quantum topology

In differential geometry, the Gauss-Bonnet theorem possesses fundamental importance as it connects a geometrical property, the gaussian curvature of a compact 2D Riemannian manifold M , to a topological property, the Euler characteristics.

In particular, if the manifold has no border, then the (topological) χ Euler characteristics is obtained simply by integration of the (geometrical) gaussian curvature K :

$$\int_M K dA = 2\pi\chi \quad (2.23)$$

Note that χ is an object which can take up only integer values.

In quantum mechanics, a geometry can also be defined, in the Hilbert space in which quantum states live.

Taking a manifold of states $|\psi(\boldsymbol{\lambda})\rangle$ dependent on the parameters $\boldsymbol{\lambda} = [\lambda_1, \lambda_2, \dots, \lambda_n]$ one can define a distance between quantum states ([44]):

$$ds^2 \equiv 1 - |\langle \psi(\boldsymbol{\lambda}) | \psi(\boldsymbol{\lambda} + d\boldsymbol{\lambda}) \rangle|^2 \quad (2.24)$$

where $d\boldsymbol{\lambda}$ is a small variation of the parameter $\boldsymbol{\lambda}$. States with bigger overlap are "closer" to each other. One can then derive the expression for the quantum geometric tensor $\chi_{\alpha\beta}(\boldsymbol{\lambda})$ as:

$$\begin{aligned} ds^2 &= d\lambda_\alpha \chi_{\alpha\beta}(\boldsymbol{\lambda}) d\lambda_\beta \\ \chi_{\alpha\beta}(\boldsymbol{\lambda}) &= \langle \partial_\alpha \psi(\boldsymbol{\lambda}) | (1 - |\psi(\boldsymbol{\lambda})\rangle \langle \psi(\boldsymbol{\lambda})|) | \partial_\beta \psi(\boldsymbol{\lambda}) \rangle \end{aligned} \quad (2.25)$$

with the simplified notation $\partial_\alpha \equiv \partial_{\lambda_\alpha}$.

$\chi_{\alpha\beta}(\boldsymbol{\lambda})$ is a Hermitian matrix and can be decomposed into a real, symmetric part and a complex, antisymmetric part related to the quantum metric $g_{\alpha\beta}$ and to the Berry curvature $\Omega_{\alpha\beta}(\boldsymbol{\lambda})$:

$$\begin{aligned} g_{\alpha\beta}(\boldsymbol{\lambda}) &= \text{Re}[\chi_{\alpha\beta}(\boldsymbol{\lambda})] \\ \Omega_{\alpha\beta}(\boldsymbol{\lambda}) &= -2 \text{Im}[\chi_{\alpha\beta}(\boldsymbol{\lambda})] \end{aligned} \quad (2.26)$$

The quantum metric $g_{\alpha\beta}(\boldsymbol{\lambda})$ is the relevant part of the geometric tensor when calculating distances between states (note that it is positive definite, and the distance between two states is always greater than zero unless they are identical) and the Berry curvature $\Omega_{\alpha\beta}(\boldsymbol{\lambda})$ is related to the phase picked up while following adiabatically a close loop in parameter space ([45]). More precisely, there is a component to this phase which is only determined by the geometry of the eigenstates, and it is called Berry phase and can be calculated by integrating the Berry curvature in the area enclosed by the loop in parameter space.

Although seemingly abstract quantities, these objects determine important system properties (e.g. the quantum metric provides a connection between geometric and conduction properties, as discovered in [46]), and could be also measured directly in experiments. The quantum geometric tensor was measured in photonic system and in coupled qubits in diamond ([47, 48]), and the Berry curvature in coupled qubits ([49]) too and in an optical lattice experiment performed in our group ([33]).

We are interested in the case where $\boldsymbol{\lambda} = \mathbf{q}$, i.e. the parameter space is represented by the quasimomentum in a Bloch band. The states $|\psi(\mathbf{q})\rangle$ we are considering are the eigenstates of the lattice Hamiltonian H_l in the lowest band (but the same considerations will hold also for another band, or for a set of bands). There the Berry curvature of the lowest band takes the form:

$$\Omega_{xy}(\mathbf{q}) = \partial_{q_x} \langle \psi(\mathbf{q}) | \partial_{q_y} | \psi(\mathbf{q}) \rangle - \partial_{q_y} \langle \psi(\mathbf{q}) | \partial_{q_x} | \psi(\mathbf{q}) \rangle \quad (2.27)$$

which can be recast in:

$$\Omega_{xy}(\mathbf{q}) = \text{Im} \sum_{n>1} \frac{\langle \psi(\mathbf{q}) | \partial_{q_x} H_l | \psi^n(\mathbf{q}) \rangle \langle \psi^n(\mathbf{q}) | \partial_{q_y} H_l | \psi(\mathbf{q}) \rangle}{(E - E_n)^2} \quad (2.28)$$

The Berry curvature of a Bloch band in the Brillouin zone satisfies the Chern-Gauss-Bonnet theorem ([50]), and its integral on the Brillouin zone (which has no boundary, because of the periodicity in momentum space) is also proportional to an integer quantity, the Chern number C .

This object dictates important transport properties like the quantum Hall effect ([51–53]) and the presence of edge states ([54]).

An important point to notice is that, for time-reversal symmetric systems, $\Omega_{xy}(\mathbf{q}) = -\Omega_{xy}(-\mathbf{q})$. Therefore in this case the integral of $\Omega_{xy}(\mathbf{q})$ over the Brillouin zone vanishes.

Time-reversal symmetry is broken e.g. by a magnetic field in the system:

$$H_{\text{kin}} = \frac{(P - \frac{e}{c} A_{\mathbf{B}})^2}{2m} \quad (2.29)$$

where c is the speed of light, $A_{\mathbf{B}}$ is the vector potential which generates the magnetic field \mathbf{B} , and for particles with charge e . This explains why one can get a Chern number in the quantum Hall effect and why the transverse conductance must be integer quantized. It was the insight of Haldane ([55]), who noticed that the main ingredient for getting the quantum Hall effect is the breaking of time-reversal symmetry, and not the magnetic field.

Neutral atoms do not experience the Lorentz force in presence of a magnetic field. In the next section, we explain how breaking of time-reversal symmetry can be achieved with Floquet Engineering.

2.3.2. Description of time-periodic Systems

Let's assume we drive periodically a system with angular frequency ω_F :

$$H(t + T_F) = H(t) \quad (2.30)$$

where $T_F = \frac{2\pi}{\omega_F}$ is called Floquet period ([56]).

Then one could try to describe the time-evolution according to a static Hamiltonian, the Floquet Hamiltonian H_F which satisfies:

$$e^{iH_F T_F} = U(0, T) \quad (2.31)$$

H_F might now possess new properties like breaking of time-reversal symmetry, which static Hamiltonians can't have. This is a powerful tool for engineering of new non trivial, and interesting Hamiltonians, also with ultracold atoms and optical lattices, as we are going to present ([57, 58]).

2.3.3. Topology via Lattice Shaking

When introducing a frequency difference $\delta\nu$ between the two beams that create an optical lattice, they produce a running wave propagating with velocity $2\pi\delta\nu/k$, where k is the lattice wavevector. When modulating this frequency difference (making $\delta\nu$ time-dependent), in the reference frame of the wave an inertial acceleration $2\pi\partial_t\delta\nu(t)/k$ is felt.

In the 1D case, writing the inertial force as $2E(t)$:

$$H_t(t) = H - 2E(t)X \quad (2.32)$$

The constant force breaks the translational symmetry of the lattice Hamiltonian H . We consider the transformation given by the translation operator in momentum space R :

$$\begin{aligned} R &= \exp\left[iX \int 2E(t)/\hbar dt\right] \\ H'_t(t) &= RHR^\dagger - i\hbar R\partial_t R^\dagger = RHR^\dagger \end{aligned} \quad (2.33)$$

The last step is obtained by noticing that $-i\hbar R\partial_t R^\dagger - 2E(t)X = 0$. Notice that this Hamiltonian is now again periodic in space, and can be solved using the quasimomentum, labeled by q , as a good quantum number.

Under adiabatic approximation, i.e. assuming that the shaking doesn't couple higher bands ([59]), the shift in momentum produced by R becomes a shift in the quasimomentum:

$$H'(q, t) = RHR^\dagger = H(q + \int 2E(t)/\hbar dt) = H(q(t)) \quad (2.34)$$

we can then interpret the quasimomentum as being time-dependent, with $q(t) = q(0) + \int 2E(t)/\hbar dt$, and eliminate the (explicit) time-dependence of the Hamiltonian. Such results can be straightforwardly extended to 2D (or 3D).

We consider now the case of periodic shaking of a 2D lattice. In our setup, we can shake the lattice in a variety of different orbits by modulating the frequency difference of two of lattice beams (with respect to the other one) e.g. in the following way:

$$\begin{aligned}\delta\nu_1 &= 0 \\ \delta\nu_2 &= 2\delta\nu(\sin(\omega_F t + \phi) + \sqrt{3}\sin(\omega_F t)) \\ \delta\nu_3 &= 2\delta\nu(-\sin(\omega_F t + \phi) + \sqrt{3}\sin(\omega_F t))\end{aligned}\tag{2.35}$$

This allows to realize circular shaking with frequency ω_F (for values of the shaking phase $\phi = \pm\pi/2$), or linear shaking along the $x \pm y$ direction (for values of the phase $\phi = 0, \pi$). Intermediate values of the shaking phase realize shaking of the lattice along elliptical orbits. Taking the time derivative of the real space orbit allows to reconstruct the orbit of the (2D) time-dependent quasimomentum:

$$\mathbf{q}_t(t) = \mathbf{q}_t(0) + m \int_0^t \ddot{\mathbf{L}}(t) dt / \hbar\tag{2.36}$$

where \mathbf{L} indicates the translation vector between the lattice and the laboratory frame.

The system is periodic in time, therefore it realizes a Floquet system. The time evolution operator over a Floquet period U_F can be defined for a given quasimomentum \mathbf{q} with the following:

$$U_F(\mathbf{q}) = \lim_{N \rightarrow \infty} \prod_{n=1}^N \left[1 - \frac{iT_F/N}{\hbar} H(\mathbf{q}_t(t = nT_F/N)) \right]\tag{2.37}$$

We truncate the Hilbert space to the linear combination of the two lowest bands of the honeycomb lattice, and calculate U_F using $N \sim 200$. We obtain then the Floquet Hamiltonian by taking the logarithm of the time evolution operator:

$$H_F(\mathbf{q}) = \frac{i\hbar}{T_F} \ln[U_F(\mathbf{q})]\tag{2.38}$$

$H_F(\mathbf{q})$ has the form of a time-independent Hamiltonian of a 2D lattice, being a function of \mathbf{q} only. But, in contrast to Hamiltonians describing time-independent lattices, it could break time-reversal symmetry, and possess a non-zero Chern number.

Shaking produces an effective Hamiltonian with complex tunneling matrix elements ([60, 61]); in the case of the honeycomb lattice this effective Hamiltonian can be mapped to the Haldane model ([55]). This can be obtained by shaking with a Floquet frequency much bigger than the energy scales of the lowest two bands of the static lattice ([9]), simulating graphene irradiated by circularly polarized light ([62]); or by shaking in resonance with the sublattice offset Δ ([33, 63–65]).

An interesting feature of this second protocol is that an abrupt stop of the shaking allows for a full state tomography, where the complete time evolution of the quantum state can be reconstructed ([33, 65–67]).

In general, lattice shaking can be used to control and engineer systems parameters, e.g. for renormalization of the tunneling coupling, as demonstrated in the realization of a Mott-insulator via shaking ([68, 69]), or for adding Peierls phases on the tunneling elements, which allowed simulation of classical magnetism ([70, 71]). Floquet states in optical lattice can also be engineered by periodic modulation of the lattice depth ([72]), and topological phases can also be produced in optical lattices by laser-assisted tunneling ([7, 8]) or, exploiting internal degrees of freedom, with artificial dimensions ([73–75]).

As a last note, there is a fundamental interest in Floquet engineered models because they possess also topological phases which can not be present in non-driven systems ([76, 77]).

2.3.4. Reconstructing the Topological Phase Diagram via Machine Learning

Topological order can not be captured by a local order parameter, as in the Landau paradigm for phase transitions ([78]). Experimentally the Chern number in the bulk of a system can be extracted in a number of ways: e.g. through center of mass transverse displacements ([79, 80]) or full state tomography ([33]), or by counting the topological charges exchanged in a band closing point ([81]).

All these examples requires several experimental shots, to e.g. either extrapolate to the linear regime or to perform the full state tomography.

Machine learning techniques can be of help also in quantum physics ([82–84]). In ([12]) it was demonstrated how an algorithm can be trained with a (limited) knowledge of the different topological phases as a function of some experimental parameters. As an input, some time-of-flight pictures from a shaken lattice are fed, together with the value of the Chern number corresponding to the parameters with which each picture was taken. These pictures exhibit complex interference patterns, making the task very difficult or nearly impossible for a human eye to identify the correct topological phase (as can be seen from the examples in figure 2.13).

The algorithm can instead "learn" to classify the topological phases also for parameters for which it has not been trained (more details on the training procedure can be found in [12, 85]).

The resulting topological phase transition can be seen in the probability of measuring $C = 1$ as a function of the Floquet frequency (figure 2.14).

It was later shown with the same data ([86]) that machine leaning algorithms can even recognize that there is a transition, even without "telling" them first which are the phases that are supposed to be found (unsupervised machine learning).

These experiments ([12])¹, and [87], represent the first applications of machine learning techniques to experimental data in cold atoms systems; in [87] an algorithm was used to compare two models describing the doped Fermi-Hubbard model, a many-body system where complex patterns arise too.

The possibility of detecting the Chern number in a yet unexplored regime could be of tremendous help for the discovery of new topological phases, in particular considering that the answer of the (trained) algorithm would take considerably less time than the experimental cycle duration.

¹Including the time-of-flight data across the Mott-Superfluid phase transition which are not presented in this work.

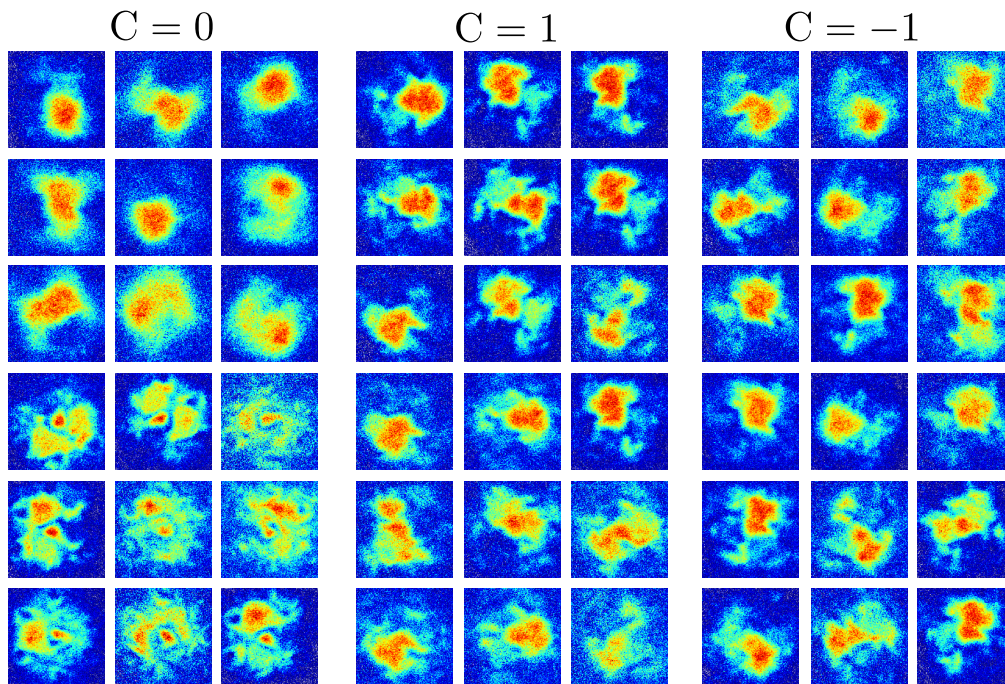


Figure 2.13.: Time of flight Pictures from systems with different Topology. Images obtained after loading a ^{40}K band insulator into a Floquet system created by circular lattice shaking. Data measured for different Floquet frequencies corresponding to different values of the Chern number C . This selection evidences, for the human reader, how identification of topological order through pattern recognition is not easy. Adapted from [12].

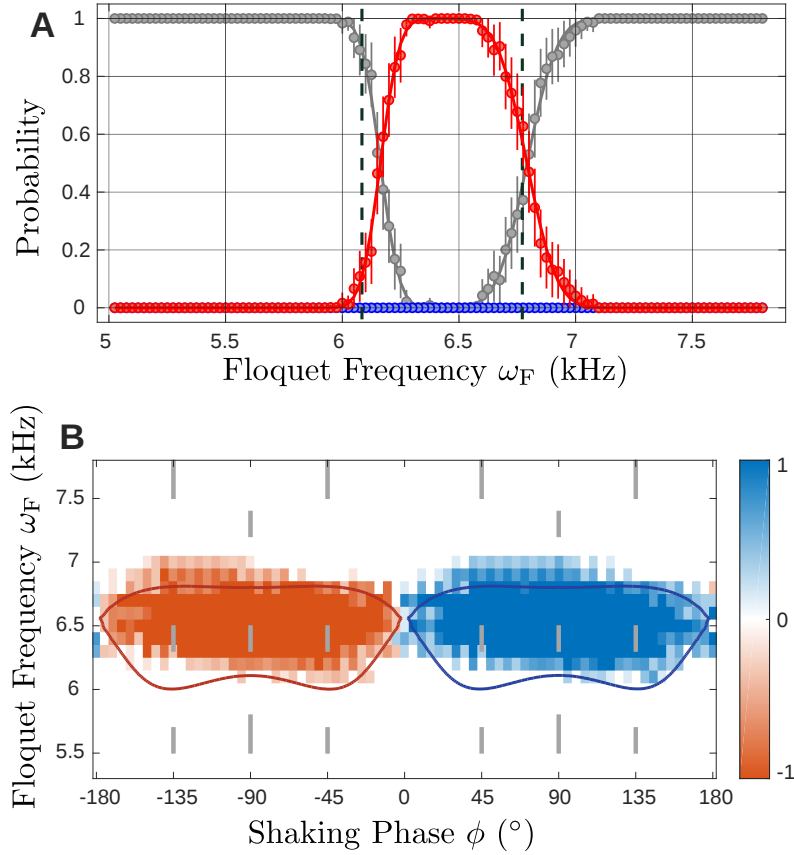


Figure 2.14.: Detecting topological Phases with Machine Learning. In **A**, the probability of the trained algorithm to produce $C = 1$ as outcome is plotted as a function of the Floquet frequency ω_F (red points). The single images analyzed by the algorithm were obtained for circular shaking (shaking phase $\phi = 90^\circ$). The expected transition points are marked by the dashed lines. Also plotted are the probability of predicting $C = 0$ (grey points) and $C = -1$ (blue points). In **B**, the Haldane phase diagram was mapped with the same method by varying both the Floquet frequency ω_F and the shaking phase ϕ . Notice that ω_F is related to the sublattice offset M (as in the Haldane model introduced in [55]), and the shaking phase ϕ to the complex phase of the next-nearest neighbours tunneling coupling ϕ of the same reference. The exact mapping between the model and this Floquet realization is described in [65]. The regions with $C = 1$ and $C = 0$ (as predicted from the numerics) are contained within the blue and red curves respectively. Grey lines represent points used to train the algorithm; notice that they represent only a small fraction of the total parameter space. Adapted from [12].

3. Circular Dichroism, or "Hearing Topology"

In 1966 the mathematician Mark Kac popularized the question of isospectrality with the paper "Can we hear the shape of a drum?" ([88]). Two shapes are said to be isospectral if they produce the same set of eigenvalue λ_n of the Laplace operator (λ_n is an eigenvalue if $u(x, y)$ can be found such that $\Delta u(x, y) = \lambda_n u(x, y)$ and $u = 0$ at the border of the shape).

The question was then if isospectral surfaces are always equivalent (up to trivial transformations like rotations or reflections) and whether the form of a shape could be deduced from its spectrum (the set of the eigenvalues, related to the frequencies which we hear of an oscillating drum).

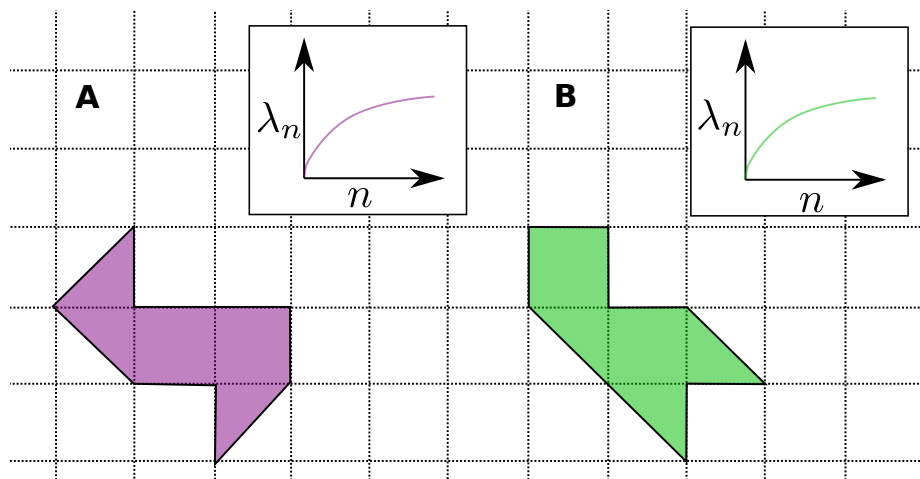


Figure 3.1.: Two isospectral surfaces. The two colored surfaces, in **A** and **B** are non-congruent but have the same spectrum $\lambda_n(n)$ (where n is an integer labeling the eigenvalues). This, and other counter examples, were presented in [89]. Notice instead, that the two surfaces have the same area, perimeter and number of holes (zero). While the exact shape cannot be deduced from the spectrum, these properties can be "heard", i.e. deduced from the spectrum.

Gordon et al. ([89, 90]) demonstrated that this is not possible by providing a method to generate counter examples (figure 3.1)¹.

But still, there are other properties of the surfaces, like the area ([92]) and the perimeter ([93]) which one can "hear", or deduce from the knowledge of the spectrum (these results were already known to Kac). Other properties can also be heard (and are therefore "spectral invariant"), like the number of corners ([94, 95]) or even the Euler characteristic i.e. the number of holes in the surface ([88, 96]), which directly gives the topology of the 2D shape.

In physics, measuring the spectrum of a system (performing a spectroscopy experiment) is a powerful tool for extracting information from the system. We have seen in the previous chapter that extracting the topological order is in general not an easy task ([12]) and, inspired from this short mathematical story, we ask ourselves whether the topology of a Chern insulator is one of the properties of a system which can be accessed via spectroscopy. Two important differences arise when comparing physical topological systems (introduced in the previous chapter) and the mathematical 2D shapes. The first one is that in Chern insulators the Berry curvature (on which a topological property, the Chern number C , depends) is a function of the eigenstates only, and not of the eigenvalues. Therefore it is strange to think of a spectroscopy experiment to reveal topological and geometrical properties. But there is also another important difference: performing spectroscopy in a physical system, we can not just ask: "is there a state at this particular energy difference?". When performing spectroscopy ("playing the drum"), we can choose among different perturbation operators (or "between e.g. playing with drumsticks or brushes, and among different stroke styles"), and the strength of the signal at each particular frequency ("the timbre") will depend on this choice.

The insight of Tran et al. ([10]), and of following publications ([97–99]) is exactly to have a look at the excitation rates (i.e. how fast we get a measurable signal), not just at the spectrum, to recover information about the geometry of the states themselves. In particular they found a spectroscopic quantity that is able to reveal the geometrical properties of a 2D Chern insulator: this quantity is the circular dichroism, which can be described as the difference in the response of the system between two situations, the first one where the perturbation forces the system to oscillate clockwise, and the second one where the system is forced to move counterclockwise.

Circular dichroism can be defined in a way (which will later be presented), such that it can be directly related to the Berry curvature, and as a consequence to the prediction that it should be quantized in term of the Chern number, making it a measurable quantity for obtaining the topology of a system.

¹Apparently, the answer is much easier for generic n -dimensional drums, and a counter example in 16 dimensions was much sooner found ([91])

In solids, geometrical properties (Berry curvature) were accessed using high-harmonics ([100, 101]), but so far the Chern number could not be extracted from a spectroscopy measurement. In our lab, we measured for the first time the quantization of circular dichroism; these findings are published in [11]. The data were taken and analyzed by me, together with my PhD colleague Matthias Tarnowski; and with Benno Rem and Nick Fläschner, under the supervision of Christof Weitenberg and Klaus Sengstock.

I calculated the numerical spectra for our system, while theoretical considerations about the separation of time-scales (of the spectroscopy probe frequencies with respect to the frequency of the probed Floquet system) were made by Duc Than Tran and Tomoki Ozawa, under the supervision of Nathan Goldman.

3.1. Heating Rates as topological Probes

A material is said to exhibit Circular Dichroism when it responds differently to the two possible orientations of the circular polarization of light. The prediction of [10] is that Circular Dichroism of a system should be quantized, and the quantization given by its Chern number.

In the following, we are going to define formally the circular dichroism and evidence the relation with the Chern number (following [10]).

Let's consider a lattice system, described by the Hamiltonian H , which might be topological ($C \neq 0$) as a function of some parameter(s). Adding the circular perturbation one can write:

$$H_t(t) = H + 2E_s \{ \cos(\omega_s t)X \pm \sin(\omega_s t)Y \} \quad (3.1)$$

where the sign \pm depends on the chirality of the perturbation.

The perturbation is non-periodic (in space) and breaks the symmetry of the lattice, but this can be recovered by going to the lattice frame, where the perturbation takes the form (see Chapter 2):

$$\begin{aligned} H'_t(q, t) &= H(q + \frac{2E_s}{\hbar\omega_s} \{ \sin(\omega_s t)\hat{q}_x \mp \cos(\omega_s t)\hat{q}_y \}) \\ &\simeq H(q) + \frac{2E_s}{\hbar\omega_s} \{ \sin(\omega_s t)\frac{\partial H}{\partial q_x} \mp \cos(\omega_s t)\frac{\partial H}{\partial q_y} \} \end{aligned} \quad (3.2)$$

where first expression is obtained by assuming adiabaticity (no band change due to the perturbation), and the second one by expanding H to first order in q_x, q_y . \hat{q}_x, \hat{q}_y are the unit vectors in quasimomentum space. Because the symmetry of the lattice is kept, the perturbation can only couple states with the same quasimomentum q .

Let's consider a state in the lowest band $|0\rangle$ with quasimomentum q and energy ϵ_0 . It can be excited to each state $|n\rangle$ with energy ϵ_n in the n^{th} band, with a total rate given by the Fermi Golden Rule, in the rotating wave approximation:

$$\Gamma_{\pm}(\omega_s) = \sum_{n>0} \frac{2\pi}{\hbar} \left(\frac{2E_s}{\hbar\omega_s}\right)^2 \left| \langle n | \frac{\partial H}{\partial q_x} \mp i \frac{\partial H}{\partial q_y} | 0 \rangle \right|^2 \delta_t(\epsilon_n - \epsilon_0 - \hbar\omega_s) \quad (3.3)$$

where $\delta_t(\epsilon) \equiv \sin(\epsilon t/2\hbar)^2/\epsilon^2$. We define then the integrated rates $\Gamma_{\pm}^{\text{int}}$ and $\Gamma_{\pm}^{\text{int}}$ obtained by averaging respectively $\Gamma_{+}(\omega)$ and $\Gamma_{-}(\omega)$ over the Brillouin Zone and by integrating over all relevant frequencies ω_s .

We consider the infinite time limit: there $\delta_t(\epsilon_n - \epsilon_0 - \hbar\omega_s) \rightarrow \delta(\epsilon_n - \epsilon_0 - \hbar\omega_s)$ (where δ is the Dirac delta) and integration over the frequencies can be done simply by removing the δ , substituting $\hbar\omega_s$ with $\epsilon_n - \epsilon_0$ and summing over all possible transitions $n > 0$.

We finally introduce the observable associated with circular dichroism, defined as:

$$\Delta\Gamma_{\pm}^{\text{int}} = (\Gamma_{+}^{\text{int}} - \Gamma_{-}^{\text{int}})/2 = \frac{4\pi(E_s/\hbar)^2}{N} \text{Im} \sum_q \sum_{n>0} \frac{\langle 0 | \frac{\partial H}{\partial q_x} | n \rangle \langle n | \frac{\partial H}{\partial q_y} | 0 \rangle}{(\epsilon - \epsilon_0)^2} \quad (3.4)$$

$\Delta\Gamma_{\pm}^{\text{int}}$ is called "differential integrated rates" (DIR). This can be directly related to the sum of the Berry curvature of the lowest band over the Brillouin zone ([102]):

$$C = \frac{4\pi}{A_{\text{sys}}} \text{Im} \sum_q \sum_{n>0} \frac{\langle 0 | \frac{\partial H}{\partial q_x} | n \rangle \langle n | \frac{\partial H}{\partial q_y} | 0 \rangle}{(\epsilon - \epsilon_0)^2} \quad (3.5)$$

The relation between $\Delta\Gamma_{\pm}^{\text{int}}$ and C is then given by:

$$C = \Delta\Gamma_{\pm}^{\text{int}} / (A_{\text{cell}}(E_s/\hbar)^2) \quad (3.6)$$

where $A_{\text{cell}} = A_{\text{sys}}/N$ is the area of the unit cell of the lattice. Notice that we choose a different convention than [10], by taking the *average* instead of *sum* over the Brillouin zone. In our definition, the depletion rates are an intensive quantity, making them easier to define in an experiment, because one does not need to know the exact area of the system. This is important not only because we didn't have in these experiments good real space resolution but also because this quantity is not well defined in a systems with a harmonic confinement. Furthermore, in our setup the system is not purely 2D (but rather a 2D lattice of "tubes") and A_{sys} , however defined, might depend from the z coordinate perpendicular to the lattice plane.

This derivation of the quantization of the DIR makes clear how geometric properties are related to the heating rates, and suggests also the possibility e.g. to measure the Berry curvature in a momentum resolved experiment. There is another route, which we present in the following, for obtaining the same relationship between the Chern number and circular dichroism.

We can start by noticing that the power P absorbed by the system upon circular perturbation is directly related to the conductivity as ([103, 104]):

$$P_{\pm}(\omega) = 4A_{\text{sys}}E_s^2(\sigma_R^{xx}(\omega) \pm \sigma_I^{xy}(\omega)) \quad (3.7)$$

where σ_R^{xx} is the real part of the parallel conductivity, and σ_I^{xy} the imaginary part of the transverse conductivity. This result can be obtained from the relations $P = \text{Re} \{ 2J \cdot E \}$ and $J = 2\sigma E$, with J the current density vector, $2E$ the rotating force with modulus $2E_s$ and σ the conductivity tensor. The depletion rates too are directly related to the absorbed power P via:

$$N\Gamma_{\pm}(\omega) = P_{\pm}(\omega)/(\hbar\omega). \quad (3.8)$$

The quantization of the differential integrated rates can be then eventually demonstrated by recalling the Kramers-Kronig relationships ([103]):

$$\sigma_R^{xy}(\omega) = \frac{2}{\pi} \int_0^{\infty} \frac{\omega' \sigma_I^{xy}}{\omega^2 - \omega'^2} d\omega' \quad (3.9)$$

from which follows, for the Hall conductivity $\sigma_H = \sigma_R^{xy}(\omega = 0)$

$$\begin{aligned} \sigma_R^{xy}(0) &= \frac{2}{\pi} \int_0^{\infty} \frac{\sigma_I^{xy}}{\omega'} d\omega' = \frac{2}{\pi} \int_0^{\infty} \frac{\hbar N(\Gamma_+ - \Gamma_-)}{8A_{\text{sys}}E_s^2} d\omega' \\ &= \frac{2\hbar}{\pi} \frac{\Delta\Gamma_{\pm}^{\text{int}}}{4A_{\text{cell}}E_s^2} = \frac{1}{h} \frac{\Delta\Gamma_{\pm}^{\text{int}}}{A_{\text{cell}}(E_s/\hbar)^2} \end{aligned} \quad (3.10)$$

Substituting in equation 3.10 the known quantization of the transverse Hall conductivity as an integer multiple of $1/h$, the quantization of the DIR as in equation 3.6 is recovered.

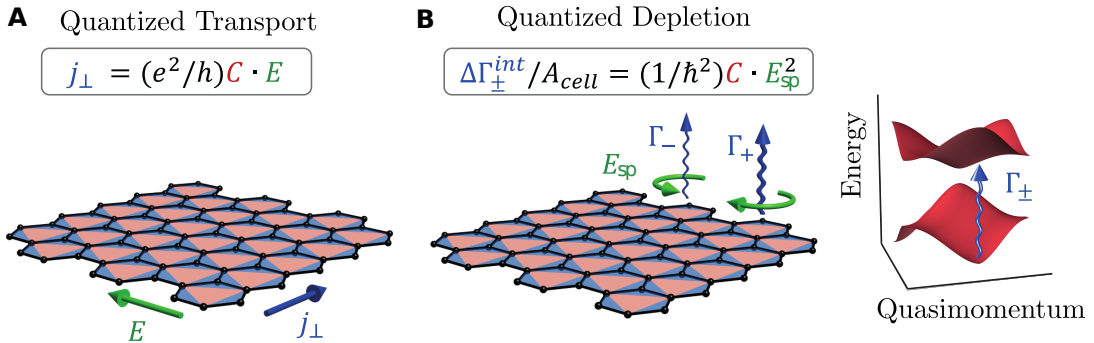


Figure 3.2.: Manifestations of Topology in Chern Insulators: quantized Hall Conductance and quantized Circular Dichroism. In **A**, representation of the Quantum Hall effect, where the transverse conductance is quantized in term of the Chern number. In **B**, representation of circular dichroism, also quantized in term of the Chern number. Although they seem different phenomena (e.g. the two effects scales differently with the strength of the perturbation, linearly in the first case and quadratically in the second) these two effects can be thought of as the "reactive" and "dissipative" manifestations of topology. Adapted from [11].

This demonstration of the quantization of the DIR, obtained by using the Kramers-Kronig relationships, allows then a new perspective on the whole field of 2D topological insulators, as schematized in figure 3.2: one could see topological response to circular drives as the "dissipative" side of topology, and the quantum Hall effect as the "reactive" side; the two of them strongly connected by the Kramers-Kronig relationships ([103]), i.e. causality. This consideration renders the first proposal ([10]) and successive measurement ([11]) of quantized circular dichroism particularly fascinating and relevant in this field.

The derivation obtained via the Kramers-Kronig relationships is also more general and for example does not assume that the system is not interacting, therefore suggesting this relation might also hold in strongly correlated systems ([105]). Notice also that it indicates how $\sigma_R^{xy}(\omega)$, for $\omega \neq 0$, could be gotten by calculating a similar integral.

As a side note, there are other sum-rules related to the circular dichroism ([106]). It was also shown that circular dichroism, also in the highly non-perturbative regime, provides an indication about topological phase transitions ([107]). Using dissipative phenomena for detecting topology is also suggested in [108] where losses from the system are proposed as a topological probe.

3.2. Experimental Implementation

3.2.1. Separation of Timescales

In order to realize the rotating field as proposed, we want to shake the lattice. This poses two conceptual problems. The first one comes from the fact that the system we intend to probe is the Floquet system which we realize via lattice shaking too. The question is then if the two drives (the Floquet, and the spectroscopy one) would interfere with each other.

The solution to this problem lies in the separation of timescales: we realize our Floquet system by shaking with a Floquet frequency ω_F close to resonance with a sublattice energy offset $\Delta_{AB}/\hbar = 6.1\text{kHz}$ of a symmetric boron-nitride-like lattice. Δ_{AB} is large compared to the tunneling element $J = \hbar \cdot 564\text{Hz}$ (the band structure of the static system is exactly the one of figure 2.9). This tunneling coupling dictates the width of the Floquet bands, therefore the relevant spectroscopy frequencies will be smaller than Floquet frequencies.

As long as these two frequencies are well separated, the two drives will not interfere, and the Floquet system can be well approximated by the time-independent Floquet Hamiltonian during the time-scale of the slower spectroscopy frequency. The analysis performed by our theory collaborators ([109]) shows that the separation of timescales present in our experiment is enough to suppress these "interference" effects, but this separation is not perfect; this could lead to systematic errors on the depletion rates of about 10%.

The second problem concerns the form of the spectroscopy in the Floquet system. The theoretical prediction assumes a particular form of the operators associated with the spectroscopy; is this form preserved also in relation to the Floquet system?

We derive then explicitly the form of the spectroscopy by starting from a time-dependent Hamiltonian H_t , which corresponds to a 2D lattice driven by circular shaking at two frequencies, ω_F and ω_s (associated with the Floquet and the spectroscopy drive, respectively):

$$H_t(t) = H + 2E_F\{\cos(\omega_F t)X + \sin(\omega_F t)Y\} + 2E_s\{\cos(\omega_s t)X \pm \sin(\omega_s t)Y\} \quad (3.11)$$

with $\omega_F \gg \omega_s$, and H being the static lattice Hamiltonian. E_F indicates the strength of the Floquet drive.

Going into the accelerated frame via $H' = RH_t(t)R^\dagger - iR\partial_t R^\dagger$, with

$$R = \exp\left[i\frac{2E_F}{\omega_F}\{\sin(\omega_F t)X - \cos(\omega_F t)Y\} + i\frac{2E_s}{\omega_s}\{\sin(\omega_s t)X \mp \cos(\omega_s t)Y\}\right], \quad (3.12)$$

we get:

$$H'_t(q, t) = H\left(q + \frac{2E_F}{\omega_F}\{\sin(\omega_F t)\hat{q}_x - \cos(\omega_F t)\hat{q}_y\} + 2\frac{2E_s}{\omega_s}\{\sin(\omega_s t)\hat{q}_x \mp \cos(\omega_s t)\hat{q}_y\}\right) \quad (3.13)$$

We use the fact the terms $\cos(\omega_s t)$ and $\sin(\omega_s t)$ evolve very slowly (compared with ω_F) and treat them as constants, by using $q' = q + \frac{2E_s}{\hbar\omega_s}\{\sin(\omega_F t)\hat{q}_x \mp \cos(\omega_s t)\hat{q}_y\}$. We consider a time interval corresponding to a Floquet period T_F , and obtain the Floquet Hamiltonian as:

$$H_F(q, t) = \lim_{N \rightarrow \infty} \frac{i\hbar}{T_F} \ln\left[\prod_{n=1}^N \left(1 - \frac{iT_F}{\hbar N} H\left(q' + \frac{2E_F}{\omega_s}\{\sin(\omega_F n T_F/N)\hat{q}_x - \cos(\omega_F n T_F/N)\hat{q}_y\}\right)\right)\right] \\ = H_F(q') \quad (3.14)$$

This is the exact expression for the Floquet Hamiltonian H_F define it, in absence of spectroscopy, calculated at quasimomentum q' instead of q . The Floquet Hamiltonian $H_F(q, t)$ describing the system has a slow time-dependence hidden in the definition of q' . Expanding for small amplitudes of the spectroscopy drive E_s one gets in the end:

$$H_F(q') = H_F(q) + \frac{2E_s}{\hbar\omega_s} \left\{ \sin(\omega_s t) \frac{\partial H_F(q)}{\partial q_x} \mp \cos(\omega_s t) \frac{\partial H_F(q)}{\partial q_y} \right\} \quad (3.15)$$

The perturbation operator maintains then the same form as in equation 3.2 also in relation to H_F , which is the Hamiltonian we want to probe.

We notice that at a crucial point we used the frame transformation operator R , which contains the frame transformation operator $R_F = e^{i\frac{2E_F}{\omega_F}(\sin(\omega_F t)X - \cos(\omega_F t)Y)}$ used for describing the orbits of the Floquet drive. Because all operators contained in R and R_F commute with each other $[R, R_F] = 0$ and the expression for the perturbation remains the same also in the Floquet picture.

While the spectroscopy drive commutes with the Floquet drive in our experiment, numerical analysis performed by our theory collaborators indicates that special care is required whenever this commutation relation is not satisfied, which could be the case in other experimental settings ([109]).

3.2.2. Characterization of Floquet Heating

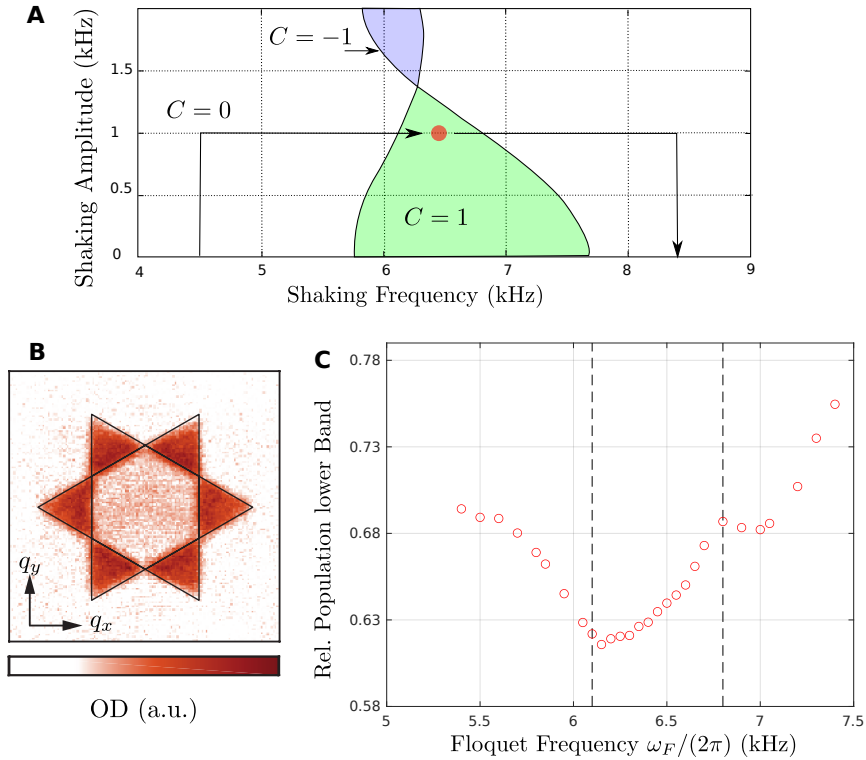


Figure 3.3.: Floquet Heating in the shaken System. In **A** is shown the topological phase diagram as a function of the shaking frequency and shaking amplitude $\delta\nu$. The latter is related to the amplitude of the frequency modulation used for circular shaking, and the resulting force is given by $E_F = 3ma_{\text{lat}}\omega_F \delta\nu$ ([11]). Areas of different colors indicate different values of the Chern number C . The arrows indicate how the shaking drive is turned on and its frequency brought to a value in the vicinity of (or in) the $C = 1$ region. At this frequency, which we label Floquet Frequency ω_F , the system is held for 10ms. Then the shaking frequency is ramped up, the shaking amplitude is ramped to zero, and we apply band-mapping. Because this procedure can be mapped to a Landau-Zener sweep, most of the atoms appear in the second Brillouin Zone (**B**). As a function of the Floquet frequency at which we hold the system, we see a different initial relative population in the first two bands (**C**). Adapted from [11].

We start our experiments by loading in 15ms an ultracold cloud of spin-polarized fermions filling up the lowest band of the (static) boron-nitride lattice. We ramp up the amplitude of the shaking $\delta\nu$ (as defined in the previous chapter) from 0 to 1kHz in 5ms, at a constant shaking frequency of 4.5kHz. We ramp then the shaking frequency to a particular target Floquet frequency ω_F , where we hold the system for a duration of 5ms. We then ramp the shaking frequency to 8.4kHz, and afterwards we ramp down the amplitude (to zero) of the shaking in 2ms. This protocol is schematized in figure 3.3.

Notice, in order to avoid confusion, that we define the Floquet frequency ω_F as the shaking frequency at which the system is hold. While the shaking frequency is ramped up during the experimental sequence, there is only one Floquet frequency for every experimental run.

The velocity of the shaking frequency ramps is kept fixed for every target Floquet frequency, and the total duration of the ramps (summing the one before and the one after the hold time in the Floquet system) is 5ms. After this sequence, dynamical Floquet bands should have been mapped to static Bloch bands: we then perform Band Mapping to measure how many atoms we transferred to the second band. The ramp protocol (with constant ramp velocity and duration) is chosen to leave systematic effects as constant as possible as a function of the Floquet frequency. This is partially related to an issue which is intrinsic in all topological systems, independent of their particular realization (cold atoms, condensed matter or photonics, e.g.), which is the fact that at the topological phase transition point ([110–114]) the band gap has to close and this sends to infinity the time needed for adiabatic evolution.

In addition to that, we also have technical Floquet heating (coupling to even higher bands) which, together with the closing of the band gap, heat the system relatively fast. This limits the total shaking time, which can not be arbitrarily high ([115]), which results in a finite Fourier broadening of the spectra. How to limit Floquet heating in such systems is still subject of current research ([116, 117]).

In figure 3.3 the lowest band population as a function of the Floquet frequency is also plotted, and shows that the ramps are indeed not perfectly adiabatic. It is a typical level in cold atom Floquet systems (compare [79]), and Floquet heating rates represent the main limitation to the duration of such experiments at the current state of the art ([79, 118]).

3.3. Results

3.3.1. Chiral Spectra

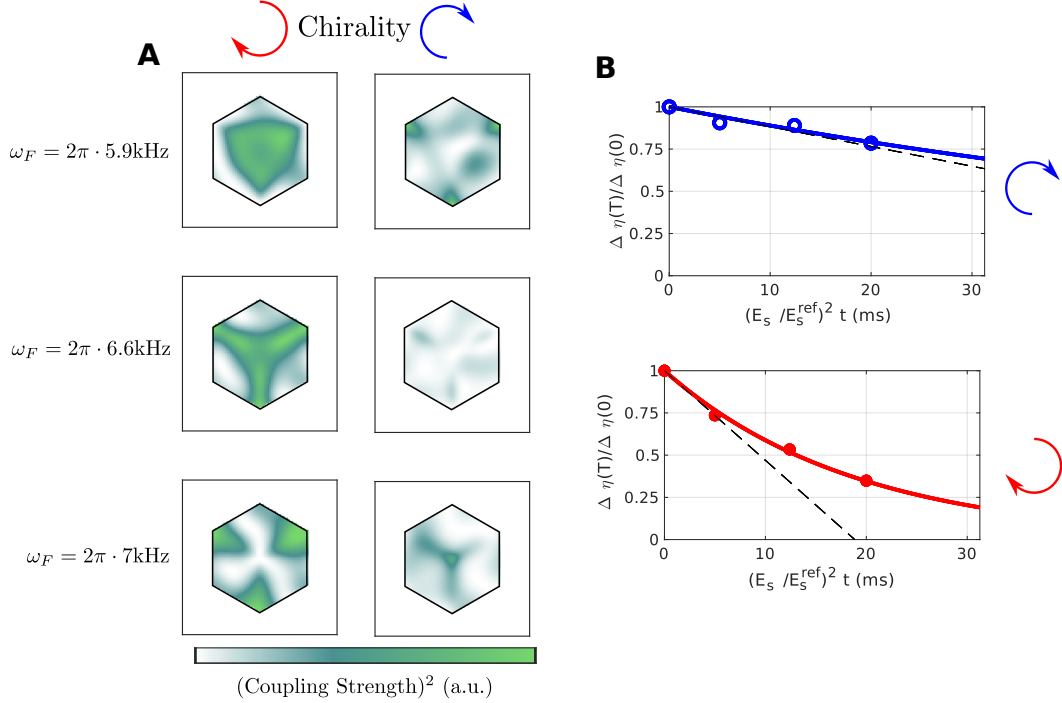


Figure 3.4.: Calculated coupling strengths and experimental depletion rates for the two spectroscopy chiralities. **A:** Numerical calculations of the coupling strength between the two lowest bands associated with the operators $(\frac{\partial H}{\partial q_x} \mp i\frac{\partial H}{\partial q_y})$, as a function of the quasimomentum, and for the two chiralities of the drive and three different Floquet frequencies ω_F . The hexagons represents the Brillouin zone. The coupling strengths depend on all these elements: ω_F , on the quasimomentum and, importantly, on the chirality of the spectroscopy. This is reflected in the experimentally measured depletion rates from the lowest band as a function of the spectroscopy amplitude E_s (**B**). On the y-axis, we have the population difference between the two bands $\Delta\eta$, normalized by its value in absence of spectroscopy. The x-axis is scaled with a reference spectroscopy amplitude E_s^{ref} and reference spectroscopy time t in order to have units of time (ms). The reference spectroscopy amplitude and time for all the experiments reported here are $E_s^{\text{ref}} = 0.006E_r/a_{\text{lat}}$ and $t = 5\text{ms}$. Adapted from [11].

Using the numerically calculated eigenstates of the Floquet Hamiltonian, we can also calculate the matrix element of the operators $(\frac{\partial H}{\partial q_x} \mp i\frac{\partial H}{\partial q_y})$ associated with the two chiralities of the perturbation. They depend indeed on the chirality, as a consequence of the fact the system itself is produced by a chiral drive. Experimentally, choosing one spectroscopy frequency and looking at the depletion rates from the lowest band as a function of the spectroscopy amplitude E_s (figure 3.4), we directly see this dependence on the chirality.

We were not able to extract any quasimomentum dependence of the signal, the distribution within the two Brillouin zones looking quite homogeneous. We attribute this partially to the Fourier broadening (determined by the 5ms duration of the spectroscopy), relevant when compared to the bandwidth of the bands and partially to the bandmapping procedure itself, which doesn't preserve the information on quasimomentum because of the harmonic confinement due to the finite waist of the light beams.

We repeat the measurements for different values of E_s , and extrapolate to the linear regime (assumed in the theory proposal). We chose to keep the spectroscopy time fixed since its variation could have induced systematic effects due to Floquet heating. We derive now how the rates could be extracted by taking measurements for different values of E_s instead. At the same time, by keeping the time fixed we also keep fixed the Fourier broadening, avoiding another source of potential systematic effects. We derive the model used to get the depletion rates, which assumes that this process can be treated as incoherent. This is motivated by the absence of oscillatory behaviour in the signal. We write the rate equations for the populations $\eta_{1,2}$ of the lowest two bands as

$$\begin{aligned}\dot{\eta}_1 &= -\Gamma(\eta_1 - \eta_2) \\ \dot{\eta}_2 &= -\Gamma(\eta_2 - \eta_1).\end{aligned}\tag{3.16}$$

The population difference $\Delta\eta = \eta_1 - \eta_2$ then obeys the rate equation $\Delta\dot{\eta} = -2\Gamma \cdot \Delta\eta$, which is solved by

$$\frac{\Delta\eta(t)}{\Delta\eta(0)} = e^{-2\Gamma t}.\tag{3.17}$$

This simple model fits well the experimental data (figure 3.4B) and allows us to extract the depletion rates as $\Gamma_{\pm} = -\frac{1}{2}s$, where s is the slope of the fit at $E_s = 0$. This is obtained by comparing equation 3.17 with the experimental data. We report the measured depletion rates Γ_{\pm} for different Floquet frequencies and for spectroscopy frequencies in the range 0.1 – 2kHz in figure 3.5.

The measured spectra typically exhibits two peaks, one at a frequency corresponding about to the average distance between the Floquet bands, and one at very small spectroscopy frequencies.

We attribute the part of the signal at small frequencies to the experimental protocol. In presence of the rotating force, due to the spectroscopy, of magnitude $2E_s$, the change in quasimomentum can be written as $q' = q + 2\frac{2E_s}{\omega_s}(\sin(\omega_F t)X - \cos(\omega_s t)Y)$. Because the spectroscopy is abruptly turned on, this implies that the quasimomentum has a discontinuity when the spectroscopy is turned on (or off), with an amplitude proportional to $1/\omega$.

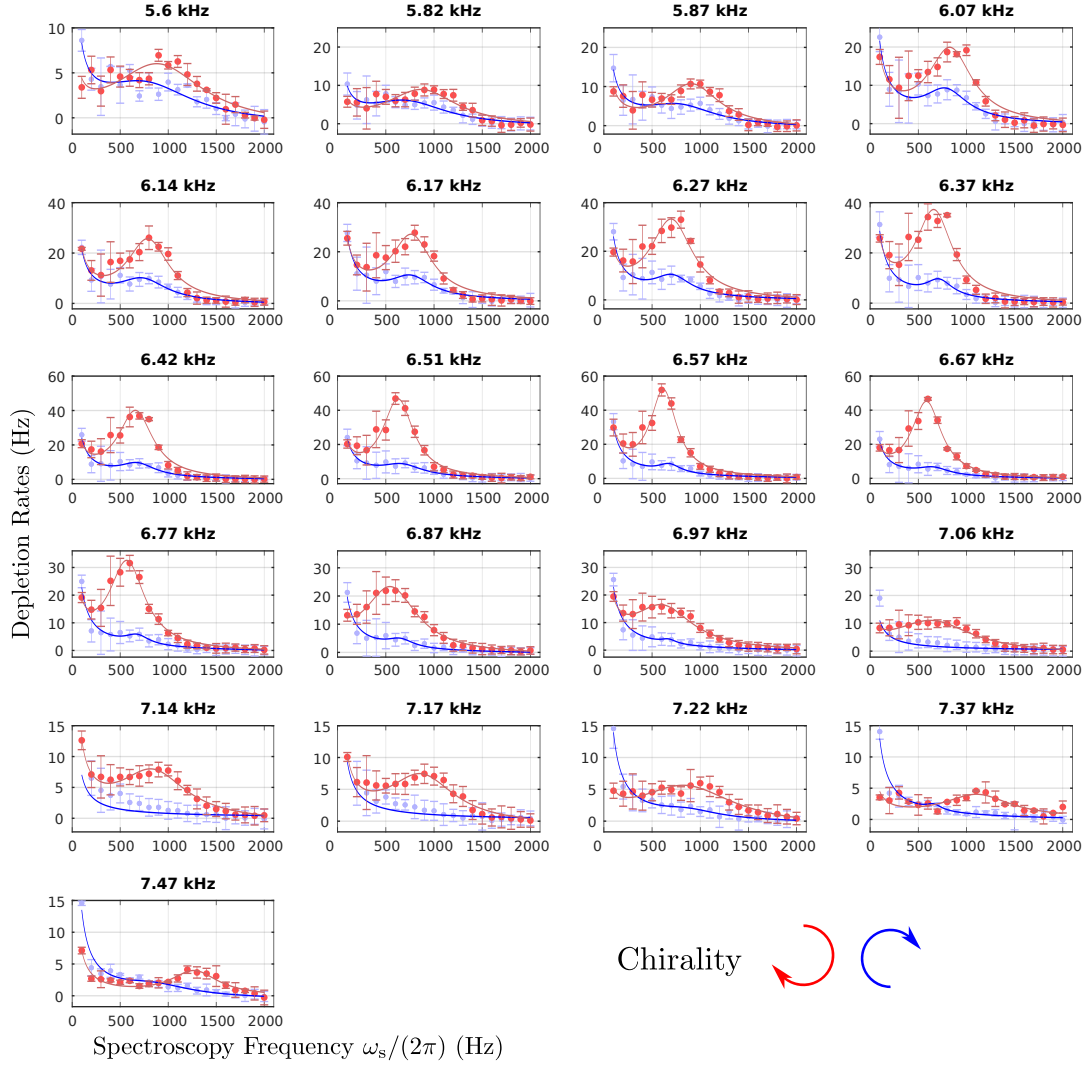


Figure 3.5.: Experimental Chiral Spectra. For different Floquet frequencies ($\omega_F/(2\pi)$, bold text above each figure) and chiralities of the spectroscopy (represented by the different colors) we plot the depletion rates, and their relative errors (one standard deviation) as obtained from the exponential fits. Depletion rates are evaluated for $E_s^{\text{ref}} = 0.006E_r/a_{\text{lat}}$. Solid lines are fits consisting of the sum of a Lorentz function, an offset, and a $1/\omega_s$ term (see main text). Notice the different y-axis. Adapted from [11].

This effect, we believe, produces this feature at small spectroscopy frequencies which is not present in the numerically calculated spectra (Figure 3.6). Indeed, only at the phase transition, where the band gap closes, see e.g. the numerical spectrum for $\omega_F = 6.13\text{kHz}$, the theory predicts very small frequencies to play an important role.

The second peak instead has a more physical origin, and corresponds to an excitation to the other Floquet band: consistently with the fact that the bands separation increases, one can see e.g. how it moves to higher spectroscopy frequencies for Floquet frequencies away from the resonance with Δ_{AB} .

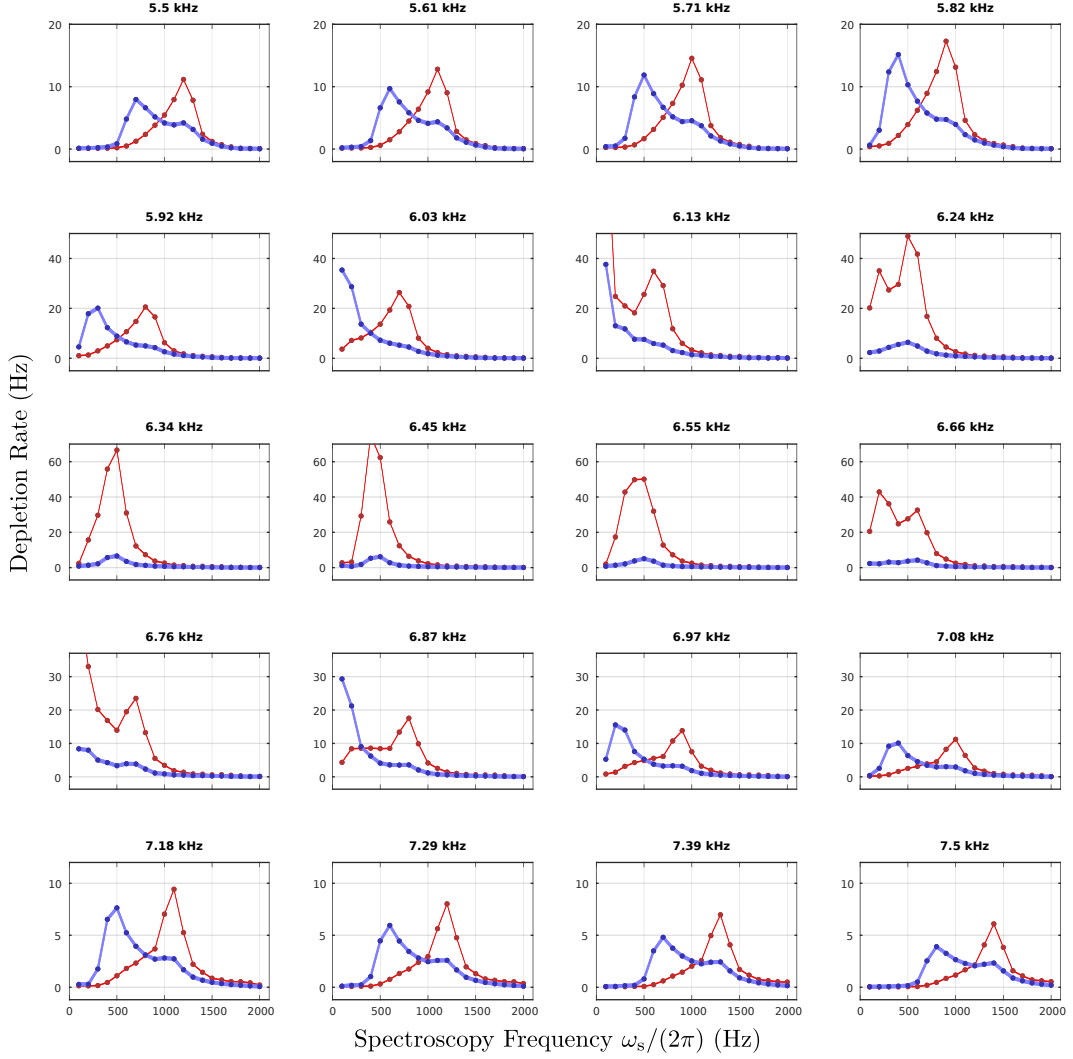


Figure 3.6.: Numerical Chiral Spectra. For different Floquet frequencies ($\omega_F/(2\pi)$, bold text above each figure) and chiralities of the spectroscopy (represented by the same color convention as for the experimental data) we plot the depletion rates, evaluated for $E_s^{\text{ref}} = 0.006E_r/a_{\text{lat}}$. Rates are calculated by averaging over the whole Brillouin zone the depletion rates calculated in the linear response regime as a function of ω_s with a finite time of 5ms. Notice the different y-axis. Adapted from [11].

As shown in figure 3.4, the coupling strength of the perturbation operators depends on the chirality and on quasimomentum. Because different quasimomenta have different energies, the exact position of this resonance will also depend on the chirality. This difference between the chiralities is not resolved in the experimental spectra as well as in the numerical ones. Notice that while the theory spectra do not consider non-linear effects in the strength of the perturbation, they take into account the finite spectroscopy time, including the Fourier broadening and the contribution from the so-called counter-rotating wave term which are neglected in the infinite time limit and in the rotating wave approximation used when deriving the Fermi Golden rule.

We recall that the differential rates are strongly related to the imaginary part of the optical conductance: this can be extracted from these data just by multiplying the differential rate $\Delta\Gamma_{\pm}^{\text{int}} = (\Gamma_{+}^{\text{int}} - \Gamma_{-}^{\text{int}})/2$ by ω . The resulting curves are shown in figure 3.7, and represent then a measurement of the transverse optical conductance as obtained via a measurement of depletion rates. The optical conductivity tensor of a neutral gas ([119]) was measured in a non-topological system ([120]), but in a setup without a gauge field and hence only with only diagonal non-zero elements.

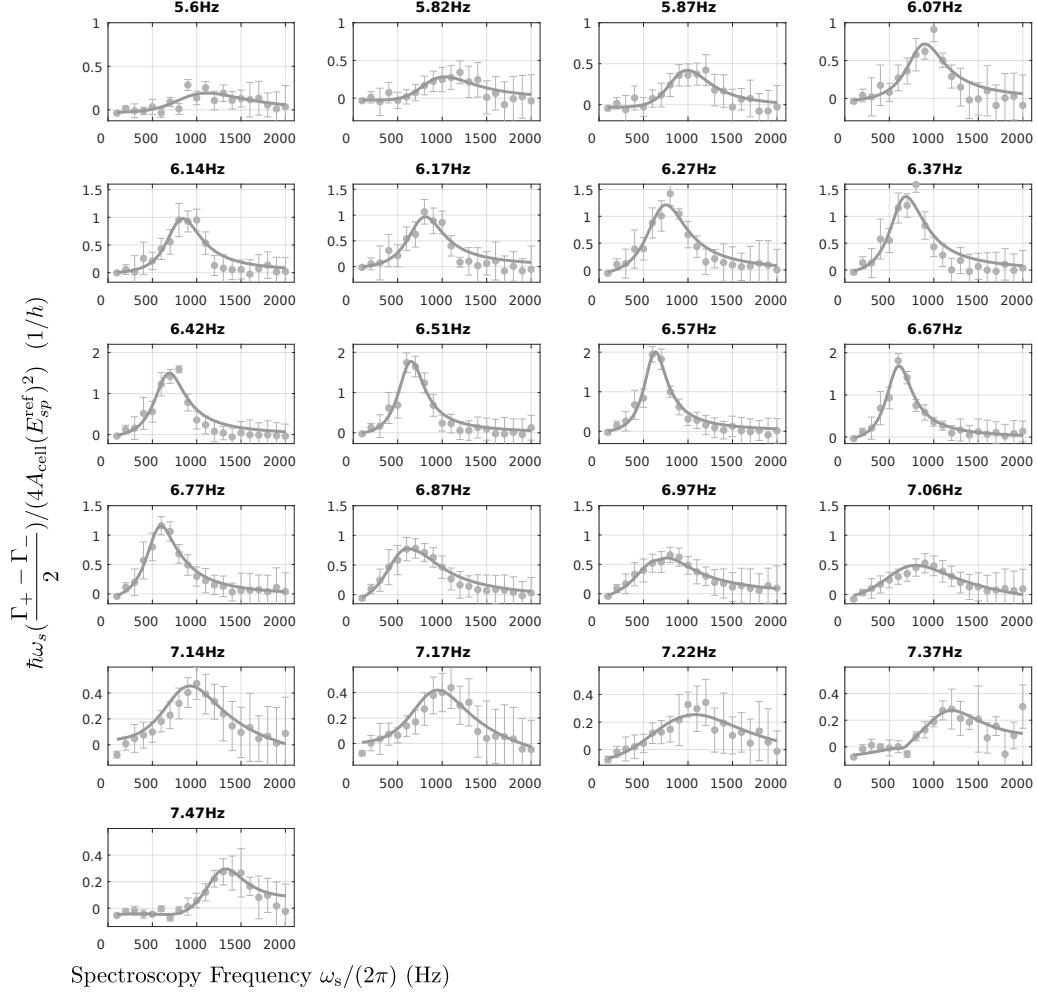


Figure 3.7.: Experimental Measurement of the imaginary part of the transverse optical conductance. For different Floquet frequencies ($\omega_F/(2\pi)$, bold text above each figure) $\hbar\omega(\frac{\Gamma_+ - \Gamma_-}{2}) / (4A_{\text{cell}}(E_s^{\text{ref}})^2)$ is plotted as a function of ω_s . The factors is chosen such that the measured quantity corresponds to $\sigma_I^{xy}(\omega)$, in conductivity units $1/h$, with the substitution of ω_s with ω . The error bars are obtained by propagation of the errors on Γ_+ , Γ_- and the fits as the difference between the fits on Γ_+ and Γ_- . Notice the different y-axis. Adapted from [11].

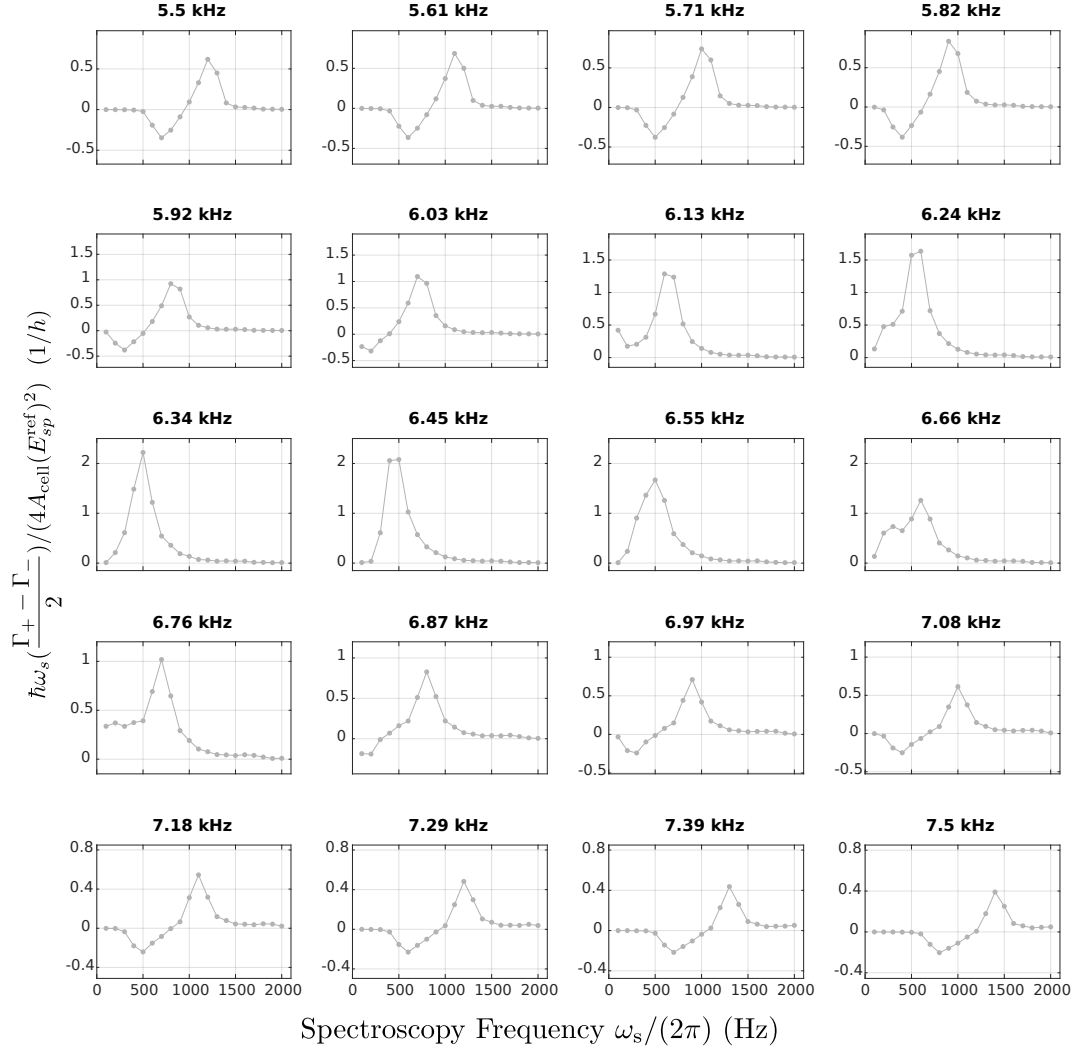


Figure 3.8.: Numerical Calculation of the imaginary part of the transverse optical conductance. For different Floquet frequencies ($\omega_F/(2\pi)$, bold text above each figure) $\hbar\omega(\frac{\Gamma_+ - \Gamma_-}{2}) / (4A_{\text{cell}}(E_s^{\text{ref}})^2)$ is plotted as a function of ω_s . Rates are calculated by averaging over the whole Brillouin zone the depletion rates calculated in the linear response regime as a function of ω_s with a finite time of 5ms. The factors is chosen such that the measured quantity corresponds to $\sigma_I^{xy}(\omega)$, in conductivity units $1/h$, with the substitution of ω_s with ω . Notice the different y-axis. These plots were made during the writing of this thesis.

Numerical calculations for the expected signal of the optical conductivity are presented in figure 3.8.

3.3.2. Measurement of Quantized Circular Dichroism

Following [10], we want now to measure the differential integrated rates.

We integrate the rates for each chirality taking the $1/\omega$ feature into account by fitting the curves with a function of the form:

$$\Gamma_{\pm} = \frac{a}{\pi\gamma} \frac{1}{1 + [(\omega_s - \omega_r)/\gamma]^2} + \frac{b}{\omega_s} + c \quad (3.18)$$

We calculate then the underlying area of each curve as

$$A = \int_{\omega_0}^{\omega_1} \frac{a}{\pi\gamma} \frac{1}{1 + [(\omega_s - \omega_r)/\gamma]^2} + c \quad (3.19)$$

where $\omega_0/2\pi = 100\text{Hz}$, $\omega_1/2\pi = 2\text{kHz}$ and a , c are determined from the fit. The $1/\omega$ term does not contribute to the integral.

From that, we get $\Delta\Gamma_{\pm}^{\text{int}} = \frac{A_+ - A_-}{2}$ and we recall the expected quantization law: $\Delta\Gamma_{\pm}^{\text{int}}/(A_{\text{cell}}) = C(E_s/\hbar)^2$.

In both topological cases the spectra look different but the integrated signal is in the first case compatible with 1 in the topological region within statistical errors and with a much lower value in the second case. It is not though compatible with zero within the statistical errors, which leads to the suspicion of systematic effects.

In figure 3.9, $\Delta\Gamma_{\pm}^{\text{int}}/(A_{\text{cell}})$ is plotted as a function of the Floquet frequency. We notice a deviation between the signal and the perfectly sharp ideal theory prediction, and discuss how this deviation could actually be a faithful indicator of the "topology" in the system. A general remark first: we notice that measuring values compatible with $C = 1$ in the middle of the topological region demonstrates not only the quantization of circular dichroism, but first the preparation of the Chern insulator with a good enough degree of adiabaticity: this is a not trivial result, as in principle (i.e. for an perfectly translationally invariant system) the Chern number is expected to be constant under adiabatic unitary evolution. The possibility of actually changing the value of the Chern number is probably related to the additional confinement of the system, which breaks partially the translational symmetry ([121]).

The ideal signal gets much smoothed out in the experimental realization, probably because of a variety of reasons. A problem could be a too small band gap in the vicinity of the topological phase transition. Such frequencies are not well probed because of the finite Fourier width and because the rotating wave approximation, used for deriving the relation between circular dichroism and the Chern number, might not be valid in these points. Moreover, topology is well defined as long as the band gap is finite, but very near the phase transitions the band gap might be smaller than the energy resolution allowed by the spectroscopy time $\sim \hbar/t$.

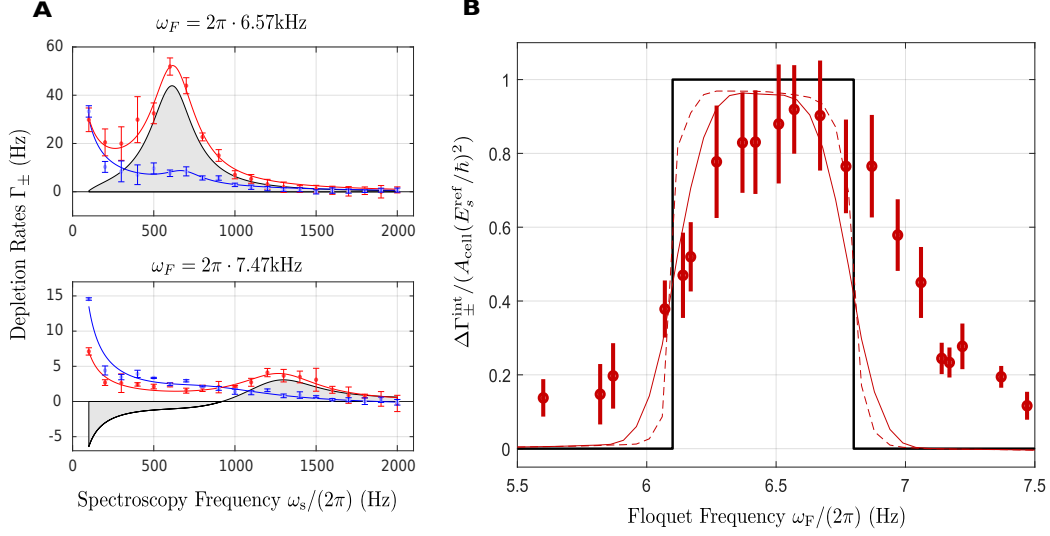


Figure 3.9.: Measurement of the Quantization of Circular Dichroism. In **A** two of the experimental spectra are selected and, added to them, the grey area obtained by taking the signed difference between the fits for positive and negative spectroscopy chirality. This quantity is predicted to be quantized in terms of the Chern number, and indeed it is finite for $\omega_F/2\pi = 6.57\text{kHz}$, in the middle of the expected $C = 1$ region, and much smaller outside, for $\omega_F/2\pi = 7.47\text{kHz}$ (notice the sign change of the area and the smaller y-axis scale there). From this area, $\Delta\Gamma_{\pm}^{\text{int}} = \int d\omega(\Gamma_+ - \Gamma_-)/2$ is extracted, considering only the contribution from the Lorentz part of the fit. In **B** $\Delta\Gamma_{\pm}^{\text{int}}$ is plotted as a function of ω_F , with a prefactor chosen such that a value of 1 is expected to be realized in the $C = 1$ region (red points). The expected value of C is indicated by the black line. The error bars are purely statistical and come from linear propagation of the errors of the rates measured in the respective chiral spectra. The red curves are obtained by integration of the theoretical spectra with cutoff frequencies of 100Hz and 200Hz (dashed and continuous line respectively). Adapted from [11].

Consider that the band gap is greater than the Fourier broadening only in the middle of the topological region. This effect could make also the topology "undefined", and this might be reflected in the smoothness of the measured signal. A similar smoothing effect is indeed also reproduced numerically by integrating the numerical spectra starting from a finite frequency.

Deep into the non-topological regions, there might be some systematical deviation, since the signal drops only very slowly to zero. In particular on the left side, as the Floquet frequency decreases the band gap increases, moving the signal toward higher frequencies, leading to a possible break-down of the separation of time scales.

As we mentioned in section 3.2.2, at the topological phase transition the band gap closes, and perfect adiabaticity can not be obtained. This could be realized in the future by more advanced loading protocols which obtain adiabaticity with a non-unitary time evolution ([122]).

Another speculation is related to the dynamical aspects of the ramping protocol: as shown in [112], one would not expect an instantaneous jump in the topological response directly after crossing the phase transition; this is in fact rather characterized by a finite time constant. It would be then of interest to see if interpretation of the data as a "buildup" of the topological response after crossing the $C = 0 \rightarrow C = 1$ phase transition (at 6.1kHz) and a "decay" after crossing the $C = 1 \rightarrow C = 0$ phase transition (at 6.8kHz). This might be supported by noticing that the symmetry axis of the measured signal appears to be shifted toward higher shaking frequencies, when compared with the numerics, an observation which can be made also for the machine learning data presented in figure 2.14A ([12]). Notice that the two experiments were conducted with basically the exact same setup.

In order to separate these effects from systematical errors one could improve the precision of the calibration (see chapter 6 for a precise measurement of the lattice "geometry") and of the numerics by taking e.g. higher bands into consideration for determining with higher precision the transition points and/or changing the ramping protocol e.g. simply by ramping from bigger to smaller shaking frequencies, and comparing the results obtained with the two ramp directions. Of course, limiting Floquet heating would be beneficial also for this aspect as it would allow slower and more adiabatic ramps.

3.3.3. Measurement of the Wannier Spread Functional

Reference [97] notices how the depletion rates from an eigenstate ψ_0 of the Hamiltonian H , obtained with a generic perturbation operator O , are related to the variance $\text{Var}(O)$ of the operator O calculated on the state ψ_0 :

$$\begin{aligned}
 H_t &= H + 2E \{ \cos(\omega t) \} O \\
 \Gamma_O^{\text{int}} &= 2\pi E^2 / \hbar^2 \sum_{n \neq 0} |\langle \psi_n | O | \psi_0 \rangle|^2 \\
 &\propto \sum_{n \neq 0} \langle \psi_0 | O | \psi_n \rangle \langle \psi_n | O | \psi_0 \rangle = \langle \psi | O^2 | \psi \rangle - \langle \psi | O | \psi \rangle^2 = \text{Var}(O)
 \end{aligned} \tag{3.20}$$

where Γ_O^{int} are the integrated depletion rates associated with the operator O , calculated using the same approximations and methods used for Γ_{\pm} .

Considering then the operators X and Y , one could measure the variances $\text{var}(X)$, $\text{var}(Y)$, related to the real space width of the wavefunction.

These operators are the ones associated with linear shaking in the two in-plane directions, as we have seen, therefore it is natural to think of measuring these quantities in a lattice.

In a lattice the *sum* of the integrated rates $\Gamma_{x,y}^{\text{int}}$ obtained via linear shaking of the spectroscopy along the x and y directions is predicted ([97, 99]) to give the gauge invariant part (the trace) of the quantum metric tensor ([123]), introduced in chapter 2.

$$\Omega_I = \frac{1}{2\pi} \Gamma_{xy}^{\text{int}} / (E_s / \hbar)^2 \tag{3.21}$$

The demonstration, omitted in this work for brevity, follows the same approximations and assumptions used for the extraction of the Berry curvature from the integrated differential rates of [10]. The quantity Ω_I is called Wannier spread functional and sets a lower bound for the quadratic spread of Wannier functions.

$$\text{var}(r) \geq \Omega_I \tag{3.22}$$

where r denotes the radial coordinate. We modified then the protocol used for circular dichroism, implementing a linear shaking of the spectroscopy in the following form:

$$\begin{aligned}
 H_t &= H_F + \sqrt{2} E_s \{ \cos(\omega t) \} X \\
 H_t &= H_F + \sqrt{2} E_s \{ \cos(\omega t) \} Y
 \end{aligned} \tag{3.23}$$

Notice that the Floquet Hamiltonian H_F that we probe is exactly the same as before, obtained with circular lattice shaking. In figure 3.10 we show the depletion rates obtained for shaking along the x and y direction. Notice that the Floquet system does not seem to exhibit (strong) linear dichroism, as also predicted by the numerics (figure 3.11).

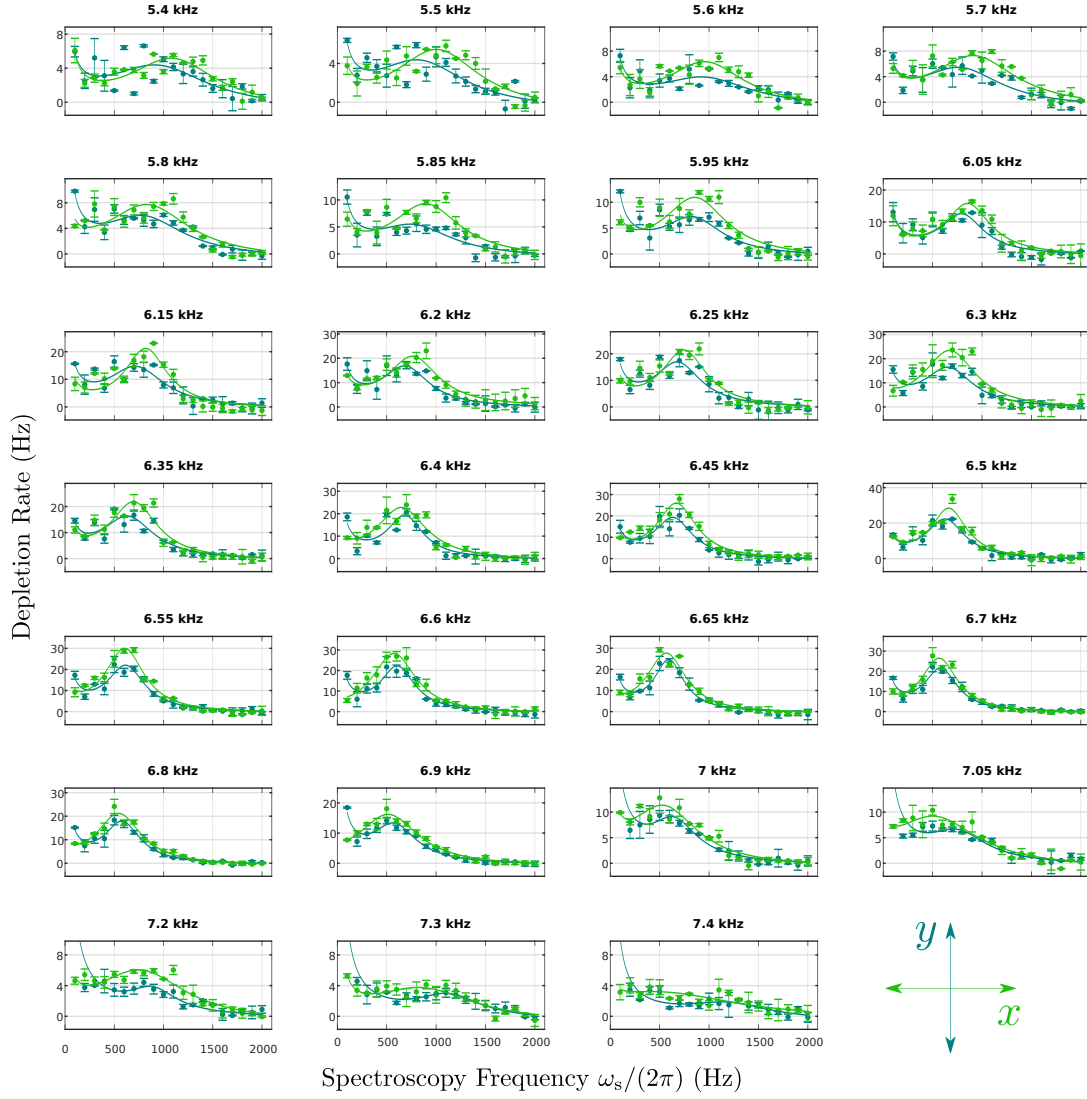


Figure 3.10.: Experimental Spectra for Linear Dichroism. For different Floquet frequencies ($\omega_F/(2\pi)$, bold text above each figure) and direction (x , y) of the spectroscopy (represented by the different colors) we plot the depletion rates, and their relative errors (one standard deviation) as obtained from exponential fits in analogy to the measurement of the depletion rates for the circular dichroism case. Depletion rates are evaluated for $E_s^{\text{ref}} = 0.006E_r/a_{\text{lat}}$. Solid lines are fits consisting of the sum of a Lorentz function, an offset, and a $1/\omega_s$ term. Notice the different y-axis. Adapted from [11].

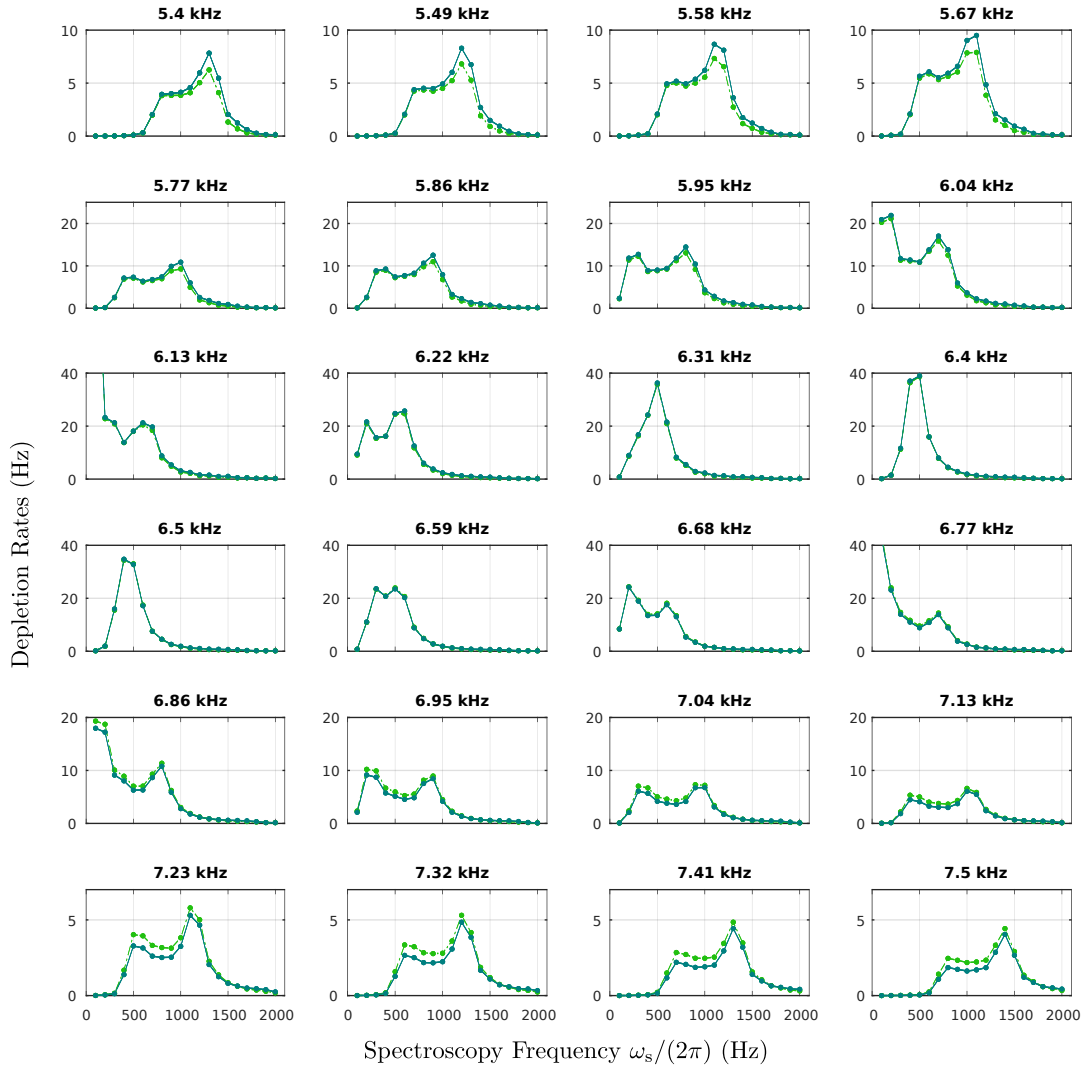


Figure 3.11.: Numerical Calculation of the Spectra for linear dichroism. For different Floquet frequencies ($\omega_F/(2\pi)$, bold text above each figure) and directions (x , y) of the spectroscopy (represented by the same color convention as for the experimental data) we plot the depletion rates, evaluated for $E_s^{\text{ref}} = 0.006E_r/a_{\text{lat}}$. Rates are calculated by averaging over the whole Brillouin zone the depletion rates calculated in the linear response regime as a function of ω_s with a finite time of 5ms. Notice the different y-axis. Adapted from [11].

We plot in figure 3.12 the summed integrated rates, defined as $\Gamma_{xy}^{\text{int}} \equiv (\Gamma_x^{\text{int}} + \Gamma_y^{\text{int}})/2A_{\text{cell}}$. $\Gamma_{x,y}^{\text{int}}$ are the depletion rates associated with the X , Y operators, obtained in the infinite time-limit, averaged over the Brillouin zone and integrated over all relevant frequencies.

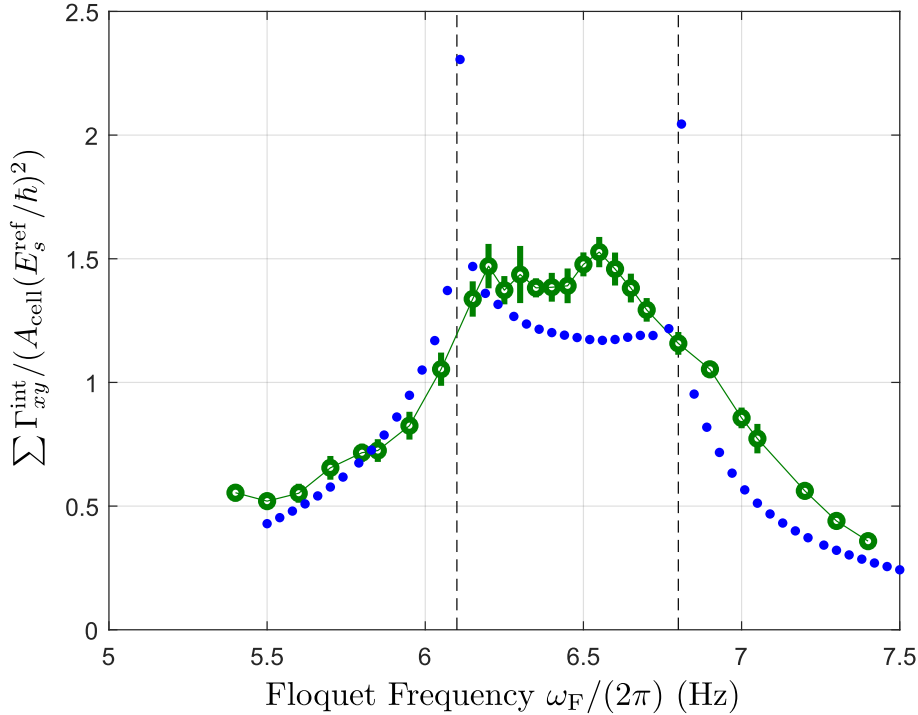


Figure 3.12.: Measurement of the Wannier Spread functional. $\Sigma\Gamma_{x,y}^{\text{int}}$ is plotted as a function of ω_F (green points). The units are the same as in the circular dichroism case and they are such that the experimental signal (green points, adapted from [11]) should correspond to $\frac{2\pi}{A_{\text{cell}}}\Omega_I$, with Ω_I the Wannier spread functional. The error bars are purely statistical and come from linear propagation of the errors of the rates measured in the respective spectra. Blue points, added in this work, are the expected signal as calculated numerically. Notice that in the topological region the Wannier functions are not expected to be exponentially localized, therefore Ω_I should diverge at the phase transition points, denoted by the dashed lines. Theory points (calculated during the writing of this thesis) very close to the phase transition are likely to be not very accurate because of the finite resolution in momentum space of the numerics.

We note a change of behavior of this quantity in the vicinity of the topological region ([99]). Notice that in the topological region exponentially localized Wannier functions are not expected, therefore the lower bound on the Wannier functions is somehow less meaningful in this region. The linear extension of the Wannier functions, which can be estimated as $\sqrt{\Omega_I}$, is about 300nm in the vicinity of the topological phase transition.

This result is particularly important, because Wannier functions are experimentally difficult to measure, and calculation requires a careful analysis ([124–129]): the fascinating aspect of this measurement is that one gets information about the orbitals in real-space without needing the resolution needed to image them.

We include here the consideration that the Wannier spread can also be obtained by summing the integrated rates $\Gamma_{+,-}^{\text{int}}$ obtained with circular shaking. This can be demonstrated by noticing that:

$$\begin{aligned}\Gamma_+^{\text{int}} + \Gamma_-^{\text{int}} &\propto |\langle n | \frac{\partial H}{\partial q_x} + i \frac{\partial H}{\partial q_y} | 0 \rangle|^2 + |\langle n | \frac{\partial H}{\partial q_x} - i \frac{\partial H}{\partial q_y} | 0 \rangle|^2 \\ &= 2 |\langle n | \frac{\partial H}{\partial q_x} | 0 \rangle|^2 + 2 |\langle n | \frac{\partial H}{\partial q_y} | 0 \rangle|^2 \propto \Gamma_x^{\text{int}} + \Gamma_y^{\text{int}}\end{aligned}\tag{3.24}$$

3.4. Conclusions

In this chapter we presented the first measurement of quantized circular dichroism in a topological system. We realized both the topological system and the chiral perturbation with Floquet engineering. This was realized through lattice shaking with two different frequencies with distinct timescales, which also allowed spectroscopy of Floquet bands. Developing techniques for driving the system at two (or more) frequencies simultaneously is of general interest in the context of Floquet engineering ([117, 130, 131]).

Through circular dichroism, the value of the Chern number of the Floquet system could be inferred. This is of interest as current measurement in trapped system (in contrary to solid state systems) might be ill-defined, but also suggests that circular dichroism could be used as a tool for probing novel phases and detecting their topology. The quantization of circular dichroism is in fact a rather general topological phenomenon and it could be extended to states out of-equilibrium ([132]), fractional quantum Hall states ([133, 134]), as studied in [105], or higher-order topological insulators ([135]), as studied in ([136]).

Further studies could be made on the relationship between circular dichroism and the Hall effect in the non-linear response regime ([137, 138]). The methods applied in this work for measuring circular dichroism also allowed to measure the imaginary part of the transverse conductivity, and the Wannier spread functional. Both observables are related to local transport and geometric properties of the system: in this work we demonstrated how they could be accessed, even without having direct access to the length scales which characterize them. In the next chapter, instead, we will present results which go exactly in the direction of gaining direct access to observables, like the mentioned Wannier functions, which hide in length scales difficult to access experimentally.

4. Quantum Gas Magnifier, or a lens for "Seeing Quantum Particles"

Neutron stars and other weird objects in our universe are really big quantum mechanical systems. But here on earth, quantum mechanics becomes necessary for describing matter only at very small scales: the size of an atom is about 10^{-10}m , which is also a typical inter-atomic spacing between atoms in a crystal. The mass of the proton is $1.672 \cdot 10^{-27}\text{kg}$ and the Planck constant, which is the fundamental constant for quantum mechanics, is $h = 6.62607015 \cdot 10^{-34}\text{Js}$. The exponents indicate the orders of magnitude which separate us from the quantum mechanics scale, and made at first appear direct application of quantum mechanics quite impossible: "It is fair to state that we are not going to experiment with single particles any more than we will raise dinosaurs in a zoo". This quote is attributed to one of the founders of quantum mechanics, Erwin Schrödinger.

Nevertheless, this scale could be reached. Scanning tunneling microscopes allows detection of single atoms ([139]), and single atomic ions can be trapped ([140]). In the quantum gas community, so-called Quantum Gas Microscopes ([4, 5]) allow single-site and single-atom detection of lattice systems, accessing not only the densities but also the quantum correlations among the particles ([141, 142]). This, in combination with the possibility of single-atom manipulation ([143]) allowed measuring particle entanglement ([144]), observing many-body localization ([145]), and performing microscopy of interacting topological models ([146]).

Bilayer systems allow also spin resolved detection ([147, 148], with a more advanced scheme based on topological pumping realized in [149]). This allows to access also particle-hole correlations ([150, 151]).

This (not exhaustive) list evidences how quantum gas microscopes are really powerful tools for investigating a wide range of quantum mechanics phenomena. Still, they have some downsides, the first one being the technical complexity of the machine, from the high-resolution optics to the cooling of the atoms in the pinning lattice to the reconstruction algorithms of the atomic distribution.

A physical limitation is that they are (with some exceptions [152, 153]) limited to 2D systems, because the high numerical aperture needed implies a very small depth of focus. Another point is that because of interactions during the imaging time, only a small atom number per lattice site n can be imaged (usually $n \leq 1, 2$; $n = 3$ in ref. [147]).

There are other high-resolution imaging techniques for cold atoms: e.g. scanning electron beams ([154]) and the ion microscope ([155]), which work for 3D systems, but have a limited detection efficiency. Super-resolution microscopes ([156, 157]) allow to get information at the sub-lattice spacing, but in a global way and with scanning techniques. We mention also the possibility of using cold atoms not as an observation object but as a tool for doing microscopy of light beams ([158]).

In [13], we introduced a new method based on a different conceptual approach than other high-resolution imaging techniques.

Using matter-wave optics, this new method consists in the magnification of the atomic wavefunction in good analogy to the magnification of optical light beams realized with an optical lens: the underlying idea is then not to try to *get* closer to the quantum system, but rather we *bring* the quantum system closer to us, extending it to more experimentally accessible length scales.

The matter-wave lens uses the wave properties of matter, and allowed us to realize a protocol where the final state has the same density distribution of the initial state, magnified by almost two orders of magnitude. This magnified cloud can be imaged with standard optical imaging, getting in a single-shot the full density profile, with very high resolution.

For particular wavepackets, the idea to use matter-wave optics to magnify quantum states was presented already in [159, 160] and recently some new interacting states which experience self-imaging in a harmonic potential were discovered ([161, 162]). The quantum gas magnifier instead, does not rely on particular assumptions about the studied wavefunction.

I conceived the quantum gas magnifier and, together with my PhD colleagues Henrik Zahn and Marcel Kosch, under the supervision of Christof Weitenberg and Klaus Sengstock, implemented and characterized it; and took and analyzed the data that are presented in this chapter. This chapter mainly focuses on the results presented in [13]. The theory part of [14] (also briefly presented in this chapter) was carried out by Vijay Pal Singh and Lukas Freystatzky, under the supervision of Ludwig Mathey.

4.1. Theory

We describe in this section how the quantum gas magnifier uses matterwave optics to produce a wavefunction $\varphi'(\mathbf{r})$, starting from a given wavefunction $\varphi(\mathbf{r})$, such that the final density distribution is the the same as the initial one, but magnified by a factor M :

$$|\varphi'(M\mathbf{r})|^2 \propto |\varphi(\mathbf{r})|^2 \quad (4.1)$$

There are just two basic components to this dynamics, a quarter period ($T/4$) evolution in a harmonic trap and a free expansion time t_{tof} (or "time-of-flight"). Let's start by a consideration about the nature of the particles under consideration during such dynamics. The classical equation of motion for a particle at position x and momentum p in presence of a 1D harmonic potential are given by the Poisson brackets with the classical Hamiltonian $H_c = \frac{p^2}{2m} + \frac{1}{2}m\omega^2 x^2$.

$$\begin{aligned} \dot{x} &= \{x, H_c\} = \frac{p}{m} \\ \dot{p} &= \{p, H_c\} = -m\omega^2 x \end{aligned} \quad (4.2)$$

The time evolution of the corresponding quantum operators X , P (in the Heisenberg representation) is obtained from their commutator with the Hamiltonian of the quantum harmonic oscillator, $H_q = \frac{P^2}{2m} + \frac{1}{2}m\omega^2 X^2$:

$$\begin{aligned} \dot{X} &= [H_q, X] = \frac{P}{m} \\ \dot{P} &= [H_q, P] = -m\omega^2 X \end{aligned} \quad (4.3)$$

The resulting equations have the exact same form of the classical Hamilton equations of motion. The same consideration holds also for time of flight, corresponding to the particular case where $\omega = 0$.

Because the equations of motion have the same form both in the classical and in the quantum representation the description that follows next, in which we are considering the evolution of the quantum operators, can also be interpreted classically by substituting the quantum operators X , P with the corresponding classical variables.

While the classical interpretation might provide a more intuitive picture, the quantum one guarantees that what we describe is valid also at the level of quantum particles. Notice that we did not make any assumption on the nature of the particle, or on the ensemble of particles (whether they have bosonic or fermionic statistics), therefore everything will be valid for both fermions and bosons (and classical particles).

The results obtained with the quantum operators show that important quantum features like density correlations are also correctly "magnified". Moreover, the formalism introduced here will also be used in chapter 5, where interference effects during the matter-wave optics are studied; these instead can not be instead mapped to a classical particles counterpart.

4.1.1. Focusing the Matter Wave Field

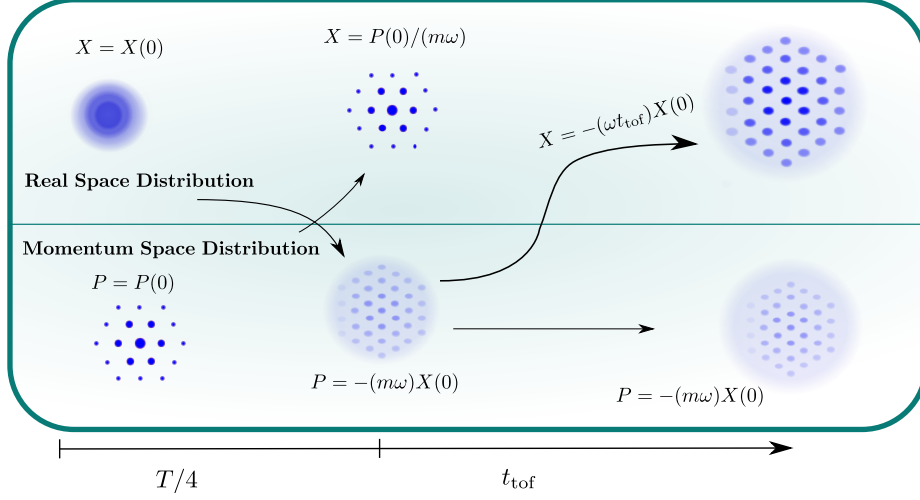


Figure 4.1.: Sketch of the Quantum Gas Magnification Principle. At $t = 0$, the lattice system has a very small density distribution, difficult to resolve. Arrows show how the information about the real space distribution is first mapped to the momentum distribution with a $T/4$ pulse and then back to real space with a free expansion time t_{tof} . Because the first mapping is characterized by the factor $-\omega m$ and the second one by t_{tof}/m the total magnification is $M = |(-m\omega)(t_{\text{tof}}/m)| = \omega t_{\text{tof}}$. At the end of the protocol, the density distribution can be resolved with high resolution.

The matter wave optics protocol used for quantum gas magnification is composed of two steps (as sketched in figure 4.1): at first we quench the potential of the system we want to observe, to that of a harmonic trap, and wait for about $T/4$. This, as mentioned in section 2.2.3, has the effect of mapping the position of the particles to the momentum as:

$$\tilde{P}(T/4) = \tilde{X}(0) \quad (4.4)$$

where $\tilde{X} = X\sqrt{\frac{m\omega}{\hbar}}$ and $\tilde{P} = \frac{P}{\sqrt{\hbar m\omega}}$ are the position and momentum operators in the natural units of the harmonic oscillator with trapping frequency ω and mass m .

One can then measure this "momentum" distribution, which actually contains the information about the real space distribution at $t = 0$, using time-of-flight. We obtain in the far-field limit:

$$\tilde{X}(T/4 + t_{\text{tof}}) \sim \omega t_{\text{tof}} \tilde{X}(0) \quad (4.5)$$

Notice that working with the operators in the natural units during time-of-flight we used $\partial_t \tilde{X} = \omega t_{\text{tof}} \tilde{P}$. Equation 4.5 tells us that, comparing the initial and the final density distribution a scale transformation has taken place, since after the protocol the position operator \tilde{X} has become ωt_{tof} times bigger than originally it was. Note that to get a magnification in 2D (3D) one gets still the same magnification if the harmonic trap is rotationally symmetric $\omega_x = \omega_y (= \omega_z)$. We are going to work in 1D but under the rotational symmetry assumption generalization is straightforward.

It can be shown that, for any finite time-of-flight, perfect focusing can be achieved (pure magnification of the original density distribution without distortion), without having to reach the far-field limit.

The equations of motion give after a time t_{ho} in the harmonic oscillator:

$$\begin{aligned} \tilde{X}(t_{\text{ho}}) &= \cos(\omega t_{\text{ho}}) \tilde{X}(0) + \sin(\omega t_{\text{ho}}) \tilde{P}(0) \\ \tilde{P}(t_{\text{ho}}) &= \cos(\omega t_{\text{ho}}) \tilde{P}(0) - \sin(\omega t_{\text{ho}}) \tilde{X}(0). \end{aligned} \quad (4.6)$$

After a time of flight expansion time t_{tof} we obtain:

$$\begin{aligned} \tilde{X}(t_{\text{ho}} + t_{\text{tof}}) &= \tilde{X}(t_{\text{ho}}) + \tilde{P}(t_{\text{ho}}) \omega t_{\text{tof}} \\ &= \tilde{X}(0) [\cos(\omega t_{\text{ho}}) - \omega t_{\text{tof}} \sin(\omega t_{\text{ho}})] + \tilde{P}(0) [\sin(\omega t_{\text{ho}}) + \omega t_{\text{tof}} \cos(\omega t_{\text{ho}})] \\ &= M [\cos(\theta_{\text{tof}}) \cos(\omega t_{\text{ho}}) - \sin(\theta_{\text{tof}}) \sin(\omega t_{\text{ho}})] \tilde{X}(0) \\ &\quad + M [\cos(\theta_{\text{tof}}) \sin(\omega t_{\text{ho}}) + \sin(\theta_{\text{tof}}) \cos(\omega t_{\text{ho}})] \tilde{P}(0) \end{aligned} \quad (4.7)$$

where we introduced:

$$\theta_{\text{tof}} = \arctan(\omega t_{\text{tof}}); \quad M = \frac{1}{|\cos(\theta_{\text{tof}})|} = \sqrt{1 + (\omega t_{\text{tof}})^2} \quad (4.8)$$

Notice that $\tilde{X}(t_{\text{ho}} + t_{\text{tof}})$ denotes, in compact form, the $\tilde{X}(t)$ operator obtained from a t_{ho} time in the harmonic oscillator followed by a free expansion time of duration t_{ho} .

Finally, one can write:

$$\tilde{X}(t_{\text{ho}} + t_{\text{tof}}) = M [\tilde{X}(0) \cos(\omega t_{\text{ho}} + \theta_{\text{tof}}) + \tilde{P}(0) \sin(\omega t_{\text{ho}} + \theta_{\text{tof}})] \quad (4.9)$$

The focusing condition, obtained by ensuring that the coefficient of $\tilde{P}(0)$ in 4.9 is 0, is given by

$$\tan(\omega t_{\text{ho}}) = -\omega t_{\text{tof}} \quad (4.10)$$

or equivalently by

$$\theta_{\text{tof}} = \arctan(\omega t_{\text{tof}}) = -\omega t_{\text{ho}} + n\pi, \quad (4.11)$$

with n integer. This implies

$$\tilde{X}(t_{\text{ho}} + t_{\text{tof}}) = (-1)^n M \tilde{X}(0) \quad (4.12)$$

The final position operator (or variable, if interpreted classically) is then the initial position operator (variable) multiplied by the magnification factor $(-1)^n M$. For n uneven, this implies also a parity reflection. The magnification strength is given by

$$M = \sqrt{1 + (\omega t_{\text{tof}})^2} \approx \omega t_{\text{tof}} \quad (4.13)$$

The approximation holds in the limit $\omega t_{\text{tof}} \gg 1$, which is often satisfied in our experiments where the trap frequency can take values up to $\omega/(2\pi) \sim 650\text{Hz}$ and we can perform time-of-flight expansion for up to $\sim 20\text{ms}$.

A graphical representation of the time-evolution of the \tilde{X} operator is presented in figure 4.2.

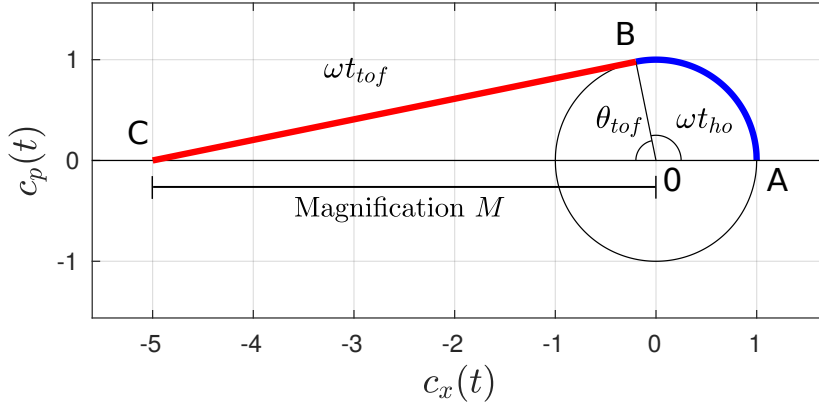


Figure 4.2.: Graphical representation of the focusing condition. Time evolution of the operator $\tilde{X} = c_x(t)\tilde{X}(0) + c_p(t)\tilde{P}(0)$ (with $c_x(t), c_p(t)$ time-dependent coefficients), as a combination of the time-independent operators $\tilde{X}(0), \tilde{P}(0)$.

The $T/4$ pulse can be described by the arc AB, that subtends a ωt_{ho} angle. The free expansion can be described by the segment BC. Because $\partial_t \tilde{X}(t) = \omega \tilde{P}(t)$, and $|\tilde{P}(t)| = 1$ (in a similar representation), the velocity in this plane is always ω . During time-of-flight $\tilde{P}(t)$ remains constant, therefore BC is a straight line, with a slope determined by the moment in which the trap is turned off (t_{ho}). To get $|c_x| = M$, $c_p = 0$ one sees that $\omega t_{\text{ho}} + \theta_{\text{tof}} = \pi$ must hold, with $\theta_{\text{tof}} = \arctan(\omega t_{\text{tof}})$, and that $M = \sqrt{1 + (\omega t_{\text{tof}})^2}$ as the hypotenuse of the right-angled triangle OBC. In the far field limit $\omega t_{\text{tof}} \rightarrow \infty$, $\omega t_{\text{ho}} \rightarrow \pi/2$ i.e. an exact $T/4$ pulse. This shows that for any finite t_{tof} , t_{ho} can be chosen such that the focusing condition is realized. Adapted from [13].

4.1.2. Deviations from the focusing Condition

We investigate now the question of how big the deviations from the ideal focusing condition can be before the imaging becomes unsharp. Let's consider equation 4.9 when $t_{\text{h.o.}} = \arctan(\omega t_{\text{tof}}) + \delta t$ i.e. a (small) δt deviation from the focusing condition. One gets then:

$$\tilde{X}(t_{\text{ho}} + t_{\text{tof}}) \sim -M [\tilde{X}(0) + \omega \delta t \tilde{P}(0)] \quad (4.14)$$

We compare this expression with the one gotten for a small time-of-flight directly after release from the lattice:

$$\tilde{X}(t_{\text{tof}} = \delta t) \sim [\tilde{X}(0) + \omega \delta t \tilde{P}(0)] \quad (4.15)$$

and notice that, up to a $-M$ magnification factor, they are identical. Our problem can therefore be mapped to another one described by the question: if we take the original wavefunction and let it expand freely, what is the maximal time δt_{max} after which the density distribution becomes unsharp?

An important point to notice here, then, is that the tolerance allowed from this condition depends on the object that we want to image, and not on M or the trap frequency (as long as the approximation of equation 4.14 is valid).

We consider the case of an optical lattice with lattice constant a_{lat} . We can then say that δt_{max} is the time it takes for the wavefunctions residing in two neighbouring sites to overlap with each other. It then depends on the momentum distribution of the Wannier functions: using a triangular lattice with $a_{\text{lat}} = 709\text{nm}$ and depth $6E_{\text{rec}}$ one finds that for times above $\delta t_{\text{max}} \approx 50\mu\text{s}$ the Rayleigh criterion for distinguishing two neighbouring lattice sites ($\sigma_{\text{site}} < 0.35a_{\text{lat}}$, where σ_{site} is the width of the expanding density distribution from a lattice site), is not satisfied.

We notice that if interference between different lattice sites is present, this condition might be tightened(relaxed) in case of positive(negative) interference ([163]).

δt_{max} sets also the maximal ellipticity of a 2D harmonic trap, which is then given by the condition $|(T_x/4) - (T_y/4)| < 2\delta t_{\text{max}}$. Notice that for a fixed ratio T_x/T_y the condition is more easily satisfied by increasing the trap frequency (reducing thus $|(T_x/4) - (T_y/4)|$).

Finally we address how the focusing condition changes when keeping fixed t_{ho} and varying t_{tof} .

This question has practical relevance because the optical imaging takes place in a finite time, and hence actually a range of values for t_{tof} are sampled. For typical parameters ($M > 30$, $t_{\text{im}} = 50\mu\text{s}$) this doesn't alter significantly the focusing: this can be quantified by considering the excess rotation angle during the imaging time $\Delta\theta_{\text{tof}} \sim t_{\text{im}}\partial_{t_{\text{tof}}}\theta_{\text{tof}} = t_{\text{im}}\frac{\omega}{1+(\omega t_{\text{tof}})^2}$.

We map once again this situation to the case of direct time-of-flight from the lattice: in that case, such a small rotation angle is obtained with a time-of-flight

$$\delta t = \frac{1}{\omega}\Delta\theta_{\text{tof}} \sim \frac{t_{\text{im}}}{(\omega t_{\text{tof}})^2} \ll \delta t_{\text{max}} \quad (4.16)$$

and hence this effect can be safely neglected.

Instead, t_{tof} mainly influences the value of M ; taking the derivative with respect to t_{tof} , for $t_{\text{tof}} \gg 1/\omega$:

$$\partial_{t_{\text{tof}}}\tilde{X}(t_{\text{ho}} + t_{\text{tof}}) \sim \partial_{t_{\text{tof}}}\omega t_{\text{tof}}\tilde{X}(0) = \omega\tilde{X}(0) \quad (4.17)$$

we can see that we can consider the atoms, at the end of the expansion time, as ballistically propagating during t_{im} at velocity ωx_0 , where x_0 is the distance of an atom from the trap center at $t = 0$ (obtained by substituting the classical variable x_0 to the operator $\tilde{X}(0)$). This leads to a displacement during the imaging $\Delta x = t_{\text{im}}\omega x_0$. Imposing $\Delta x < a_{\text{lat}}/2$ one gets the maximal distance from the trap center allowed before the signals from lattice sites at distance Ma_{lat} (after magnification) will start to overlap: $x_{\text{max}} = \frac{Ma_{\text{lat}}}{2t_{\text{im}}\omega} \sim a_{\text{lat}}\frac{t_{\text{tof}}}{t_{\text{im}}}$. For parameters $t_{\text{tof}} = 20\text{ms}$, $t_{\text{im}} = 50\mu\text{s}$, one obtains a size of about 400 lattice sites. It can be increased by reducing t_{im} , if there is enough signal to noise.

The atoms might also have a velocity component (in the imaging plane) because of gravity if they are (as in our case) in free fall during the time-of-flight. At the end of the time-of-flight expansion of duration $t_{\text{tof}} = 25\text{ms}$, they have acquired a velocity $v = gt_{\text{tof}} = 0.25\text{m/s}$, where $g = 9,81\text{m/s}^2$ is the gravitational acceleration. To keep the displacement during the imagine pulse of length t_{im} below a magnified lattice constant $Ma_{\text{lat}} = 50\mu\text{m}$ (with $M = 71$), it is restricted to $t_{\text{im}} \ll Ma_{\text{lat}}/v = \omega_{\text{ho}}a_{\text{lat}}/g = 200\mu\text{s}$. This is no limitation to standard absorption imaging, but might play a role in experiments where single-atom sensitivity is desired, because it would need a longer imaging time for collecting enough fluorescence photons.

4.1.3. Time Dependent Parameters

We derived analytically the focusing condition assuming a perfectly constant trap frequency for $t < t_{\text{h.o.}}$ and that it can be turned off instantly at $t = t_{\text{h.o.}}$.

Experimentally, that might not be the case: magnetic fields can only be switched off in a finite time due to the inductance of the coils, and optical potential have also a finite turning on time. In this case, we demonstrated ([164]) that varying the set value of t_{ho} , denoted t'_{ho} , one can find the one which realizes perfect focusing. The existence of such a value is guaranteed by continuity, because the coefficient $c_p(t'_{\text{ho}} + t_{\text{tof}})$ changes sign as a function of t'_{ho} (compare with figure 4.2; the same expression $\tilde{X}(t'_{\text{ho}} + t_{\text{tof}}) = c_x(t'_{\text{ho}} + t_{\text{tof}})\tilde{X}(0) + c_p(t'_{\text{ho}} + t_{\text{tof}})\tilde{P}(0)$ is implied here) therefore it must exist a t'_{ho} such that $c_p = 0$.

We notice that in presence of a time-dependent trap frequency, the center of the trap might oscillate because of forces like gravity in the imaging plane. As long as the atoms don't probe regions with strong anharmonicity, this is not a problem since in the equations of motion for the operators \tilde{X} and \tilde{P} now the shift enters just as a real number, after the total evolution this gets mapped to a shift in the position of the cloud and a "kick" in velocity.

4.1.4. Imaging the Velocity Field

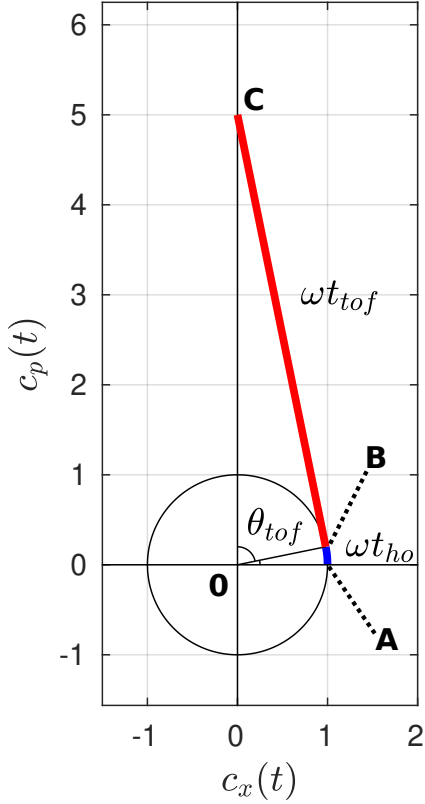


Figure 4.3.: Putting the momentum distribution into focus. Time evolution of the operator $\tilde{X} = c_x(t)\tilde{X}(0) + c_p(t)\tilde{P}(0)$ (with $c_x(t), c_p(t)$ time-dependent coefficients), as a combination of the time-independent operators $\tilde{X}(0), \tilde{P}(0)$. The evolution starts at $A = (1, 0)$ and performs a rotation in the HO for a duration t_{ho} . Upon reaching point B , time-of-flight begins, as described by the straight line BC (since during tof $\tilde{P} = \partial_t \tilde{X} = \text{const.}$) of length ωt_{tof} (since at all times the velocity in this plane is ω). To get $|c_x| = 0$, $c_p = M$ one sees that $\omega t_{\text{ho}} + \theta_{\text{tof}} = \pi/2$ must hold, adding up to the quarter circle with $\theta_{\text{tof}} = \arctan(\omega t_{\text{tof}})$, and that $M = \sqrt{1 + (\omega t_{\text{tof}})^2}$ as the hypotenuse of the right-angled triangle $0BC$.

When choosing $\cot(\omega t_{\text{ho}}) = \omega t_{\text{tof}}$ (to be substituted in equation 4.9) one gets $\tilde{X} = M\tilde{P}(0)$, i.e. one can measure the momentum distribution without distortion even for finite ToF expansion time t_{tof} . The focusing of the momentum distribution is schematized in figure 4.3.

This allows to tune the magnification arbitrarily in the range $1 - \sim \omega t_{\text{tof}}$. The meaning of M in the mapping of the momentum distribution to real space is somewhat arbitrary because the dimensional conversion factor depends on ω : in this convention $M = 1$ is obtained with a pure $T/4$ evolution in the trap ([36, 37, 165]) and $\sim \omega t_{\text{tof}}$ by a pure time of flight evolution. Time of flight experiments where the far-field condition is not perfectly met could use this to improve the momentum resolution, and at the same time experiments using the $T/4$ technique could add some time of-flight to increase the magnification to increase further the resolution.

In general, all consideration made so far for imaging the real space distribution are valid also in this case and could be applied in this case by substituting $t_{\text{ho}} \rightarrow t_{\text{ho}} - T/4$.

4.1.5. Other Magnification Schemes

In our experiment we obtain magnifications of up to $M = 93$ via relatively large trap frequencies. Other possibilities for obtaining a high magnification or increasing it further could e.g. be a longer time-of-flight via magnetic levitation (provided the levitating potential can be well approximated by a perfectly linear gradient), or the scheme can be generalized to include other matter-wave elements: in analogy to the suggestion in [37] for magnifying the momentum distribution, one could think of an alternating scheme between two trap frequencies, as illustrated in the following. At first a quarter period evolution could be performed in a trap with frequency ω_1 , then a second one in a trap with frequency $\omega_2 < \omega_1$. This magnifies the density distribution a factor $\frac{\omega_1}{\omega_2}$. This could be iterated n times and at the end, adding one last quarter period evolution followed by time of flight, this brings the total magnification to $M \sim \omega_1 t_{\text{tof}} \left(\frac{\omega_1}{\omega_2}\right)^n$.

The magnification could also be increased by adding an additional time evolution in a harmonic anti-confinement as proposed for the magnification of the momentum distribution in [36].

We notice here that in order to obtain $M > 1$ the anti-confinement pulse should follow the evolution in the harmonic potential, and not the other way round. An anti-confinement pulse of duration t_a has the effect of correlating the operators \tilde{X} and \tilde{P} as follows:

$$\begin{pmatrix} \tilde{X}(t_1 + t_a) \\ \tilde{P}(t_1 + t_a) \end{pmatrix} = \begin{pmatrix} C & \frac{\omega}{\omega_a} S \\ \frac{\omega_a}{\omega} S & C \end{pmatrix} \begin{pmatrix} \tilde{X}(t_1) \\ \tilde{P}(t_1) \end{pmatrix}; \quad C \equiv \cosh(\omega_a t_a), \quad S \equiv \sinh(\omega_a t_a) \quad (4.18)$$

where ω_a is the frequency that enters the anti-confinement potential $-\frac{1}{2}m\omega_a^2 x^2$ which is applied for a time t_a . The factors $\frac{\omega}{\omega_a}$, $\frac{\omega_a}{\omega}$ appear because we are still using ω as the reference frequency for defining the natural units. The dynamics in the harmonic oscillator with frequency ω is described by:

$$\begin{pmatrix} \tilde{X}(t_1 + t_{\text{ho}}) \\ \tilde{P}(t_1 + t_{\text{ho}}) \end{pmatrix} = \begin{pmatrix} c & s \\ -s & c \end{pmatrix} \begin{pmatrix} \tilde{X}(t_1) \\ \tilde{P}(t_1) \end{pmatrix}; \quad c \equiv \cos(\omega t_{\text{ho}}), \quad s \equiv \sin(\omega t_{\text{ho}}) \quad (4.19)$$

Executing the confinement pulse after the anti-confinement results in the following expression for \tilde{X} , obtained by multiplication in the corresponding order of the matrices above:

$$\tilde{X}(t_a + t_{\text{ho}}) = (cC + \frac{\omega_a}{\omega} sS) \tilde{X}(0) + (\frac{\omega}{\omega_a} cS + sC) \tilde{P}(0) \quad (4.20)$$

The momentum distribution can be imaged if $c = \frac{-\omega_a sS}{\omega C}$; substituting this expression yields:

$$\tilde{X}(t_a + t_{\text{ho}}) = \frac{\omega_a}{\omega} \left(-\frac{sS}{C} C + sS\right) \tilde{X}(0) + \left(\frac{-sS^2 + sC^2}{C}\right) \tilde{P}(0) = \left(\frac{s}{C}\right) \tilde{P}(0) \quad (4.21)$$

For the last step we used $C^2 - S^2 = 1$. This produces a magnification $s/C < 1$ (because $s \leq 1$; $C > 1$), i.e. smaller as the one obtained with one single $T/4$ pulse.

Instead, by performing the anti-confinement pulse *after* the confinement pulse, one obtains:

$$\tilde{X}(t_{\text{ho}} + t_a) = (Cc - \frac{\omega}{\omega_a}Ss)\tilde{X}(0) + (\frac{\omega}{\omega_a}Sc + Cs)\tilde{P}(0) \quad (4.22)$$

The momentum distribution can now be imaged if $c = \frac{\omega Ss}{\omega_a C}$:

$$\begin{aligned} \tilde{X}(t_{\text{ho}} + t_a) &= \frac{\omega}{\omega_a}(-\frac{sS}{C}C + sS)\tilde{X}(0) + (\frac{(\omega/\omega_a)^2 sS^2}{C} + sC)\tilde{P}(0) = \\ &= \frac{s((\omega/\omega_a)^2 S^2 + C^2)}{C}\tilde{P}(0) = C\sqrt{1 + (\frac{\omega S}{\omega_a C})^2}\tilde{P}(0) \end{aligned} \quad (4.23)$$

or the real space distribution can be imaged if $c = -\frac{\omega_a Cs}{\omega S}$:

$$\begin{aligned} \tilde{X}(t_{\text{ho}} + t_a) &= (-\frac{\omega_a sC^2}{\omega S} - \frac{\omega}{\omega_a}sS)\tilde{X}(0) + (-sC + sC)\tilde{P}(0) = \\ &= -(\frac{\omega_a sC^2}{\omega S} + \frac{\omega sS}{\omega_a})\tilde{X}(0) = -C\sqrt{1 + (\frac{\omega S}{\omega_a C})^2}\tilde{X}(0) \end{aligned} \quad (4.24)$$

In both cases¹, the magnification is (much) bigger than 1, for large enough $\omega_a t_a$.

For example for $\omega_a = \omega$, keeping in mind that for $\omega_a t_a > 1$, $S \approx C \approx \frac{1}{2}e^{\omega_a t_a}$, one can focus the momentum distribution by choosing $\tan(\omega t_{\text{ho}}) = \frac{c}{s} = \frac{S}{C} \approx 1$, (about a $T/8$ pulse), or the real space distribution by choosing $\tan(\omega t_{\text{ho}}) = \frac{c}{s} = -\frac{S}{C} \approx -1$, (about a $3T/8$ pulse); the magnification M simplifies to $\sim e^{\omega_a t_a}/\sqrt{2}$.

These protocols could be combined with a subsequent time-of-flight t_{tof} , getting an additional $\sim \omega t_{\text{tof}}$ factor in the total magnification M . The focusing condition can be exactly found, as before, by fine adjustment of t_{ho} , for fixed t_a and t_{tof} .

An initial anti-confinement pulse might be beneficial, though, for a fast initial reduction of the density along the third direction in cases where interactions during the matter wave optics are detrimental. Notice that although the scaling of M with the two schemes presented here are exponential, letting the wavefunction expand too much before time-of-flight might cause it to sample more of the non-harmonic part of the potential.

¹the last step in equations 4.23 and 4.24 can be obtained by substituting $s = t/\sqrt{t^2 + 1}$, with $t = \frac{c}{s} = \omega_a C/(\omega S)$ in equation 4.23 and $t = \frac{c}{s} = -\omega S/(\omega_a C)$ in equation 4.24; this passage is omitted here for brevity.

4.2. Experimental Characterization

We test these ideas in our setup, consisting of ^{87}Rb atoms in the combined potential of a triangular/honeycomb optical lattice and a magnetic trap. We use atoms in the $F, m_f = 2, 2$ state, which is the one which sees the deepest trap with corresponding frequencies up to almost $\sim 700\text{Hz}$.

We initialize the magnification protocol by switching off the optical lattice, therefore quenching directly into the harmonic confinement provided by the magnetic trap (which was already on in presence of the lattice). Experimentally we notice that there is a distinction to make between system with or without coherence between different lattice sites at the moment in which the magnification protocol is started.

Directly imaging the density distribution of coherent systems present some additional difficulties, which we believe are related to the higher densities realized during the matter-wave dynamics, because of matter-wave interference. In particular a periodic wavefunction expanding experiences periodic revivals of the lattice structure (known as Talbot revivals, see chapter 5) and at $t_{\text{ho}} = T/4$ the real space distribution becomes the initial momentum distribution, characterized by sharp Bragg peaks. In order to give an idea why it is beneficial to work with systems without coherence, we note that the density of such peaks scales $\propto N \cdot \sigma_{\text{sys}}^2$, while the density in the momentum distribution of an incoherent sample scales $\propto N \cdot \sigma_{\text{lat}}^2$, where σ_{lat} is the width of the density distribution in a single lattice site. Since for our parameters $\sigma_{\text{lat}} \sim 50 - 100\text{nm}$ and $\sigma_{\text{sys}} \sim 1 - 10\mu\text{m}$ the density effects at $t = T/4$ for an incoherent sample, compared to an incoherent one, can be reduced up to 3 or 4 orders of magnitude. We are going to address more in detail aspects of the dynamics of coherent wave packets in chapter 5.

We present here the results obtained with incoherent systems and also the scheme that we used us to image density distribution of coherent systems in a triangular lattice: the imaging is preceded by a step in which the lattice depth is suddenly set to the maximum value, "freezing" a snapshot of the density distribution in the deep lattice for about 10ms. During this time there is no relevant tunneling coupling and dephasing takes place, removing the coherence between different lattice sites.

We initialize the protocol by abruptly removing all optical potentials (realized via a radio-frequency switch on the modulation of the AOMs of the lattice beams. Therefore the time scale is given by the time it takes for the radio frequency to travel the AOM which is about 100ns, fast enough to be considered instantaneous). The magnetic trap is characterized to be rotationally symmetric (we estimate a deviation of less than 1% between the trapping frequency in x and y direction), therefore leading to the same magnification in both in-plane dimensions.

4.2.1. Results for different Lattice Geometries and Magnifications

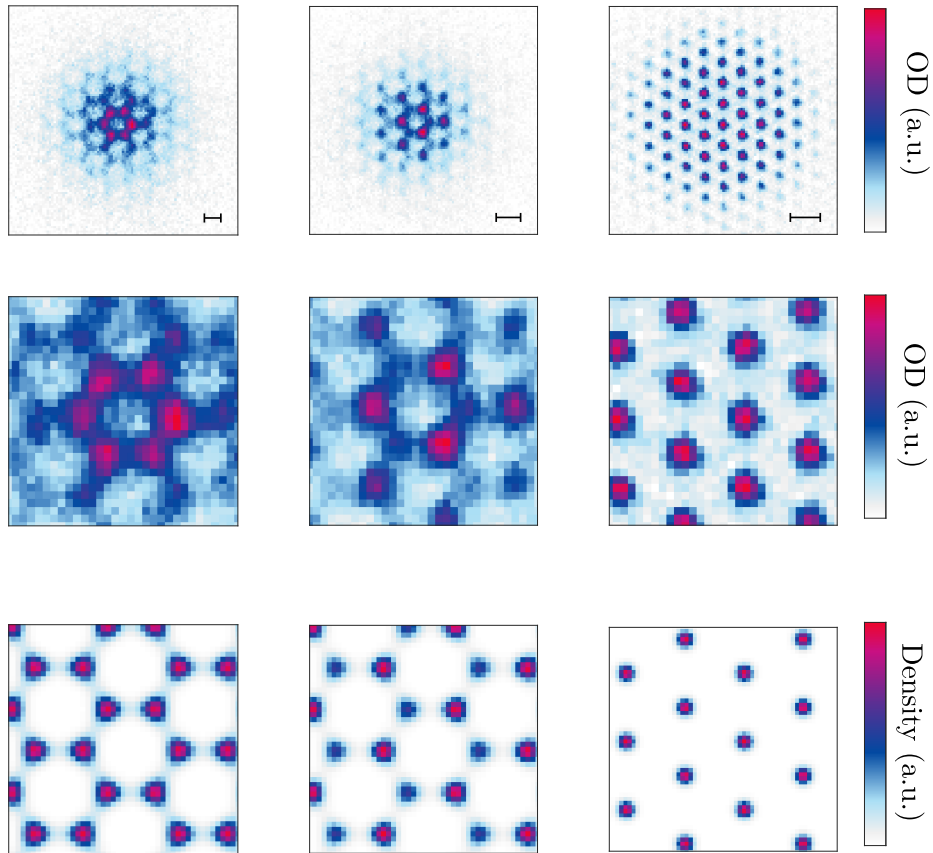


Figure 4.4.: Quantum Gas Magnification of different lattice geometries. In the first row, experimental images are shown which result from different lattice geometries (honeycomb, boron-nitride with a sublattice offset of $\Delta/(2\pi) = 4.6\text{kHz}$ and triangular lattice). Black lines correspond to $1\mu\text{m}$ (before magnification). $M = 89(1), 89(1), 80(1)$ for the three images. We map linearly the measured optical density to an atomic density distribution in the lattice. In the second row, a zoom is performed into the center of the cloud in order to compare the density distribution with that of the corresponding ground state, as obtained by our band structure calculations (lowest row). The same colorbar, normalized to the maximum density in each image, is used for all images. Apart from a finite background level and a broadening of the expected distribution widths, the experimental data and theory are in good qualitative agreement. This is remarkable in particular in the case of honeycomb/boron nitride lattices where there is a richer sub-lattice structure. Adapted from [13].

In figure 4.4 some examples of single-shot images for different lattice geometries are presented. We technically measure an optical density but we interpret this quantity as the real space atomic density, with the conversion factor between the two given by the knowledge of the conversion factor between optical density and atom number (per pixel), and of the lattice spacing $a_{\text{lat}} = 709\text{nm}$.

We notice that while quantum gas microscopy of triangular lattices was recently realized in [166, 167], the pictures of the honeycomb and boron-nitride lattice represent the first single-site-resolved images of ultracold atoms in a non-separable optical lattice.

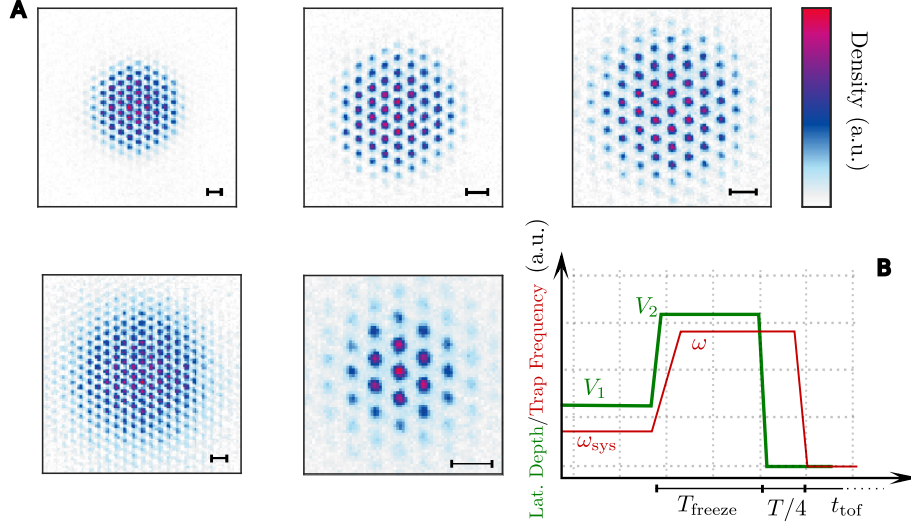


Figure 4.5.: Tuning the magnifications. **A** Raw experimental images for different values of the trapping frequency in the system and during the matterwave optics. The black lines correspond to $1\mu\text{m}$. **B**: The protocol which allows changing the trap frequency is schematized. In a deep lattice (typically $V_2 = 6E_{rec}$) the density distribution is frozen and the trap frequency in the system ω_{sys} can be ramped up in $\sim 2\text{ms}$ to the desired value ω for magnification. A wait time for the removal of coherence is also necessary. Afterwards, the lattice is switched off and after $T/4$ also the magnetic trap. In the examples presented here $V_1 = V_2 = 6E_{rec}$. The first three images in **A** correspond to the same initial system size, given by the confinement $\omega_{sys}/(2\pi) = 225\text{Hz}$ but with different magnifications ($M = 43(1), 65(1), 80(1)$ respectively) tuned by different values of ω . A much bigger initial system can be obtained with $\omega_{sys}/(2\pi) = 89\text{Hz}$ and imaged with using $M = 43(1)$ (first picture, lower row). In the last image, we demonstrate the possibility to create a very focused wavepacket of Gaussian width $1.5\mu\text{m}$ with $\omega_{sys} = 610\text{Hz}$ (imaged then with $M = 83(1)$). Adapted from [13].

In figure 4.5 the tunability of the magnification by changing the trap frequency is illustrated. A schematic is also presented for the protocol which makes it possible to tune independently the trap frequency ω_{sys} of the triangular optical lattice system from the trap frequency used during the magnification ω . We can then obtain single site resolution of a system with more than hundred populated sites (with size $\sim 4\mu\text{m}$) obtained with a trap frequency $\omega_{sys}/(2\pi) = 89\text{Hz}$ and imaged by freezing the density distribution and then ramping up the trap frequency in order to image with single-site resolution.

At the same time using a bigger system trap frequency ω_{sys} we can prepare a very localized wavepacket as small as $\sim 1.5\mu\text{m}$, populating just a few lattice sites.

Larger systems possess a higher translational symmetry and can be better described by band theory. At the same time, the possibility to create and detect very localized wavepackets could be used to probe topological interfaces ([168]) or for placing impurities of atoms tightly held in the trap, in a cloud of atoms which do not feel the trapping potential (e.g. atoms in state $m_F = 0$ for the magnetic trap), thus engineering interesting interacting states like polarons ([169, 170]).

We used a localized wavepacket also to characterize the lattice phase drifts (notice that we do not use a phase lock in our setup for keeping the lattice position fixed). We found that over a hold time of 6s in a deep lattice the position drifts by less than a lattice site with respect to the center of the magnetic trap, thus demonstrating that the lattice setup has an excellent intrinsic phase stability. We also notice that the lattice relative position between consecutive experimental runs seems to be completely uncorrelated: we thus assume to have a random lattice position in each run, but constant over the whole duration of the hold time in the lattice.

The highest magnification that we can obtain is about 93(1). We measure the magnification by fitting a lattice structure on the experimental images and comparing the measured lattice constant with the *in situ* value. The error on M is the fit error. The lowest magnification is about 35. Below that, we can still apply the protocol but we are not able to check whether the focusing condition is realized because the magnified lattice spacing is not big enough to be resolved from our camera with an effective pixel size of $6.04\mu\text{m}$.

4.2.2. Focusing Condition

Because of the effects previously mentioned, the optimal focusing time might be not so easy to determine beforehand, therefore in practice for a given trap frequency the focusing condition is found experimentally.

We load the atoms in a deep triangular lattice and image the system after a variable hold time around $\frac{1}{4} \frac{2\pi}{\omega}$ in the magnetic trap (where ω is determined independently) and after a fixed time of flight (4.6). The atomic distribution is then imaged with a $50\mu\text{s}$ pulse of the optical imaging beam, whose profile arrives on the camera a factor of ~ 2 magnified. We determine the focusing condition by introducing the contrast of the quantum gas magnifier, which we define as the relative amplitude of the peaks in the Fourier transformation at the reciprocal lattice wavevectors. We then determine via a Gaussian fit the focusing condition. At the same time, from the knowledge of the effective pixel size and of the lattice constant, we determine experimentally the magnification.

We observe that the focusing condition depends on the atom number (figure 4.6C). We attribute this dependence as a shift towards lower values of the trapping frequency, due to the repulsive interactions between Rubidium atoms. We model this effect in a mean-field picture as follows.

Along the z -direction the trapping frequency is much smaller, and we expect there a much slower dynamics, with the result that the cloud expands in this direction less than a factor of two, without incurring into depth-of focus problems with the imaging beam. At the same time, we took also measurements with a lattice in the z -direction, without noticing a decrease of the quality of the imaging because of the greater energy stored in z -direction. We can not measure with precision the size of the tubes in z -direction, but we estimate this as a Thomas-Fermi profile for a tube of 1000 atoms, a $6E_r$ deep triangular lattice and a transverse confinement of $\omega_z/2\pi = 30\text{Hz}$; from that we get a Thomas-Fermi radius of $30\mu\text{m}$. We neglect the dynamics in this direction during the time in the magnetic trap, since it happens on time scales given by the much smaller ω_z , and model the in-plane density distribution ρ , after release from the lattice, as described by a Gaussian function with time-dependent width $\sigma_{\text{sys}}(t)$. The resulting mean field potential E_{int} for a cloud of atoms without a defined phase relation can then be written as ([171]):

$$E_{\text{int}}(r) = 2Ng_0\bar{\rho}_z\rho(r) = 2Ng_0\bar{\rho}_z \frac{1}{2\pi\sigma_{\text{sys}}(t)^2} e^{-r^2/2\sigma_{\text{sys}}(t)^2} \quad (4.25)$$

where r is the radial coordinate in the lattice plane. $\bar{\rho}_z$ is the normalized density in z -direction. With the Taylor expansion $E_{\text{int}}(r) = E_{\text{int}}(0) - \frac{1}{2}m\omega_{\text{int}}^2 r^2$ one obtains an effective trap frequency (in the center of the system) given by

$$\omega_{\text{eff}} = \sqrt{\omega^2 - \omega_{\text{int}}^2}; \quad \omega_{\text{int}}^2 = \frac{4Ng_0\bar{\rho}_z}{m} \frac{1}{4\pi\sigma_{\text{sys}}^4} \quad (4.26)$$

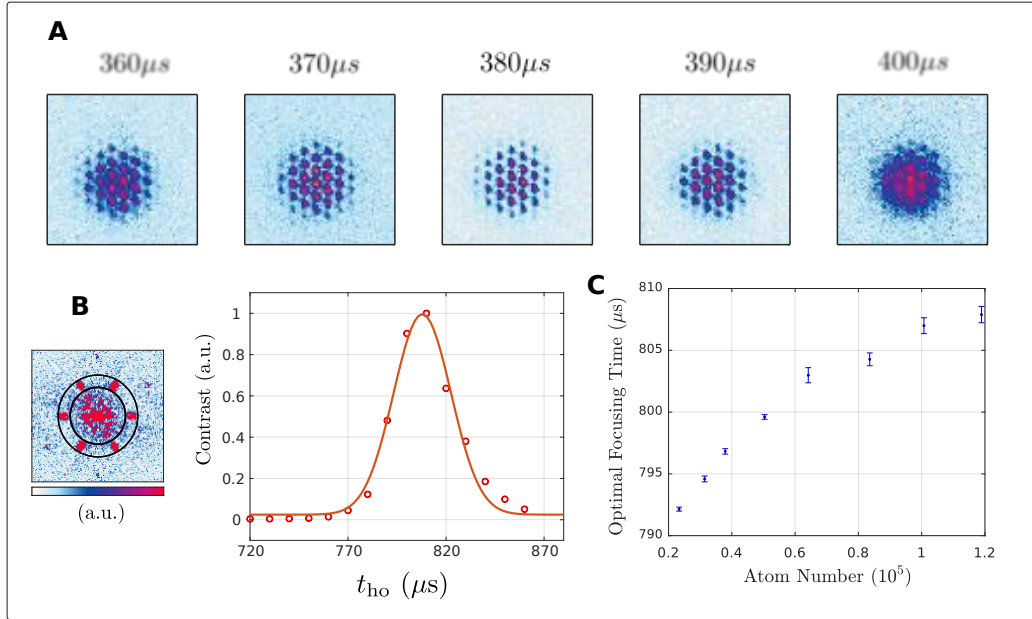


Figure 4.6.: Placing the matter wave lens. **A:** Measured density distributions for different hold times in the harmonic potential ($\omega \sim 2\pi \cdot 650\text{Hz}$), for a fixed time-of-flight. This shows how, for our parameters, often a few shots are sufficient for determining experimentally the focusing condition. **B:** In the inset, an exemplary Fourier transformation of an experimental image. The contrast of the image is defined as the integrated sum of the signal in the mask denoted by the two rings, chosen to include the reciprocal lattice wavevectors. For a given atom number, the optimal focusing time is obtained from a Gaussian fit to the image contrast as a function of t_{ho} . In this example, with atom number $N \sim 10^5$ and $\omega/(2\pi) = 318\text{Hz}$, we find a $1/\sqrt{e}$ width of the fit of $10\mu\text{s}$, in agreement with the limit of $t_{\text{max}} \sim 50\mu\text{s}$ for being able to distinguish at all neighbouring lattice sites. **C:** Higher atom numbers lead to a reduction of the effective trap frequencies because of a mean field potential shift. Points are the experimental determination of the optimal focusing time from such fits as a function of the atom number. Error bars denote 68% confidence interval. Adapted from [13].

At $t = T/4$, we estimate $\sigma_{\text{sys}}(T/4) = \frac{\hbar}{\sqrt{2\omega a_{\text{osc}}}}$, assuming that the momentum distribution is given by the local oscillator length a_{osc} in a lattice site, calculated as $\sqrt{\frac{\hbar}{m\omega_{\text{osc}}}}$, with ω_{osc} the local oscillator frequency at the lattice sites. The factor $\sqrt{2}$ takes into account the ratio of the width of a wavefunction to that of the associated density distribution.

For our parameters, if ω is high enough, the density is highest at $t = T/4$, and ω_{int} can be on the same order of magnitude as ω , demonstrating that this effect indeed is not negligible. Notice that the measured relative shift is then only 2 – 3%, and this can be explained because the calculation holds only in the middle of the cloud, and for a limited time range around $t = T/4$, and these same interaction effects might prevent the cloud for reaching so high densities.

A quantitative explanation of the measured optimal time shift is hence yet to be done. With a similar procedure, we also estimated the instantaneous scattering rates ([36]) as

$$\Gamma(t) = 8\pi a_{22}^2 v(t) \bar{\rho}(t) \quad (4.27)$$

where $v(t)$ is the mean velocity of the atoms, $\bar{\rho}(t)$ is the average density and $a_{22} = 95a_{Bohr}$ is the scattering length between two Rubidium atoms. $\bar{\rho}(t)$ is estimated as $N\rho_z/(4\pi\sigma_{sys}(t)^2)$ with the form for σ_{sys} which assumes that the real space and momentum space distribution are not correlated:

$$\sigma_{sys}(t) = \sqrt{(\cos(\omega t)\sigma_{sys}(0))^2 + (\sin(\omega t)\sigma_{sys}(T/4))^2} \quad (4.28)$$

v is calculated as $(v_{2D}^2 v_z)^{\frac{1}{3}}$, with v_{2D} estimated as $\sigma_P(t)/m$ with:

$$\sigma_P(t) = \sqrt{(\cos(\omega t) \frac{\hbar}{\sqrt{2}\omega\sigma_{osc}})^2 + (\sin(\omega t) m\omega\sigma_{sys}(0))^2} \quad (4.29)$$

The width for the momentum distribution at $t = 0$ is obtained assuming it is given by the momentum distribution of the Wannier functions (approximated as a Gaussian function of width σ_{osc}), and at $t = T/4$ it is obtained from the initial real-space distribution of width $\sigma_{sys}(0)$.

v_z is estimated using $\rho_z \frac{\hbar}{m}$. $v(t)$ is then on the order of $\sim 10^{-3}$ m/s.

Integration of $\Gamma(t)$ over $T/4$ produces no more than 1% scattering probability which we can then safely neglect. This is consistent with the observation of basically no background also in the density distributions showing sharp features of section 4.16. Notice also that this evidences how mean-field calculation and scattering rates calculations are not equivalent description of the dynamics.

4.2.3. Anharmonicity

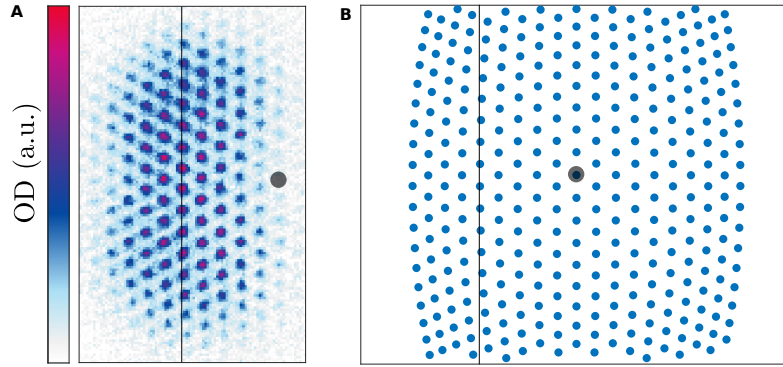


Figure 4.7.: Effects of the Anharmonicity of the Trap on the Density Distribution. In **A**, the sum signal of two clouds moved away from the trap center (indicated by the grey dot) is shown. The straight line serves as a reference for noticing that the lattice appears distorted. Still, the lattice sites remain well separated allowing their relative populations to be measured. In **B** is shown the velocity distribution after $T/4$ for classical particles located initially at the lattice sites, as obtained in a numerical simulation which considers the anharmonicity of the trap. The straight line serves as a reference, and evidence qualitative agreement between predicted and measured positions of the local maxima of the density. Adapted from [13].

We investigate now experimentally what happens when the assumption about the harmonicity of the trap does not hold anymore. For our magnetic trap, such aberrations become visible only for very large magnifications and for large systems or when displacing the cloud relative to the trap center. In order to control and characterize this anharmonicity we image a cloud shifted off-center in a very strong magnetic trap with a trap frequency in the $x - y$ plane of $\omega_{\text{ho}} = 2\pi \cdot 641$ Hz, which results from a gradient $B_1 = 1.69 \cdot 10^4$ G/m, a trap bottom $B_0 = 0.112$ G and an anti-curvature $B_2 = 7.1 \cdot 10^5$ G/m² (figure 4.7). The trap potential U_{trap} can then be written as

$$U_{\text{trap}}/h = 78.4 \text{ kHz} + 1756 \text{ Hz}(r/\mu\text{m})^2 - 7.2 \text{ Hz}(r/\mu\text{m})^4 \quad (4.30)$$

where r is the distance from the trap center and 78.4kHz is the resonance to the $m_F = 1$ state in the center of the trap. Magnetic traps have the advantage, when compared to optical dipole traps, of being smooth and defect-free, and more tunable. Optical traps instead can be faster and if sufficiently detuned also spin-independent. Therefore we give a comparison of the anharmonicity of an optical trap, as it might be helpful for experiments which want to implement the quantum gas magnifier with optical techniques.

For an optical dipole trap formed by a Gaussian beam with waist w , the potential can be described by $E_{\text{pot}}(r) = ae^{-2\frac{r^2}{w^2}}$. Expanding in r^2/w^2 gives:

$$E_{\text{pot}} \sim a\left(1 - 2\frac{r^2}{w^2} + 2\frac{r^4}{w^4}\right) \quad (4.31)$$

and hence the quartic to quadratic term ratio can be evaluated as $1/w^2$. Equating $1/w^2 = 7.2\text{Hz } \mu\text{m}^{-4}/(1756\text{Hz } \mu\text{m}^{-2})$ gives $w = 16\mu\text{m}$, which is then the minimal beam waist required in order not to exceed the anharmonicity degree used in this experiment.

The magnetic trap used here has a relatively high anharmonicity degree; for example we could get a trap frequency as high as $2\pi \cdot 200\text{ Hz}$ with an anharmonicity corresponding to a $135\mu\text{m}$ waist optical trap. For suitable parameters of an optical trap with small anharmonicity, intensity requirements for reaching the high trapping frequencies might be an important factor. The small distortion of the image is no limitation when one is interested in the lattice site occupations.

However, the density distribution during the $\text{T}/4$ evolution is not harmonic and the anharmonicity can lead to distortions of the image similar to the anharmonicity of the trap itself. We estimate that the quartic part of the mean field potential for our typical parameters can be of the same order of magnitude, but with opposite sign, as the quartic part of the trap. A more quantitative theoretical analysis of the influence of interactions on the resolution of the quantum gas magnifier is left for future work.

4.2.4. Resolution of the Quantum Gas Magnifier

We characterize experimentally the resolution of the quantum gas magnifier for the case of a triangular lattice.

The results of figure 4.8 evidence how the localization of the atomic distribution around the lattice sites depends on the atom number, therefore we are interested in understanding how much this effect is related to a "real" broadening of the Wannier functions due to interactions, and how important are interactions during the magnification protocol, which could decrease the resolution and influence the measured width of Wannier functions.

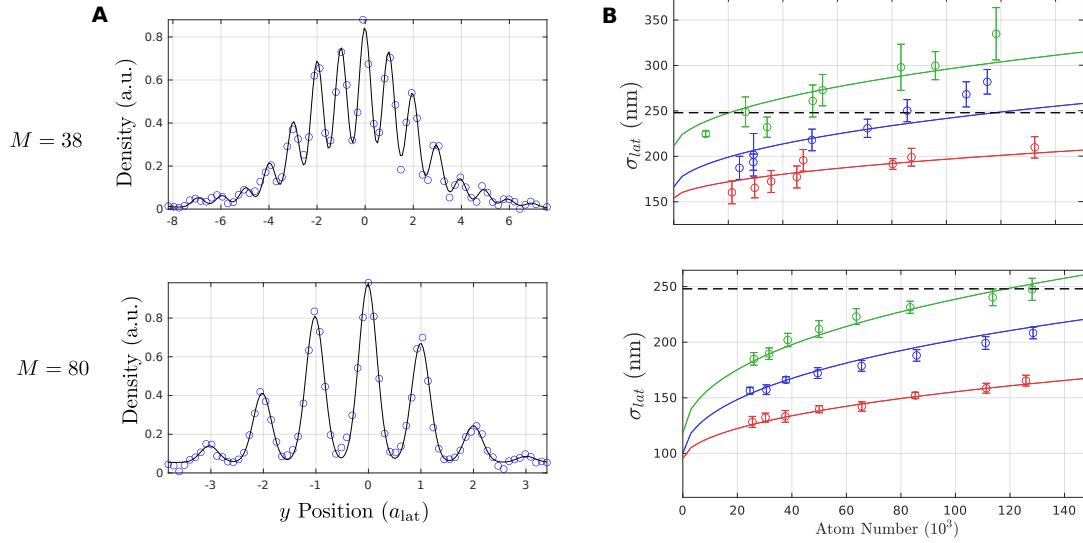


Figure 4.8.: Resolution of the Quantum Gas Magnifier. **A:** Density distributions for magnifications $M = 38(1)$ and $M = 80(1)$ in a cut along the central lattice site and parallel to the lattice vector connecting neighbouring sites. They can be fitted by an array of Gaussian functions of width σ_{lat} spaced by a_{lat} . In **B**, we plot σ_{lat} as a function of the atom number, for magnifications $M = 38(1)$ and $M = 80(1)$ and for different relay steps n (obtained by choosing $t_{\text{ho}} \sim \frac{2n+1}{T/4}$). $n = 0, 1, 2$ corresponds to the red, blue, green points and curves. Error bars indicates 68% confidence interval. Continuous lines are fits to the data with the form given in the main text. The dashed line indicates $0.35a_{\text{lat}}$, under which the Rayleigh criterion is satisfied. Adapted from [13].

We use an Ansatz for the Wannier function as a Gaussian distribution of width σ_{osc} in the lattice plane with a Thomas-Fermi profile in z -direction. We calculate the expectation value for the energy, summing the contributions from the interaction, kinetic and potential energy for the 2D harmonic oscillator of frequency ω_{osc} :

$$\begin{aligned}
 E(\sigma_{\text{osc}}) &= E_{\text{int}}(\sigma_{\text{osc}}) + E_{\text{kin}}(\sigma_{\text{osc}}) + E_{\text{pot}}(\sigma_{\text{osc}}) \\
 &= \frac{3^{2/3}2^{1/3}}{5}(m\omega_z^2)^{1/3}(Ng_0\bar{\rho}_{2D})^{2/3} + \hbar\omega_{\text{osc}}\left(\frac{1}{2}\frac{\sigma_0^2}{\sigma_{\text{osc}}^2} + \frac{1}{2}\frac{\sigma_{\text{osc}}^2}{\sigma_0^2}\right)
 \end{aligned} \tag{4.32}$$

with the averaged normalized 2D density $\bar{\rho}_{2D}$ being given by $1/(2\pi\sigma_{\text{osc}}^2)$. σ_0 is oscillator length associated to ω_{osc} ; for $V = 6E_r$, $\omega_{\text{osc}}/(2\pi) = 21\text{kHz}$. Minimization of E with respect to σ_{osc} for $N = 1000$ yields $\sigma_{\text{osc}} = 1.09\sigma_0$.

The width of the density distribution in a lattice site is then given by $\sim \frac{1}{\sqrt{2}}\sigma_0 = 52\text{nm}$, which is much smaller than the resolution we measure, in the range $100 - 200\text{nm}$ depending on magnification and atom number. The dependence on the atom number of figure 4.8 can then be interpreted mainly as a broadening effect introduced during the matter-wave optics, where the actual broadening of the distribution in the lattice due to interactions can be neglected.

Still, this calculations could be instructive because it shows, putting the numbers in, that $E_{\text{int}}/h \sim 5\text{kHz}$. This energy is converted very quickly into kinetic energy in the first expansion moments after the switch-off of the lattice; understanding how exactly this effect can broaden the measured single site distributions needs further theoretical investigation.

Also the contributions from the interactions and from the anharmonicity can be decoupled from each other: we take data also for $t_{\text{ho}} = 3T/4$ and $t_{\text{ho}} = 5T/4$: while in absence of interactions and anharmonicity these times should be all equivalent (up to a parity reflection), in practice they amplify deviations from the ideal picture, allowing a more precise estimation of the dependence of the measured lattice site width on the atom number. The data can be well fitted with the phenomenological form:

$$\sigma_{\text{meas}}^2 = (M\sigma_{\text{lat}})^2 + (\sigma_{\text{opt}})^2 + ([2n+1]^{p_1} N^{p_2} M\sigma_{\text{int}})^2 + ([2n+1]^{p_3} \sigma_{\text{an}})^2 \quad (4.33)$$

where the outcome is the quadratic sum of a contribution from the real density distribution width σ_{lat} (M times magnified), a term coming from the finite optical resolution of the system σ_{opt} , a term taking into account the interactions σ_{int} and one taking into account the anharmonicity σ_{an} . $n = 0, 1, 2$ indicates the number relay steps as $t_{\text{ho}} = \frac{2n+1}{4}T$.

We obtain $\sigma_{\text{opt}} = 5.3(3)\mu\text{m}$, in line with the pixel size of $6\mu\text{m}$, and $\sigma_{\text{lat}} = 68(24)\text{nm}$, also in line with the calculated value of 52nm . Interestingly, $\sigma_{\text{an}} = 0.42(46)$ is compatible with zero ($p_3 = 1.6(7)$). We found $\sigma_{\text{int}} = 4.2(4)\text{nm}$ ($p_1 = 0.29(5)$ and $p_2 = 0.33(5)$) suggesting that the interactions are the main source of broadening². It would be then very interesting to repeat these measurements with e.g. spin polarized fermions (which experience no contact interactions because of the Pauli exclusion principle).

Concluding, we can read out the lattice site populations with great precision for most of the parameters atom number and magnification. For the experiments presented in this chapter, we always use deep lattices and no coherence before imaging, either by starting with a deep lattice or by addition of the "freezing" step before imaging.

Considerations about the resolution of the quantum gas magnifier in a honeycomb lattice/boron-nitride lattice are made in section 4.4, where the density distribution is studied within the Wigner Seitz cell. In the next chapter, we are going to discuss the situation with coherent systems.

²Notice that the prefactor $[2n+1]^{p_1} N^{p_2} M$ when comparing σ_{int} and σ_{an} . The effect of the latter is in a first approximation assumed to be independent of M because with higher trap frequencies the harmonic region gets smaller, as does the density distribution.

4.3. Precision Thermometry

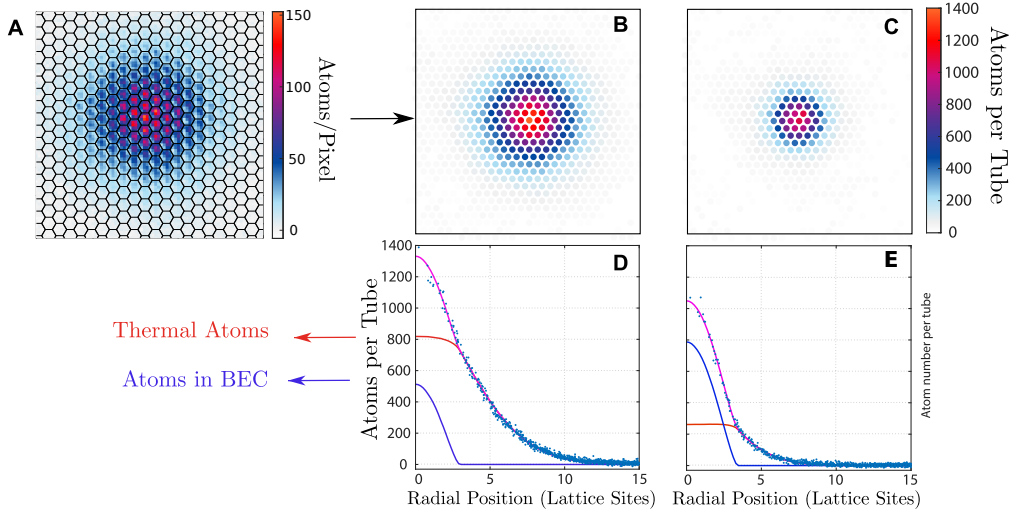


Figure 4.9.: Lattice Thermometry. **A:** raw picture obtained by loading a cloud of a certain temperature adiabatically in a shallow lattice, freezing and imaging the density distribution. The image can be subdivided into Wigner-Seitz cells around every lattice site, and summing the signal in each them produces the corresponding populations, as shown in **B**. Repeating for a lower temperature, as shown in **C**, produces a much narrower distribution. **D** and **E** show the corresponding populations of **B** and **C**, respectively, plotted as a function from the distance to the center of mass, with a bimodal fit with a condensed and a thermal component. Adapted from [13].

We study as a first application of the quantum gas magnifier more in detail the density distributions in the lattice for different temperatures of the cloud.

We load the atoms adiabatically in a triangular lattice of depth $V = 1E_r$, and a magnetic trap of $\omega/2\pi = 305\text{Hz}$. We chose a shallow lattice in order to guarantee the adiabaticity of the ramping process. We then ramp the lattice depth to $6E_r$, corresponding to a tunneling coupling of $J/h = 0.001\text{Hz}$ and wait there for coherence removal. We then image the density distribution.

We study the profile, i.e. the populations as a function of the in-plane radius. We first extract them, using the fact that the lattice sites are well separated, by integrating the atomic signal in the corresponding Wigner-Seitz cell. We then fit the profile with a bimodal model, containing two components, the BEC fraction n_0 and the thermal fraction (the procedure is sketched in figure 4.9, and more details on it can be found in [13, 172]).

We are now interested in seeing how the BEC fraction n_0 and temperature relate to each other. Because the critical temperature for BEC condensation is atom-number dependent, we developed a theory for extracting the critical temperature as a function of the atom number in our system (Appendix A).

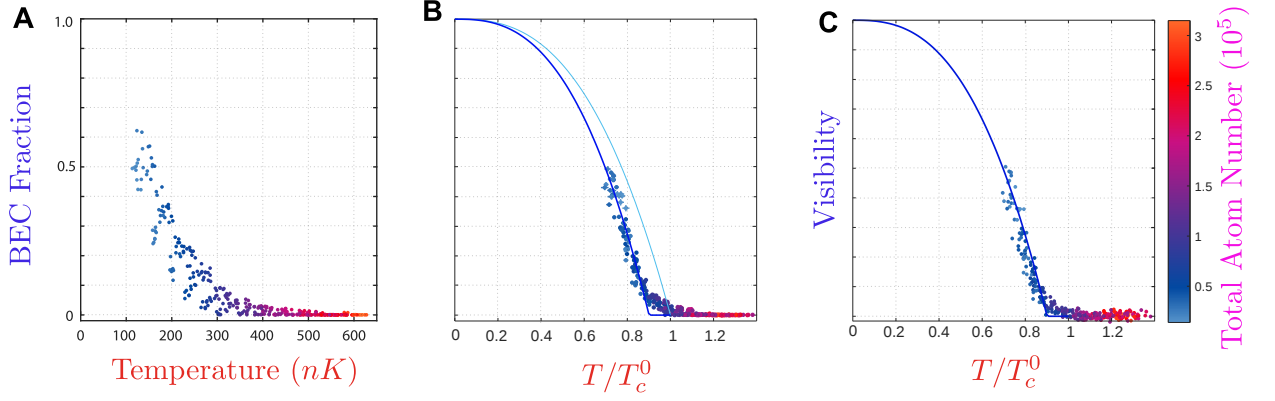


Figure 4.10.: BEC fraction as a function of temperature. We varied the frequency and duration of the evaporation in the magnetic trap (corresponding to different temperatures and atom numbers in the lattice). From each measurement we extract the BEC fraction and the temperature (**A**). For every atom number we calculate the critical temperature and plot the data as a function of the normalized temperature T/T_c^0 , where T_c^0 is the predicted critical temperature from the interaction-free theory (**B**). The data collapse into one single curve. The critical temperature T_c can be obtained with high precision by a fit (dark blue line) of the form $n_0 = (1 - (T/T_c)^\alpha)$ with $\alpha = 2.69$ (obtained numerically, see Appendix A). The light blue curve is the theory prediction for non-interacting particles. **C**: Comparison with the Bragg peaks visibility measurement from time-of-flight from the optical lattice. It follows the form given by the fit to the data taken "in situ" (dark blue line). Adapted from [13].

With this theoretical setup, we are able to extract the theoretical critical temperature T_c^0 for every atom number that we measure.

We can then obtain the curve $n_0(T/T_c^0)$ (figure 4.10) from measurements with different atom numbers and temperatures. n_0 and T are obtained from the fits to the density profiles, and T_c^0 is the critical temperature corresponding to the measured atom number extracted from our theoretical setup.

We also notice a very similar behaviour of $n_0(T/T_c^0)$ and of the visibility from time-of-flight pictures (as a function of the temperature measured *in situ* for the corresponding parameters) thus validating the measurement of the phase transition point. We notice that this appears to be shifted with respect to the prediction of the theory, which does not include interaction effects. Further details on how interactions (could) shift the critical temperature, and how this relates to finite size effects are included in [13, 164, 172].

Notice that thermometry in a lattice is difficult from time-of-flight images, requiring advanced theoretical tools ([173–175]). Instead, *in situ* measurements showed that this can be more easily obtained ([5, 176]) and even that the density distribution reveals the presence of different quantum phases in the trap ([177]).

4.4. Sub-lattice Dynamics Measurement

In the experiments we just presented, the relevant information which was extracted from the experimental picture was the occupation, or the population, of the single lattice sites, obtained by summing the signal in the corresponding Wigner-Seitz unit cells.

This neglects the information regarding the atomic distribution *within* the Wigner-Seitz cell. We want to study this aspect in detail now, by observing how the atomic distribution reacts to changes in the lattice geometry induced by an imbalance between the lattice depths. We study at first the changes in the ground states due to beam imbalance, and then we look at what happens when this beam balance is rapidly changed as a function of time.

4.4.1. Lattice Dimerization via Beam Imbalance

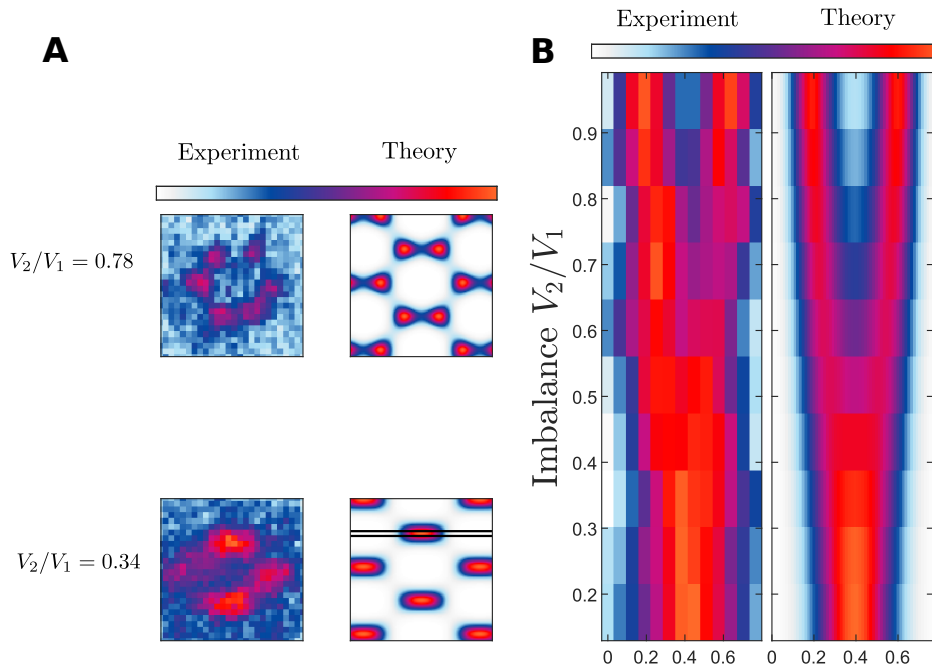


Figure 4.11.: Effects of the beam balance on the ground state density. A: Density distribution for two different values of the imbalance V_2/V_1 , with a comparison with the single-particle theory prediction (right). **B:** Density distribution comparison between experiment and theory, integrated in the vertical direction in the cut drawn in **A**. Notice that because the lattice position with respect to the magnetic trap center is not fixed, the experimental cuts have a global uncertainty on the x position of about one experimental pixel (after magnification) $\sim 65\text{nm}$.

We use a honeycomb lattice with sublattice offset $\Delta = 0$ (see chapter 6 for its realization) and study how the position of the minima of the potential come closer together as a function of the imbalance of the lattice beams.

Changing the beam balance is equivalent to applying some strain in real graphene. At a certain point, real graphene breaks apart ([178]). An optical lattice instead cannot break and one can observe the merging transition of massless Dirac Points ([179]) or even of the Bloch defects associated with massive Dirac Points ([180]). Here we could observe "in situ" how, going a little bit further, another "merging transition" takes place, when the s-orbitals merge with each other (figure 4.11).

4.4.2. Theoretical Description of the Dynamics after a Lattice Quench

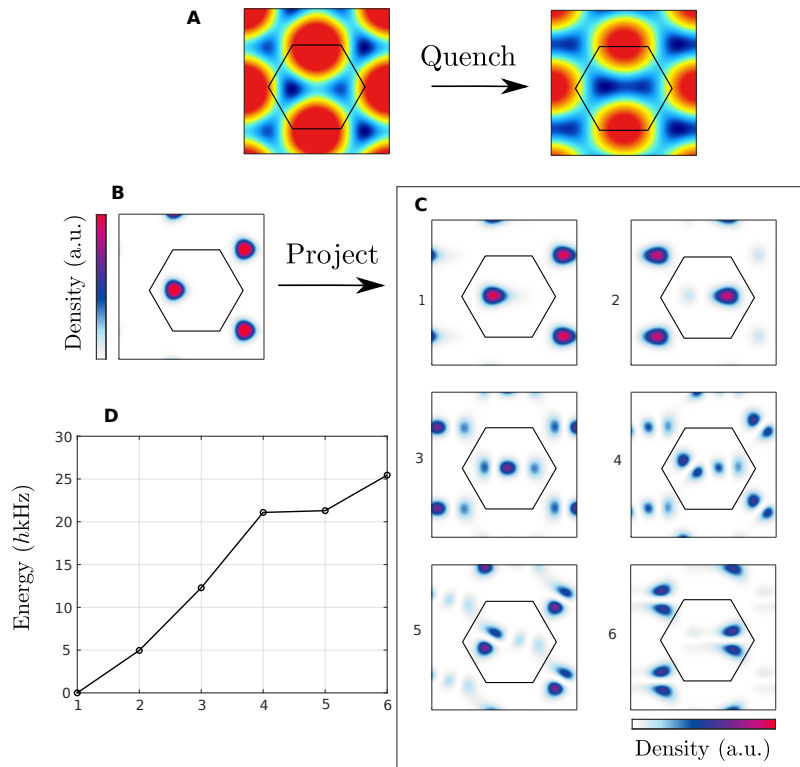


Figure 4.12.: Quench of the lattice potential to a dimers configuration. **A:** Lattice potential before and after the quench. Afterwards, the lattice minima corresponding to the two sublattices come closer to each other in the x direction, becoming also separated from the other "dimers". **B:** Density profile of the ground state wavefunction with quasimomentum $q = \Gamma$ before the quench. **C:** Density profile of the states with $q = \Gamma$ for the six lowest bands after the potential quench. The Wigner-Seitz cell which correspond to the central dimer in the quenched potential is shown. **D:** Corresponding energy of these states in the quenched potential.

We want now to investigate a situation where the form of the potential, and hence of the respective lowest lying states is dynamically changed. We start in a boron-nitride configuration, where all the atoms are sitting in the A sites. By suddenly quenching the potential depth, the original wavefunction is projected to different eigenstates of the new potential (figure 4.12). The relative phase due to their energy differences produces then a dynamics which can be detected by monitoring the density distribution. Because the lattice potential after the quench has the effect of decoupling the dimers from each other, the dependence on quasimomentum of the eigenvalues and of the eigenstates becomes negligible and we consider for simplicity only the states at the Γ point in the Brillouin zone.

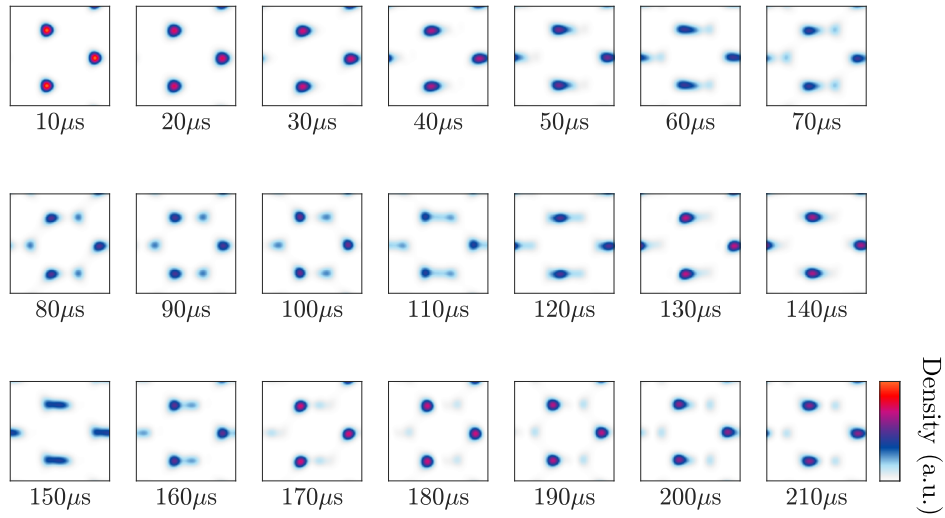


Figure 4.13.: Theory images for the different times after the quench. At $t = 0$ the density is localized at the A-sites of the lattice, forming a triangular lattice pattern. After the quench, the atoms oscillate towards the B-sites, eventually also tunneling to the other sublattice site (at $t \sim 80 - 90 \mu s$) and continue to oscillate back and forth afterwards. Notice that the dimers are aligned horizontally and between dimers the density is always (almost) zero.

Upon changing the lattice intensity the lattice sites come closer to each other along one particular direction, and the atomic distribution is now off-center with respect to the potential minimum, and start to oscillate in within the site, but also to tunnel to the other one (figure 4.13).

The lattice potential is calculated taking into account the vector light shift, which is relevant for Rubidium in determining the AB Offset (Appendix C).

At time $t = 0$, I_2 and I_3 are set to $0.5 \cdot I_1$; the intensities change on the time scale of the intensity lock system (about $20 \mu s$). For every time step ($5 \mu s$) we diagonalize the Hamiltonian in plane-wave basis of the instantaneous periodic

potential and let the state evolve according to the instantaneous eigenstates and eigenvalues. The global lattice depth is the only free parameter and it is calibrated by comparison with the experimental results.

For a quench of this magnitude, the first six orbitals are found to contain most of the atomic population (99.5%). For this particular symmetry, also the sixth state has a negligible population.

4.4.3. Experimental Results

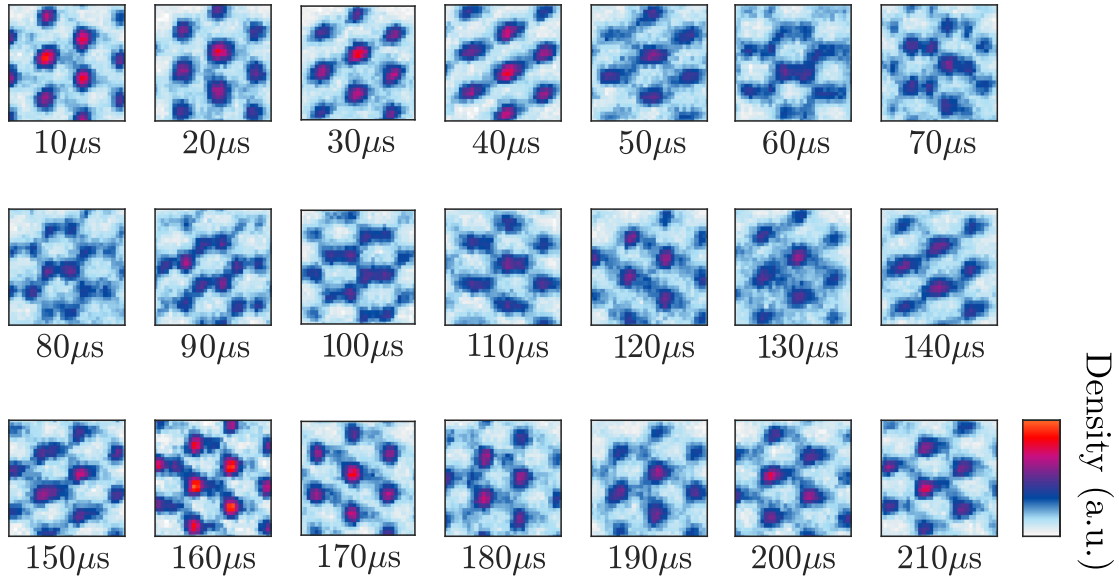


Figure 4.14.: Experimental images for the different times after the quench. Images obtained for the same parameters as calculated. The cloud is also confined in a tight trap, which is used for producing a magnification $M = 93(1)$. Images are zoomed in the center of the cloud; notice that a larger area than in the theory is taken under consideration. The signal in each pixel is divided by the total atom number of that particular shot. A very similar dynamics as calculated can be recognized.

We start with a deep lattice and a deep magnetic trap. The reason for this two is that we want now to image with big magnification without needing the freezing step.

We are able to see directly *in situ* the tunneling but also the oscillations within the lattice site (figure 4.14). There seems to be very good agreement between experiment and theory, in particular concerning the periods of the oscillations and of the tunneling time. It seems the atoms spread more into the second sublattice than predicted.

For a more direct comparison we select a cut of 65nm width (corresponding, after magnification, to one camera pixel) along the dimers and plot the density distribution along it as a function of time. We find a better qualitative agreement between the two by adding a 76nm wide Gaussian filter to the theory (figure 4.15). Note that because the position of the lattice is not kept fixed but only reconstructed x -axis might appear shifted in the comparison with the calculation. It seems that in the experiment the tunneling dynamic is much pronounced, and more population is transferred. The importance of the width of the Gaussian filter is that we can get an idea of the optical resolution, which is most probably limited by the optical resolution (1 pixel corresponds, after magnification, to about 64nm).

After the quench, most of the probability distribution of the time-evolved state is found to lie in the lowest six bands, according to the numerical simulation. Thus the dynamics can be described as resulting from the interference among the two s orbitals and four p orbitals, the latter being the smallest in-plane excitations within a lattice site. Since the dynamics is almost completely described by these states, the fact that we were able to detect it means that we were able to detect interference at the smallest possible (in plane) excitation level.

Higher orbitals are important for artificial dimensions ([181]), for topology ([182]) and for condensation in non trivial-regimes([183–187]), and quantum gas magnification looks very promising for accessing the orbital information in real space.

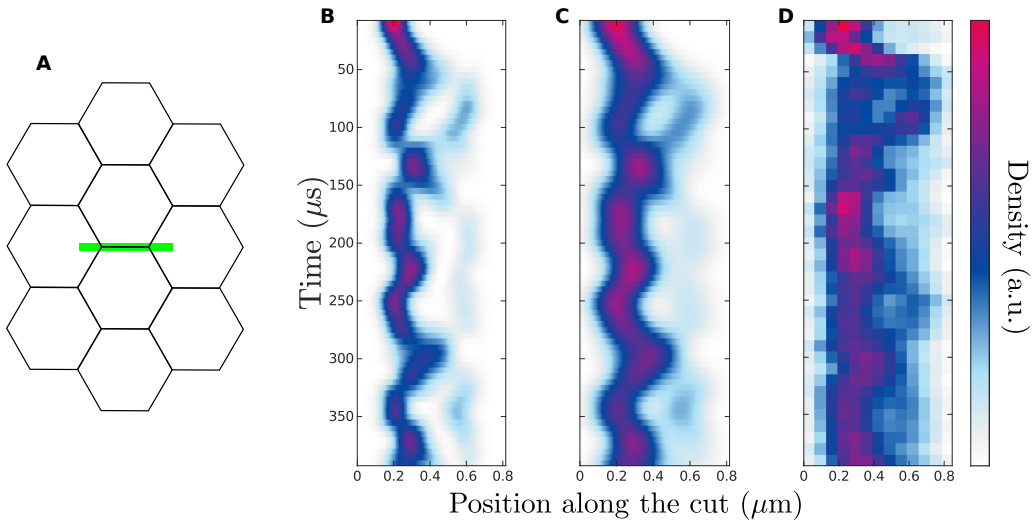


Figure 4.15.: Nanoscale dynamics in a honeycomb optical lattice. The cut along the dimers in which the dynamics is analyzed is shown in **A** (green area). In **B**, the theory prediction, in **D** the experimental results. A lattice vector corresponds to 10.9 pixel with a magnification of $M = 93(1)$. In **C** the simulation data are convoluted with a Gauss filter of 76 nm width and an offset is added. Adapted from [13].

4.5. Shaping of the Density Distribution with Radio-Frequencies

Quantum gas microscopes have the possibility to shape the density distribution at the single-site and single-atom level ([143, 188]), using high-resolution objectives to focus light beams with a waist on the order of the lattice spacing. Also a focused electronic beam can be used to the same end ([154]). Here we demonstrate that also by more standard RF-techniques ([189, 190]) we can imprint density pattern at the single site level, and what is crucial is the possibility to look at the atomic distribution and control the result.

We can empty selectively certain lattice sites employing resonances from the $m_F = 2$ state to the $m_F = 1$ state. The latter is a state subject to losses because two atoms colliding can relax into the $F = 1$ manifold, and can not be trapped anymore in the lattice because of the high gained kinetic energy ($\sim 6.8\text{GHz}$).

In this way, we could realize several density patterns in a deep triangular lattice, by selectively removing atoms as a function of the radial coordinate in the magnetic trap (figure 4.16). The lattice depth is chosen high enough such that the atoms don't undergo any dynamics during the procedure. This allows also to move the cloud around the magnetic trap without changing the density distribution in order to increase the range of possibilities, otherwise limited by the circular symmetry of the trap.

In particular we demonstrate single-site resolution by leaving just one row populated, or by emptying just the central lattice site.

As an example we studied how by removing atoms from half of the system (as in the image on the upper right corner of figure 4.16) we create a highly excited state and study its following thermalization dynamics ([13, 191]). This is of interest in the context of many interesting physical phenomena, like probing localization due to disorder or many-body interactions ([145]).

The duration of the RF-sweeps/pulses was about 100 – 200ms, faster than the tunneling time in a deep triangular lattice. In principle by optimizing the protocol and increasing the lattice depth further, one could think of obtaining any desired density distribution by "sculpting", i.e. starting from a distribution with more atoms than desired in every site and, iteratively, by putting every site at the center of the trap and removing the excess atom number (similarly to [154]). On the other hand, it is also of interest to study the regime where the removal is not much faster than the dynamical scales, a scenario which resembles the quantum Zeno effect ([192]).

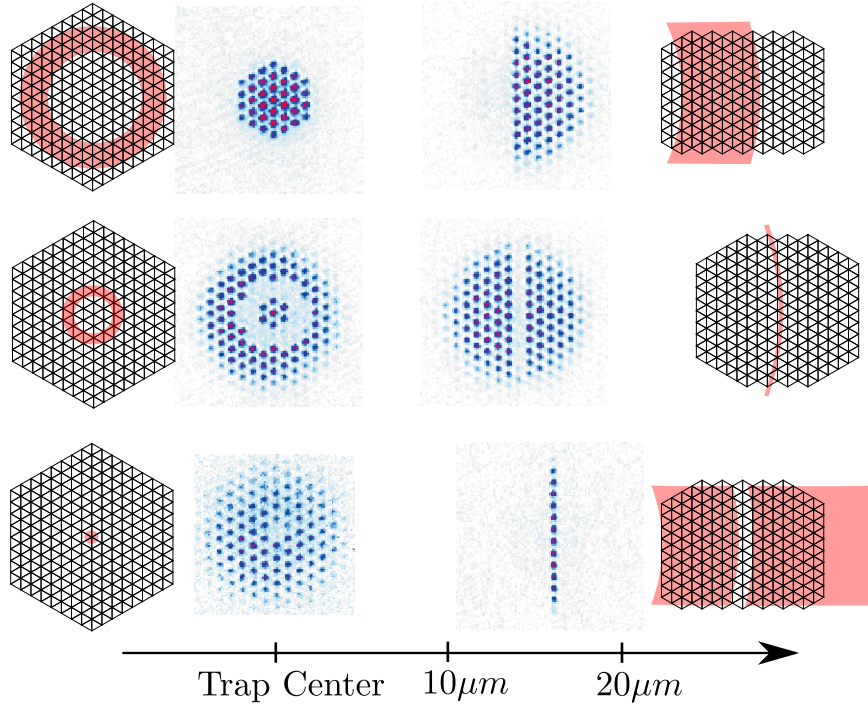


Figure 4.16.: Shaping the Density Profile. The images on the left are obtained via a RF-sweep or pulse transferring atoms to the $|F = 2, m_F = 1\rangle$ state. Atoms in this state can collide and leave the trap, resulting in an almost total reduction of the density in the area brought in resonance with the transition (indicated by the light red areas in the schemes). The images on the right are obtained by freezing the density distribution, shifting it along x such that RF-sweeps can remove atoms as a function of their x -coordinate, and then by shifting the cloud back to the center of the magnetic trap for imaging without anharmonicity effects. The position on the x axis of the experimental images indicates the shift used before applying the radio-frequency pulse/sweep. Images on the left are produced without the shift, and resulting density distribution has rotational symmetry. Adapted from [13].

These measurements also offer a double-check of the stability of the lattice setup, because the density patterns depend only on the relative position of the lattice with respect to the magnetic trap during the radio-frequency pulse, thus offering a way of characterizing lattice position drifts due to phase fluctuations independently of possible fluctuations in the imaging process (including both the quantum gas magnification and optical imaging parts). These results confirm the intrinsic stability of the lattice setup (an idea of the reproducibility of the outcomes is given in figure 4.17).

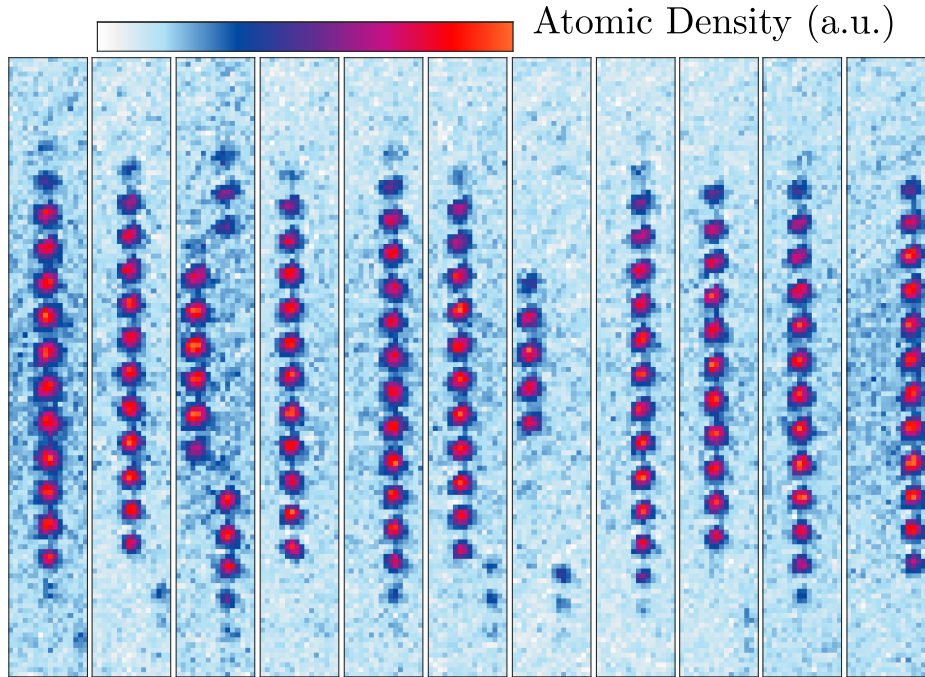


Figure 4.17.: Density profile away from the trap center after two RF sweeps. 11 consecutive images obtained with the same protocol: shift left (along x) the cloud and perform two RF sweeps removing atoms left and right of the selected row. We can observe that the selected density pattern (the single row) is quite stable, even though its apparent position can fluctuate up to the projection along x of the lattice vector (compare e.g. the first and the last picture). Sometimes the outcome is not as good as expected (3rd and 7th picture from the left), and this might be because of the outcome of the lattice position in these particular runs, if it takes up a value for which not all the lattice sites in the same row are brought to resonance, or not all of them avoid being brought to resonance.

4.6. Spontaneous Density Wave Formation

The possibility to image the whole density distribution in a single shot not only speeds up the data taking process, but it is also crucial for accessing the particles correlations, and for studying phenomena where the outcome might be different from shot to shot. Specifically with the latter we refer to systems where a symmetry is spontaneously broken, having as a consequence that the system will arrange in one of two (or more) possible phases in each realization.

We discovered experimentally that a BEC in an optical lattice subject to a constant force (a "tilt") spontaneously breaks the translational invariance of the lattice, by developing a density wave (i.e. a modulation of the density distribution) with typically alternating local maxima and minima of the density (integrated perpendicular to the tilt, as shown in figure 4.18). These findings are reported in a separate publication ([14], in collaboration with the theory group of Ludwig Mathey).

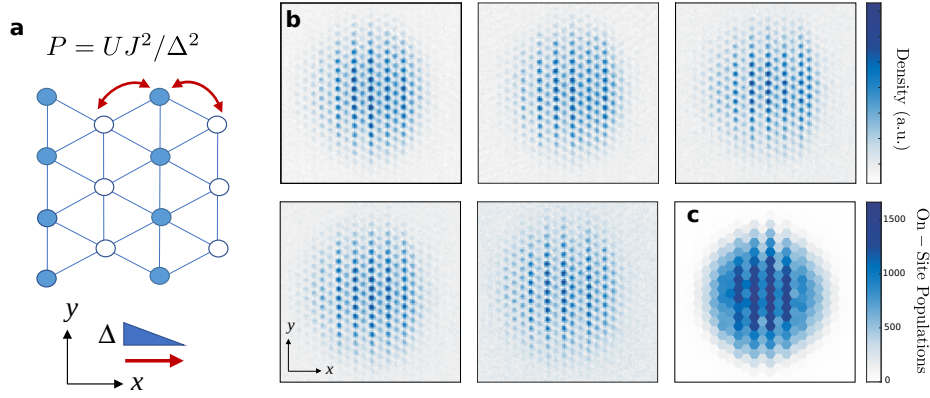


Figure 4.18.: Density Wave in a tilted Lattice. We looked at the situation sketched in **a**, where a constant force along x suppresses single-particle tunneling, leaving correlated pair tunneling as the dominant dynamical process. **b**: Experimental density distributions obtained after loading a BEC in the lattice and subjecting the cloud to a tilt $\Delta = h \cdot (1.4, 1.4, 1.4, 1.4, 1.5)$ kHz, and waiting for a variable time $t_{\text{DW}} = (60, 80, 80, 120400)$ ms. The lattice depth was also varied, resulting in a tunneling coupling $J = h \cdot (7.2, 7.2, 13, 7.2, 4.2)$. Atomic clouds are shifted back to the center of the trap for matter wave imaging. **c**: A c-field simulation (in this example with $t_{\text{DW}} = 60$ ms, $\Delta = h \cdot 1.4$ kHz, $J = h \cdot 13$ Hz), reproduces the spontaneous symmetry breaking due to thermal fluctuations in the initial wavefunction. Adapted from [14].

The dynamics that results from such a system can not be described in a single-particle picture; we give here a schematic description of the dynamics in the tilted lattice, and why it becomes correlated.

Consider the process $|n_1, n_2\rangle \rightarrow |n_1 + 1, n_2 - 1\rangle$, describing the hopping of a particle from one site with initially n_1 particles to one with initially n_2 particles. In presence of a tilt it becomes off-resonant, and the amplitude of the oscillations gets reduced.

The second order process $|1\rangle = |n_1, n_2, n_3\rangle \rightarrow |4\rangle = |n_1 + 1, n_2 - 2, n_3 + 1\rangle$ which involves now three lattice sites, instead, is resonant, because there is no center of mass movement with respect to the tilt. It can happen via two intermediate states, $|2\rangle = |n_1 + 1, n_2 - 1, n_3\rangle$ and $|3\rangle = |n_1, n_2 - 1, n_3 + 1\rangle$. The coupling between $|1\rangle$ and $|4\rangle$ obtained by summing the contributions from both paths is zero, because $|2\rangle$ and $|3\rangle$ have opposite energy differences with respect to the energy of $|1\rangle$ and $|4\rangle$.

Interactions can shift the energy levels such that this is no more the case, giving rise to a correlated dynamics described by simultaneous hopping of two particles. The resulting system can be better described by a formalism which we only describe in the following. We refer to [14, 172] for a more detailed discussion.

The tilted system can be mapped to a periodically driven system, with the substitution $b_j \rightarrow \hat{b}_j e^{ix_j \Delta t / \hbar}$, with b_j creation operators on lattice site j . x_j is the index of the row of site j .

In complete analogy to the high-frequency derivation of Floquet Hamiltonians of driven systems ([193]), one can derive an effective Hamiltonian using a second order Magnus expansion ([14, 194]); this Hamiltonian contains, as main dynamical term, a pair tunneling term of the form:

$$H_P = -P \sum_{\langle kjl \rangle} \hat{b}_j^\dagger \hat{b}_j^\dagger \hat{b}_k \hat{b}_l + \text{h.c.} \quad (4.34)$$

This describes the simultaneous hopping of two particles from sites k and l to site j (and the hermitian conjugate process) with amplitude $P = UJ^2/\Delta^2$. U is the Hubbard parameter quantifying the on-site interactions strength and can be estimated for typical atom numbers and $V = 1E_r$ to be given by $U = \hbar \cdot 2.3\text{Hz}$. Sites k and l must have opposite potential energy differences with respect to site j (notice that in the triangular lattice, there are four possible processes of this kind for a given j).

There are some interesting points to notice from this expression: first, quite counterintuitively, the dynamics is driven by on-site interactions as can be seen by noticing that $H_p \propto U$ ([195, 196]).

Also, because of the second order nature of the process, it happens at a time scale proportional to the atom number. While the timescale associated to UJ^2/Δ^2 is very long, about $\sim 10^2\text{s}$, when considering a factor 10^3 as a typical atom number in a tube we get a timescale on the order of $\sim 10^2\text{ms}$, which is under experimental reach. Notice that the use of quantum gas magnification is crucial for being able to observe at all this phenomenon, because it allows measuring high *in situ* densities at the single site level.

While we still lack a complete quantitative understanding of the dynamics, we could point to initial thermal fluctuations in the condensate as fundamental ingredient for the density wave formation. These fluctuations might act as a seed ([116, 197]) and decide the direction of the current between different lattice rows, as in a Josephson junction, dictating which row will have a high or low population.

Lastly, this experiment represents also a step towards quantum simulation of extended Hubbard models ([198–200]) with a DC driven field ([201]), in a complementary fashion to periodically driven systems.

4.7. Conclusions

We developed a new technique for imaging quantum particles with high resolution. This is based on a magnification of the matterwave prior to standard imaging, and we demonstrated it with ultracold Rubidium atoms in a variety of optical lattice geometries (triangular, honeycomb lattice: boron-nitride- and graphene-like). In particular, it was the first time that ultracold atoms in the honeycomb lattice were imaged. The interesting feature is that the technique is not limited to 2D systems or systems with a low atom number, making it suitable for studies complementary to the possibilities of conventional quantum gas microscopes. The technique seems also to be quite versatile and relatively easy to implement, and its applications have (potential) overlap with several other high-resolution imaging techniques, as schematized in table 4.1.

Table 4.1.: Properties of real-space Imaging Techniques. This table provides an overview of the features and limitations of different imaging techniques for ultracold atoms. Note that the Boolean 'Yes' or 'No' carry some degree of arbitrariness, and depend much on the definition e.g. we wrote 'No' also for techniques other than the quantum gas magnifier where the possibility in question might be conceivable, but we are not aware of a proposal. The purpose of this table is just to demonstrate the versatility of the quantum gas magnifier approach since it provides/could provide many of the features of the other mentioned techniques.

Technique	Quantum Gas Magnifier ([13])	Quantum Gas Microscopes ([4, 5],...)	Ion/Electron Microscopes ([154, 155])	Superres. microscopes ([156, 157])
3D systems	Yes	No	Yes	Yes
High n	Yes	No	Yes	Yes
3D imaging	not complete, but conceivable	Sparse systems[152, 153]	Yes ([155])	No
Single-shot sub-lattice resolution	Yes	Yes	No	No
single atom	Yes	No	Yes	Yes
spin resolved	Conceivable	Yes	No	No
	Conceivable	Yes	No	No

In this chapter, we introduced the formalism used to describe quantum gas magnification of the density distribution in an optical lattice. We will use this formalism also in chapter 5, where quantum gas magnification of coherent phenomena is studied.

We described the results of quantum gas magnification with an application to thermometry of a lattice cloud in an additional harmonic confinement.

We demonstrated also the possibility to manipulate the gas at the single-lattice site level by selectively emptying selected sites. We discovered a new phenomenon thanks to the possibility of taking single-shot images of 3D systems, which was not possible in other schemes like ([154, 155]). We were able to observe dynamics at the nanoscale level after the excitation of higher bands in the honeycomb lattice, which opens the door for orbital physics in real space.

The protocol is quite generalizable to other setups and dimensions. Using an optical trap, it could be applied to spin-mixtures, with spin-resolved resolution provided by Stern-Gerlach separation during time-of-flight.

We mention the possibility to image in a position-momentum ($x - p_y$) hybrid space ([202]), with asymmetric trap potentials such that magnification in one spatial direction and mapping of momentum to real space in the other are achieved; or the possibility to image the spatial and the momentum distribution in a single shot by coupling half of the atoms to $m_F = 0$ before the initializing the magnification protocol. The two components, which could be detected independently after Stern-Gerlach separation, would then image respectively the real space and the momentum distribution (also useful in the context of spontaneous symmetry breaking).

Among the many possible future directions, we mention that quantum gas magnification could be applied to atomic species or even molecules which can be imaged in a quantum gas microscope only indirectly after dissociation ([203]).

In the future, one could extend it to single-atom imaging ([204–207]) to reach the strongly correlated regime. It would be also useful for more complex geometries with a typically lower lattice spacing like e.g. the Kagome Lattice ([208]) or sub-wavelength lattices ([209–212]).

5. Microscopy of coherent phenomena

Quantum Simulation and research depends on the possibility to extract information from the system. So far, we have dealt with the measurement of the density of an atomic distribution, even at the sub-lattice level. But still, this is just a fraction of the information contained in a quantum system: a generic single-particle state can be described by the density matrix, whose entries are defined like

$$\rho_{ab} = \langle\langle \psi_a^\dagger \psi_b \rangle\rangle \quad (5.1)$$

where the expectation value has to be taken over the state in the case of a pure state or over the statistical mixture of states when dealing with a mixed state. Diagonal element of the density matrix correspond to occupations N_a of state a : $\rho_a = \langle\langle \psi_a^\dagger \psi_a \rangle\rangle = N_a$ and off-diagonal elements, which make up most of the elements of the density matrix, are related to the coherence between different states.

Coherence of matter waves is a typical quantum phenomenon and it is of much relevance because it e.g. is related to transport properties, with conducting states characterized by a high degree of coherence over the sample. Coherence is very well accessible already in cold atoms experiments in time-of-flight or band mapping protocols, but only as a global measurements of the coherence in the system ([213]).

In the previous chapter, we introduced the Quantum Gas Magnifier as technique for measuring the density distribution in an optical lattice, with single site resolution: here we extend its application to coherent phenomena, studied at the microscopic level.

The first case under consideration is the Talbot effect, where revivals of the lattice structure are generated after diffraction from a lattice. We are going to present a simple theoretical model for detection with high spatial resolution of Talbot revivals after release from the optical lattice with the quantum gas magnifier, expanding on the idea presented in [164].

We also present some preliminary data, taken in the simple case of a 1D lattice, and some data taken across the Mott-superfluid phase transition in the triangular lattice, where the change in coherence range as a function of the lattice depth is reflected in the number of detectable Talbot revivals.

In the second part of this chapter we present a theoretical proposal on the measurement of the off-diagonal elements of the density matrix in an optical lattice with single site-resolution using the quantum gas magnifier.

5.1. Talbot Effect

The Talbot effect in optics describes the revival of a lattice structure with spatial periodicity $L_{\text{Talbot}} = 2(Ma_{\text{lat}})^2/\lambda_L$ after transmission of light with wavelength L through a periodic potential with lattice constant a_{lat} .

The Talbot effect presents itself also with matter waves ([214–216]) and can be understood as follows: a periodic 1D wavefunction with periodicity a_{lat} can be decomposed in the plane wave basis using wavevectors which are multiples of $k = 2\pi/a_{\text{lat}}$. After adiabatic loading into the ground state of the lattice and a subsequent time of flight expansion, the dynamics is given by the corresponding kinetic energies which are then $E_n = n^2(\hbar k)^2/(2m)$; in particular we notice that they are integer multiples of the same fundamental frequency. The inverse of this frequency is then called the Talbot period T_{Talbot} and in a perfectly periodic infinite system one would expect at multiples of T_{Talbot} the wavefunction to be exactly the same as for $t = 0$ (phenomenon described as "Talbot revival").

In a real system with finite correlation length, it was demonstrated that the strength of the n^{th} revival, defined as the overlap between the state at time nT_{Talbot} and the initial state, is directly proportional to the g_1 correlation function between lattice sites of distance $2n$, while the correlation function between sites of distance $2n - 1$ is directly proportional to the strength of the n^{th} anti-revival (a revival of the lattice structure occurring at $t = \frac{2n-1}{2}T_{\text{Talbot}}$ with a $\lambda/2$ displacement with respect to the original wavefunction) ([217]). In these works ([217, 218]), the strength of the revivals was measured globally over the whole sample by turning on again the lattice and measuring the number of atoms which remained in the first band of the lattice.

By directly imaging the Talbot revivals with the quantum gas magnifier instead, as we now propose, one could obtain a spatially resolved measurement of the coherence properties.

5.1.1. Talbot Effect in Presence of a harmonic Trap

The simplest, and most direct protocol for imaging Talbot revivals with the quantum gas magnifier would look something like this: switch off instantaneously the lattice (and the trap if present), let the atom expand for a given time t , and then turn instantaneously on the trap for initiating the matterwave magnification. This is quite challenging since $T_{\text{Talbot}} \simeq 160\mu\text{s}$ (calculated for the wavevector modulus $|\mathbf{b}_i|$ in our system) is much smaller than the switch-on time of the magnetic trap. We show here that also if the release of the atoms from the lattice happens in a harmonic trap instead of free-space, one still can expect Talbot revivals, regardless of the relationship between the trap frequency and the other relevant energy scales. We demonstrate how the mapping between the two situations can be done, and how the presence of the trap just shifts the times at which Talbot revivals are to be expected and the lattice constant which characterizes them, but without introducing any distortion, as long as the trap is harmonic.

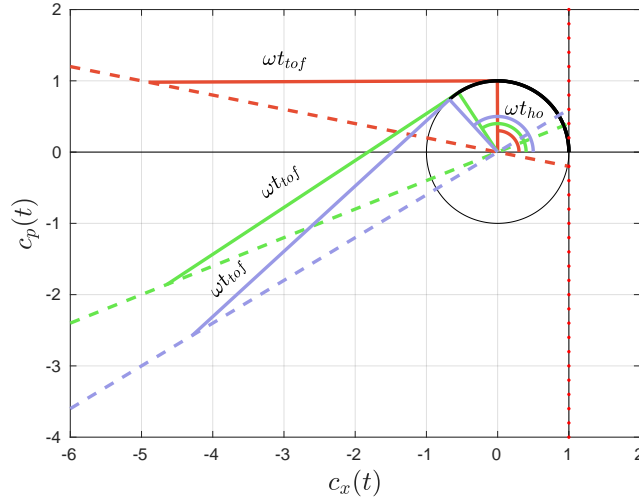


Figure 5.1.: Sketch of the Mapping between evolution in free-space to evolution in a harmonic trap. The vertical line at $c_x = 1$ indicates the realizations of the time-dependent operator $\tilde{X}(t) = c_x(t)\tilde{X}(0) + c_p\tilde{P}(0)$ during time-of-flight. Red points indicates the (integer) Talbot revivals and are separated by ωT_{Talbot} . For a given t_{tof} , one can image different Talbot revivals by tuning t_{ho} (red, green and blue circular arc). The end points of the evolution after time-of-flight (straight lines) correspond to Talbot revivals as indicated by the dashed lines. The magnification factor is given by $-\sqrt{((\omega t_{\text{tof}})^2 + 1)} / ((\omega n T_{\text{Talbot}})^2 + 1)$. $n = -1, 2, 3$ in the examples (red, green and blue trajectories). Notice that for $t_{\text{ho}} < \arctan(\omega t_{\text{tof}})$ also negative order ($n < 0$) Talbot revivals can be imaged.

The free-space evolution of the atomic density in the traditional Talbot effect can be mapped to the evolution in a harmonic oscillator by considering the dynamics of the \tilde{X} operator (\tilde{X} , \tilde{P} are the position and momentum operator in the natural harmonic oscillator units, as introduced in chapter 4). In free space we have after a time of flight nT_{Talbot} corresponding to the n^{th} Talbot revival:

$$\tilde{X}(nT_{\text{Talbot}}) = \tilde{X}(0) + \omega nT_{\text{Talbot}} \tilde{P}(0) \quad (5.2)$$

Recalling that the evolution for a time t_{ho} in the harmonic trap is given by:

$$\tilde{X}(t_{\text{ho}}) = \cos(\omega t_{\text{ho}}) \tilde{X}(0) + \sin(\omega t_{\text{ho}}) \tilde{P}(0) \quad (5.3)$$

One can see that for $t_{\text{ho}} = \frac{1}{\omega} \arctan(\omega nT_{\text{Talbot}})$

$$\tilde{X}(t_{\text{ho}}) = \frac{1}{M'} \tilde{X}(nT_{\text{Talbot}}) \quad (5.4)$$

with $M' = \sqrt{1 + (\omega nT_{\text{Talbot}})^2} = 1/\cos(\omega t_{\text{ho}})$. A graphical representation of this mapping is illustrated in figure 5.1.

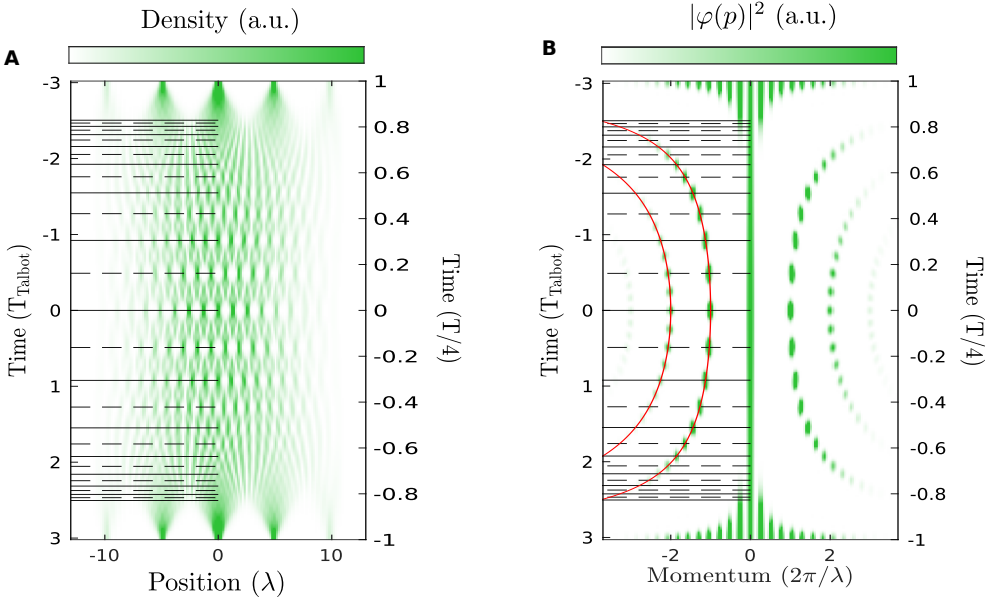


Figure 5.2.: Numerical Simulation of the Talbot effect in a 1D lattice in presence of a harmonic trap. The revivals of the lattice structure in the atomic density(left plot) appear at times predicted by the equation. 5.5 (black lines). Note that in the 1D case between revivals a so-called anti-revival is to be seen (dashed lines). In the Fourier transformation of the density (right plot) a change in the wavevector of the lattice is to be seen, as described by the M' factor (red lines). Notice that because the wavefunction is real at $t = 0$, time-reversal symmetry is kept around $t = 0$. Negative times acquire physical significance in the harmonic oscillator, unlike in time-of-flight since they can be mapped to positive times by an integer multiple of the trap period T_{trap} .

This shows that the dynamics in the trap can be mapped to the dynamics in free-space upon rescaling positions with a factor $1/M'$ and rescaling of the evolution times via the relation

$$t_{\text{ho}} = \frac{1}{\omega} \arctan(\omega n T_{\text{Talbot}}). \quad (5.5)$$

The distribution in the trap at time t_{ho} corresponding to the n^{th} Talbot revival can be then magnified by a factor M just by letting the system remain in the trap for an additional $\sim T/4$ and subsequent t_{tof} expansion (with $M = \sqrt{(\omega t_{\text{tof}})^2 + 1}$, as previously defined). One gets in the end:

$$\tilde{X} = -\frac{M}{M'} \tilde{X}(nT_{\text{Talbot}}) \sim -M \tilde{X}(nT_{\text{Talbot}}) \quad (5.6)$$

(where the approximation for the magnification factor can be done when considering Talbot revivals of not too high order n such that $n\omega T_{\text{Talbot}} \ll 1$. This results were verified numerically for a 1D lattice (figure 5.2).

As derived in reference [217] for the 1D case, the strength of the Talbot revivals is a measure of the phase correlation function. We argue that the decay of the contrast with the order of the revival is related to the phase correlation function also in the case of a 2D lattice. We note that the quantum gas magnifier would allow access the contrast and therefore the phase correlation function in a spatially resolved manner. This is particularly relevant for inhomogeneous systems, as typically is the case for harmonically trapped quantum gases. Furthermore, imaging of continuous systems away from the focusing condition of the quantum gas magnifier can be used to gain information on phase profiles of the wavefunction, where phase fluctuations of low-dimensional systems are transformed into density fluctuations ([219, 220]).

5.1.2. Talbot effect in a Honeycomb/triangular Lattice

We note that in 2D Talbot revivals also appear in the case of triangular and honeycomb lattice because here the allowed wavevectors are $\mathbf{b}_{n,m} = n\mathbf{b}_1 + m\mathbf{b}_2$ with $\mathbf{b}_1 = 2\pi\sqrt{3}(0, 1)/\lambda$, $\mathbf{b}_2 = 2\pi\sqrt{3}(\frac{\sqrt{3}}{2}, -\frac{1}{2})/\lambda$ and n, m integers, with associated kinetic energies $E_{n,m} \propto |\mathbf{b}_{n,m}|^2 \propto n^2 + m^2 + m \cdot n$. All energies are then integer multiples of the fundamental energy E_{rec} .

Notice that while distorted triangular/honeycomb lattices can be realized also without a 120° incidence angle between the laser beams, here a commensurate angle between them is a necessary condition for the appearance of Talbot revivals.

Figures 5.4 and 5.3 show numerical calculations for the density distribution of Talbot revivals in a small 2D system in a triangular and honeycomb lattice respectively.

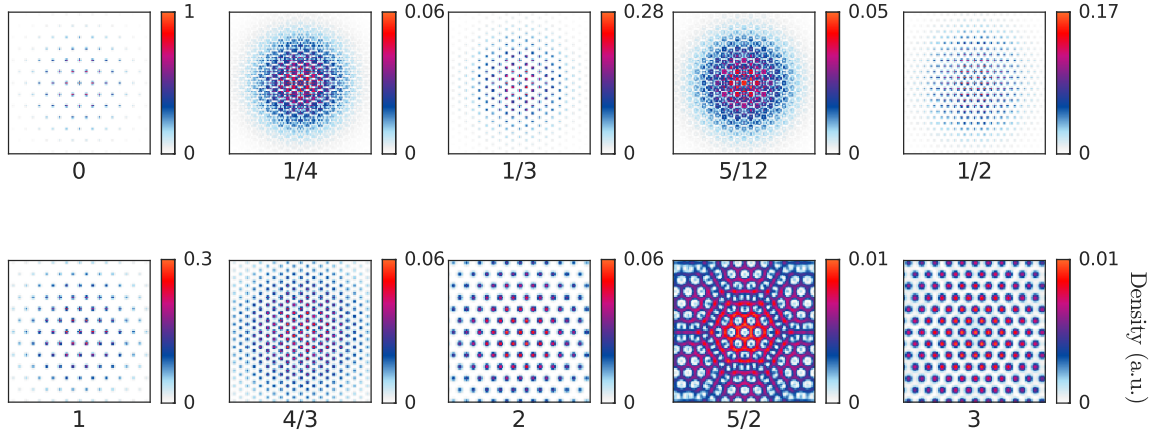


Figure 5.3.: Numerical Simulations for Talbot Revivals after time of flight from a triangular lattice. The original density distribution (upper left figure) has a gaussian width of $2.8\mu\text{m}$. The numbers indicate the evolution time in units of the Talbot Time T_{talbot} . For integer multiples the original lattice structure can be recognized, and also for some of the fractional multiples a smaller periodicity can be seen. Notice the different peak densities for the different times.

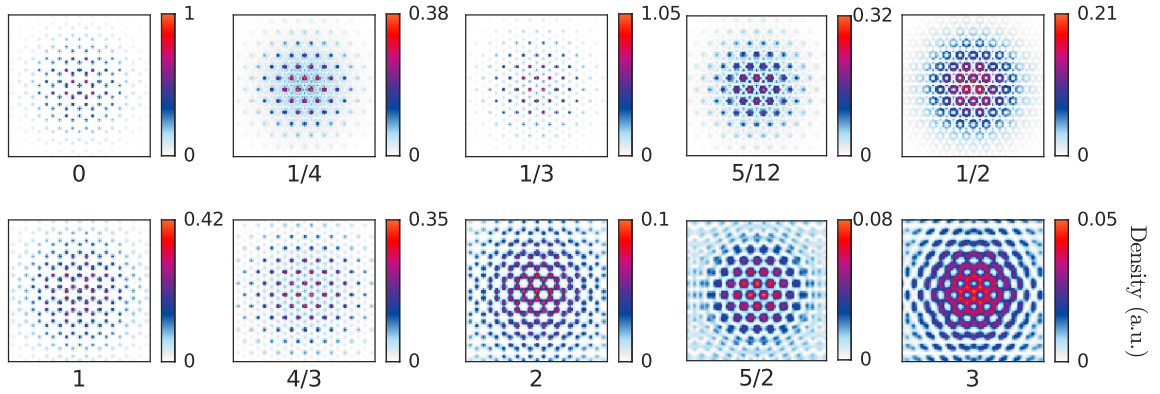


Figure 5.4.: Numerical Simulations for Talbot Revivals after time of flight from a honeycomb lattice. The original density distribution (upper left figure) has a gaussian width of $2.8\mu\text{m}$. The numbers indicate the evolution time in units of the Talbot Time T_{talbot} . For integer multiples the original lattice structure can be recognized, and also for some of the fractional multiples a smaller periodicity can be seen. Notice the different peak densities for the different times.

5.1.3. 1D Measurement

Similarly as when focusing the matterwave field for quantum gas magnification, we are now going to vary the time in the magnetic trap before a time-of-flight of fixed duration, but in a broader range and without removing the coherence in the system first. We start with a single 1D lattice where a simpler analysis is possible. Some examples of the density distributions are reported in figure 5.5. The modulation of the density distributions due to the lattice can be clearly seen, but it is much weaker than what the interactions-free theory predicts. As mentioned in the previous chapter, we attribute this to the presence of interatomic interactions during the magnification protocol, because of the realization of the peaked momentum distribution at $t = T/4$ and because of the Talbot revivals themselves.

Nevertheless, we are able to see a signature of Talbot revivals as the modulation of the lattice oscillates as a function of time in the magnetic trap (figure 5.5).

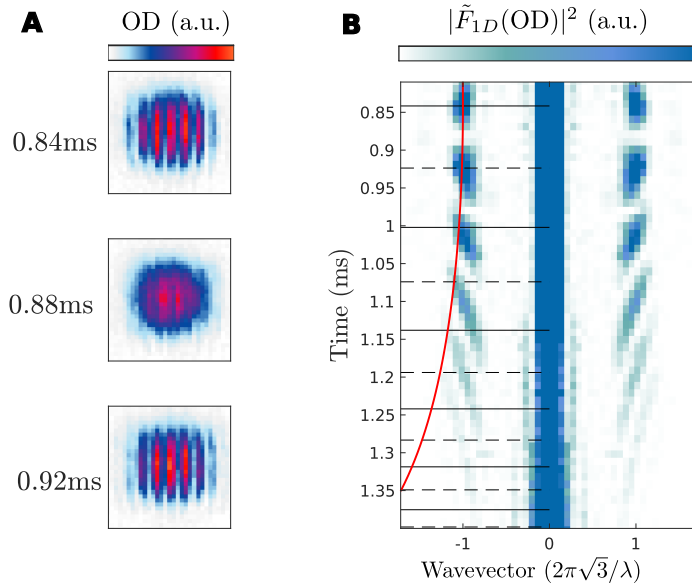


Figure 5.5.: Talbot effect in a 1D lattice. In **A**, three examples of the density distribution after loading in a 1D optical lattice. It can be seen that the contrast has a non monotonic behaviour as a function of the hold time in the magnetic trap before a time-of-flight of 19ms. In **B** the absolute value (squared) of the Fourier transformation \tilde{F}_{1D} of a vertical cut in the density distributions is plotted as a function of time and wavevector. In correspondence of the reciprocal lattice wavevector $2\pi\sqrt{3}/\lambda$ the signal exhibits a peak which oscillates as a function of time. The position of the 0th revival is found to be at $t = 840\mu s$, and ω is determined as $2\pi/(4 \cdot 840\mu s)$. For comparison the straight black lines and dashed black lines indicates the predicted position of the revivals and anti-revivals, respectively, according to the prediction of equation 5.4, calculated for a non-interacting system. The red line indicates the expected position of the revivals wavevectors. There is qualitative agreement with the predictions: the measured revivals possess a similar spacing and appear at always greater wavevectors.

5.1.4. Mott Insulator-Superfluid Transition

In a 3D lattice we can explore the transition from a superfluid to a Mott insulator ([6]), where we expect the correlation length to zero as a function of the lattice depth. As we expect the number of revivals to be related to the correlation length in the system, we expect to see a decreasing number of revivals as a function of the 3D lattice depth. We add a 1D lattice in z -direction perpendicular to the 2D lattice plane. The data we are going to present were obtained with the following protocol: we load into the 3D lattice system, we switch off of the 2D lattice and wait for a variable time t_{hold} in the potential formed by the magnetic trap and the z -lattice. We then switch off of the z -lattice and hold the system for a fixed time (about $T/4 - 40\mu\text{s}$) in the magnetic trap. The idea is then to let the revivals happen in the different planes created by the z -lattice (as a function of t_{hold}), and then image them by quantum gas magnification, summing the signal over all these planes.

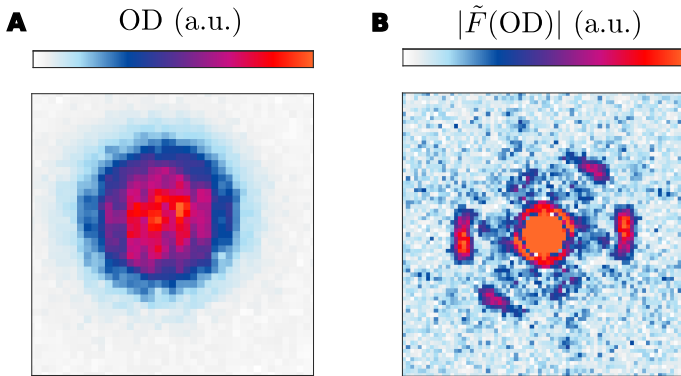


Figure 5.6.: Density distribution for a triangular lattice in the superfluid regime. In **A** an exemplary density distribution (as measured via quantum gas magnification) of a system with coherence is shown. In **B** the corresponding 2D Fourier transformation. Notice that while the density distribution shows barely some modulation, its Fourier transform show a clear signal in correspondence of the reciprocal lattice wavevectors. The three-fold symmetry is broken probably due to the magnified lattice constant being too close to the limit of two pixels and to the optical resolution.

In the superfluid regime the density modulation from the lattice is very weak but measurable (figure 5.6).

We repeat the measurement of the density distribution for different hold times and lattice depths of the 3D lattice. We analyze than the Fourier transformation of the density averaging over momenta with the same magnitude, as a function of the hold time and of the absolute value of the momentum. We repeat the analysis for different lattice depths and plot the results in figure 5.7. The data show a clear decrease in the number of detectable revivals for increasing lattice depth. At the same time, as coherence is less and less present in the system for increasing lattice depth, the contrast of the quantum gas magnifier increases.

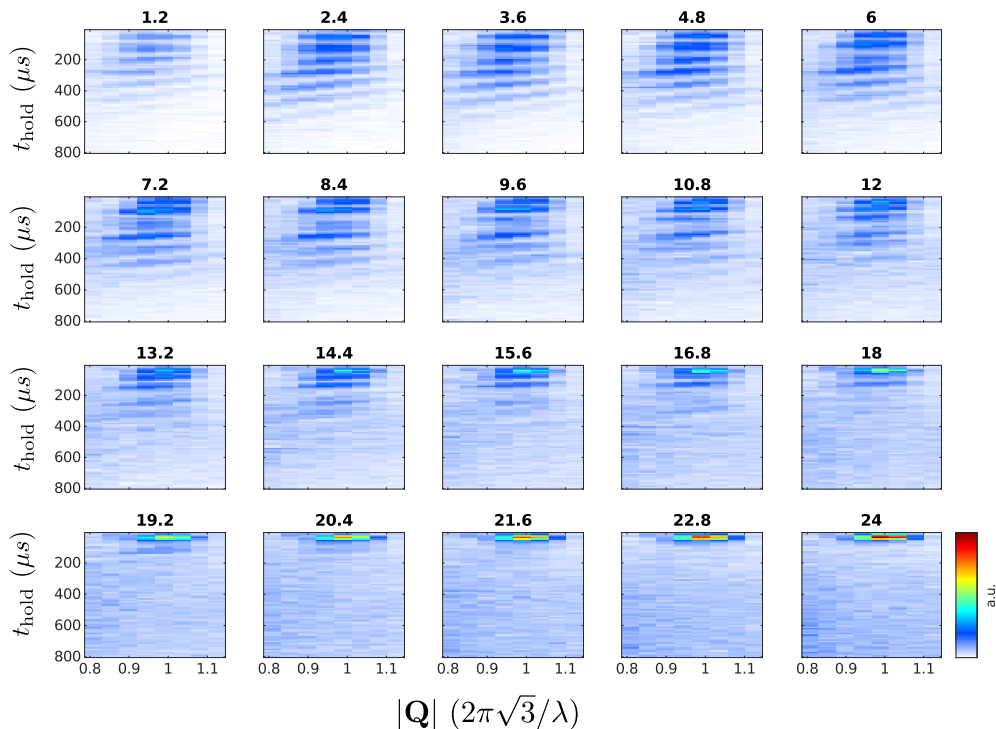


Figure 5.7.: Talbot revivals in a (3D) triangular lattice for different lattice depths. The Fourier transformed signal of experimental density distributions obtained for different lattice depths (indicated on every image, in arbitrary units) as a function of the modulus of the wavevector $|\mathbf{Q}|$ and of the hold time in the z -lattice t_{hold} . Notice that imaging of the real space distribution is expected for $t_{\text{hold}} \sim 40\mu\text{s}$ and Talbot revivals are expected to appear at later times, as it is seen experimentally in correspondence of the reciprocal lattice wavenumber $2\pi\sqrt{3}/\lambda$. The number of observable revivals decreases with the lattice depth. In a very deep lattice, only one peak can be seen, corresponding to the Fourier transformation of the *in situ* density distribution of the atoms.

These data can be presented in a more compact form, by integrating the Fourier transformation signal in an interval of wavevectors around $2\pi\sqrt{3}/\lambda$. This reveals, surprisingly, that the position of the Talbot revivals is not constant but it shifts towards smaller times as a function of the lattice depth, and also the spacing between different revivals seems to change (figure 5.8).

We attribute this effect to interactions during the magnification protocol quite much in analogy to the mean-field shift of the effective trap frequency reported in figure 4.6. The density is higher for smaller lattice depths because of the higher degree of coherence there present; hence there is a lower effective trap frequency and revivals appear at later times going to lower depths.

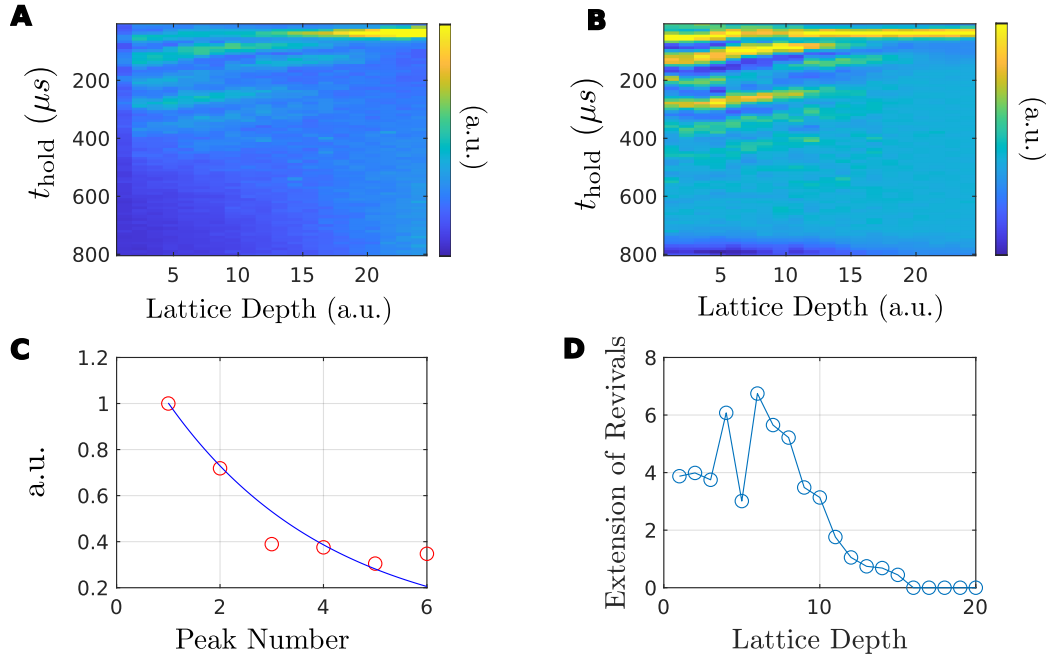


Figure 5.8.: Shift of the Talbot revivals as a function of the lattice depth. In **A**, the Fourier transformation of the density distribution (figure 5.7), integrated over all wavevectors \mathbf{Q} with $0.8 < \frac{|\mathbf{Q}|}{2\pi\sqrt{3}/\lambda} < 1.1$ and plotted as a function of the hold time in the z -lattice t_{hold} and the lattice depth. A "shift" of the revival position towards smaller times can be seen. In **B**, the same quantity convoluted with a band pass suppressing slow and fast frequencies. From this, we can apply a peak finding routine and fit the heights of the peaks (normalized to the highest one) with an negative exponential function. In **C**, it is shown how the fit always converges (in this example, for $V = 10\text{a.u.}$) but does not seem to capture the complete behaviour of the system. If only one peak is found, the decay constant is put equal to zero. In **D**, the decay constant is plotted as a function of the lattice depth. It can be seen how it builds up for shallower lattice and how it decays to zero for deeper ones.

This effect makes a complete analysis particularly challenging, adding to the presence of a variety of revivals (including the fractional ones, with a different density distribution) whose exact strength might depend strongly on details of the interacting system.

At this point, we can foresee two strategies to get a more complete understanding of these phenomena. One could be a more thorough theoretical analysis, which should include interaction effect for the description of the initial state and in particular for the matterwave dynamics itself. Even in the relative simple case of two interfering condensates it was shown that a mean-field approach is often not sufficient for describing accurately the matterwave dynamics ([221]), therefore such an analysis goes beyond the scope of this thesis.

This is particularly challenging because of the 3D nature of the problem, which is quite complex as seen in the description of interaction effects in the previous chapter, with the addition of coherence and of the crossover between two regimes.

The other strategy would be to reduce the interactions: while we could with ^{87}Rb only reduce the atom number, other atomic species could be magnified with an optical potential while a Feshbach resonance could be used to tune the interactions to zero during the protocol.

Although not all experimental and theoretical questions are completely understood, we can measure the extension of the revivals in time. From that we can get an idea of the behaviour of the coherence length in the 2D plane as a function of the lattice depth (figure 5.8D).

5.1.5. Detection of magnetic Domains and Vortices

We worked so far with systems where the coherence properties were homogeneous, as far as the relative phase of the atoms in different lattice sites was concerned. The real advantage of quantum gas magnification would be then in situations where this is not the case, making local observations of the coherence possible. We notice that the resolution would then be given by the order of the Talbot revival under consideration, as phase correlations at distance d can not be well defined with resolution smaller than d .

As an example, we suggest Talbot revivals could be used to detect domains of magnetic order encoded in the condensate phases ([70, 71]). This non trivial situation can be induced by shaking a triangular lattice up to the point where the tunneling coupling between sites becomes positive ([69]), leading to a frustration of the phase. This degeneracy could lead to magnetic domains (also [222]), when different areas of the system condense at different quasimomenta, in correspondence of equally degenerate minima. Another interesting phase pattern are vortices ([223, 224]) which marks one phase of the BKT phase diagram ([225, 226]).

In figure 5.9 it is shown how the presence of such phase patterns drastically change the Talbot revivals density distribution.

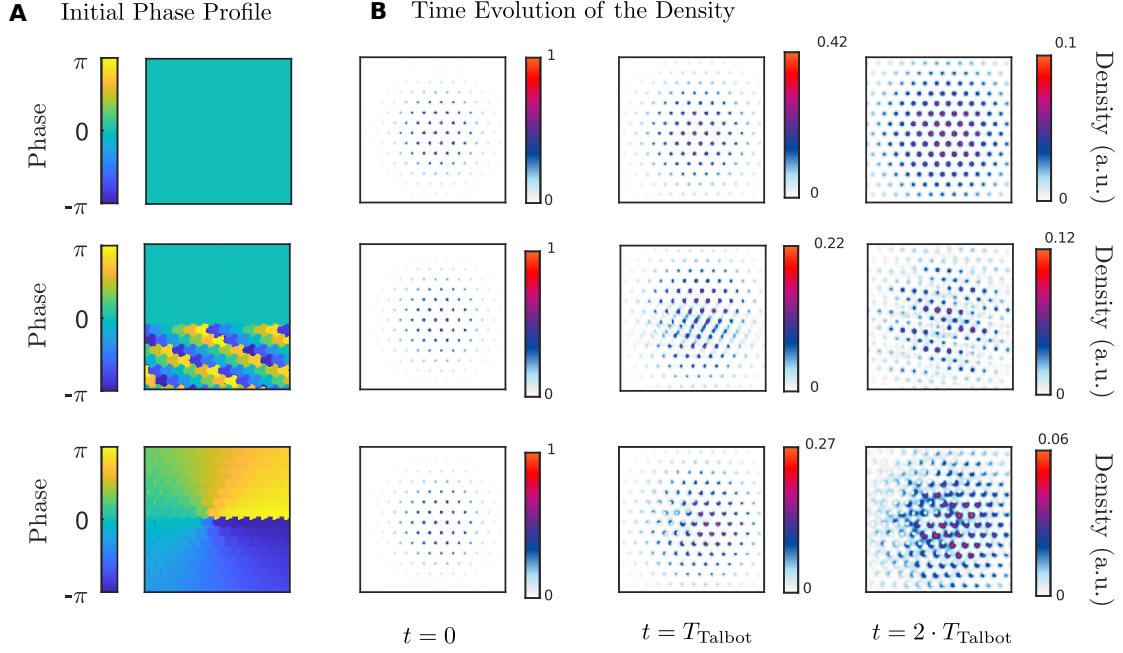


Figure 5.9.: Talbot Revivals in systems with different phase patterns. In each row, the initial phase profile is plotted in the first subfigure. The initial density profile (second subfigure) is identical for all phase patterns. One sees that the initial phase pattern, containing a domain in the second row and a vortex in the third row, influences the resulting interference pattern at $t = T_{\text{Talbot}}$ and $t = 2T_{\text{Talbot}}$. In the case of a domain between two regions of different quasimomentum (second row) the domain can be identified as the region where the revival at $t = T_{\text{Talbot}}$ of the lattice structure is less strong. At $t = 2T_{\text{Talbot}}$ a superlattice with periodicity given by the difference of the two quasimomenta is to be seen. Similarly, in the case where the initial phase profile presents a vortex (third row) the revival of the lattice structure at $t = T_{\text{Talbot}}$ is less strong at the position of the vortex. At $t = 2T_{\text{Talbot}}$, interestingly, the distribution presents many local maxima spaced with the initial lattice constant but the form of the distribution around this maxima is not rotationally symmetric, and the orientation of this form seems to be related to the position with respect to the initial vortex. Indeed, reconstructing the structure of the initial phase pattern from a Talbot revival distribution seems like a good application for machine learning techniques ([227]).

5.2. Accessing the single Particle Density-Matrix

The measurement of the density as we mentioned is just a fraction of the information about the state of a single particle (without mentioning many body systems), representing only the diagonal part of the density matrix. One could get information about the g_1 correlation function by selecting atoms (via local coupling to another state) from two points in the cloud and studying the resulting interference pattern ([228, 229]). In [230], it is suggested how to obtain the real space correlation function by Fourier transformation of high resolution measurements of the correlation function in momentum space.

In a lattice basis off-diagonal terms can only be inferred indirectly; [231] proposes to engineer a coupling channel between two sites with an additional high-resolution light potential. This proposal requires the apparatus of a quantum gas microscope, and is limited to fermions or hard-core bosons.

In this chapter we propose a protocol where matter wave optics is used to access these off-diagonal elements with single site resolution, for bosons and fermions alike, using the quantum gas magnifier.

5.2.1. Realizing non-local Coupling

The potential of a 1D lattice, which is turned on during a small pulse of duration t_p , can be written as $E_{\text{pot}} = 2V_p \cos(\mathbf{b} \cdot \mathbf{r} + \varphi_l)$, where V_p is the lattice depth of the pulsed potential, \mathbf{b} its wavevector (we assume that \mathbf{b} is parallel to the x -direction in the following), and φ_l is the lattice phase and determines its position with respect to the center of system. This potential couples all momentum states $|\mathbf{Q}_1\rangle$ and $|\mathbf{Q}_2\rangle$ with wave-vectors satisfying $\mathbf{Q}_2 = \mathbf{Q}_1 \pm \mathbf{b}$.

If the pulse is fast enough, and neglecting the kinetic energy (Raman-Nath approximation), the time evolution during the pulse can be described by the following ([232]):

$$U_p = e^{-i2V_p t_p \cos(\mathbf{b}X + \varphi_l)/\hbar} = \sum_n i^n e^{-in\varphi_l} J_n(\alpha) e^{-in|\mathbf{b}|X} \quad (5.7)$$

where $\alpha \equiv 2V_p t_p/\hbar$ and J_n is the Bessel function of the first kind of order n , with n integer. This expression determines the resulting momentum distribution, with different momenta spaced by $|\mathbf{b}|$ that are coupled. Notice that the operator $e^{in|\mathbf{b}|X}$ translates by a quantity $n|\mathbf{b}|$ in momentum space. This expression is used when calibrating the depth of optical lattices after so-called Kapitza-Dirac scattering.

We consider now the case when the fast 1D lattice pulse is performed during a quantum gas magnification protocol, in particular exactly after the $T/4$ hold time in the harmonic oscillator. Recalling that at this point $X(T/4) = P(0)/m\omega$, and $P(T/4) = m(0)$, it follows that the 1D lattice pulse effectively couples distant points in real space. This idea is sketched in figure 5.10.

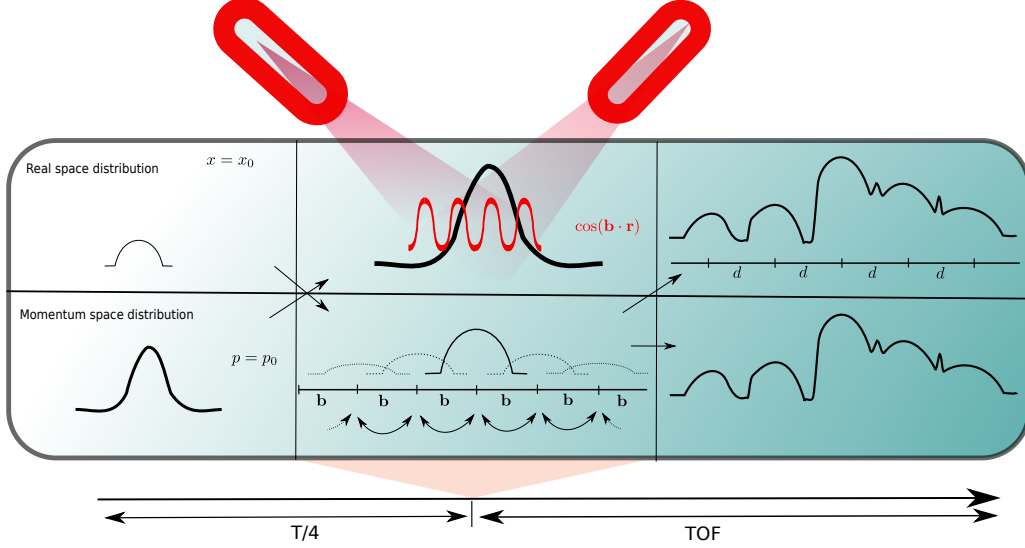


Figure 5.10.: Sketch of the coupling between distant points in real space. After the $T/4$ evolution, the real space distribution gets mapped to the momentum distribution. Then, a quick pulse of a 1D lattice of wavevector \mathbf{b} has the effect of coupling points at relative distance \mathbf{b} . The momentum distribution so obtained is measured after time-of-flight: different "copies" of the original cloud are reproduced and at their overlap the magnified density distribution carries information about the phase relations between point in the original cloud at distance $\mathbf{d} = \mathbf{b}/(m\omega)$.

A more formal derivation can be obtained by writing the total time evolution operator, consisting of the $T/4$ evolution, the 1D lattice pulse, and final time-of-flight for a time t_{tof} . We consider only the system degrees of freedom along x (with P as the momentum component along this direction), and assume they are decoupled from the others:

$$\begin{aligned}
 U &= e^{-i/\hbar P^2/2m t_{\text{tof}}} e^{-i/\hbar 2V_p \cos(\mathbf{b}X + \varphi_l)t_p} e^{-i/\hbar (\frac{1}{2} m\omega^2 X^2 + P^2/2m)T/4} = \\
 U &= e^{-i/\hbar P^2/2m t_{\text{tof}}} e^{-i/\hbar (\frac{1}{2} m\omega^2 x^2 + P^2/2m)T/4} e^{-i/\hbar 2V_p \cos(\mathbf{b}\frac{P}{m\omega} + \varphi_l)t_p} \quad (5.8) \\
 U &= U_M e^{-i/\hbar 2V_p \cos(\mathbf{b}\frac{P}{m\omega} + \varphi_l)t_p}
 \end{aligned}$$

where the first step is obtained by commutation with the $T/4$ evolution operator; this has the effect of replacing the X operator with $\frac{P}{m\omega}$.¹ In the second step we recognized that $e^{-iP^2/2m t_{\text{tof}}} e^{-i/\hbar (m\omega^2 X^2/2 + P^2/2m)T/4}$ describes the time evolution operator (denoted U_M) during quantum gas magnification.

¹For a given analytical function $f(X)$ of the position operator X , with the Taylor expansion $f(X) = \sum_n c_n X^n$, the action of the operator $U_1 = e^{-i/\hbar (m\omega^2 X^2/2 + P^2/2m)T/4}$ can be written as: $f(X)U_1 = \sum_n c_n (U_1 U_1^\dagger X)^n U_1 = \sum_n c_n U_1 (U_1^\dagger X U_1)^n = U_1 \sum_n c_n (\frac{P}{m\omega})^n = U_1 f(\frac{P}{m\omega})$.

Therefore we neglect the magnification term for simplicity, and just assume in the following that single-site resolution is available.

We label the remaining operator U'_p , and notice that it also can be recast as a sum of translation operators:

$$U'_p = e^{-i2V_p \cos(\mathbf{b}\frac{P}{m\omega} + \varphi_l)t_p} = \sum_n i^n e^{-in\varphi_l} J_n(\alpha) e^{-ink\frac{P}{\hbar m\omega}} \quad (5.9)$$

with the difference that the operators $e^{id\frac{P}{\hbar}}$ are associated with a translation in *real* space, with the translation distance given by a multiple of $\mathbf{d} = \frac{\mathbf{b}}{m\omega}$. The definition of α remains the same: $\alpha = 2\frac{V_p t_p}{\hbar}$.

Using the field operators $\psi(\mathbf{r})$, we can multiply by the identity $\int_r \psi^\dagger(r)\psi(r)$ and get:

$$U'_p = \sum_n i^n e^{-in\varphi_l} J_n(\alpha) e^{-in\mathbf{b}\frac{P}{m\omega}} \int_r \psi^\dagger(r)\psi(r) = \sum_n i^n e^{-in\varphi_l} J_n(\alpha) \int_r \psi^\dagger(r + n\frac{\mathbf{b}}{m\omega})\psi(r) \quad (5.10)$$

This can be interpreted as an operator which acting on a wavefunction creates a superposition of different "copies" of the same wavefunction, each displaced by a distance given by nd . Notice that the relative phase between them depends also on the lattice phase φ_l . Because we didn't specify which commutation relation the operators have to obey, these results will hold for both bosons and fermions.

We note the related proposal of using matterwave optics and specifically tailored potentials after a $T/4$ evolution to realize cold atomic version of optical techniques to access coherence properties of a 2D superfluid system in [233].

5.2.2. Coherence between Lattice Sites

We consider the case of an optical lattice, with atoms residing in the first band, described by s -orbitals. In this basis one is interested in the coherence defined as $\psi^\dagger_a \psi_b$ where ψ_a and ψ_b are the annihilation operators corresponding to the orbitals residing at lattice sites a and b . We derive how this coherence can be gotten using the above presented protocol. We write a generic lattice wavefunction, isolating the part residing on the two lattice sites of choice:

$$\phi(\mathbf{r}) = \sqrt{\rho_a} e^{i\theta_a} W(\mathbf{r} - \mathbf{r}_a) + \sqrt{\rho_b} e^{i\theta_b} W(\mathbf{r} - \mathbf{r}_b) + \phi'(\mathbf{r}) \quad (5.11)$$

where $\rho_{a,b}$ are the populations (the diagonal terms of the density matrix) of the sites a and b , $\theta_{a,b}$ their respective phases, and $W(\mathbf{r})$ is the normalized Wannier function describing the s -orbital. $\phi'(\mathbf{r})$ contains the information about the part of the wavefunction located away from these two sites.

Let's choose $\mathbf{d} = \mathbf{r}_b - \mathbf{r}_a$ to be exactly the lattice vector connecting the two sites (figure 5.11A). This can be done by tuning ω and the pulsed lattice wavevector \mathbf{b} . Notice that the pulsed lattice can be also another laser source than that of the lattice in which the atoms sit at the beginning of the sequence. In our experimental setup the the wavevectors $\mathbf{b}_{1,2,3}$ of the 2D lattice are aligned along the nearest neighbour distance vector in the honeycomb lattice, and along the next-nearest neighbours distance vector (and multiples of this quantity) in the triangular lattice, so they could be used to probe the 2D lattice as we are suggesting, without needing an additional 1D lattice.

We assume that $|\mathbf{d}| = \frac{|\mathbf{b}|}{m\omega} > \sigma_{\text{sys}}$ (where σ_{sys} is the system size), such that interference happens at the overlap of two "copies", but not more than two (as in figure 5.10), simplifying the interference pattern as dependent only on the relative phase between the two copies with non-vanishing signals in the regions under consideration.

The final wavefunction $\phi_f(\mathbf{r})$ can be written as:

$$\phi_f(\mathbf{r}) = U'_p \phi(\mathbf{r}) = \sum_n i^n e^{in\varphi_l} J_n(\alpha) \phi(\mathbf{r} - n\mathbf{d}) \quad (5.12)$$

We expand $U'_p \phi$ and writing explicitly only the non-vanishing term around \mathbf{r}_a :

$$\phi_f(\mathbf{r}) = J_0(\alpha) \sqrt{\rho_a} e^{i\theta_a} W(\mathbf{r} - \mathbf{r}_a) + i e^{i\varphi_l} J_1(\alpha) \sqrt{\rho_b} e^{i\theta_b} W(\mathbf{r} - \mathbf{r}_b + \mathbf{d}) + \text{other terms} \quad (5.13)$$

Rewriting after substituting $\mathbf{r}_b - \mathbf{d} = \mathbf{r}_a$ yields:

$$\phi_f(\mathbf{r}) = \left[J_0(\alpha) \sqrt{\rho_a} e^{i\theta_a} + i e^{i\varphi_l} J_1(\alpha) \sqrt{\rho_b} e^{i\theta_b} \right] W(\mathbf{r} - \mathbf{r}_a) + \text{other terms} \quad (5.14)$$

Integrating the density in the Wigner-Seitz cell, assuming $\int_{WS} |W|^2 d\mathbf{r} = 1$, gives:

$$\int_{WS} |\phi_f(\mathbf{r})|^2 = J_0(\alpha)^2 \rho_a + J_1(\alpha)^2 \rho_b + 2\text{Re}\{ i e^{i\varphi_l} e^{\theta_b - \theta_a} J_0(\alpha) J_1(\alpha) \sqrt{\rho_a \rho_b} \} \quad (5.15)$$

where the incoherent sum of the signals can be recognized ($J_0(\alpha)^2 \rho_a + J_1(\alpha)^2 \rho_b$), plus an interference term $I(\varphi_l)$ which can be recast in the form:

$$I(\varphi_l) = -2 \sin(\varphi_l + \theta_b - \theta_a) J_0(\alpha) J_1(\alpha) \sqrt{\rho_a \rho_b} \quad (5.16)$$

Notice that $\rho_{a,b}$ can be measured independently (with a normal magnification protocol) and α can be obtained by calibration of the pulsed lattice; this guarantees the complete reconstruction of the off-diagonal density matrix ρ_{ab} . The interference term $I(\varphi_l)$ has a sinusoidal dependence on φ_l , therefore one could repeat the measurement for different values of φ_l and extract $\theta_b - \theta_a$ from the phase of the oscillating signal as a function of φ_l , and $\sqrt{\rho_a \rho_b}$ from the amplitude of the oscillation.

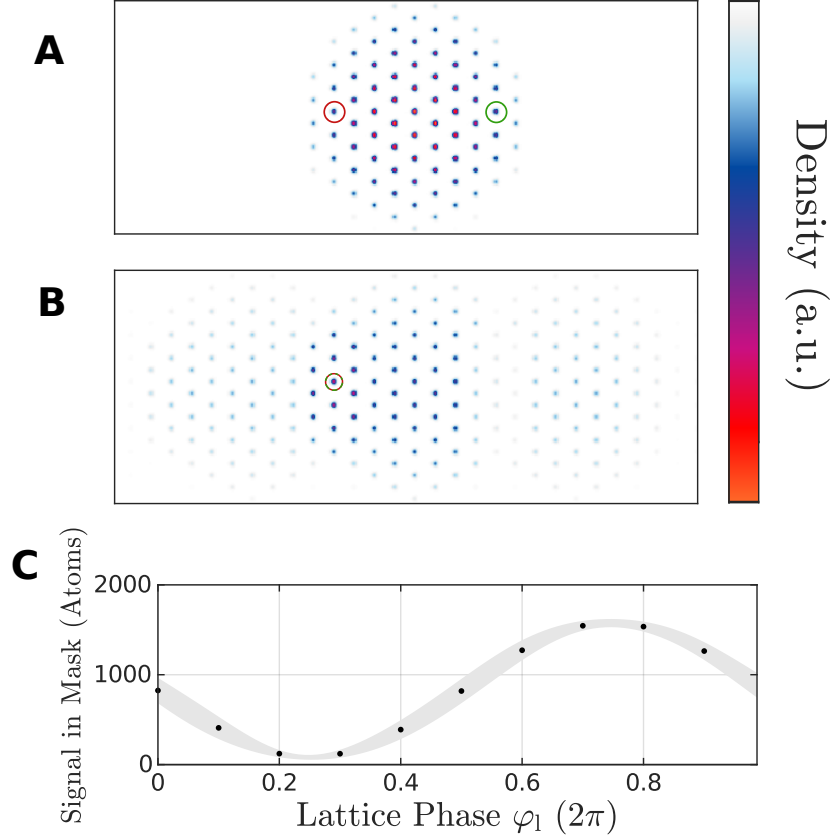


Figure 5.11.: Numerical Simulation of the Interference Signal as a function of the Lattice Phase. **A:** 'In situ' density distribution. The circles denotes the lattice sites between corresponding to the parts of the wavefunction of which we want to measure the relative coherence. **B:** Density distribution predicted from equation 5.12 using a fast 1D lattice pulse with phase $\varphi_l = -\pi/2$ with respect to the center of the trap and modulation index $\alpha = 1.1$. **C:** Signal in the circular mask of radius $a_{\text{lat}}/2$ (drawn in **B**) as a function of the lattice phase φ_l . The grey areas indicate fluctuations due to the error sources described in the text.

In a numerical simulation we consider 10^5 bosonic atoms in the same lattice state and apply the suggested protocol with $\alpha = 1.1$ and $|\mathbf{d}| = 4 a_{\text{lat}}$.

We study the resulting density distribution, and analyze the part of this signal determined by the interference of two lattice sites, with $\rho_a J_0(\alpha)^2 \sim \rho_b J_1(\alpha)^2 \sim 800$ atoms (figure 5.11).

We include in the numerical simulation some possible source of errors, expected to be present in a realistic experiment. We assume a 0.2π precision in the determination of the lattice phase φ_l (which is distributed randomly) reproducing the case where phase of the pulsed lattice is not controlled but only inferred from the final density distribution (as in the experiments presented in chapter 4), assuming the pulsed lattice was also used for creating the 2D lattice. After determining the atom number for every lattice phase, we extract a measurement assuming a poissonian distribution with this atom number as mean.

From the signal so obtained, which shows the predicted behaviour of equation 5.16, amplitude and phase can be easily extracted, thus making thinkable to access off-diagonal elements of the density matrix in an experiment.

Notice that in the case of a mixed state, the amplitude of the oscillations would be given by $|J_0(\alpha)J_1(\alpha)\rho_{ab}|$ instead of $J_0(\alpha)J_1(\alpha)\sqrt{\rho_a\rho_b}$.

Notice that all the entries of the density matrix relative to pairs of lattice sites at distance \mathbf{d} are obtained at the same time, by performing the analysis at each lattice site (instead, the proposal of [231] would need repeating the whole procedure for every pair of lattice sites).

Using another laser, one might not be able to read the pulsed lattice phase directly from the density distribution. Without the knowledge of φ_l , one can not access the phase of ρ_{ab} anymore. The absolute value $|\rho_{ab}|$ could still be inferred by repeating the experiment for various (unknown random) values of φ_l and by looking at the distribution of the signal in the mask, which should be contained within the values $J_0(\alpha)^2\rho_a + J_1(\alpha)^2\rho_b \pm |J_0(\alpha)J_1(\alpha)\rho_{ab}|$ (A similar procedure was used in [234], where the phase correlation length was extracted from the intensity correlation length after interference of two copies of a expanding BEC with thermal fluctuations. Note that in that case we speak of "copies" in the sense that the interfering clouds had the same density profile. In the experiments [234, 235] neither the density nor the phase profile of the copies were the same as that of the original cloud, as we are proposing in this chapter).

5.2.3. Tuning the coupling Distance \mathbf{d}

The coupling vector \mathbf{d} can be tuned by varying the wavevector of the pulsed lattice. This could be tuned arbitrarily using an auxiliary laser setup with movable mirrors ([236, 237]). The distance $|\mathbf{d}|$ can be tuned also by varying the trap frequency ω . The matter-wave protocol could be adapted in order to set independently from each other the trap frequency in the system under study, the trap frequency used in the determination of $|\mathbf{d}|$, and the magnification factor M .

Assuming that the s -orbitals have constant phase, we can calculate how the overlap will be reduced in case the condition for coupling two distant sites is not be precisely met: $\mathbf{d} = \mathbf{r}_b - \mathbf{r}_a + \epsilon$, with ϵ representing a small deviation, which we assume to be also along x . Then the amplitude of the oscillations $A = \max[I(\varphi_l)] - \min[I(\varphi_l)]$ as a function of φ_l is proportional to:

$$A \propto \int_{WS} W^*(\mathbf{r} + \epsilon)W(\mathbf{r}) = \int_{WS} W^*(r)e^{iP\epsilon/\hbar}W(\mathbf{r}) \simeq \int_{WS} W^*(\mathbf{r})(1 + iP\epsilon/\hbar - P^2\epsilon^2/\hbar^2)W(r) \quad (5.17)$$

Approximating W with the ground state of the harmonic oscillator with oscillator length a_{ho} , we can rewrite $P = \frac{i\hbar}{2a_{\text{ho}}}(a^\dagger - a)$, with a^\dagger, a creation/annihilation operators of the harmonic oscillator.

Noticing that only the terms proportional to 1 and to aa^\dagger have a finite expectation value, this yields:

$$A \propto \left(1 - \frac{\epsilon^2}{4a_{\text{ho}}^2}\right) \quad (5.18)$$

which implies that, intuitively, the coupling distance \mathbf{d} must be set with a precision at least at the level of the linear extension of the Wannier functions.

Notice that in a lattice with multiple s -orbitals, like the honeycomb or the Kagome lattice, the overlap between Wannier functions belonging to different sublattices would be always smaller than 1. This should be taken into account when interpreting the result of a measurement by e.g. rescaling the signal taking the finite overlap into account.

Finally, we conclude with the remark that in order to couple two lattice sites, the initial real space distribution must be precisely mapped to the momentum distribution during the 1D lattice pulse. This condition holds for a time interval not longer than δt_{max} around $T/4$ (δt_{max} is the time during which two lattice sites remain well spatially separated after release from the lattice, as introduced in the previous chapter). Therefore the duration of the pulse t_p must be smaller than δt_{max} . For realistic parameters of $V_p/\hbar = 50\text{kHz}$, $t_p = 1\mu\text{s} < t_{\text{max}}$ one obtains $\alpha = 2V_p t_p/\hbar \simeq 0.63$, which should produce a very good signal, as $J_1(\alpha)$ is on the same order of magnitude as $J_0(\alpha)$.

5.3. Conclusions

In this chapter we presented some preliminary experimental results and considerations about the possibility of using the Quantum Gas Magnifier to access coherence properties of a quantum system at the microscopic level.

We derived how the Talbot effect would look like in presence of a harmonic trap and verified numerically the framework introduced here for the prediction of times at which the system experiences Talbot revivals. We presented results of the Talbot effect observed at the microscopic level in different geometries; Talbot revivals were observed as an oscillation of the lattice modulation of the density distribution of the atoms as a function of the time in the trap.

Although we were not able to make a quantitative comparison with some theory because of interactions during the protocol we believe this is a promising research direction, maybe with another atomic species. This effect could be used to access coherence properties of a system in a real-space, which would be very useful for inhomogeneous systems, as coherence was typically investigated in a global way. As an example, we performed a numerical simulation of two systems with a inhomogeneous distribution of the phase (a magnetic domain wall, and a magnetic vortex), and have shown how the Talbot revivals could be a very sensitive measurement for phase patterns. We notice that the mapping between Talbot revivals in a harmonic oscillator and in free-space and the direct imaging with the quantum gas magnifier also allows to measure Talbot revivals corresponding to negative orders (or for an equivalent negative time-of-flight). This could be used to detect chiral states which break time-reversal symmetry.

We also presented a proposal for the direct measurement of off-diagonal elements of the single-particle density matrix, in a single site-resolved fashion. The proposal is based on the engineering of non-local coupling terms between distant lattice sites, using matter wave optics. We demonstrated numerically that in a setup much like ours it could be easily implemented and should produce a measurable signal.

In the example presented here, a fast optical lattice pulse after a $T/4$ evolution creates many displaced "copies" of the original wavefunction which interfere where they overlap, and can be magnified with time-of-flight. In order to perform a simpler analysis, we limited ourselves to the case where the displacement $|\mathbf{d}|$ is bigger than the system size. It could be of interest not to have this limitation, e.g. by creating a superposition of just two displaced "copies" of the original wavefunction $\phi(\mathbf{r})$ in a form similar to: $\phi_f(\mathbf{r}) \propto \phi(\mathbf{r} + \mathbf{d}) + \phi(\mathbf{r})$.

This protocol requires being able to image coherent systems in the first place, therefore, as before, we don't expect an implementation with ^{87}Rb in our setup, because we can not tune the interactions to zero during the measurement protocol. It could be done with an atomic species where the scattering length can be tuned (dynamically) to 0 near a Feshbach resonance, or with spin-polarized fermions.

The case of fermionic atoms could be particularly interesting, as they tend to fill homogeneously lattice bands, allowing for a quantized topological response. Coherence between lattice sites is a fundamental requirement for topological bands: the local Chern marker, which in the bulk of a topological system approaches the Chern number, can be expressed as a function of the off-diagonal density matrix elements in different pairs of lattice sites ([238]). Note that in momentum space, the density matrix gives the global Chern number of a system ([239]). Relevantly for an experimental application, a finite number of such elements need to be measured to get a good approximation of the local Chern marker ([240]). In a system with fermions occupying different levels in z -direction (e.g. in a lattice of "tubes") the measured density matrix will be then averaged over the degrees of freedom corresponding to the z direction, but if this direction can be considered decoupled from the other, averaging just increases the signal to noise ratio.

If performing a $T/4$ ($3T/4$) evolution after the application of the 1D lattice pulse, one could recapture the atoms in the original lattice, but at a lattice site at distance d from the previous occupied one. This could be used to move qubits over long distances as a resource for quantum computation ([241]) or, when repeating the protocol, in a Floquet realization, for engineering long range tunneling.

A general remark on both type of measurements proposed in this chapter (the Talbot revivals and the measurement of the density matrix): they are strongly related to each other, because both depend on the phase correlation function. The advantage of the Talbot method could be that it needs a simpler protocol, and in principle one could obtain with a single destructive measurement much of the relevant information about the phase distribution of the system as we have shown in the numerical simulations, making it more suitable for phase patterns like magnetic vortices of domains which might be different from realization to realization.

Instead if the phase pattern is stable (constant for every experimental realization) having access to the correlation function between any two lattice sites is enough to obtain the complete information of the system at the single particle level, which would be then a fundamental aid in studying complex many-body problems.

6. Multi-Frequency Lattice

Control of the potential is crucial in optical lattice experiments ([242]), and in particular e.g. with experiments that deal with topology, where the topological features depend on the system parameters. The control to which we are referring can be static as well as dynamic.

The optical honeycomb lattice ([33, 243]), can be realized in a variety of geometries tuned via the polarization of the laser beams, but this does not allow a full dynamic control of the geometry. This can be achieved using a more near-detuned laser to exploit the dependence from the direction of the quantization magnetic field ([244]), or using a setup with piezo mirrors ([126, 179]). The geometry in a bipartite square lattice can also be controlled in a similar fashion ([185]).

During my PhD I conceived and developed what we called the "multi-frequency lattice", an extension to the optical honeycomb/triangular lattice which allows a precise full dynamical control over the geometry of the lattice. Implementation and characterization of the multi-frequency lattice in our setup was done together with Henrik Zahn and Marcel Kosch, under the supervision of Christof Weitenberg and Klaus Sengstock. The multi-frequency lattice is based on driving each of the three laser beams with two frequencies, such that they interfere pairwise with each other but with a different frequency for each 1D lattice forming the total potential. We show how this allows lattice geometry control.

Other schemes for generating optical lattices which rely on multiple frequencies are Fourier synthesized lattices ([210]), beat-note lattice ([245]), two wavelengths lattices like e.g. the Kagome lattice.

The multi-frequency lattice does not require phase lock like most of the multi-frequency techniques used for generating optical lattices (e.g. [187]). Also polarization synthesized lattices ([246]) need a precise phase lock.

We demonstrate the stability of the multi-frequency lattice and present some measurements where dynamical control of the geometry is demonstrated.

6.1. Tunable Lattice Geometry via Frequency Control

Three interfering laser beams propagating in two dimensions always lead to a stable geometrical configuration with respect to phase fluctuations ([247]). We give a demonstration using a convention which will be used in the rest of the chapter.

Without loss of generality, one can write the lattice potential as $E_{\text{pot}}(\mathbf{r}) = 2 \sum_i V_i \cos(\varphi_i)$ where $\varphi_i = \mathbf{b}_i \cdot \mathbf{r} + \varphi_i^0$, and $\mathbf{b}_i = \epsilon_{ijl} \frac{\mathbf{k}_j - \mathbf{k}_l}{2}$ (with $\mathbf{b}_{1,2,3}$ the reciprocal lattice vectors obtained by cyclic combination of the wavevectors of the lattice beams $\mathbf{k}_{1,2,3}$); \mathbf{r} is the vector of the coordinates in the 2D plane.

Let's consider a phase fluctuation $\delta\varphi$ on beam 1, for example. This modifies two of the phases entering the definition of the potential:

$$\begin{aligned}\varphi_1 &= \mathbf{b}_1 \cdot \mathbf{r} + \varphi_1^0 \\ \varphi_2 &= \mathbf{b}_2 \cdot \mathbf{r} + \varphi_2^0 + \delta\varphi \\ \varphi_3 &= \mathbf{b}_3 \cdot \mathbf{r} + \varphi_3^0 - \delta\varphi\end{aligned}\tag{6.1}$$

One can recover the exact same potential just by an appropriate position shift of the lattice $\mathbf{r} = \mathbf{r}' - \delta\varphi \frac{\mathbf{b}_2 - \mathbf{b}_3}{(\mathbf{b}_2 - \mathbf{b}_3) \cdot \mathbf{b}_2}$:

$$\begin{aligned}\varphi_1 &= \mathbf{b}_1 \cdot \mathbf{r}' - \mathbf{b}_1 \cdot \delta\varphi \frac{\mathbf{b}_2 - \mathbf{b}_3}{(\mathbf{b}_2 - \mathbf{b}_3) \cdot \mathbf{b}_2} + \varphi_1^0 = \mathbf{b}_1 \cdot \mathbf{r}' + \varphi_1^0 \\ \varphi_2 &= \mathbf{b}_2 \cdot \mathbf{r}' - \mathbf{b}_2 \cdot \delta\varphi \frac{\mathbf{b}_2 - \mathbf{b}_3}{(\mathbf{b}_2 - \mathbf{b}_3) \cdot \mathbf{b}_2} + \varphi_2^0 + \delta\varphi = \mathbf{b}_2 \cdot \mathbf{r}' + \varphi_2^0 \\ \varphi_3 &= \mathbf{b}_3 \cdot \mathbf{r}' - \mathbf{b}_3 \cdot \delta\varphi \frac{\mathbf{b}_2 - \mathbf{b}_3}{(\mathbf{b}_2 - \mathbf{b}_3) \cdot \mathbf{b}_2} + \varphi_3^0 - \delta\varphi = \mathbf{b}_3 \cdot \mathbf{r}' + \varphi_3^0\end{aligned}\tag{6.2}$$

Where we used $\mathbf{b}_1 \cdot (\mathbf{b}_2 - \mathbf{b}_3) = (-\mathbf{b}_2 - \mathbf{b}_3) \cdot (\mathbf{b}_2 - \mathbf{b}_3) = 0$ for the first phase and $(\mathbf{b}_2 - \mathbf{b}_3) \cdot \mathbf{b}_2 = -(\mathbf{b}_2 - \mathbf{b}_3) \cdot \mathbf{b}_3$ in the last one. Therefore, the lattice geometry remained constant and only the position of the lattice changed. This effect is explicitly used by lattice shaking, which moves in space the lattice structure with controlled phase shifts of the lattice beams.

Having a second look at equation 6.1 we notice that there is a quantity which is unchanged under phase shifts:

$$\varphi_g = \sum_i \varphi_n\tag{6.3}$$

Equivalently, also position shifts $\mathbf{r} = \mathbf{r}' - \delta\mathbf{r}$ don't change φ_g , because the apparent dependence of φ_g on \mathbf{r} is trivial, since $\sum_i \mathbf{b}_i = \sum_i \epsilon_{ijz} \frac{\mathbf{k}_j - \mathbf{k}_z}{2} = 0$.

We call φ_g then "geometry phase", arguing that it plays a major role in determining the geometry of the optical 2D lattice.

The potentials obtained for the different values of φ_g for the symmetric case where $V_{1,2,3} = V$ and when the beams interfere under a 120° degree angle, are plotted in figure 6.1. When $\varphi_g = 0$ one gets a honeycomb lattice, and if $\varphi_g = \pi$, a triangular lattice. The energy levels as a function of φ_g are plotted in figure 6.2, where one notices the honeycomb lattice with sublattice offset $\Delta = 0$ as the point where the first two bands touch, closing the gap at the K and K' points of the Brillouin Zone. The 2D lattice potential E_{pot} is described by six parameters (three V_i and three φ_i) but two degrees of freedom are associated with the in-plane position; therefore just 4 parameters are needed for a complete description of the geometry of the lattice: the 1D lattice depths V_i and φ_g .

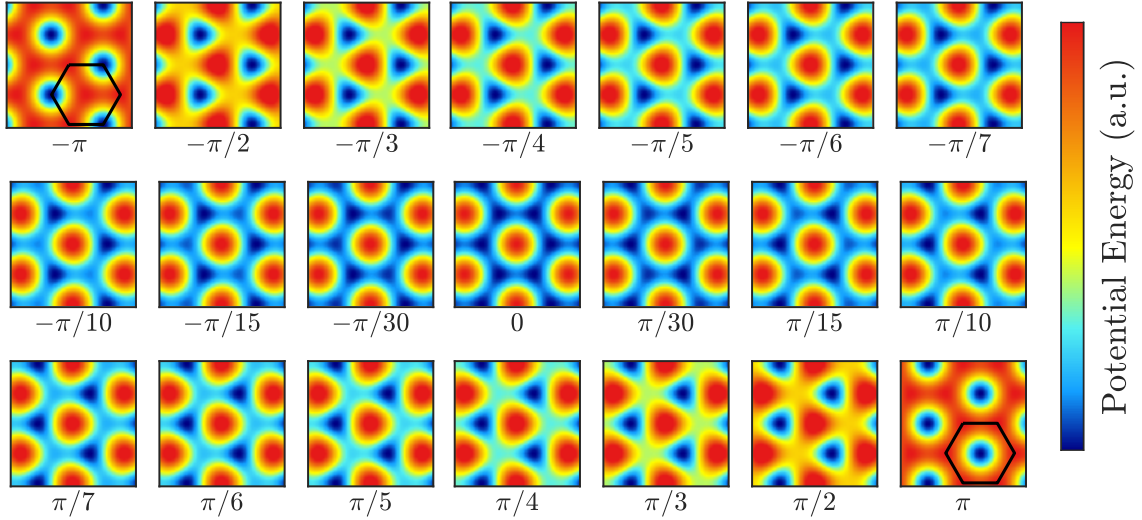


Figure 6.1.: Potential landscapes for different geometry phases φ_g .

Potentials calculated as $E_{\text{pot}}(\mathbf{r}) = \sum_i \cos(\mathbf{b}_i \cdot \mathbf{r} + \varphi_g/3)$ for different values of φ_g . An offset is added such that all minima for all potentials are at $E_{\text{pot}} = 0$. Notice that the range of φ_g scanned is not linear, and therefore a honeycomb or boron-nitride lattice can be found in a relatively much smaller range than a triangular lattice. After 2π the geometry is the same as in the beginning but the lattice position is shifted, as can be seen by comparing the position of the minima with the reference unit cell drawn in the first and in the last plot.

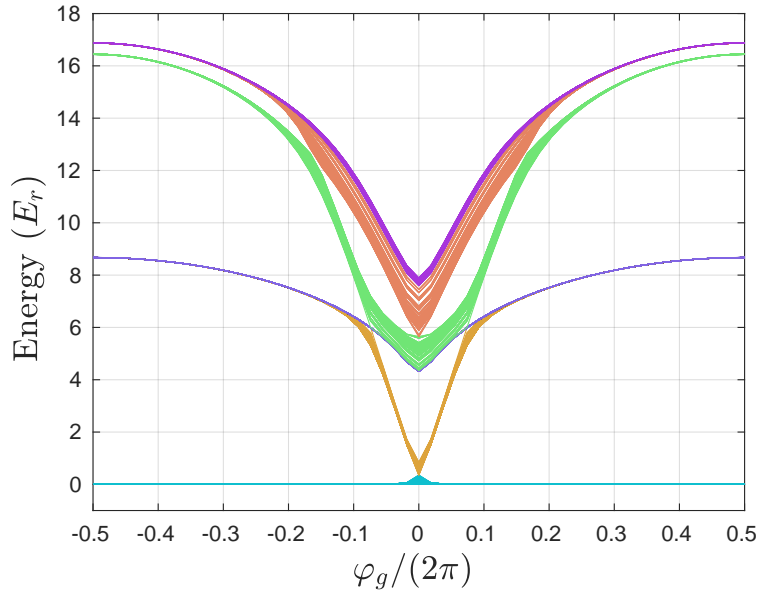


Figure 6.2.: Band structure as a function of the geometry phase φ_g . The band structure is calculated for a fixed lattice depth of $V = 5E_r$ and integrated over the Brillouin zone. Different colors corresponds to different bands. Notice that in the triangular lattice regime bands are completely flat, while there is some dispersion in the lowest bands of the honeycomb lattice. The band gap increases approximately linearly in $|\varphi_g|$ around $\varphi_g = 0$, until the s-orbital state with bigger energy gets hybridized with the p-orbital state residing in the lattice site with lower energy.

It is then evident that, in order to change φ_g , one needs complete independent control over all phases φ_i . This can be done statically by polarization control (as described in chapter 2), but every geometry change requires careful setting of the polarization angles and calibrations, and dynamical change might be possible only using motorized rotation plates ([248]). These can not be driven arbitrarily fast and require accurate calibration and care in disentangling the waveplates angles (one needs two waveplates in order to set an arbitrary polarization in one beam) from the 1D lattices depths V_i and phases φ_i .

The sketch of the multi-frequency lattice, with which we chose to realize dynamic control of the geometry, is presented in 6.3. The main idea is that each laser beams is driven at two different frequencies. For each pair of beams, a frequency is shared, creating the corresponding 1D lattice. Now the phase of each 1D lattice can be tuned independently of the phases of the other 1D lattices, acting selectively on the relative phase of the right frequency component.

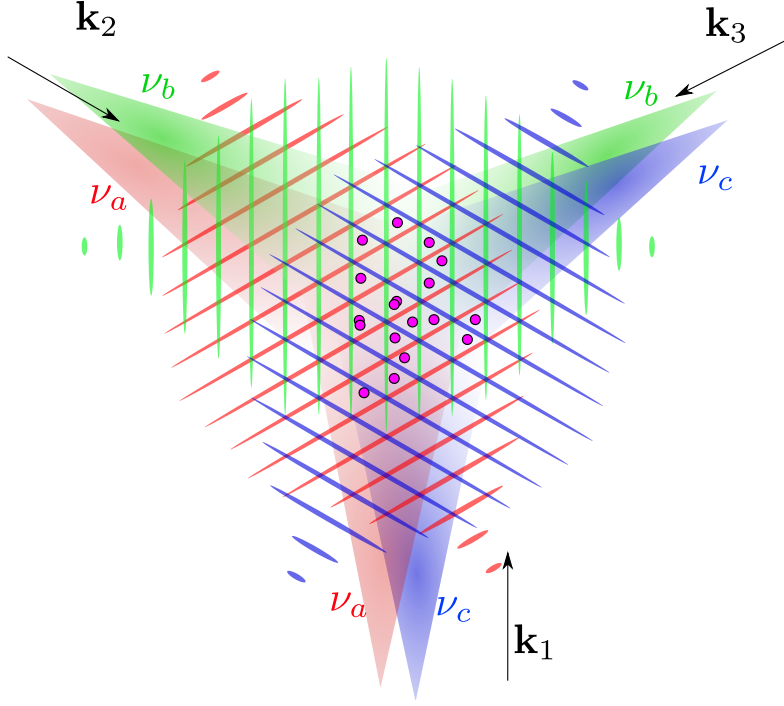


Figure 6.3.: Sketch of the multi-frequency lattice.

Each laser beam is driven by two frequencies. For every couple of beam there is a frequency in common ($\nu_{a,b,c}$), such that a 1D lattice at that particular frequency is created, with wavevector given by the difference of the corresponding photon wavevectors $\mathbf{k}_{1,2,3}$. Atoms sitting in the minima of the total lattice potential are represented by purple circles. The phase of each 1D lattice can be individually controlled independently of the other two by changing the relative phase in the corresponding frequency component. For example by changing $\varphi_{b2} - \varphi_{b3}$ the "green" lattice can be shifted along its wavevector leaving the others in place. The actual differences between frequencies can be as small as some MHz, and the spatial separation between different frequency components in the same beam is introduced for clarity.

In this way, one has that φ_g is given by:

$$\varphi_g = \sum_i \varphi_i^0 = (\varphi_{a1} - \varphi_{a2}) + (\varphi_{b2} - \varphi_{b3}) + (\varphi_{c3} - \varphi_{c1}) \quad (6.4)$$

where φ_{xn} is the phase of the frequency component x on beam n . Grouped in the same parenthesis are phases relevant for the same 1D lattice. Since all of the phases are now independently controllable, one could vary any of them to set φ_g to the desired values. In this way, one could realize all the symmetric static potentials possible with the given wavevectors with polarization control ([32]).

In particular we note the possibility to set with great precision the offset Δ in a honeycomb lattice situation, where it determines the topological region ([9, 11, 65]). We note also that for (red-detuned) linearly in-plane polarized light φ_g is not automatically 0 because of the vector light shift (see Appendix C), which is more relevant for laser light detunings which are not much bigger than the fine structure of the atoms ([249]); note that this holds unless working with the $m_F = 0$ hyperfine state and/or having also in-plane orientation of the quantization axis ([244]). The multi-frequency lattice allows to compensate naturally for this phase offset and to set the offset between sublattices in the honeycomb lattice $\Delta = 0$. On the other side, since in this scheme the geometry can be set for a given m_F state independently of the polarization, one could use the polarization angle to tune the dependence of the potential on the internal atomic state, with the possibility to cancel it completely with out-of-plane polarization.

We also notice that some asymmetric potentials that are difficult to achieve with polarization control become easily realizable with the multi-frequency lattice; as an example the distorted quadratic lattice (see figure 6.4) of the form $\sum_{i=2}^3 \cos(\mathbf{b}_i \cdot \mathbf{r})$, can be obtained with the multi-frequency lattice simply by turning off the frequency component for the 1D lattice at wavevector \mathbf{b}_1 .

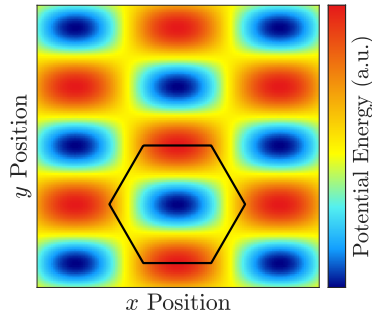


Figure 6.4.: Distorted Quadratic lattice. Optical lattice as described by $\sum_{i=2}^3 \cos(\mathbf{b}_i \cdot \mathbf{r})$. The tight binding-description of the lowest band of this potential can be mapped directly to the one of a symmetric square lattice. The black hexagon marks (a possible choice of) the unit cell.

This potential could be realized in a polarization lattice only with a careful tuning of the polarization angles ([21]). Being able to measure both in a quadratic and e.g. in a triangular lattice in the same experimental setup could allow to investigate the role of geometrical elements like frustration or connectivity (number of nearest neighbours) in various physical settings ([250]).

This possibility of easily realizing particular geometries is mentioned only as an example to demonstrate the tunability of the multi-frequency lattice, and of course the interest in this new scheme lies in the possibility of changing the geometry of the lattice in a dynamical fashion, for studying dynamics in new regimes and/or engineering novel Floquet protocols.

6.2. Implementation

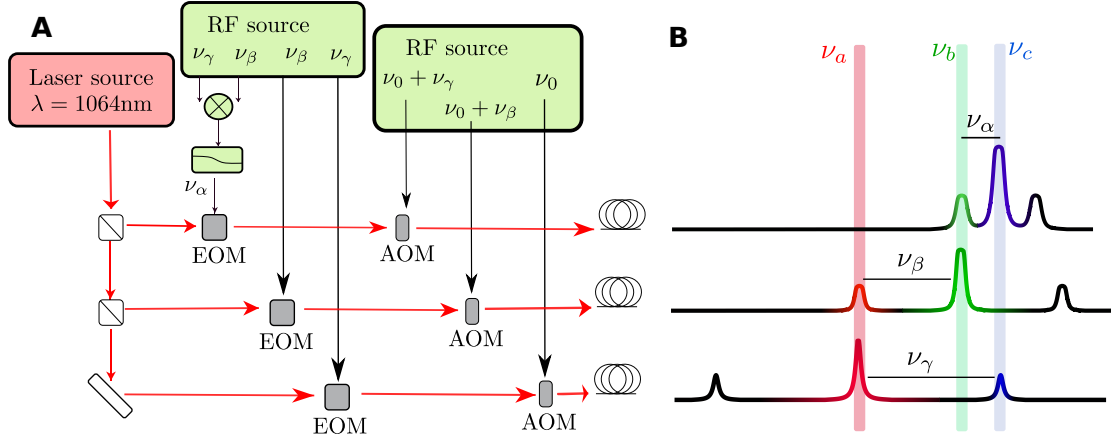


Figure 6.5.: Schematic of the Experimental setup. In **A** the implementation of the multi-frequency lattice is sketched. The laser light is splitted into the three beams. Each of them is first modulated by an EOM and then diffracted by an AOM. The modulation frequency ν_α is obtained after mixing the frequencies ν_γ and ν_β and using a 2MHz low pass filter in order to guarantee perfect relative phase stability from the side of the radio-frequency sources. All beams are sent to the experiment table through separate optical fibers. In **B**, the spectrum for each beam is represented and shows that every beam pair has one (and only one) frequency in common ($\nu_{a,b,c}$).

Our implementation of the multi-frequency lattice is sketched in fig. 6.5. We detuned the three beams with respect to each other by driving the AOMs at frequencies $\nu_0 + \nu_\gamma = 114.995\text{MHz}$, $\nu_0 + \nu_\beta = 112.775\text{MHz}$, $\nu_0 = 105.005\text{MHz}$. This frequency separations are much bigger than typical on-site trap frequencies of the lattice, creating a running wave which would not influence the atoms. We establish interference by using EOMs by Qubig with tunable resonance frequency driven at $\nu_\alpha = 2.22\text{MHz}$, $\nu_\beta = 7.77\text{MHz}$, and $\nu_\gamma = 9.99\text{MHz}$. Thus each modulation creates a sideband exactly at resonance with another beam.

The lattice depth of a 1D lattice is proportional to the product of the relative electric field components at the same frequency of the two corresponding laser beams. Because every 1D lattice is formed via interference of a sideband and of a carrier, the lattice depth is proportional to $J_0(n)J_1(n)$ (with $J_o(n)$ being the Bessel functions of the first kind of order o , assuming n to be the modulation index for all EOMs). We set then $n \simeq 1.08$ which maximizes the product giving $J_0(n)J_1(n) \sim 0.34$. We do this by first calibrating the modulation index as a function of the incoming radio frequency amplitude via a Fabry-Perot cavity, where the spectrum of the laser beam can be seen and the modulation index inferred from the relative height of the peaks in the spectrum. Since the polarization of the laser beams is no more decisive for the geometry, we used linear polarization of the laser beams and turn it perpendicular to the lattice plane for maximal interference.

In this way, in order e.g. to realize with the multi-frequency lattice the boron-nitride-like lattice used in the circular Dichroismus chapter, we calculate a factor of ~ 0.77 between the lattice depths obtained with the two methods, for the same total laser power (the lattice obtained via polarization control being deeper). For the triangular lattice, where the lattice depth is not really a limitation (because of the greater lattice spacing between nearest neighbours it can reach much smaller tunneling elements being, effectively, much deeper) this factor becomes ~ 0.34 . We notice then that for obtaining the exact same lattice potential, the realization with the multi-frequency lattice requires more laser power: this has to be taken into account when calculating the additional confinement due to the spatial variation of the intensity of the lattice beams, particularly relevant in the z -direction in our setup.

The modulation frequencies were chosen with the (to some degree, arbitrary) constraints of staying below 10MHz with the biggest energy difference between the AOM driving frequencies, and having the smallest running wave frequency above 1MHz. The first constraint was motivated by the efficiency range of the AOMs being finite; and we did not want to change AOMs in order to make the switch between multi-frequency and polarization lattice easier in both directions. Putting the EOMs in place was a relatively non-invasive operation (up to a small power loss due to the transmission efficiency of the EOMs); when switching to the multi-frequency lattice we had only to change the AOMs frequencies and recouple the beams in the AOMs and subsequently in the fibers. After we verified that the setup was working, we turned the polarization of the lattice beams out of plane.

The second constraint for choosing the modulation frequencies is given by the typical energy scales of the atoms in the lattice: by taking the difference between any two frequency components on two beams one gets a frequency associated with a running wave in the system. Notice that while the strongest running waves have frequencies equal to the differences between AOM driving frequencies, the smallest running wave frequency is given by 1.11MHz (obtained by taking into considerations also higher order sidebands, with much reduced relative weight).

By imposing that all the possible frequency differences must be above 1MHz (much greater than the lattice depth) we make sure that these frequencies don't couple to dynamical degrees of freedom.

We note that Raman transitions to other spin states should be avoided, by choosing the polarization of the laser beams to be parallel to the quantization axis and/or choosing a separation of the m_F states (given by the amplitude of the quantization field) which is not a multiple of the lowest running wave frequency (in our case, 1.11MHz). On the other hand, it would be interesting in the future to study how using explicitly Raman transitions could modify the picture ([251, 252], or [253] in momentum space).

There are also components to the static lattice which come from the interference of higher order sidebands, e.g. we notice that because $\nu_a - 6\nu_\alpha = \nu_b - 2\nu_\beta$ the -6^{th} sideband on EOM 1 will be resonant with the -2^{nd} sideband on EOM 2; the corresponding lattice depth is proportional to $J_{-6}(n)J_{-2}(n)$ and, for our low modulation index, can be safely neglected (all such interference terms are at least a factor 10^5 suppressed with respect to the desired ones). The choice of the frequencies as a multiple of an integer sequence (2,7,9) is simply mainly due to simplicity for the individuation of such higher order resonances, and for being able to identify a periodic evolution of the time-dependent potential, since all the frequencies present in the system are multiples of 1.11MHz, which then becomes the smallest frequency a running wave can have (incommensurate choice of the frequencies, instead, leads to a quasiperiodic evolution of the potential). Among the possible triples we found 2,7,9 to be the best in term of relative impact of the higher order resonances we just discussed.

We obtain an important information over the stability of the geometry by taking the time derivative of φ from equation 6.4 and grouping the phases in the following order:

$$\partial_t \varphi_g = \partial_t((\varphi_{a1} - \varphi_{c1}) + (\varphi_{b2} - \varphi_{a2}) + (\varphi_{c3} - \varphi_{b3})) = \nu_\alpha + \nu_\beta - \nu_\gamma \quad (6.5)$$

Notice that the different sign for ν_γ comes from the fact that we are using the opposite sideband there as compared with the other two. This tells us that the geometry is stable as long as:

$$\nu_\gamma = \nu_\alpha + \nu_\beta. \quad (6.6)$$

making only the EOMs responsible for the stability of the geometry. This requirement is actually not so easy to realize as it looks, because the necessary precision is very high: on the time scale of several experimental runs (~ 30 minutes), or of complete measurements ($\sim 1 - 10$ hours) a deviation of just $\sim 10^{-4}$ Hz would change completely the geometry.

We found a solution to this issue in obtaining the frequency ν_α from mixing of ν_β and ν_γ . We chose this configuration for the mixing since it produces the most distant frequencies: $\nu_\gamma - \nu_\beta = 2.22$ MHz and $\nu_\gamma + \nu_\beta = 17.6$ MHz; we suppress the second (unwanted) one using a 2MHz low-pass filter. As a remark, the EOM resonance is very sharp and hence other frequencies are not expected to play a role. Since the phase of the mixed signal is the difference of the phases, we can use the phase of one of the two mixer inputs to control the phase of the corresponding 1D lattice (φ_a).

We use then two output channels at ν_β and two output channels at ν_γ coming from the same digital device. This guarantees perfect phase stability in the pairs of output channels with the same frequency, needed for the condition of equation 6.6.

The radiofrequency source is a custom-made source developed in our group ([22, 254]). It is referenced to a 500MHz clock and has the possibility to set frequencies in the 0 – 200MHz range and a 14 bit precision of the phase of $2\pi/2^{14} = 3.8 \cdot 10^{-4}$ rad on four independent output channels.

The EOMs are temperature stabilized with a Peltier element, because the resonance frequency is temperature dependent. The stabilization is thus necessary for both keeping the modulation amplitude constant (and hence also the lattice depth) and for not picking up additional phases due to the mismatch in the resonance condition of the EOM (and hence keeping the lattice geometry constant). We indeed observe that the modulation phase depends slightly on the modulation amplitude.

Similarly, the position of the lattice drifts with a velocity which depends on the relative error of the frequency sources; we note that here the requirement on the precision is much less strict since even errors on the order of 1Hz would just displace the lattice less than about a lattice site over 1s, which is typically much longer than the experimental time-scale. In practice we observed no drift for a hold time in the lattice of up to 6s (measured by magnifying the density distribution of a deep triangular lattice and considering fluctuations of the center of mass of the atoms with respect to the center of the magnetic trap).

6.2.1. Calibration of the Geometry Phase φ_g

We want now to know which geometry phase φ_g we get as a function of the phases $\varphi_{a,b,c}$ that we set on the EOM modulation frequencies. While we expect a simple dependence in a linear form:

$$\varphi_g = \varphi_a + \varphi_b - \varphi_c + C. \quad (6.7)$$

the exact value of the phase shift constant C might be difficult to predict because of radiofrequency delays in the setup, or (relative) phases that the light might pick up while travelling in the optical fibers.

In order to measure this factor (or, to "calibrate the phase"), we found an effective method to get quickly an idea on the whereabouts of the shift; we present this protocol because it also suggests the possibility of geometric effects in momentum space and is nicely explained using gauge field theories. Notice that effects of the geometry on the momentum distribution after time-of-flight have been studied in [255, 256].

The experimental protocol is quite simple: we load a BEC into a asymmetric lattice with $V_2 \sim V_3 \sim 0.5V_1$, and measure the atomic density after time-of-flight. As a result of the symmetry breaking, the intensity of the Bragg peaks is not three-fold symmetric anymore, and the Bragg peaks corresponding to the \mathbf{b}_1 reciprocal wavevector are more pronounced than the others.

Interestingly, the relative population of the atoms in the Bragg peaks corresponding to the \mathbf{b}_1 reciprocal wavevector depends on φ_g , and it has a maximum around $\varphi_g = 0$ (figure 6.6).

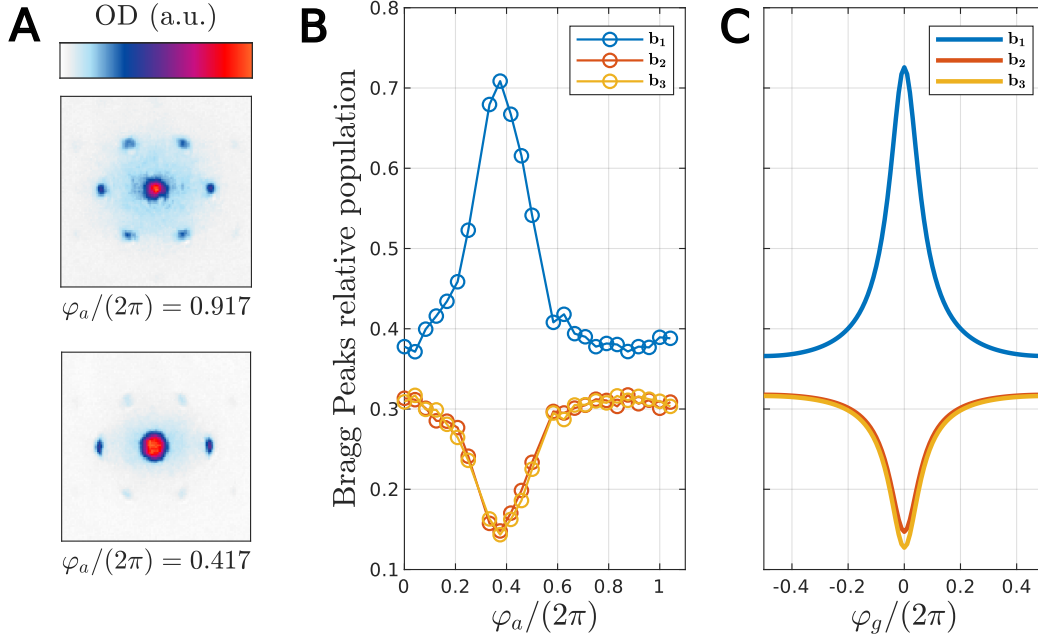


Figure 6.6.: Bragg peaks intensities dependence on the phase. In **A**, time-of-flight images for two different values of φ_g , which evidence a different momentum distribution. In **B**, the dependence of the relative populations of the Bragg peaks correspondent to the 3 reciprocal lattice wavevectors is shown. The relative population corresponding to wavevector \mathbf{b}_1 exhibits a clear maximum. In **C**, theory prediction for $V_2 \simeq V_3 = 0.5 \cdot V_1$, $V_1 = 2.13 E_r$ is shown.

An intuitive picture for explaining this phenomenon can be found by looking in momentum space, and by noticing that the geometry phase has a direct link to the staggered magnetic flux Φ in the reciprocal lattice as:

$$\Phi = \pi + \varphi_g \quad (6.8)$$

The derivation of equation 6.8 is presented in Appendix C.2.

The asymmetry in the lattice depths (interpreted as the coupling terms between different momenta in reciprocal space, as introduced in chapter 2) would tend to populate more in the ground state of the lattice the momenta with wavevectors $\mathbf{Q} = \pm \mathbf{b}_1$, but when $\varphi_g \sim \pi \rightarrow \Phi \sim 0$, the energy is sunk by delocalization over the different momenta, and as a result states with wavevectors $\pm \mathbf{q}_{1,2,3}$ possess similar populations. Instead, if $\varphi_g \sim 0 \rightarrow \Phi \sim \pi$, the system is frustrated and delocalization over momenta $\mathbf{Q} = \pm \mathbf{b}_{2,3}$ is no more convenient energetically. As a result, momenta $\mathbf{Q} = \pm \mathbf{b}_1$ are much more populated.

This measurement also provides the insight that a honeycomb lattice is best for calibration of the lattice balance between different lattice beams, made by maximizing 60° rotational symmetry of time-of-flight pictures as a function of the lattice beam intensities.

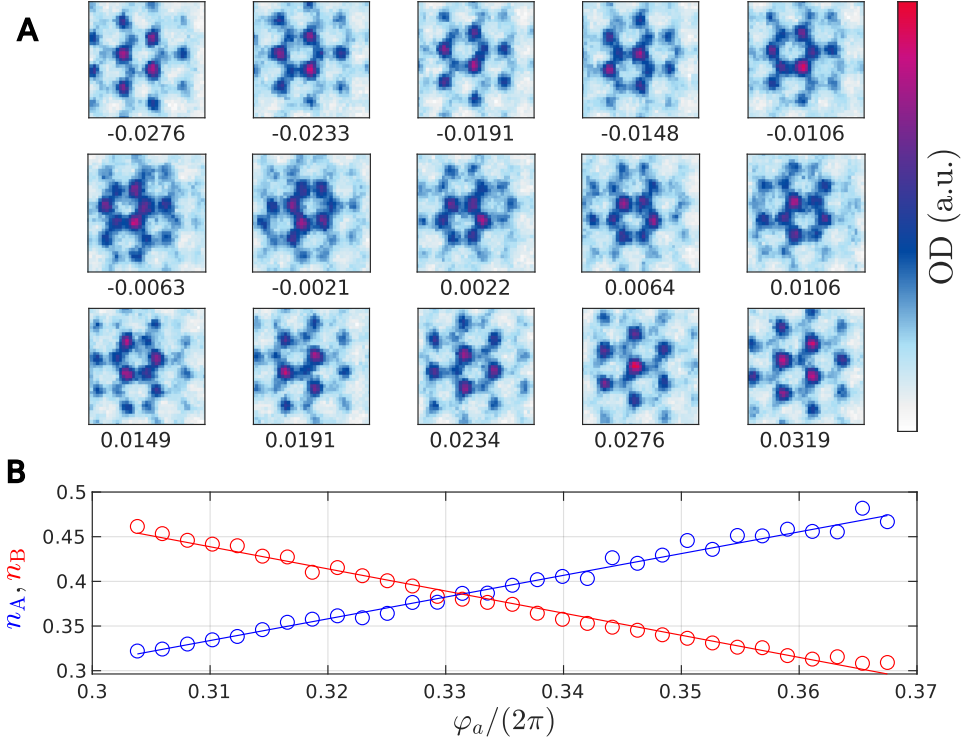


Figure 6.7.: 'In Situ' density distributions for different values of φ_g . In **A** the density distributions for a given values of $(\varphi_a - \varphi_a^{\text{hc}})/(2\pi)$ are shown. φ_a^{hc} is defined as the phase that has to be set by the modulation frequency ν_a assuming $\varphi_{b,c} = 0, \pi$ to get a honeycomb lattice with sublattice offset $\Delta = 0$. φ_a^{hc} is obtained from the fit in **B**. When φ_g changes sign, so does the offset; as a result the atoms populate then mostly the sublattice with lower energy. For values of $\varphi_g \sim 0$ an almost equal populations of the two sublattices is to be observed. The relative populations $n_{A,B}$ can be directly extracted by summing the signal around the corresponding lattice sites, and normalizing to the total atom number. In **B**, n_A and n_B are plotted as a function of φ_a . They can be well fitted by a linear function. From the intersection between the two linear fits one gets a really precise calibration of the geometry phase with an uncertainty below $0.001 \cdot 2\pi$.

Once we locate the region where $\varphi_g \sim 0$, we proceed with a finer calibration, which is then performed with spectroscopy techniques, as illustrated in section 6.3, or directly in real space, by looking at the density distribution of the atoms in the lattice and measuring the relative occupation of the two sublattices (as described in fig. 6.7).

The complete calibration of the lattice is achieved by typically balancing the 1D lattice depths from time-of-flight images from perfect honeycomb lattices or using diffraction from the lattices (Kapitza Dirac scattering) and/or using spectroscopy techniques to calibrate the global lattice depth.

6.2.2. Phase Drifts in Time and Space

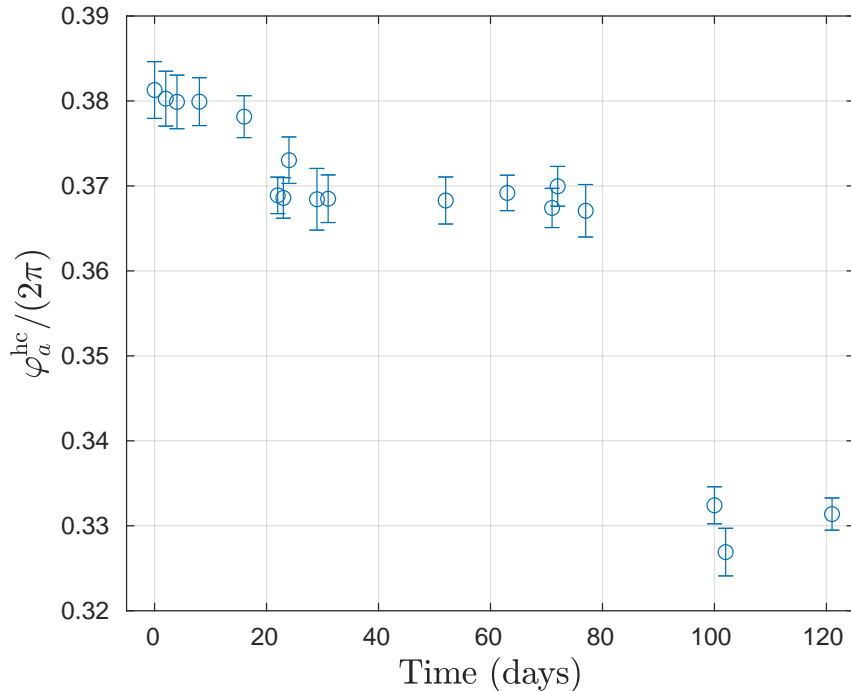


Figure 6.8.: φ_a^{hc} Drifts. Plotted are the φ_a^{hc} calibration results (errors included) with the method described in the previous section, over a period of about four months. We have the impression these drifts could be described by "plateau" periods separated by "jumps", but we could not pinpoint a particular change in the lab conditions which directly correlates with this time dependence.

We found that φ_a^{hc} is not constant in time, but it has fluctuations on a timescale of several days, as illustrated in figure 6.8, which might be at times a little bit annoying, but is not problematic for measurements. We tried to identify factors which could cause a shift in time of this calibration, but could not correlate these fluctuations with variations of other parameters in the setup or in the laboratory. At the same time, we observed that when replacing the radio-frequency source device the phase jumped to another value, so actually it might be somehow related to the radio-frequency part of the setup. We could also speculate that a slow change in the temperature stabilization system would result in phase drifts, but were so far not successful in pinpointing the exact cause of such a change.

For the sake of this work, we were content to see that the phase is stable enough on the timescale of several days. This is of relevance when doing experiments with the honeycomb lattice where the possibility to set exactly $\Delta = 0$ is important, and pretty much negligible for the triangular lattice.

We now turn to the spatial variations of the geometry: we take into considerations the small differences in wavevector that the 1D lattices have (because of the slightly different light frequencies), which cause the condition $\sum_i \mathbf{b}_i = 0$ not be valid anymore making thus φ effectively space-dependent (compare with the definition of φ_g in 6.3):

$$|\mathbf{b}_i| = \frac{1}{c}(\nu_a + \delta\nu_i) \quad (6.9)$$

where $\delta\nu_1 = 0$, $\delta\nu_2 = \nu_\beta$, $\delta\nu_3 = \nu_\gamma$; this implies that φ_g has a spatial dependence described by:

$$\varphi_g(\mathbf{r}) = \varphi_g(\mathbf{0}) + \sum_i \mathbf{b}_i \cdot \mathbf{r} = \varphi_g(\mathbf{0}) + \mathbf{B} \cdot \mathbf{r} \quad (6.10)$$

with the wavevector \mathbf{B} having amplitude $|\mathbf{B}| \sim 0.33 \text{rad/m}$. This corresponds in our case, to a (very small) phase drift of about $3 \cdot 10^{-4} \text{rad}$ in a region of 1mm size, which is much bigger than the lattice size itself. This effect can therefore be neglected. We notice that choosing frequency differences between different 1D lattices in the $\sim 10 - 100 \text{GHz}$ regime one could realize a bigger spatial change of the geometry, which could allow e.g. to realize an interface between areas of different topology ([168]).

6.3. Spectroscopy via Offset Modulation

As we have seen in chapter 3, the choice of the perturbation operator is of great importance for spectroscopy measurements. As a first application of the multi-frequency lattice in a dynamical context, we want to modulate Δ , the offset between sublattices of the honeycomb lattice, periodically in time with frequency ω and amplitude Δ_m , around a given value Δ_0 :

$$\Delta(t) = \Delta_0 + \Delta_m \sin(\omega t) \quad (6.11)$$

At first we need to know how Δ depends on φ : we obtain from band structure calculations that Δ has a linear dependence from φ_g , as shown in fig. 6.9. This is in contrast with the dependence of Δ from the polarization angles in a polarization lattice, which is quadratic. Even in a setup with motorized waveplates, changing dynamically the sign of Δ would then be quite challenging.

Thus the knowledge of V and φ gives the possibility to set the desired offset Δ . When varying Δ dynamically, care has to be taken not to couple this modulation to position shifts, if not desired. This is achieved by symmetric modulation of all 1D lattices:

$$\varphi_{a,b}(t) = \varphi_{a,b}(0) + \frac{\Delta_m}{3c} \sin \omega t; \quad \varphi_c(t) = \varphi_c(0) - \frac{\Delta_m}{3c} \sin(\omega t) \quad (6.12)$$

Where c is the coefficient which describe the relation between φ_g and Δ in the linear regime as $\Delta = c\varphi_g$. Notice that the third EOM is modulated with a π phase shift because it produces interference using the opposite sideband (figure 6.3).

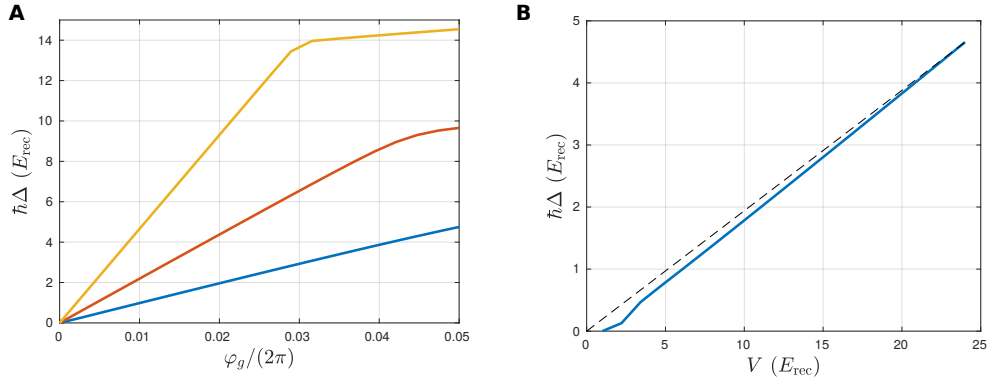


Figure 6.9.: Sublattice offset Δ as a function of φ_g . The three curves of **A** corresponds to lattice depths of $A = 6, 12, 24E_{\text{rec}}$ (blue, red, yellow). Δ is antisymmetric in φ_g , and here only the $\varphi_g > 0$ part is shown. The offset increases linearly until the band gap to the third band closes (see fig. 6.2); at this point the tight binding description with just two sublattices breaks down. Notice that, for deeper lattices, this happens for smaller values of φ_g . This can be understood by noticing that the separation from the first to the third band scales with \sqrt{V} , while Δ (which dictates the separation between the first and the second band) scales in good approximation linearly in A , as can be seen in **B**. There $\varphi_g/(2\pi) = 0.01$ is used. The dashed line is plotted for clarity and evidences the deviation from a (not to be expected) perfectly linear model.

In figure 6.10 we show that this type of modulation couples the first two bands in a honeycomb lattice; this spectroscopy experiment allows obtaining φ_a^0 and V with great precision.

We notice that the EOMs have a finite bandwidth of a few kHz. This means that modulating with too big amplitude Δ_m might result in a change of the modulations index and, as a consequence, of the lattice depth. Therefore, also the tunneling couplings could be modulated as a side-effect.

Spectroscopy in an optical lattice can be done by different methods, which are characterized by a different perturbation operator, like amplitude modulation ([257, 258]) or shaking ([259]). Because the honeycomb/triangular lattice potential can be described by 6 parameters (3 V_i , φ_g and the position in the 2D plane \mathbf{r}), the modulation of φ_g completes the list of possible perturbations which preserve the symmetry of the lattice, the others being spectroscopy via amplitude modulation ([258]) of the 3 independent lattice depths V_i , and lattice shaking ([259]), of which two independent perturbations are e.g. the ones associated with negative and positive shaking chirality.

We mention that there are also plenty of methods which instead break the translational symmetry of the lattice like Bragg spectroscopy ([236, 237]), Raman spectroscopy, phasonic spectroscopy (obtained by modulation of an additional incommensurate lattice in [260]), or methods based on internal degrees of freedom like Raman spectroscopy, microwave/radio-frequency spectroscopy.

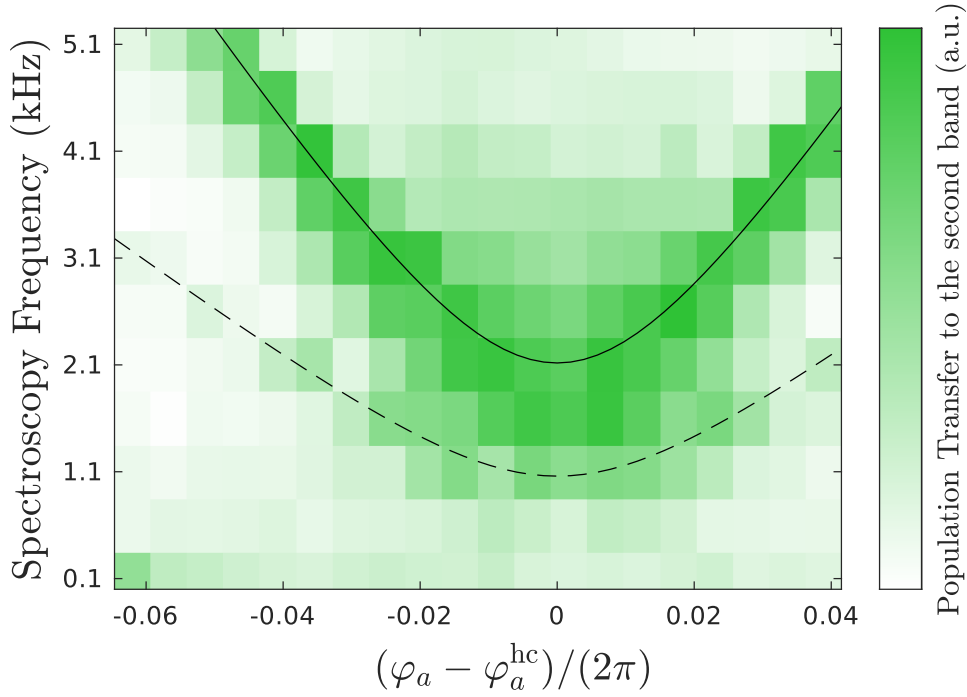


Figure 6.10.: Band Spectroscopy with sublattice offset Δ modulation. Plotted is the signal in the 2^{nd} Brillouin zone after modulation of the offset Δ and subsequent band-mapping, as a function of the spectroscopy frequency and the initial geometry phase φ_g . Experiment performed with ^{87}Rb atoms initially "filling" (not homogeneously) the lowest band. From a fit to the resonance points of the form $E/h = \sqrt{c^2(\varphi_a - \varphi_a^{\text{hc}})^2 + E_0^2}$ we can determine φ_a^{hc} with a precision under 0.01rad. From the value of c (15kHz/rad from the fit) also the lattice depth can be extracted. We plot E/h as obtained from the fit (solid line) and its half value $E/2h$ (dashed line), in correspondence of one- and two-photon transitions, respectively.

The possibility to modulate out out-of-phase the two sublattices opens also possibilities for engineering the dynamical properties of the system (much in analogy to amplitude modulation in resonance with a potential offset, as e.g. in [261, 262]) and thus for more possibilities of quantum simulations with driven quantum gases in optical lattices.

6.4. Generalization to 3D

In 3D, one could have up to 4 laser beams interfering at the same frequency producing a stable lattice geometry (also in this case, phase fluctuations would just imply a shift in space of the lattice structure, without changing the geometry).

The total 3D lattice potential E_{pot}^{3D} can be written as ([247]):

$$E_{\text{pot}}^{3D}(\mathbf{r}) = \sum_{i < j} V_{ij} \cos(\mathbf{b}_{ij} + \varphi_{ij}) \quad (6.13)$$

with $\frac{4(4-1)}{2} = 6$ independent wavevectors $\mathbf{b}_{ij} = \mathbf{k}_i - \mathbf{k}_j$. The corresponding 1D lattices are characterized by intensities V_{ij} and phases φ_{ij} . Beam polarization should be chosen such that orthogonal pairs are avoided, and all beams can interfere with each other.

To create a 3D multi-frequency lattice, then, one would need to create each 1D lattice with interference from radio-frequency modulation. Because there are now 6 phases (each for every 1D lattice) and 3 parameters associated with spatial shifts (because of the three dimensions), the geometry is then described by $6 - 3 = 3$ phase parameters, in addition to the V_{ij} , becoming much more richer than in 2D.

Phase calibration of this setup could be done as follows: by removing one of the 4 beams, one is left with a 2D lattice, whose phase can be calibrated as demonstrated in this chapter. Calibration of three (of the possible four) 2D lattices yields then complete knowledge over the system geometry.

A simple sketch of a possible 3D realization of the multi-frequency lattice is presented in fig. 6.11. Although this proposal is not fully developed yet, it serves as a proof-of-principle that there is no fundamental limitation as to why this scheme couldn't be extended to 3 dimensions.

The combination of being able to set and dynamically manipulate complex 3D potentials, united with the possibility to image the (integrated) density distribution of 3D systems would open really interesting new avenues for quantum simulations of 3D solid state systems, in particular of complex non-separable potentials, which might be challenging to realize with polarization control. A fundamental interest in increasing the dimensionality is provided e.g. by the greater variety of topological phenomena, e.g. conducting hinge states in higher-order topological insulators ([135, 263]), or those present in Weyl semimetals ([264, 265]).

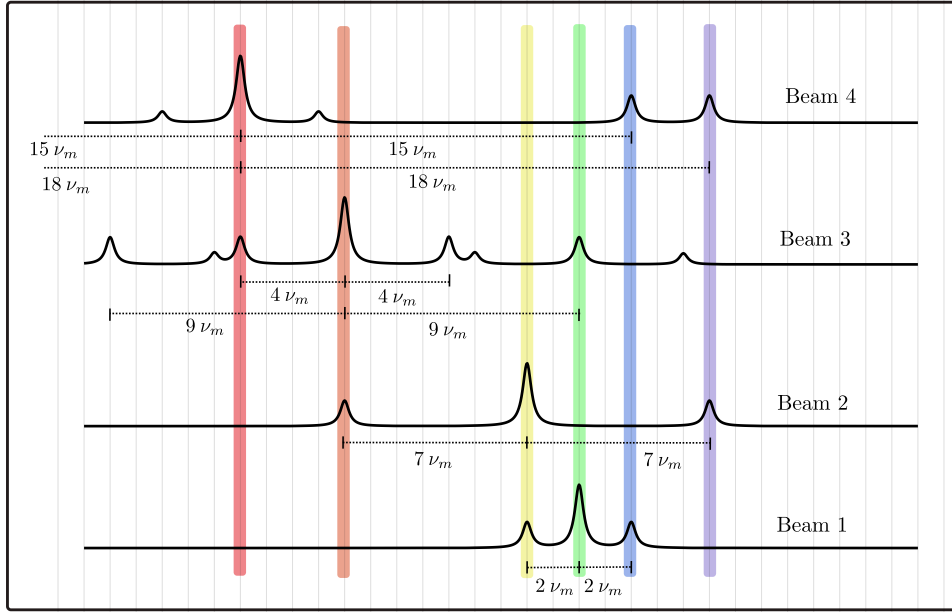


Figure 6.11.: Possible modulation Spectra for a 3D multi-frequency lattice.

Beam 1 (going from bottom to top) is modulated with frequency $2\nu_m$, beam 2 with frequency $7\nu_m$, where ν_m is the fundamental running wave frequency; the grid spacing is also in units of ν_m . Beam 3 is modulated with two EOMs, one at frequency $9\nu_m$, the other at frequency $4\nu_m$. The spectrum now possesses much more frequency components, of which only the ones with relative intensity at least equal to $J_1(n)^4 \sim 0.05$ (with modulation index $n = 1.08$) are shown. Beam 4 is also modulated with two EOMs, one at frequency $15\nu_m$, the other at frequency $18\nu_m$. Every beam pair shares only one frequency component. This corresponds to a 1D lattice whose phase can be set by controlling the modulation phase of the corresponding EOM. Notice that the frequency at which the lattice with indices $ij = 1, 4$ ($2, 4$) runs is produced in both beams as a modulation sideband; since the phase of the EOM in beam 1(2) determines also the phase of the lattice with indices $1, 2$ ($2, 3$) the modulation phase of the EOM in beam 4 has to be used to set the corresponding lattice phase, taking into account the modulation phase in beam 1(2). The upper two spectra are scaled up a factor of 2 for clarity.

Interestingly, the non-linear photogalvanic effect ([266]) is predicted to be quantized in some materials including Weyl semimetals ([267]), and [268] evidenced the relation between this quantization and the one of quantized circular dichroism, and proposed the latter as a possible probe mechanism. This possible implementation of a highly tunable 3D lattice presented here suggests then a possible convergence of the results presented in chapters 3, 4 and 6, and is therefore a nice way to approach the conclusions of the last chapter of this work.

6.5. Conclusions

We implemented a new optical lattice setup with full dynamical control of the geometry, from triangular lattice to boron-nitride with controllable offset between the two sublattices. We demonstrated how to calibrate the geometry of such a lattice and characterized the stability of this setup. In particular, we tested the stability by reproducing some of the data presented in the previous chapters, without noticing a decrease in the lifetime. The geometry change could be directly seen in the real-space density distributions of the atoms in the lattice, with the use of the imaging technique introduced in chapter 4. We also demonstrated the realization of a new type of spectroscopy, where the local potential energies of the two sublattices in a honeycomb geometry are modulated out-of-phase with respect to each other.

This setup will be useful for studying physical effects in different geometries within the same setup. The higher tunability could be used e.g. for a measurement of heating in driven systems as a function of the geometry for determination of the parameters maximizing the lifetime in Floquet system.

The possibility of inverting the offset in the honeycomb lattice would allow selective population of higher bands ([186, 187]). This would be particularly interesting also in combination with the possibility of imaging the corresponding orbitals using quantum gas magnification.

The state tomography scheme ([66]) demonstrated in [33] requires quenching the offset Δ . This could be done naturally with the multi-frequency lattice decoupling the offset characterizing the physical system under study from the offset used during the tomography.

Complete dynamical control over the geometry would also allow for richer Floquet drive protocols e.g. for the creation of new topological phases, in combination with already established techniques like lattice shaking ([9, 11, 33]) and amplitude modulation ([77]).

7. Conclusions

This thesis focused on the issues of measuring and controlling optical lattice systems for quantum simulation. Different systems were taken into consideration: in chapter 3 we considered spin-polarized fermions in a Floquet band. We demonstrated experimentally that the topology of the system (given by the Chern number) could be extracted via a spectroscopy measurement. The topological system breaks time-reversal symmetry and hence reacted differently to circularly polarized spectroscopy probes with different chiralities; the excitations were measured after a band-mapping procedure. This difference in the response between positive and negative chirality (circular dichroism) is quantized in terms of the Chern number and hence allows its detection. With this type of spectroscopy, also the imaginary part of the transverse conductivity and the Wannier spread functional could be measured, without direct access to the real space distribution of the atoms. This measurements could be in the future performed also with interacting systems (e.g. fractional quantum Hall states), and be used as a way of probing topology in novel systems.

In chapter 4, a new method for accessing the real space distribution of the atoms in the lattice system was presented. This technique, named "quantum gas magnification", consists in a matter-wave protocol which, as the name suggests, magnifies the density distribution, which can be then imaged with higher resolution. We presented theoretical considerations and experimental results. The magnification allowed to get single-shot images of the distribution in the lattice with sub-lattice resolution, even to the point that the dynamics within a single lattice site following a quench of the lattice geometry could be resolved. We also demonstrated the measurement of the temperature obtained from the spatial distribution of non-condensed atoms in the lattice, and the possibility to use radio-frequency techniques to shape the density distribution at the single-site level which could be used for creating out-of-equilibrium systems. Also, we discovered a surprising dynamics in the lattice upon application of a constant force, which sets a correlated pair tunneling to be the relevant dynamical process.

Quantum gas magnification promises to be quite a versatile technique, which could be applied in a variety of different contexts. It could be e.g. combined with single-atom fluorescence imaging for studying strongly correlated systems. Magnification via optical potentials could be applied to spin systems, in particular to system with atoms in more than two internal states for which no microscopy technique exists yet, and the spin-resolved detection could be done in combination with a Stern-Gerlach separation.

Increasing further the magnification could allow to obtain information not only on the relative population of single lattice sites but also on the relative population of different orbitals within the site.

In chapter 5 it was investigated how quantum gas magnification could be used to access the coherence properties of lattice systems with high resolution. We introduced a theoretical model for the mapping of the Talbot effect in a trapped system to a system without confinement, and presented some preliminary results showing direct imaging of the Talbot effect with matter-waves. We also proposed a protocol for measuring the single-particle density matrix with the use of quantum gas magnification.

In chapter 6 a new setup for the realization of optical lattices with tunable geometry was presented and results were shown. It was demonstrated how the geometry can be tuned among a variety of lattice geometries also in a dynamical fashion, which allowed e.g. the modulation of the sublattice offset in a honeycomb lattice. We also presented a scheme for the generalization to completely tunable 3D lattice. Further research could be done in the direction of investigating the much bigger parameter space to find particularly interesting geometries.

7.1. Outlook

New future research directions could be given by the combination of results presented in different chapters of this thesis: e.g. circular dichroism could be studied in real space, after mapping the Floquet bands to static bands corresponding to different sublattices, which can be distinguished with quantum gas magnification. This would allow a space-resolved measurement of topology which could be of interest in a system featuring an interface between parts of the systems with different topology.

Quantum gas magnification could also be used for detecting coherence properties of topological systems, as suggested in chapter 5.

New Floquet systems could be produced using the dynamical change of the geometry allowed by the multi-frequency lattice. Not only the lattice potential could be varied in time but also e.g. the correlated pair tunneling (by e.g. rotating the force used to make it the dominant process). A way for probing novel topological states could then be provided by circular dichroism.

The effect of correlated tunneling could be studied in other geometries, including the honeycomb lattice where the interplay between the pair tunneling and the internal lattice structure might result in a different dynamics, or in a non-separable 3D lattice.

Other scenarios include adding new ingredients to the ones presented in this work: they might be e.g. steeper potentials for engineering topological interfaces, on which edge currents are localized or the use of more complex lattice structures (like the double-wavelength Kagome lattice). Both systems could be imaged with quantum gas magnification. Another possibility is to change the statistics of the particles (repeating with ^{40}K the experiments performed with ^{87}Rb , and vice versa, or with a mixture of both).

These ideas are probably just a fraction of what is possible with such systems, and making predictions can be quite difficult. Another route for discovering new physics is, in conclusion, provided often just by asking oneself: "What happens if...?", in particular with the possibility to find the answer with a direct look into the system with a matter-wave lens, as already happened to us many times.

Appendix A.

Density of states for precision thermometry

We want to derive a description for the density of states for the system used during the precision thermometry experiment reported in section 4.3.

Because the degrees of freedom in the z-direction can be decoupled from the others, we consider first the case of a perfect $2D$ system characterized by an optical lattice of depth $1E_{\text{rec}}$ and a harmonic trap potential of strength $\omega_{\text{sys}}/(2\pi) = 305\text{Hz}$.

We derive an analytical expression for the density of states with the aid of an exact diagonalization of a $2D$ system of size $9.6\mu\text{m}\times 9.6\mu\text{m}$, with a triangular lattice potential of depth $V = 1E_{\text{rec}}$.

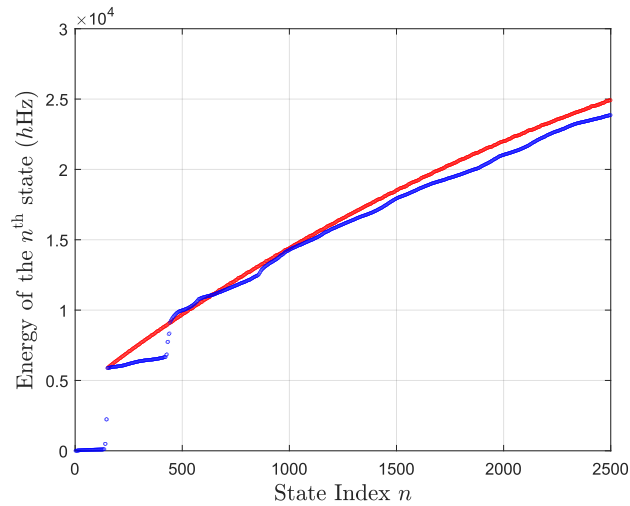


Figure A.1.: Energy as a function of the state number in absence of the harmonic confinement. Blue is the energy of the n^{th} state as a function of n , as obtained by exact diagonalization of a $2D$ system for a $V = 1E_r$ deep optical lattice, and without external harmonic confinement $\omega_{\text{sys}} = 0$. In red, the same quantity but also in absence of the lattice $V = 0$, shifted in both axis in order to start from the first blue point after the first band gap. The curvature of both curves comes from the finite size of system.

We sort the states according to their energies and label them with the index n . In figure A.1 we compare how their energies grow as a function of n with and without the optical lattice potential, in absence of the trap ($\omega_{\text{sys}} = 0$). We can clearly identify the opening of only two band-gaps due to the lattice, and find that after the first band gap the energy behaviour is well captured also without taking the lattice into account.

Also in presence of the trap we distinguish then states that are bound in the lattice from states that do not feel its presence. We model then $n^{3D}(E)$ of the 3D system as such:

$$n^{3D}(E) = n_s(E) + n_{\text{trap}}(E - \delta_g) \quad (\text{A.1})$$

where $n_s(E)$ refers to the states corresponding to the s -orbitals of the lattice and scales like $n_s(e) = (E/E_0)^2$, with $E_0 = \sqrt{\hbar A_{WS} m \bar{\omega}_{\text{sys}}^3 / \pi} = h \cdot 57 \text{Hz}$, where A_{WS} is the area of the Wigner-Seitz cell, m is the particles mass and $\bar{\omega}_{\text{sys}}$ the geometrical average of the trap frequency in the three directions (this result can be gotten by counting how many in-plane localized states have total energy less than E). The z -direction is taken into account both in the analytical model and in the numerics by assuming the spectrum in this degree of freedom is described by $n_z \omega_z$, with $n_z \geq 0$ integer.

$n_{\text{trap}}(E - \delta_g)$ is the number of states up to energy $E - \delta_g$, for $E - \delta_g > 0$, in a 3D harmonic trap: $n_{\text{trap}}(E - \delta_g) = \frac{1}{6} \left(\frac{E - \delta_g}{\hbar \bar{\omega}_{\text{sys}}} \right)^3$. The shift factor $-\delta_g$ is added such that these state start to appear at energies above the band gap δ_g .

The analytical model for n^{3D} agrees with the numerics (figure A.2), and allows to extrapolate the behaviour of the density of states also to higher energies.

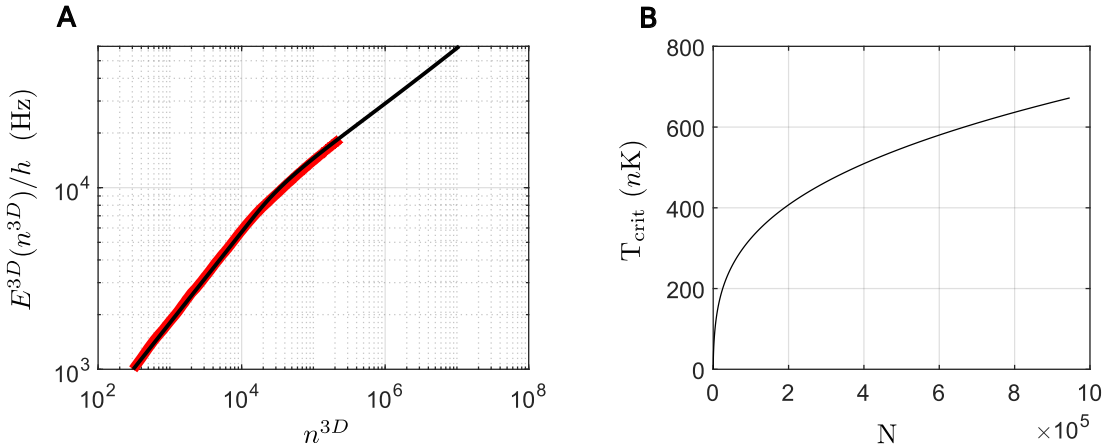


Figure A.2.: Determination of the critical temperature. In **A**, $E^{3D}(n^{3D})$ is plotted, in red as obtained by exact diagonalization, in black the analytical approximation (adapted from [13]). This allows to obtain the critical temperature as a function of the atom number, as plotted in **B**. Notice that while the biggest measured atom number was about $3 \cdot 10^5$ it is important to describe correctly also states with index $n^{3D} \sim 10^6$ or more which also become populated by higher temperatures.

This description for the density of states might look a little bit complex, because we are not in a well defined regime; but this brings with it also fascinating aspects: for example, from this we can suppose that the coherence in the ground state is interaction induced ([184, 269]): the single-particle eigenstates are completely localized, but because of interactions, atoms in the BEC tend to delocalize over several lattice sites maintaining phase coherence, as detected in time of flight (4.10). More often, instead, coherence is destroyed by interactions ([6]).

Appendix B.

Quantum Gas Magnification in the Schrödinger Representation

In this appendix we provide the derivation for the quantum gas magnification and the focusing condition in the Schrödinger picture, adapting a calculation presented already in [164]. We add then also some general remarks.

The Schrödinger picture is completely equivalent to that of Heisenberg, but it is useful because it describes the evolution of the quantum field operators illustrating that the matter wave optics also reproduces quantum correlations. This possibility will allow for future fundamental studies in single-atom resolved regimes with the quantum gas magnifier.

We make use of the generating function G of the Hermite polynomials $h_n(x)$ given by

$$G(x, g) = e^{-\frac{1}{2}x^2 + 2xg - g^2} = \sum_n e^{-\frac{1}{2}x^2} h_n(x) \frac{g^n}{n!}. \quad (\text{B.1})$$

Using the operator $\hat{O}_n = (\partial g)^n|_{g=0}$, one gets

$$\hat{O}_n G(x, g) = e^{-\frac{1}{2}x^2} h_n(x) = \psi_n(x) \quad (\text{B.2})$$

with $\psi_n(x)$ being the n^{th} eigenstate of the $1D$ harmonic oscillator and with x being the spatial coordinate in natural units. Up to a global phase (i.e. which does not depend on n), the time evolution in the harmonic oscillator $U(t_{\text{ho}})$ can be described by

$$U(t_{\text{ho}})G(x, g) = G(x, ge^{-i\omega t_{\text{ho}}}) \quad (\text{B.3})$$

which is proven by checking that ψ_n picks up a phase

$$\phi_{\text{ho},n} = -n\omega t_{\text{ho}}:$$

$$U(t_{\text{ho}})\psi_n(x) = \hat{O}_n G(x, ge^{-i\omega t_{\text{ho}}}) = \psi_n(x)e^{-in\omega t_{\text{ho}}}. \quad (\text{B.4})$$

The time of flight evolution $U(t_{\text{tof}})$ of G can be described by

$$U(t_{\text{tof}})G(x, g) = F^{-1}(\sqrt{2\pi} \int dx' e^{-\frac{1}{2}x'^2 + 2x'g - g^2} e^{ikx' - ik^2 \frac{T}{2}}) \quad (\text{B.5})$$

with $T = \omega t_{\text{tof}}$ and F^{-1} being the inverse Fourier Transform operator. It follows:

$$\begin{aligned}
& F^{-1}\left(\sqrt{2\pi} \int dx' e^{-\frac{1}{2}(x'-2g-ik)^2 - \frac{1}{2}k^2 - ik^2\frac{T}{2} + 2ikg + g^2}\right) \\
&= F^{-1}\left(e^{-\frac{1}{2}k^2 + g^2 - ik^2\frac{T}{2} + 2ikg}\right) \\
&= \sqrt{2\pi} \int dk e^{-\frac{1}{2}\left(k^2 D - \frac{2ig}{\sqrt{D}} + \frac{ix}{\sqrt{D}}\right)^2 + g^2 + \frac{1}{2D}(-4g^2 - x^2 + 4xg)}
\end{aligned} \tag{B.6}$$

with $D = 1 + iT$. One gets, recalling $M = \sqrt{1 + T^2}$:

$$\begin{aligned}
&= \frac{1}{\sqrt{D}} e^{-\frac{x^2}{2D} + \frac{2xg}{D} + g^2(1 - \frac{2}{D})} \\
&= \frac{1}{\sqrt{D}} e^{\frac{x^2}{2} \frac{iT}{1+T^2}} e^{-\frac{x^2}{2} \frac{1}{1+T^2} + \frac{2xg}{1+iT} - \frac{1-iT}{1+iT} g^2} \\
&= \frac{1}{\sqrt{M}} e^{-i\frac{\arctan(T)}{2} + \frac{iT}{2}\left(\frac{x}{M}\right)^2} G\left(\frac{x}{M}, g \cdot e^{-i\arctan(T)}\right)
\end{aligned} \tag{B.7}$$

It follows:

$$\begin{aligned}
U(t_{\text{tof}})\psi_n(x) &= \hat{O}_n U(t_{\text{tof}})G(x, g) \\
&= \frac{1}{\sqrt{M}} e^{-i\frac{\arctan(T)}{2} + \frac{iT}{2}\left(\frac{x}{M}\right)^2} \psi_n\left(\frac{x}{M}\right) e^{-in\arctan(T)}
\end{aligned} \tag{B.8}$$

One gets a normalization factor $\frac{1}{\sqrt{M}}$ and a n -independent phase $e^{i\phi(x,T)} = e^{-i\frac{\arctan(T)}{2} + \frac{iT}{2}\left(\frac{x}{M}\right)^2}$. During time of flight, ψ_n gets magnified by a factor M and picks up a phase $\phi_{\text{tof},n} = -n \cdot \arctan(T)$. The total time evolution of a generic wavefunction $\psi(x) = \sum_n c_n \psi_n(x)$ during the magnification protocol is then:

$$U(t_{\text{tof}})U(t_{\text{ho}})\psi(x) = \frac{1}{\sqrt{M}} e^{i\phi(x,T)} \sum_n c_n \psi_n\left(\frac{x}{M}\right) e^{i\phi_n} \tag{B.9}$$

and the focusing condition equation (4.10) for the magnified imaging can then be obtained by requiring that

$$\phi_n = \phi_{\text{ho},n} + \phi_{\text{tof},n} = -n \cdot [\omega t_{\text{ho}} + \arctan(\omega t_{\text{tof}})] = -n \cdot \pi \tag{B.10}$$

As a consequence, the terms in the superposition with n even (odd), corresponding to states $\psi_n(x)$ symmetric (antisymmetric) with respect to $x = 0$, pick up a phase 0 (π), as if under the action of the parity operator $P\psi(x) = \psi(-x)$; for this reason the distribution is inverted. The phase factor $e^{\frac{iTx^2}{2M^2}}$ means that although density correlations $g_2(r)$ are reproduced via the scaling $g_2(r') = g_2(M \cdot r)$, phase correlations $g_1(r)$ have to be treated with care. This comes from the fact that the protocol presented here simply rescales the real space positions, but not the momentum operator.

B.1. General Remarks

In general, this comparison between the two representations evidences how the working of the magnifier in the Heisenberg's one is much simpler to derive, probably because this representation is more connected with the measurement process itself (the operators are the dynamical variables) than the object of the measurement (the wavefunction, on which no assumption are made). On the other hand, in cases where the wavefunction is important (e.g. when calculating the evolution in presence of interactions) the Schrödinger representation could be better suited.

In the Heisenberg representation, quantum gas magnification can be condensed in the formula:

$$X(t_f) = \pm M X(t_i) \quad (\text{B.11})$$

Where t_i and t_f are the initial and final time of the evolution. As a last remark, we note that X might be generalized to any continuous operator, provided one finds an evolution such that equation B.11 is realized.

Also the "Fourier space" stage might be not necessary (unavoidable in conventional "light" optics and in the matter-wave schemes presented or mentioned in this work), if one could e.g. engineer an Hamiltonian of the form:

$$H = XP + PX; \quad [X, P] = i \quad (\text{B.12})$$

Where X, P are now generic Hermitian operators which satisfy the above commutation relation. Then one gets:

$$\partial_t X = i[H, X] = 2X \rightarrow X(t_i + t) = e^{2t} \cdot X(t_i) \quad (\text{B.13})$$

which represents a pure magnification, with $X(t)$ exactly proportional to $X(t_i)$ (or, equivalently, without $P(t_i)$ component), for every time t .

Appendix C.

Band Structure Calculation with Vector Light Shift and for the Multi-Frequency Lattice

C.1. Vector light Shift

The vector light shift causes a different response in different m_F states dependently on the light polarization. This effect has to be taken into account when calculating the geometry of a polarization lattice, because it influences strongly the sublattice offset Δ_{AB} in the honeycomb lattice. This effect is used can be exploited for tuning Δ_{AB} by rotating the quantization field ([244]).

The potential energy E_{pot} associated to different polarization components of a dipole trap or of an optical lattice can be written as ([249]):

$$E_{\text{pot}}(\sigma) \propto \left(1 + \frac{1}{\sqrt{3}}\gamma\sigma\right)I_\sigma \quad (\text{C.1})$$

where σ can take the values 0 for light polarized along the quantization axis or 1(-1) for right(left) circularly polarized light with respect to the quantization axis. I_σ is the light intensity with polarization σ .

γ is calculated as such:

$$\gamma = -\frac{1}{\sqrt{3}}g_F m_F \frac{\Delta_{fs}}{\Delta} \quad (\text{C.2})$$

where g_F is the Landé factor, m_F indicates the Zeeman substate, Δ is the detuning of the lattice frequency with respect to the atomic transition to the excited p state and $h\Delta_{fs}$ is the hyperfine structure splitting in the p state. For the $F = 2$, $m_F = 2$ ground state of ^{87}Rb , and considering light of wavelength $\lambda = 1064\text{nm}$, $\gamma \sim 0.042$. For the $F = 9/2$, $m_F = 9/2$ ground state of ^{40}K , and for the same wavelength, $\gamma \sim 0.016$ (because of the smaller hyperfine splitting).

We consider the 1D lattice with wavevector \mathbf{b}_1 (using the convention presented in chapter 2). The potential form can be obtained by summing the spatial dependent part of the intensities of the different polarization vectors, weighted with the $1 + \frac{1}{\sqrt{3}}\sigma\gamma$ factor:

$$E_{\text{pot}}(\mathbf{r}) \propto - \sum_{\sigma} \left(1 + \frac{1}{\sqrt{3}}\sigma\gamma\right) \left| (\mathbf{e}_2 \cdot \mathbf{p}_{\sigma})^* (\mathbf{e}_3 \cdot \mathbf{p}_{\sigma}) \right| \cos(\mathbf{b}_1 \cdot \mathbf{r} - \theta_{\sigma}) \quad (\text{C.3})$$

where \mathbf{p}_{σ} is the unit polarization vector for σ polarized light, $\mathbf{e}_{2,3}$ are the polarization vectors of beams with indexed 2 and 3 generating the 1D lattice under consideration. and $\theta_{\sigma} = \arg\{ \sum_{\sigma} (\mathbf{e}_2 \cdot \mathbf{p}_{\sigma})^* (\mathbf{e}_3 \cdot \mathbf{p}_{\sigma}) \}$.

We calculate then the coupling elements between plane waves with wavevectors \mathbf{Q} and $\mathbf{Q} + \mathbf{b}_1$ as:

$$\langle \mathbf{Q} + \mathbf{b}_1 | E_{\text{pot}}(\mathbf{r}) | \mathbf{Q} \rangle = \frac{V^0}{\mathbf{e}_2^* \cdot \mathbf{e}_3} \sum_{\sigma} \left(1 + \frac{1}{\sqrt{3}}\sigma\gamma\right) (\mathbf{e}_2 \cdot \mathbf{p}_{\sigma})^* (\mathbf{e}_3 \cdot \mathbf{p}_{\sigma}) \quad (\text{C.4})$$

where V^0 is the coupling matrix element for the $m_F = 0$ state (to prove this, $\sum_{\sigma} (\mathbf{e}_2 \cdot \mathbf{p}_{\sigma})^* (\mathbf{e}_3 \cdot \mathbf{p}_{\sigma}) = \mathbf{e}_2^* \cdot \mathbf{e}_3$ must be noticed). The same results hold for the other 2D lattices. Notice that we don't need to use the exact factor which relates the lattice depth with the light intensity, which can not be measured at the position of the atoms. Instead, the lattice depth is directly obtained by calibration of the 1D lattices.

We show how the vector light shift can influence the geometric phase in the case where the quantization field points in the z -direction and the three lattice beams with equal intensity of the 2D hexagonal lattice are in-plane polarized. In that case the polarization vectors can be decomposed as a sum of left and right circularly polarized light (with respect to the quantization axis). We provide the expression for the spatial dependent part of the $\sigma = \pm 1$ polarized light which is given by:

$$I_{\sigma} = - |I_0| \sum_i [\cos(\mathbf{b}_i \cdot \mathbf{r}) + \sqrt{3} \sin(\mathbf{b}_i \cdot \mathbf{r})] \quad (\text{C.5})$$

where I_0 is a reference intensity.

The resulting potential calculated using equation C.3 is given by:

$$\begin{aligned} E_{\text{pot}}(\mathbf{r}) &= V^0 [\cos(\mathbf{b}_i \cdot \mathbf{r}) + \gamma \sin(\mathbf{b}_i \cdot \mathbf{r})] \\ &= V^0 \sqrt{1 + \gamma^2} \sum_i \cos(\mathbf{b}_i \cdot \mathbf{r} + \arctan(\gamma)) \end{aligned} \quad (\text{C.6})$$

From this expression it can be seen that the lattice depth is only minimally influenced when considering the vector light shift but that the geometry phase φ_g (introduced in chapter 2 and more studied in chapter 6) becomes:

$$\varphi_g = 3 \arctan(\gamma) = 0.126 \text{rad}. \quad (\text{C.7})$$

This value is calculated for the $m_F = 2$ state of ^{87}Rb . It is not negligible in many experimental situations (compare with the results of chapter 6).

C.2. Multi-Frequency Lattice

When calculating the band structure for the multi-frequency lattice, exact knowledge of the polarization vectors is not required anymore. We obtain the depths $V_{1,2,3}$ of the 1D lattices (usually after Kapitza-Dirac scattering from the 1D lattices). From these measurements, and from the measurement of φ_g as presented in chapter 6, one gets all the parameters needed to describe the geometry for a single m_F state.

Another method is balancing the lattice depths trying to obtain rotational symmetry from time-of-flight measurement from a honeycomb lattice (as presented in chapter 6, at $\varphi_g = 0$ the measurement is most sensitive to beam imbalances), and then get the (global) lattice depth by spectroscopy.

After having determined the experimental parameters V_i , φ_g we can get the off-diagonal couplings in the plane wave basis due to the potential $E_{\text{pot}}(\mathbf{r})$ as:

$$E_{\text{pot}}(\mathbf{r}) = 2 \sum_i V_i \cos(\mathbf{b}_i \cdot \mathbf{r} + \varphi_g/3) \quad (\text{C.8})$$

$$\langle \mathbf{Q} + \mathbf{b}_i | E_{\text{pot}}(\mathbf{r}) | \mathbf{Q} \rangle = V_i e^{-i\varphi_g/3}.$$

All other off-diagonal terms can be gotten by Hermitian conjugation, while the diagonal terms of the Hamiltonian are calculated as:

$$E_{\text{kin}} = \frac{(\hbar \mathbf{Q})^2}{2m}. \quad (\text{C.9})$$

and diagonalization of the Hamiltonian for every quasimomentum one gets the complete band structure and the eigenstates (eigenstates in real space can be simply gotten by Fourier transformation).

Interestingly, this description makes clear that in momentum space a staggered flux Φ is generated. This can be seen by mapping the Hamiltonian for a given quasimomentum \mathbf{q} to a tight-binding triangular lattice with "sites" represented by the plane-waves with wavevectors $\mathbf{Q} = \mathbf{q} + m\mathbf{b}_1 + n\mathbf{b}_2$, with m, n integers. The diagonal terms of the Hamiltonian in this representation $\frac{(\hbar \mathbf{Q})^2}{2m}$ can be interpreted as a harmonic "confinement". As conventionally the tunneling coupling terms between lattice sites α and β in a tight-binding Hamiltonian are written as $-J(a_\alpha^\dagger a_\beta) + \text{h.c.}$ (notice the minus sign; a_α^\dagger , a_β are the creation/annihilation operators for the lattice sites with corresponding indexes), the "tunneling" coupling J_i along the reciprocal lattice vectors \mathbf{b}_i in this mapping to real space is given by $J_i = -V_i e^{-i\varphi_g/3} = |V_i| e^{i(\pi - \varphi_g/3)}$.

It can be seen that a particle picks up a phase $e^{i(\pi - \varphi_g/3)}$ while "tunneling" and as a result a staggered flux per plaquette $\Phi = 3\pi - \varphi_g \equiv \pi - \varphi_g$ is created (as illustrated in figure C.1). The flux has to be staggered because the lattice potential does not break time-reversal symmetry.

This interpretation of the geometry phase as related to a magnetic flux in momentum space suggests then an application of the multi-frequency lattice for generating gauge-fields in momentum space ([270, 271]).

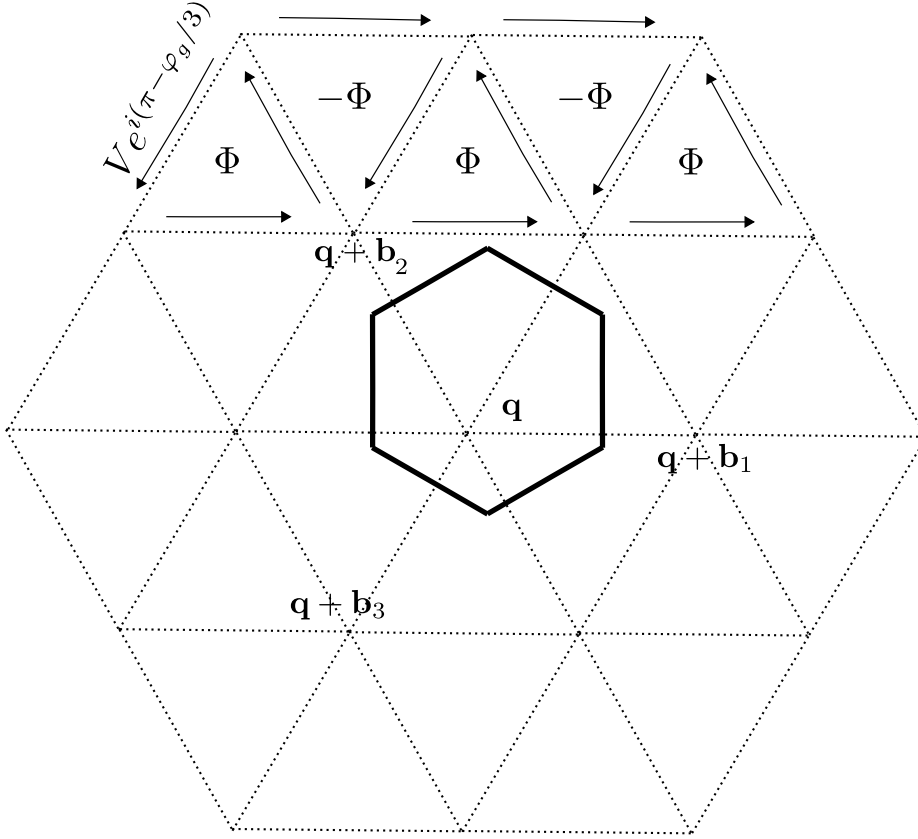


Figure C.1.: Graphical representation of the couplings between plane-waves induced by the lattice.

The band structure is calculated by considering separately each quasimomentum in the Brillouin Zone (solid lines hexagon). For a given quasimomentum \mathbf{q} the Hamiltonian can be mapped to a triangular lattice in momentum space described by the plane-waves with wavevectors $\mathbf{Q} = \mathbf{q} + m\mathbf{b}_1 + n\mathbf{b}_2$, with m, n integers (notice that $\mathbf{b}_3 = -\mathbf{b}_1 - \mathbf{b}_2$). A particle picks up a phase $e^{i(\pi - \varphi_g/3)}$ while "tunneling", as represented by the arrows, and as a result there is a flux per plaquette $\Phi = 3\pi - \varphi_g \equiv \pi - \varphi_g$ which is staggered, with an alternating sign between "up" plaquettes and "down" plaquettes. Notice that Φ does not depend on the quasimomentum \mathbf{q} .

Acknowledgements

I am grateful to many people for having being able to reach the point of submitting my PhD thesis.

I am grateful to Klaus for the possibility to start here, but also for his enthusiasm which is really felt in discussions about ongoing experiments, and for having created such a great environment for research. I am grateful to Christof, for his passion for physics and energy in the daily brainstorming sessions, with a constant flux of ideas while also leaving the space for others to bring their own. It was fun to do research with the two of you, and I am looking forward to future projects.

I am grateful to the "old" generation of the BFM experiment, Matthias, Benno und Nick; I learned a lot from you, and I learned as much from the "new" generation, Henrik und Marcel.

I am grateful to all the people in our group, to all former and present members of the Lithium team, to Juliette and Christoph also (but not only) in representation of the other projects, to the magic tricks of Ortwin and others helping with the vacuum chamber, and to all other persons involved in the group that I have met, and also in general to all the people contributing to the nice atmosphere at ILP/ZOQ. I would also like to thank the theory teams of Nathan and Ludwig.

Thanks to Silvia, Henrik and Marcel for reading part of this manuscript, and Christof for the many comments.

Grazie a Silvia per avermi consigliato di seguire le lezioni di computazione quantistica tenute da Oliver Morsch, e grazie a Oliver e Donatella per tutto quello che ho imparato nel loro lab. Grazie a Rosati che mi ha fatto notare la posizione libera ad Amburgo.

Grazie ai miei genitori, a mia sorella e a mio fratello. Grazie a Gesa, per tutto; and thanks to all the roommates I have had in this period.

Thanks to my family and friends, those who are always there and those who are not there anymore.

Bibliography

- [1] R. P. Feynman: “Simulating physics with computers”, *International Journal of Theoretical Physics* **21** (6), 467–488 (1982). 1, 11
- [2] I. Bloch: “Ultracold quantum gases in optical lattices”, *Nature Physics* **1** (1), 23–30 (2005). 1
- [3] C. Chin, R. Grimm, P. Julienne and E. Tiesinga: “Feshbach resonances in ultracold gases”, *Rev. Mod. Phys.* **82**, 1225–1286 (2010). 1
- [4] W. S. Bakr, A. Peng, M. E. Tai, R. Ma, J. Simon, J. I. Gillen, S. Fölling, L. Pollet and M. Greiner: “Probing the superfluid-to-Mott insulator transition at the single-atom level.”, *Science* **329**, 547–550 (2010). 1, 53, 88
- [5] J. F. Sherson, C. Weitenberg, M. Endres, M. Cheneau, I. Bloch and S. Kuhr: “Single-atom-resolved fluorescence imaging of an atomic Mott insulator.”, *Nature* **467**, 68–72 (2010). 1, 53, 77, 88
- [6] M. Greiner, O. Mandel, T. Esslinger, T. W. Hänsch and I. Bloch: “Quantum phase transition from a superfluid to a Mott insulator in a gas of ultracold atoms”, *Nature* **415** (6867), 39–44 (2002). 1, 98, 139
- [7] M. Aidelsburger, M. Atala, M. Lohse, J. T. Barreiro, B. Paredes and I. Bloch: “Realization of the Hofstadter Hamiltonian with Ultracold Atoms in Optical Lattices”, *Phys. Rev. Lett.* **111**, 185301 (2013). 2, 25
- [8] H. Miyake, G. A. Siviloglou, C. J. Kennedy, W. C. Burton and W. Ketterle: “Realizing the Harper Hamiltonian with Laser-Assisted Tunneling in Optical Lattices”, *Phys. Rev. Lett.* **111**, 185302 (2013). 25
- [9] G. Jotzu, M. Messer, R. Desbuquois, M. Lebrat, T. Uehlinger, D. Greif and T. Esslinger: “Experimental realization of the topological Haldane model with ultracold fermions”, *Nature* **515** (7526), 237–240 (2014). 2, 24, 118, 131
- [10] D. T. Tran, A. Dauphin, A. G. Grushin, P. Zoller and N. Goldman: “Probing topology by “heating”:: Quantized circular dichroism in ultracold atoms”, *Science Advances* **3** (8), e1701207 (2017). 2, 30, 31, 32, 34, 45, 48
- [11] L. Asteria, D. T. Tran, T. Ozawa, M. Tarnowski, B. S. Rem, N. Fläschner, K. Sengstock, N. Goldman and C. Weitenberg: “Measuring quantized circular dichroism in ultracold topological matter”, *Nature Physics* **15** (5), 449–454 (2019). 2, 4, 5, 31, 33, 34, 37, 39, 41, 42, 43, 46, 49, 50, 51, 118, 131

- [12] B. S. Rem, N. Käming, M. Tarnowski, L. Asteria, N. Fläschner, C. Becker, K. Sengstock and C. Weitenberg: “Identifying quantum phase transitions using artificial neural networks on experimental data”, *Nature Physics* **15** (9), 917–920 (2019). 2, 4, 5, 26, 27, 28, 30, 47
- [13] L. Asteria, H. P. Zahn, M. N. Kosch, K. Sengstock and C. Weitenberg: “Quantum gas magnifier for sub-lattice-resolved imaging of 3D quantum systems”, *Nature* **599** (7886), 571–575 (2021). 2, 4, 54, 58, 66, 67, 70, 72, 74, 76, 77, 82, 83, 84, 88, 138
- [14] H. P. Zahn, V. P. Singh, M. N. Kosch, L. Asteria, L. Freystatzky, K. Sengstock, L. Mathey and C. Weitenberg: “Formation of spontaneous density-wave patterns in DC driven lattices”, (2021). 4, 54, 85, 86, 87
- [15] M. Z. Hasan and C. L. Kane: “Colloquium: topological insulators”, *Reviews of Modern Physics* **82** (4), 3045 (2010). 5
- [16] C. Ospelkaus: “Fermi-Bose mixtures - From mean-field interactions to ultracold chemistry ”, Ph.D. thesis, University of Hamburg (2006). 6, 8, 9
- [17] S. Ospelkaus-Schwarzer: “Quantum Degenerate Fermi-Bose Mixtures of ^{40}K and ^{87}Rb in 3D optical lattices”, Ph.D. thesis, University of Hamburg (2006). 6, 11
- [18] P. Ernst: “Bragg Spectroscopy in Optical Lattices and the Physics of Quantum Gas Mixtures”, Ph.D. thesis, University of Hamburg (2009). 6
- [19] J. Heinze: “From Higher Bands to Higher Spins: ultracold Fermions in novel Regimes”, Ph.D. thesis, University of Hamburg (2013).
- [20] S. Krauser: “Coherent Spin Dynamics in Fermionic Quantum Gases: From Two-Body to Many-Body Physics”, Ph.D. thesis, University of Hamburg (2014).
- [21] N. Fläschner: “Ultracold Fermions in Tunable Hexagonal Lattices: from High-precision Spectroscopy to the Measurement of Berry Curvature”, Ph.D. thesis, University of Hamburg (2016). 6, 12, 118
- [22] D. Vogel: “Measuring Geometry and Topology of Floquet-Bloch States in and out of Equilibrium with ultracold Fermions”, Ph.D. thesis, University of Hamburg (2007). 6, 20, 121
- [23] M. Tarnowski: “Implementation and Characterization of a Gray Molasses and of Tunable Hexagonal Optical Lattices for ^{40}K ”, Master thesis, Universität Hamburg (2015). 6
- [24] M. Erhard: “Experimente mit mehrkomponentigen Bose-Einstein-Kondensaten”, Ph.D. thesis, University of Hamburg (2016). 8, 20

- [25] R. Dinter: “Aufbau und Charakterisierung einer Magnetfalle zur simultanen Speicherung von ^{40}K und ^{87}Rb ”, Diploma thesis, Universität Hamburg (2004). 8, 9
- [26] M. Lewenstein, A. Sanpera, V. Ahufinger, B. Damski, A. Sen(De) and U. Sen: “Ultracold atomic gases in optical lattices: mimicking condensed matter physics and beyond”, *Advances in Physics* **56** (2), 243–379 (2007). 11
- [27] C. Gross and I. Bloch: “Quantum simulations with ultracold atoms in optical lattices”, *Science* **357** (6355), 995–1001 (2017). 11
- [28] T. Esslinger: “Fermi-Hubbard Physics with Atoms in an Optical Lattice”, *Annual Review of Condensed Matter Physics* **1** (1), 129–152 (2010). 11
- [29] O. Morsch and M. Oberthaler: “Dynamics of Bose-Einstein condensates in optical lattices”, *Rev. Mod. Phys.* **78**, 179–215 (2006). 11
- [30] S. Ospelkaus, C. Ospelkaus, L. Humbert, K. Sengstock and K. Bongs: “Tuning of Heteronuclear Interactions in a Degenerate Fermi-Bose Mixture”, *Phys. Rev. Lett.* **97**, 120403 (2006). 11
- [31] S. Ospelkaus, C. Ospelkaus, O. Wille, M. Succo, P. Ernst, K. Sengstock and K. Bongs: “Localization of Bosonic Atoms by Fermionic Impurities in a Three-Dimensional Optical Lattice”, *Phys. Rev. Lett.* **96**, 180403 (2006). 11
- [32] C. Becker, P. Soltan-Panahi, J. Kronjäger, S. Dörscher, K. Bongs and K. Sengstock: “Ultracold quantum gases in triangular optical lattices”, *New Journal of Physics* **12** (6), 065025 (2010). 12, 117
- [33] N. Fläschner, B. S. Rem, M. Tarnowski, D. Vogel, D.-S. Lühmann, K. Sengstock and C. Weitenberg: “Experimental reconstruction of the Berry curvature in a Floquet Bloch band”, *Science* **352**, 1091–1094 (2016). 14, 22, 24, 25, 26, 113, 131
- [34] F. Bloch: “Über die Quantenmechanik der Elektronen in Kristallgittern”, *Zeitschrift für Physik* **52** (7), 555–600 (1929). 15
- [35] A. H. Castro Neto, F. Guinea, N. M. R. Peres, K. S. Novoselov and A. K. Geim: “The electronic properties of graphene”, *Rev. Mod. Phys.* **81**, 109–162 (2009). 16
- [36] P. A. Murthy, D. Kedar, T. Lompe, M. Neidig, M. G. Ries, A. N. Wenz, G. Zürn and S. Jochim: “Matter-wave Fourier optics with a strongly interacting two-dimensional Fermi gas”, *Phys. Rev. A* **90**, 043611 (2014). 19, 62, 63, 71
- [37] K. Hueck, N. Luick, L. Sobirey, J. Siegl, T. Lompe and H. Moritz: “Two-Dimensional Homogeneous Fermi Gases”, *Physical Review Letters* **120** (6), 60402 (2018). 19, 62, 63

- [38] G. Condon, A. Fortun, J. Billy and D. Guéry-Odelin: “Phase-space manipulations of many-body wave functions”, *Phys. Rev. A* **90**, 063616 (2014). 20
- [39] T. Kovachy, J. M. Hogan, A. Sugarbaker, S. M. Dickerson, C. A. Donnelly, C. Overstreet and M. A. Kasevich: “Matter wave lensing to picokelvin temperatures”, *Phys. Rev. Lett.* **114**, 143004 (2015).
- [40] L. Dupays, D. C. Spierings, A. M. Steinberg and A. del Campo: “Delta-kick cooling, time-optimal control of scale-invariant dynamics, and shortcuts to adiabaticity assisted by kicks”, *Phys. Rev. Research* **3**, 033261 (2021). 20
- [41] W. Ketterle, D. S. Durfee and D. M. Stamper-Kurn: “Making, probing and understanding Bose-Einstein condensates”, arXiv e-prints cond-mat/9904034 (1999). 20
- [42] C. F. Ockeloen, A. F. Tauschinsky, R. J. C. Spreeuw and S. Whitlock: “Detection of small atom numbers through image processing”, *Phys. Rev. A* **82**, 061606 (2010). 20
- [43] J. Kronjäger: “Coherent dynamics of spinor Bose-Einstein condensates”, Ph.D. thesis, University of Hamburg (2007). 20
- [44] J. P. Provost and G. Vallee: “Riemannian structure on manifolds of quantum states”, *Communications in Mathematical Physics* **76** (3), 289–301 (1980). 21
- [45] M. V. Berry: “Quantal Phase Factors Accompanying Adiabatic Changes”, *Proceedings of the Royal Society of London Series A* **392** (1802), 45–57 (1984). 21
- [46] S. Peotta and P. Törmä: “Superfluidity in topologically nontrivial flat bands”, *Nature Communications* **6** (1), 8944 (2015). 22
- [47] O. Bleu, D. D. Solnyshkov and G. Malpuech: “Measuring the quantum geometric tensor in two-dimensional photonic and exciton-polariton systems”, *Phys. Rev. B* **97**, 195422 (2018). 22
- [48] M. Yu, P. Yang, M. Gong, Q. Cao, Q. Lu, H. Liu, S. Zhang, M. B. Plenio, F. Jelezko, T. Ozawa, N. Goldman and J. Cai: “Experimental measurement of the quantum geometric tensor using coupled qubits in diamond”, *National Science Review* **7** (2), 254–260 (2019). 22
- [49] P. Roushan, C. Neill, Y. Chen, M. Kolodrubetz, C. Quintana, N. Leung, M. Fang, R. Barends, B. Campbell, Z. Chen *et al.*: “Observation of topological transitions in interacting quantum circuits”, *Nature* **515** (7526), 241 (2014). 22
- [50] S. s. Chern: “On the Curvatura Integra in a Riemannian Manifold”, *Annals of Mathematics* **46** (4), 674–684 (1945). 22

- [51] K. v. Klitzing, G. Dorda and M. Pepper: “New Method for High-Accuracy Determination of the Fine-Structure Constant Based on Quantized Hall Resistance”, *Phys. Rev. Lett.* **45**, 494–497 (1980). 22
- [52] K. von Klitzing: “The quantized Hall effect”, *Rev. Mod. Phys.* **58**, 519–531 (1986).
- [53] D. J. Thouless, M. Kohmoto, M. P. Nightingale and M. den Nijs: “Quantized Hall Conductance in a Two-Dimensional Periodic Potential”, *Phys. Rev. Lett.* **49**, 405–408 (1982). 22
- [54] Y. Hatsugai: “Chern number and edge states in the integer quantum Hall effect”, *Phys. Rev. Lett.* **71**, 3697–3700 (1993). 22
- [55] F. D. M. Haldane: “Model for a Quantum Hall Effect without Landau Levels: Condensed-Matter Realization of the Parity Anomaly”, *Phys. Rev. Lett.* **61** (18), 2015 (1988). 22, 24, 28
- [56] G. Floquet: “Sur les équations différentielles linéaires à coefficients périodiques”, *Annales scientifiques de l’École Normale Supérieure* **2e série**, **12**, 47–88 (1883). 23
- [57] A. Eckardt: “Colloquium: Atomic quantum gases in periodically driven optical lattices”, *Rev. Mod. Phys.* **89**, 011004 (2017). 23
- [58] C. Weitenberg and J. Simonet: “Tailoring quantum gases by Floquet engineering”, *Nature Physics* (2021). 23
- [59] O. Morsch, J. H. Müller, M. Cristiani, D. Ciampini and E. Arimondo: “Bloch Oscillations and Mean-Field Effects of Bose-Einstein Condensates in 1D Optical Lattices”, *Phys. Rev. Lett.* **87**, 140402 (2001). 23
- [60] J. Struck, C. Ölschläger, M. Weinberg, P. Hauke, J. Simonet, A. Eckardt, M. Lewenstein, K. Sengstock and P. Windpassinger: “Tunable Gauge Potential for Neutral and Spinless Particles in Driven Optical Lattices”, *Phys. Rev. Lett.* **108**, 225304 (2012). 24
- [61] K. Jiménez-García, L. J. LeBlanc, R. A. Williams, M. C. Beeler, A. R. Perry and I. B. Spielman: “Peierls Substitution in an Engineered Lattice Potential”, *Phys. Rev. Lett.* **108**, 225303 (2012). 24
- [62] T. Oka and H. Aoki: “Photovoltaic Hall effect in graphene”, *Phys. Rev. B* **79**, 081406 (2009). 24
- [63] W. Zheng and H. Zhai: “Floquet topological states in shaking optical lattices”, *Phys. Rev. A* **89**, 061603 (2014). 24
- [64] N. Fläschner, D. Vogel, M. Tarnowski, B. S. Rem, D.-S. Lühmann, M. Heyl, J. C. Budich, L. Mathey, K. Sengstock and C. Weitenberg: “Observation of dynamical vortices after quenches in a system with topology”, *Nature Physics* **14** (3), 265–268 (2018).

- [65] M. Tarnowski, F. N. Ünal, N. Fläschner, B. S. Rem, A. Eckardt, K. Sengstock and C. Weitenberg: “Measuring topology from dynamics by obtaining the Chern number from a linking number”, *Nature Communications* **10** (1), 1728 (2019). 24, 25, 28, 118
- [66] P. Hauke, M. Lewenstein and A. Eckardt: “Tomography of band insulators from quench dynamics”, *Phys. Rev. Lett.* **113**, 045303 (2014). 131
- [67] N. Fläschner, D. Vogel, M. Tarnowski, B. S. Rem, D. S. Lühmann, M. Heyl, J. C. Budich, L. Mathey, K. Sengstock and C. Weitenberg: “Observation of dynamical vortices after quenches in a system with topology”, *Nature Physics* **14** (3), 265–268 (2018). 25
- [68] A. Eckardt, C. Weiss and M. Holthaus: “Superfluid-Insulator Transition in a Periodically Driven Optical Lattice”, *Phys. Rev. Lett.* **95**, 260404 (2005). 25
- [69] H. Lignier, C. Sias, D. Ciampini, Y. Singh, A. Zenesini, O. Morsch and E. Arimondo: “Dynamical Control of Matter-Wave Tunneling in Periodic Potentials”, *Phys. Rev. Lett.* **99**, 220403 (2007). 25, 101
- [70] J. Struck, C. Ölschläger, R. Le Targat, P. Soltan-Panahi, A. Eckardt, M. Lewenstein, P. Windpassinger and K. Sengstock: “Quantum Simulation of Frustrated Classical Magnetism in Triangular Optical Lattices”, *Science* **333** (6045), 996–999 (2011). 25, 101
- [71] J. Struck, M. Weinberg, C. Ölschläger, P. Windpassinger, J. Simonet, K. Sengstock, R. Höppner, P. Hauke, A. Eckardt, M. Lewenstein and L. Mathey: “Engineering Ising-XY spin-models in a triangular lattice using tunable artificial gauge fields”, *Nature Physics* **9** (11), 738–743 (2013). 25, 101
- [72] A. Hemmerich: “Effective time-independent description of optical lattices with periodic driving”, *Phys. Rev. A* **81**, 063626 (2010). 25
- [73] A. Celi, P. Massignan, J. Ruseckas, N. Goldman, I. B. Spielman, G. Juzeliūnas and M. Lewenstein: “Synthetic Gauge Fields in Synthetic Dimensions”, *Phys. Rev. Lett.* **112**, 043001 (2014). 25
- [74] M. Mancini, G. Pagano, G. Cappellini, L. Livi, M. Rider, J. Catani, C. Sias, P. Zoller, M. Inguscio, M. Dalmonte and L. Fallani: “Observation of chiral edge states with neutral fermions in synthetic Hall ribbons”, *Science* **349**, 510 (2015).
- [75] B. K. Stuhl, H.-I. Lu, L. M. Aycock, D. Genkina and I. B. Spielman: “Visualizing edge states with an atomic Bose gas in the quantum Hall regime”, *Science* **349**, 1514 (2015). 25
- [76] T. Kitagawa, E. Berg, M. Rudner and E. Demler: “Topological characterization of periodically driven quantum systems”, *Phys. Rev. B* **82**, 235114 (2010). 25

- [77] K. Wintersperger, C. Braun, F. N. Ünal, A. Eckardt, M. D. Liberto, N. Goldman, I. Bloch and M. Aidelsburger: “Realization of an anomalous Floquet topological system with ultracold atoms”, *Nature Physics* **16** (10), 1058–1063 (2020). 25, 131
- [78] L. D. Landau and E. M. Lifshitz: *Statistical Physics Part I*, Elsevier, Amsterdam, 3rd edition (1980), bibtex: landa;b;sp80. 26
- [79] M. Aidelsburger, M. Lohse, C. Schweizer, M. Atala, J. T. Barreiro, S. Nascimbène, N. R. Cooper, I. Bloch and N. Goldman: “Measuring the Chern number of Hofstadter bands with ultracold bosonic atoms”, *Nature Phys.* **11** (February), 162–166 (2015). 26, 38
- [80] H. M. Price, O. Zilberberg, T. Ozawa, I. Carusotto and N. Goldman: “Measurement of Chern numbers through center-of-mass responses”, *Phys. Rev. B* **93**, 245113 (2016). 26
- [81] F. N. Ünal, B. Seradjeh and A. Eckardt: “How to Directly Measure Floquet Topological Invariants in Optical Lattices”, *Phys. Rev. Lett.* **122**, 253601 (2019). 26
- [82] J. Carrasquilla and R. G. Melko: “Machine learning phases of matter”, *Nature Physics* **13** (5), 431–434 (2017). 26
- [83] G. Carleo and M. Troyer: “Solving the quantum many-body problem with artificial neural networks”, *Science* **355** (6325), 602–606 (2017).
- [84] X. Gao and L.-M. Duan: “Efficient representation of quantum many-body states with deep neural networks”, *Nature Communications* **8** (1), 662 (2017). 26
- [85] N. Käming: “Analyzing Many Body Physics with Machine Learning”, Master thesis, Universität Hamburg (2020). 26
- [86] N. Käming, A. Dawid, K. Kottmann, M. Lewenstein, K. Sengstock, A. Dauphin and C. Weitenberg: “Unsupervised machine learning of topological phase transitions from experimental data”, *Machine Learning: Science and Technology* **2** (3), 035037 (2021). 26
- [87] A. Bohrdt, C. S. Chiu, G. Ji, M. Xu, D. Greif, M. Greiner, E. Demler, F. Grusdt and M. Knap: “Classifying snapshots of the doped Hubbard model with machine learning”, *Nature Physics* **15** (9), 921–924 (2019). 26
- [88] M. Kac: “Can One Hear the Shape of a Drum?”, *The American Mathematical Monthly* **73** (4), 1–23 (1966). 29, 30
- [89] C. Gordon, D. Webb and S. Wolpert: “Isospectral plane domains and surfaces via Riemannian orbifolds”, *Inventiones mathematicae* **110** (1), 1–22 (1992). 29, 30

- [90] C. Gordon and D. Webb: “You Can’t Hear the Shape of a Drum”, *American Scientist* **84** (1), 46–55 (1996). 30
- [91] J. Milnor: “Eigenvalues of the Laplace Operator on certain Manifolds”, *Proceedings of the National Academy of Sciences* **51** (4), 542–542 (1964). 30
- [92] H. Weyl: “Das asymptotische Verteilungsgesetz der Eigenwerte linearer partieller Differentialgleichungen (mit einer Anwendung auf die Theorie der Hohlraumstrahlung)”, *Mathematische Annalen* **71** (4), 441–479 (1912). 30
- [93] A. Pleijel: “A study of certain Green’s functions with applications in the theory of vibrating membranes”, *Arkiv för Matematik* **2** (6), 553 – 569 (1954). 30
- [94] Z. Lu and J. M. Rowlett: “One can hear the corners of a drum”, *Bulletin of the London Mathematical Society* **48** (1), 85–93 (2016). 30
- [95] M. Nursultanov, J. Rowlett and D. Sher: *How to Hear the Corners of a Drum*, pages 243–278, Springer International Publishing, Cham (2019), ISBN 978-3-030-04161-8. 30
- [96] J. H. P. McKean and I. M. Singer: “Curvature and the eigenvalues of the Laplacian”, *Journal of Differential Geometry* **1** (1-2), 43 – 69 (1967). 30
- [97] T. Ozawa and N. Goldman: “Extracting the quantum metric tensor through periodic driving”, *Phys. Rev. B* **97**, 201117 (2018). 30, 48
- [98] D. T. Tran, N. R. Cooper and N. Goldman: “Quantized Rabi oscillations and circular dichroism in quantum Hall systems”, *Phys. Rev. A* **97**, 061602 (2018).
- [99] T. Ozawa and N. Goldman: “Probing localization and quantum geometry by spectroscopy”, *Phys. Rev. Research* **1**, 032019 (2019). 30, 48, 51
- [100] T. T. Luu and H. J. Wörner: “Measurement of the Berry curvature of solids using high-harmonic spectroscopy”, *Nature Communications* **9** (1), 916 (2018). 31
- [101] H. K. Avetissian and G. F. Mkrtchian: “High laser harmonics induced by the Berry curvature in time-reversal invariant materials”, *Phys. Rev. B* **102**, 245422 (2020). 31
- [102] D. Xiao, M.-C. Chang and Q. Niu: “Berry phase effects on electronic properties”, *Reviews of modern physics* **82** (3), 1959 (2010). 32
- [103] H. S. Bennett and E. A. Stern: “Faraday effect in solids”, *Physical Review* **137**, A448 (1965). 33, 34
- [104] D. T. Tran: “Novel aspects of topological insulators: Quasi-crystals, Floquet-engineered states and circular dichroism.”, Ph.D. thesis, Université Libre de Bruxelles (2018). 33

- [105] C. Repellin and N. Goldman: “Detecting Fractional Chern Insulators through Circular Dichroism”, *Phys. Rev. Lett.* **122**, 166801 (2019). 34, 52
- [106] I. Souza and D. Vanderbilt: “Dichroic f -sum rule and the orbital magnetization of crystals”, *Phys. Rev. B* **77**, 054438 (2008). 34
- [107] A. Chacón, D. Kim, W. Zhu, S. P. Kelly, A. Dauphin, E. Pisanty, A. S. Maxwell, A. Picón, M. F. Ciappina, D. E. Kim, C. Ticknor, A. Saxena and M. Lewenstein: “Circular dichroism in higher-order harmonic generation: Heralding topological phases and transitions in Chern insulators”, *Phys. Rev. B* **102**, 134115 (2020). 34
- [108] T. Rakovszky, J. K. Asbóth and A. Alberti: “Detecting topological invariants in chiral symmetric insulators via losses”, *Phys. Rev. B* **95**, 201407 (2017). 34
- [109] L. Asteria, D. T. Tran, T. Ozawa, M. Tarnowski, B. S. Rem, N. Fläschner, K. Sengstock, N. Goldman and C. Weitenberg: “Measuring quantized circular dichroism in ultracold topological matter, *Supplementary Information*”, *Nature Physics* **15** (5), 449–454 (2019). 35, 36
- [110] M. D. Caio, N. R. Cooper and M. J. Bhaseen: “Quantum Quenches in Chern Insulators”, *Phys. Rev. Lett.* **115**, 236403 (2015). 38
- [111] F. N. Ünal, E. J. Mueller and M. O. Oktel: “Nonequilibrium fractional Hall response after a topological quench”, *Phys. Rev. A* **94**, 053604 (2016).
- [112] Y. Hu, P. Zoller and J. C. Budich: “Dynamical Buildup of a Quantized Hall Response from Nontopological States”, *Phys. Rev. Lett.* **117**, 126803 (2016). 47
- [113] M. McGinley and N. R. Cooper: “Topology of One-Dimensional Quantum Systems Out of Equilibrium”, *Phys. Rev. Lett.* **121**, 090401 (2018).
- [114] M. D. Caio, G. Möller, N. R. Cooper and M. J. Bhaseen: “Topological marker currents in Chern insulators”, *Nature Physics* **15** (3), 257–261 (2019). 38
- [115] G. Sun and A. Eckardt: “Optimal frequency window for Floquet engineering in optical lattices”, *Phys. Rev. Research* **2**, 013241 (2020). 38
- [116] K. Wintersperger, M. Bukov, J. Näger, S. Lellouch, E. Demler, U. Schneider, I. Bloch, N. Goldman and M. Aidelsburger: “Parametric Instabilities of Interacting Bosons in Periodically Driven 1D Optical Lattices”, *Phys. Rev. X* **10**, 011030 (2020). 38, 87
- [117] K. Viebahn, J. Minguzzi, K. Sandholzer, A.-S. Walter, M. Sajnani, F. Görg and T. Esslinger: “Suppressing Dissipation in a Floquet-Hubbard System”, *Phys. Rev. X* **11**, 011057 (2021). 38, 52
- [118] S. Sugawa, F. Salces-Carcoba, A. R. Perry, Y. Yue and I. B. Spielman: “Second Chern number of a quantum-simulated non-Abelian Yang monopole”, *Science* **360** (6396), 1429–1434 (2018). 38

- [119] Z. Wu, E. Taylor and E. Zaremba: “Probing the optical conductivity of trapped charge-neutral quantum gases”, *Eur. Phys. Lett.* **110** (2), 26002 (2015). 43
- [120] R. Anderson, F. Wang, P. Xu, V. Venu, S. Trotzky, F. Chevy and J. H. Thywissen: “Conductivity Spectrum of Ultracold Atoms in an Optical Lattice”, *Phys. Rev. Lett.* **122**, 153602 (2019). 43
- [121] L. D’Alessio and M. Rigol: “Dynamical preparation of Floquet Chern insulators”, *Nature Communications* **6** (1), 8336 (2015). 45
- [122] S. Barbarino, J. Yu, P. Zoller and J. C. Budich: “Preparing Atomic Topological Quantum Matter by Adiabatic Nonunitary Dynamics”, *Phys. Rev. Lett.* **124**, 010401 (2020). 46
- [123] N. Marzari and D. Vanderbilt: “Maximally localized generalized Wannier functions for composite energy bands”, *Physical review B* **56** (20), 12847 (1997). 48
- [124] R. Walters, G. Cotugno, T. H. Johnson, S. R. Clark and D. Jaksch: “Ab initio derivation of Hubbard models for cold atoms in optical lattices”, *Phys. Rev. A* **87**, 043613 (2013). 52
- [125] J. Ibañez Azpiroz, A. Eiguren, A. Bergara, G. Pettini and M. Modugno: “Tight-binding models for ultracold atoms in honeycomb optical lattices”, *Phys. Rev. A* **87**, 011602 (2013).
- [126] T. Uehlinger, G. Jotzu, M. Messer, D. Greif, W. Hofstetter, U. Bissbort and T. Esslinger: “Artificial Graphene with Tunable Interactions”, *Phys. Rev. Lett.* **111**, 185307 (2013). 113
- [127] D.-S. Lühmann, O. Jürgensen, M. Weinberg, J. Simonet, P. Soltan-Panahi and K. Sengstock: “Quantum phases in tunable state-dependent hexagonal optical lattices”, *Phys. Rev. A* **90**, 013614 (2014).
- [128] S. Paul and E. Tiesinga: “Wannier functions using a discrete variable representation for optical lattices”, *Phys. Rev. A* **94**, 033606 (2016).
- [129] M. Modugno, J. Ibañez-Azpiroz and G. Pettini: “Tight-binding models for ultracold atoms in optical lattices: general formulation and applications”, *Science China Physics, Mechanics & Astronomy* **59** (6), 660001 (2016). 52
- [130] K. Sandholzer, A.-S. Walter, J. Minguzzi, Z. Zhu, K. Viebahn and T. Esslinger: “Floquet engineering of individual band gaps in an optical lattice using a two-tone drive”, (2021). 52
- [131] J. Minguzzi, Z. Zhu, K. Sandholzer, A.-S. Walter, K. Viebahn and T. Esslinger: “Topological pumping in a Floquet-Bloch band”, (2021). 52

- [132] M. Schüler and P. Werner: “Tracing the nonequilibrium topological state of Chern insulators”, *Phys. Rev. B* **96**, 155122 (2017). 52
- [133] H. L. Stormer, D. C. Tsui and A. C. Gossard: “The fractional quantum Hall effect”, *Rev. Mod. Phys.* **71**, S298–S305 (1999). 52
- [134] T. Neupert, C. Chamon, T. Iadecola, L. H. Santos and C. Mudry: “Fractional (Chern and topological) insulators”, *Physica Scripta* **T164**, 014005 (2015). 52
- [135] F. Schindler, A. M. Cook, M. G. Vergniory, Z. Wang, S. S. P. Parkin, B. A. Bernevig and T. Neupert: “High-order topological insulators”, *Science Advances* **4** (6), eaat0346 (2018). 52, 129
- [136] O. Pozo, C. Repellin and A. G. Grushin: “Quantization in Chiral Higher Order Topological Insulators: Circular Dichroism and Local Chern Marker”, *Phys. Rev. Lett.* **123**, 247401 (2019). 52
- [137] I. Sodemann and L. Fu: “Quantum Nonlinear Hall Effect Induced by Berry Curvature Dipole in Time-Reversal Invariant Materials”, *Phys. Rev. Lett.* **115**, 216806 (2015). 52
- [138] O. Matsyshyn and I. Sodemann: “Nonlinear Hall Acceleration and the Quantum Rectification Sum Rule”, *Phys. Rev. Lett.* **123**, 246602 (2019). 52
- [139] G. Binnig and H. Rohrer: “Scanning tunneling microscopy—from birth to adolescence”, *Rev. Mod. Phys.* **59**, 615–625 (1987). 53
- [140] W. Neuhauser, M. Hohenstatt, P. E. Toschek and H. Dehmelt: *Resonance Fluorescence From Single Ions at Rest*, pages 1045–1070, De Gruyter (2019). 53
- [141] M. Endres, M. Cheneau, T. Fukuhara, C. Weitenberg, P. Schauß, C. Gross, L. Mazza, M. C. Bañuls, L. Pollet, I. Bloch and S. Kuhr: “Observation of Correlated Particle-Hole Pairs and String Order in Low-Dimensional Mott Insulators”, *Science* **334** (6053), 200–203 (2011). 53
- [142] A. Mazurenko, C. S. Chiu, G. Ji, M. F. Parsons, M. Kanász-Nagy, R. Schmidt, F. Grusdt, E. Demler, D. Greif and M. Greiner: “A cold-atom Fermi–Hubbard antiferromagnet”, *Nature* **545** (7655), 462–466 (2017). 53
- [143] C. Weitenberg, M. Endres, J. F. Sherson, M. Cheneau, P. Schauß, T. Fukuhara, I. Bloch and S. Kuhr: “Single-spin addressing in an atomic Mott insulator”, *Nature* **471**, 319–324 (2011). 53, 83
- [144] A. Lukin, M. Rispoli, R. Schittko, M. E. Tai, A. M. Kaufman, S. Choi, V. Khemani, J. Léonard and M. Greiner: “Probing entanglement in a many-body localized system”, *Science* **364** (6437), 256–260 (2019). 53
- [145] J.-y. Choi, S. Hild, J. Zeiher, P. Schauß, A. Rubio-Abadal, T. Yefsah, V. Khemani, D. A. Huse, I. Bloch and C. Gross: “Exploring the Many-body Localization Transition in Two Dimensions”, *Science* **352**, 1547 (2016). 53, 83

- [146] M. E. Tai, A. Lukin, M. Rispoli, R. Schittko, T. Menke, D. Borgnia, P. M. Preiss, F. Grusdt, A. M. Kaufman and M. Greiner: “Microscopy of the interacting Harper–Hofstadter model in the two-body limit”, *Nature* **546** (7659), 519–523 (2017). 53
- [147] P. M. Preiss, R. Ma, M. E. Tai, J. Simon and M. Greiner: “Quantum gas microscopy with spin, atom-number, and multilayer readout”, *Phys. Rev. A* **91**, 041602 (2015). 53, 54
- [148] M. Boll, T. A. Hilker, G. Salomon, A. Omran, J. Nespolo, L. Pollet, I. Bloch and C. Gross: “Spin- and density-resolved microscopy of antiferromagnetic correlations in Fermi-Hubbard chains”, *Science* **353** (6305), 1257–1260 (2016). 53
- [149] J. Koepsell, S. Hirthe, D. Bourgund, P. Sompet, J. Vijayan, G. Salomon, C. Gross and I. Bloch: “Robust Bilayer Charge Pumping for Spin- and Density-Resolved Quantum Gas Microscopy”, *Phys. Rev. Lett.* **125**, 010403 (2020). 53
- [150] J. Koepsell, J. Vijayan, P. Sompet, F. Grusdt, T. A. Hilker, E. Demler, G. Salomon, I. Bloch and C. Gross: “Imaging magnetic polarons in the doped Fermi–Hubbard model”, *Nature* **572** (7769), 358–362 (2019). 53
- [151] J. Koepsell, D. Bourgund, P. Sompet, S. Hirthe, A. Bohrdt, Y. Wang, F. Grusdt, E. Demler, G. Salomon, C. Gross and I. Bloch: “Microscopic evolution of doped Mott insulators from polaronic metal to Fermi liquid”, *Science* **374** (6563), 82–86 (2021). 53
- [152] K. D. Nelson, X. Li and D. S. Weiss: “Imaging single atoms in a three-dimensional array”, *Nature Physics* **3** (8), 556–560 (2007). 54, 88
- [153] O. Eliasson, J. S. Laustsen, R. Heck, R. Müller, J. J. Arlt, C. A. Weidner and J. F. Sherson: “Spatial tomography of individual atoms in a quantum gas microscope”, *Phys. Rev. A* **102**, 053311 (2020). 54, 88
- [154] P. Würtz, T. Langen, T. Gericke, A. Koglbauer and H. Ott: “Experimental Demonstration of Single-Site Addressability in a Two-Dimensional Optical Lattice”, *Phys. Rev. Lett.* **103**, 080404 (2009). 54, 83, 88, 89
- [155] C. Veit, N. Zuber, O. A. Herrera-Sancho, V. S. V. Anasuri, T. Schmid, F. Meinert, R. Löw and T. Pfau: “Pulsed Ion Microscope to Probe Quantum Gases”, *Phys. Rev. X* **11**, 011036 (2021). 54, 88, 89
- [156] S. Subhankar, Y. Wang, T. C. Tsui, S. L. Rolston and J. V. Porto: “Nanoscale Atomic Density Microscopy”, *Physical Review X* **9** (2), 21002 (2019). 54, 88
- [157] M. McDonald, J. Trisnadi, K. X. Yao and C. Chin: “Superresolution Microscopy of Cold Atoms in an Optical Lattice”, *Physical Review X* **9** (2), 21001 (2019). 54, 88

- [158] E. Deist, Y.-H. Lu, J. A. Gerber, J. Zeiher and D. M. Stamper-Kurn: “Super-resolution microscopy of optical fields using tweezer-trapped single atoms”, (2021). 54
- [159] A. del Campo: “Frictionless quantum quenches in ultracold gases: A quantum-dynamical microscope”, *Phys. Rev. A* **84**, 031606 (2011). 54
- [160] N. Read and N. R. Cooper: “Free expansion of lowest-Landau-level states of trapped atoms: A wave-function microscope”, *Phys. Rev. A* **68**, 035601 (2003). 54
- [161] R. Saint-Jalm, P. C. M. Castilho, E. Le Cerf, B. Bakkali-Hassani, J.-L. Ville, S. Nascimbene, J. Beugnon and J. Dalibard: “Dynamical Symmetry and Breathers in a Two-Dimensional Bose Gas”, *Phys. Rev. X* **9**, 021035 (2019). 54
- [162] Z.-Y. Shi, C. Gao and H. Zhai: “Idealized Hydrodynamics”, (2020). 54
- [163] E. Brainis, C. Muldoon, L. Brandt and A. Kuhn: “Coherent imaging of extended objects”, *Optics Communications* **282** (4), 465–472 (2009). 59
- [164] L. Asteria, H. P. Zahn, M. N. Kosch, K. Sengstock and C. Weitenberg: “Quantum gas magnifier for sub-lattice-resolved imaging of 3D quantum systems, *Supplementary Information*”, *Nature* **599** (7886), 571–575 (2021). 61, 77, 91, 141
- [165] S. Tung, G. Lamporesi, D. Lobser, L. Xia and E. A. Cornell: “Observation of the presuperfluid regime in a two-dimensional Bose gas”, *Phys. Rev. Lett.* **105**, 230408 (2010). 62
- [166] R. Yamamoto, H. Ozawa, D. C. Nak, I. Nakamura and T. Fukuhara: “Single-site-resolved imaging of ultracold atoms in a triangular optical lattice”, *New Journal of Physics* **22** (12), 123028 (2020). 67
- [167] J. Yang, L. Liu, J. Mongkolkiattichai and P. Schauss: “Site-Resolved Imaging of Ultracold Fermions in a Triangular-Lattice Quantum Gas Microscope”, *PRX Quantum* **2**, 020344 (2021). 67
- [168] N. Goldman, G. Jotzu, M. Messer, F. Görg, R. Desbuquois and T. Esslinger: “Creating topological interfaces and detecting chiral edge modes in a two-dimensional optical lattice”, *Phys. Rev. A* **94**, 043611 (2016). 68, 126
- [169] A. Camacho-Guardian, N. Goldman, P. Massignan and G. M. Bruun: “Dropping an impurity into a Chern insulator: A polaron view on topological matter”, *Phys. Rev. B* **99**, 081105 (2019). 68
- [170] C. Franchini, M. Reticcioli, M. Setvin and U. Diebold: “Polarons in materials”, *Nature Reviews Materials* **6** (7), 560–586 (2021). 68
- [171] C. J. Pethick and H. Smith: *Bose–Einstein Condensation in Dilute Gases*, Cambridge University Press, Cambridge (2002). 69

- [172] H. Zahn: “*in preparation*”, Ph.D. thesis, University of Hamburg (2021). 76, 77, 86
- [173] D. McKay, M. White and B. DeMarco: “Lattice thermodynamics for ultracold atoms”, *Phys. Rev. A* **79**, 063605 (2009). 77
- [174] S. Trotzky, L. Pollet, F. Gerbier, U. Schnorrberger, I. Bloch, N. V. Prokof'ev, B. Svistunov and M. Troyer: “Suppression of the critical temperature for superfluidity near the Mott transition”, *Nature Physics* **6** (12), 998–1004 (2010).
- [175] H. Cayla, C. Carcy, Q. Bouton, R. Chang, G. Carleo, M. Mancini and D. Clément: “Single-atom-resolved probing of lattice gases in momentum space”, *Phys. Rev. A* **97**, 061609 (2018). 77
- [176] C. Weitenberg: “Single-Atom Resolved Imaging and Manipulation in an Atomic Mott Insulator”, Ph.D. thesis, Ludwig-Maximilians-Universität München (2011). 77
- [177] S. Fölling, A. Widera, T. Müller, F. Gerbier and I. Bloch: “Formation of Spatial Shell Structure in the Superfluid to Mott Insulator Transition”, *Phys. Rev. Lett.* **97**, 060403 (2006). 77
- [178] V. M. Pereira, A. H. Castro Neto and N. M. R. Peres: “Tight-binding approach to uniaxial strain in graphene”, *Phys. Rev. B* **80**, 045401 (2009). 79
- [179] L. Tarruell, D. Greif, T. Uehlinger, G. Jotzu and T. Esslinger: “Creating, moving and merging Dirac points with a Fermi gas in a tunable honeycomb lattice”, *Nature* **483** (7389), 302–305 (2012). 79, 113
- [180] M. Tarnowski, M. Nuske, N. Fläschner, B. Rem, D. Vogel, L. Freystatzky, K. Sengstock, L. Mathey and C. Weitenberg: “Observation of Topological Bloch-State Defects and Their Merging Transition”, *Phys. Rev. Lett.* **118**, 240403 (2017). 79
- [181] H. M. Price, T. Ozawa and N. Goldman: “Synthetic dimensions for cold atoms from shaking a harmonic trap”, *Phys. Rev. A* **95**, 023607 (2017). 82
- [182] H. Chen and W. V. Liu: “Intertwined space-time symmetry, orbital magnetism, and dynamical Berry connection in a circularly shaken optical lattice”, *Phys. Rev. A* **104**, 013308 (2021). 82
- [183] M. Ölschläger, G. Wirth and A. Hemmerich: “Unconventional Superfluid Order in the F Band of a Bipartite Optical Square Lattice”, *Phys. Rev. Lett.* **106**, 015302 (2011). 82
- [184] M. Ölschläger, T. Kock, G. Wirth, A. Ewerbeck, C. M. Smith and A. Hemmerich: “Interaction-induced chiral $px \pm ipy$ superfluid order of bosons in an optical lattice”, *New Journal of Physics* **15** (8), 083041 (2013). 139

- [185] T. Kock, C. Hippler, A. Ewerbeck and A. Hemmerich: “Orbital optical lattices with bosons”, *Journal of Physics B: Atomic, Molecular and Optical Physics* **49** (4), 042001 (2016). 113
- [186] T. Klafka: “Bose-Einstein Condensation in higher Bloch bands of the optical honeycomb lattice”, Ph.D. thesis, University of Hamburg (2016). 131
- [187] X.-Q. Wang, G.-Q. Luo, J.-Y. Liu, W. V. Liu, A. Hemmerich and Z.-F. Xu: “Evidence for an atomic chiral superfluid with topological excitations”, *Nature* **596** (7871), 227–231 (2021). 82, 113, 131
- [188] P. M. Preiss, R. Ma, M. E. Tai, A. Lukin, M. Rispoli, P. Zupancic, Y. Lahini, R. Islam and M. Greiner: “Strongly correlated quantum walks in optical lattices”, *Science* **347**, 1229 (2015). 83
- [189] M. Karski, L. Förster, J. M. Choi, A. Steffen, N. Belmechri, W. Alt, D. Meschede and A. Widera: “Imprinting patterns of neutral atoms in an optical lattice using magnetic resonance techniques”, *New Journal of Physics* **12**, 065027 (2010). 83
- [190] P. B. Wigley, L. M. Starkey, S. S. Szigeti, M. Jasperse, J. J. Hope, L. D. Turner and R. P. Anderson: “Precise wave-function engineering with magnetic resonance”, *Phys. Rev. A* **96**, 013612 (2017). 83
- [191] M. Kosch: “*in preparation*”, Ph.D. thesis, University of Hamburg. 83
- [192] R. Labouvie, B. Santra, S. Heun and H. Ott: “Bistability in a Driven-Dissipative Superfluid”, *Phys. Rev. Lett.* **116**, 235302 (2016). 83
- [193] A. Eckardt and E. Anisimovas: “High-frequency approximation for periodically driven quantum systems from a Floquet-space perspective”, *New Journal of physics* **17** (9), 093039 (2015). 87
- [194] W. Magnus: “On the exponential solution of differential equations for a linear operator”, *Communications on Pure and Applied Mathematics* **7** (4), 649–673 (1954). 87
- [195] S. Scherg, T. Kohlert, P. Sala, F. Pollmann, B. Hebbe Madhusudhana, I. Bloch and M. Aidelsburger: “Observing non-ergodicity due to kinetic constraints in tilted Fermi-Hubbard chains”, *Nature Communications* **12** (1), 4490 (2021). 87
- [196] T. Kohlert, S. Scherg, P. Sala, F. Pollmann, B. H. Madhusudhana, I. Bloch and M. Aidelsburger: “Experimental realization of fragmented models in tilted Fermi-Hubbard chains”, (2021). 87
- [197] N. Gemelke, E. Sarajlic, Y. Bidel, S. Hong and S. Chu: “Parametric Amplification of Matter Waves in Periodically Translated Optical Lattices”, *Phys. Rev. Lett.* **95**, 170404 (2005). 87

- [198] S. Greschner, L. Santos and D. Poletti: “Exploring Unconventional Hubbard Models with Doubly Modulated Lattice Gases”, *Phys. Rev. Lett.* **113**, 183002 (2014). 87
- [199] F. Meinert, M. J. Mark, K. Lauber, A. J. Daley and H.-C. Nägerl: “Floquet Engineering of Correlated Tunneling in the Bose-Hubbard Model with Ultracold Atoms”, *Phys. Rev. Lett.* **116**, 205301 (2016).
- [200] S. Baier, M. J. Mark, D. Petter, K. Aikawa, L. Chomaz, Z. Cai, M. Baranov, P. Zoller and F. Ferlaino: “Extended Bose-Hubbard models with ultracold magnetic atoms”, *Science* **352** (6282), 201–205 (2016). 87
- [201] I. Dimitrova, N. Jepsen, A. Buyskikh, A. Venegas-Gomez, J. Amato-Grill, A. Daley and W. Ketterle: “Enhanced Superexchange in a Tilted Mott Insulator”, *Phys. Rev. Lett.* **124**, 043204 (2020). 87
- [202] T. Ozawa: “Artificial magnetic field for synthetic quantum matter without dynamical modulation”, *Phys. Rev. A* **103**, 033318 (2021). 89
- [203] J. S. Rosenberg, L. Christakis, E. Guardado-Sanchez, Z. Z. Yan and W. S. Bakr: “Observation of the Hanbury Brown and Twiss Effect with Ultracold Molecules”, (2021). 89
- [204] R. Bücker, A. Perrin, S. Manz, T. Betz, C. Koller, T. Plisson, J. Rottmann, T. Schumm and J. Schmiedmayer: “Single-particle-sensitive imaging of freely propagating ultracold atoms”, *New Journal of Physics* **11**, 103039 (2009). 89
- [205] A. Fuhrmanek, A. M. Lance, C. Tuchendler, P. Grangier, Y. R. P. Sortais and A. Browaeys: “Imaging a single atom in a time-of-flight experiment”, *New Journal of Physics* **12** (5), 053028 (2010).
- [206] C. J. Picken, R. Legaie and J. D. Pritchard: “Single atom imaging with an sCMOS camera”, *Applied Physics Letters* **111** (16), 164102 (2017).
- [207] A. Bergschneider, V. M. Klinkhamer, J. H. Becher, R. Klemt, G. Zürn, P. M. Preiss and S. Jochim: “Spin-resolved single-atom imaging of ${}^6\text{Li}$ in free space”, *Phys. Rev. A* **97**, 063613 (2018). 89
- [208] G.-B. Jo, J. Guzman, C. K. Thomas, P. Hosur, A. Vishwanath and D. M. Stamper-Kurn: “Ultracold Atoms in a Tunable Optical Kagome Lattice”, *Phys. Rev. Lett.* **108**, 045305 (2012). 89
- [209] S. Nascimbene, N. Goldman, N. R. Cooper and J. Dalibard: “Dynamic Optical Lattices of Subwavelength Spacing for Ultracold Atoms”, *Phys. Rev. Lett.* **115**, 140401 (2015). 89
- [210] G. Ritt, C. Geckeler, T. Salger, G. Cennini and M. Weitz: “Fourier synthesis of optical potentials for atomic quantum gases”, *Phys. Rev. A* **74**, 063622 (2006). 113

- [211] Y. Wang, S. Subhankar, P. Bienias, M. Łącki, T.-C. Tsui, M. A. Baranov, A. V. Gorshkov, P. Zoller, J. V. Porto and S. L. Rolston: “Dark State Optical Lattice with a Subwavelength Spatial Structure”, *Phys. Rev. Lett.* **120**, 083601 (2018).
- [212] R. P. Anderson, D. Trypogeorgos, A. Valdés-Curiel, Q.-Y. Liang, J. Tao, M. Zhao, T. Andrijauskas, G. Juzeliūnas and I. B. Spielman: “Realization of a deeply subwavelength adiabatic optical lattice”, *Phys. Rev. Research* **2**, 013149 (2020). 89
- [213] F. Gerbier, S. Trotzky, S. Fölling, U. Schnorrberger, J. D. Thompson, A. Widera, I. Bloch, L. Pollet, M. Troyer, B. Capogrosso-Sansone, N. V. Prokof’ev and B. V. Svistunov: “Expansion of a Quantum Gas Released from an Optical Lattice”, *Phys. Rev. Lett.* **101**, 155303 (2008). 91
- [214] J. F. Clauser and S. Li: “Talbot-vonLau atom interferometry with cold slow potassium”, *Physical Review A* **49**, 2213–2217 (1994). 92
- [215] M. S. Chapman, C. R. Ekstrom, T. D. Hammond, J. Schmiedmayer, B. E. Tannian, S. Wehinger and D. E. Pritchard: “Near-field imaging of atom diffraction gratings: The atomic Talbot effect”, *Phys. Rev. A* **51**, R14–R17 (1995).
- [216] S. Nowak, C. Kurtsiefer, T. Pfau and C. David: “High-order Talbot fringes for atomic matter waves”, *Optics Letters* **22** (18), 1430 (1997). 92
- [217] B. Santra, C. Baals, R. Labouvie, A. B. Bhattacharjee, A. Pelster and H. Ott: “Measuring finite-range phase coherence in an optical lattice using Talbot interferometry”, *Nature Communications* **8**, 15601 (2017). 92, 95
- [218] P. Höllmer, J.-S. Bernier, C. Kollath, C. Baals, B. Santra and H. Ott: “Talbot effect in the presence of interactions”, *Phys. Rev. A* **100**, 063613 (2019). 92
- [219] S. Dettmer, D. Hellweg, P. Ryytty, J. J. Arlt, W. Ertmer, K. Sengstock, D. S. Petrov, G. V. Shlyapnikov, H. Kreutzmann, L. Santos and M. Lewenstein: “Observation of Phase Fluctuations in Elongated Bose-Einstein Condensates”, *Phys. Rev. Lett.* **87**, 160406 (2001). 95
- [220] J.-y. Choi, S. W. Seo, W. J. Kwon and Y.-i. Shin: “Probing Phase Fluctuations in a 2D Degenerate Bose Gas by Free Expansion”, *Phys. Rev. Lett.* **109**, 125301 (2012). 95
- [221] A. Burchianti, C. D’Errico, L. Marconi, F. Minardi, C. Fort and M. Modugno: “Effect of interactions in the interference pattern of Bose-Einstein condensates”, *Phys. Rev. A* **102**, 043314 (2020). 100
- [222] C. V. Parker, L. C. Ha and C. Chin: “Direct observation of effective ferromagnetic domains of cold atoms in a shaken optical lattice”, *Nature Phys.* **9**, 769 (2013). 101

- [223] V. Schweikhard, S. Tung and E. A. Cornell: “Vortex Proliferation in the Berezinskii-Kosterlitz-Thouless Regime on a Two-Dimensional Lattice of Bose-Einstein Condensates”, *Phys. Rev. Lett.* **99**, 030401 (2007). 101
- [224] S. Tung, V. Schweikhard and E. A. Cornell: “Observation of Vortex Pinning in Bose-Einstein Condensates”, *Phys. Rev. Lett.* **97**, 240402 (2006). 101
- [225] V. L. Berezinskii: “Destruction of Long-range Order in One-dimensional and Two-dimensional Systems having a Continuous Symmetry Group II. Quantum Systems”, *Sov. Phys. JETP* **34**, 610–616 (1971). 101
- [226] J. M. Kosterlitz and D. J. Thouless: “Ordering, metastability and phase transitions in two-dimensional systems”, *Journal of Physics C: Solid State Physics* **6** (7), 1181–1203 (1973). 101
- [227] S. Guo, A. R. Fritsch, C. Greenberg, I. B. Spielman and J. P. Zwolak: “Machine-learning enhanced dark soliton detection in Bose-Einstein condensates”, *Machine Learning: Science and Technology* **2** (3), 035020 (2021). 102
- [228] I. Bloch, T. W. Hänsch and T. Esslinger: “Measurement of the spatial coherence of a trapped Bose gas at the phase transition”, *Nature* **403** (6766), 166–170 (2000). 103
- [229] R. Saint-Jalm: “Exploring two-dimensional physics with Bose gases in box potentials: phase ordering and dynamical symmetry.”, Ph.D. thesis, Université Paris Sciences et Lettres (2019). 103
- [230] L.-M. Duan: “Detecting Correlation Functions of Ultracold Atoms through Fourier Sampling of Time-of-Flight Images”, *Phys. Rev. Lett.* **96**, 103201 (2006). 103
- [231] L. A. Peña Ardila, M. Heyl and A. Eckardt: “Measuring the Single-Particle Density Matrix for Fermions and Hard-Core Bosons in an Optical Lattice”, *Phys. Rev. Lett.* **121**, 260401 (2018). 103, 108
- [232] S. Gupta, A. E. Leanhardt, A. D. Cronin and D. E. Pritchard: “Coherent manipulation of atoms with standing light waves”, *Comptes Rendus de l’Académie des Sciences - Series IV - Physics* **2** (3), 479–495 (2001). 103
- [233] P. A. Murthy and S. Jochim: “Direct imaging of the order parameter of an atomic superfluid using matterwave optics”, arXiv:1911.10824 (2019). 105
- [234] D. Hellweg, L. Cacciapuoti, M. Kottke, T. Schulte, K. Sengstock, W. Ertmer and J. J. Arlt: “Measurement of the Spatial Correlation Function of Phase Fluctuating Bose-Einstein Condensates”, *Phys. Rev. Lett.* **91**, 010406 (2003). 108

- [235] J. E. Simsarian, J. Denschlag, M. Edwards, C. W. Clark, L. Deng, E. W. Hagley, K. Helmerson, S. L. Rolston and W. D. Phillips: “Imaging the Phase of an Evolving Bose-Einstein Condensate Wave Function”, *Phys. Rev. Lett.* **85**, 2040–2043 (2000). 108
- [236] D. Clément, N. Fabbri, L. Fallani, C. Fort and M. Inguscio: “Multi-band spectroscopy of inhomogeneous Mott-insulator states of ultracold bosons”, *New Journal of Physics* **11** (10), 103030 (2009). 109, 127
- [237] P. T. Ernst, S. Götzke, J. S. Krauser, K. Pyka, D.-S. Lühmann, D. Pfannkuche and K. Sengstock: “Probing superfluids in optical lattices by momentum-resolved Bragg spectroscopy”, *Nature Physics* **6** (1), 56–61 (2010). 109, 127
- [238] R. Bianco and R. Resta: “Mapping topological order in coordinate space”, *Phys. Rev. B* **84**, 241106 (2011). 111
- [239] J.-H. Zheng, B. Irsigler, L. Jiang, C. Weitenberg and W. Hofstetter: “Measuring an interaction-induced topological phase transition via the single-particle density matrix”, *Phys. Rev. A* **101**, 013631 (2020). 111
- [240] B. Irsigler, J.-H. Zheng and W. Hofstetter: “Microscopic characteristics and tomography scheme of the local Chern marker”, *Phys. Rev. A* **100**, 023610 (2019). 111
- [241] J. Nemirovsky and Y. Sagi: “Fast universal two-qubit gate for neutral fermionic atoms in optical tweezers”, *Phys. Rev. Research* **3**, 013113 (2021). 111
- [242] P. Windpassinger and K. Sengstock: “Engineering novel optical lattices”, *Reports on Progress in Physics* **76** (8), 086401 (2013). 113
- [243] L. Duca, T. Li, M. Reitter, I. Bloch, M. Schleier-Smith and U. Schneider: “An Aharonov-Bohm interferometer for determining Bloch band topology”, *Science* **347** (6219), 288–292 (2015). 113
- [244] M. Weinberg, C. Staarmann, C. Ölschläger, J. Simonet and K. Sengstock: “Breaking inversion symmetry in a state-dependent honeycomb lattice: artificial graphene with tunable band gap”, *2D Materials* **3** (2), 024005 (2016). 113, 118, 145
- [245] L. Masi, T. Petrucciani, G. Ferioli, G. Semeghini, G. Modugno, M. Inguscio and M. Fattori: “Spatial Bloch Oscillations of a Quantum Gas in a “Beat-Note” Superlattice”, *Phys. Rev. Lett.* **127**, 020601 (2021). 113
- [246] C. Robens, J. Zopes, W. Alt, S. Brakhane, D. Meschede and A. Alberti: “Low-Entropy States of Neutral Atoms in Polarization-Synthesized Optical Lattices”, *Phys. Rev. Lett.* **118**, 065302 (2017). 113

- [247] K. I. Petsas, A. B. Coates and G. Grynberg: “Crystallography of optical lattices”, *Phys. Rev. A* **50**, 5173–5189 (1994). 114, 129
- [248] H. Schmidt: “Dynamische Kontrolle der Geometrie optischer Gitter”, Diploma thesis, Universität Hamburg (2015). 116
- [249] R. Grimm, M. Weidemüller and Y. B. Ovchinnikov: “Optical Dipole Traps for Neutral Atoms”, volume 42 of *Advances In Atomic, Molecular, and Optical Physics*, pages 95–170, Academic Press (2000). 118, 145
- [250] C. K. Thomas, T. H. Barter, T.-H. Leung, M. Okano, G.-B. Jo, J. Guzman, I. Kimchi, A. Vishwanath and D. M. Stamper-Kurn: “Mean-Field Scaling of the Superfluid to Mott Insulator Transition in a 2D Optical Superlattice”, *Phys. Rev. Lett.* **119**, 100402 (2017). 118
- [251] Y.-J. Lin, R. L. Compton, K. Jiménez-García, J. V. Porto and I. B. Spielman: “Synthetic magnetic fields for ultracold neutral atoms”, *Nature* **462** (7273), 628–632 (2009). 120
- [252] Y.-J. Lin, R. L. Compton, K. Jiménez-García, W. D. Phillips, J. V. Porto and I. B. Spielman: “A synthetic electric force acting on neutral atoms”, *Nature Physics* **7** (7), 531–534 (2011). 120
- [253] N. R. Cooper and J. Dalibard: “Reaching Fractional Quantum Hall States with Optical Flux Lattices”, *Phys. Rev. Lett.* **110**, 185301 (2013). 120
- [254] A. Kerkmann: “A novel Apparatus for Quantum Gas Microscopy of Lithium Atoms”, Ph.D. thesis, University of Hamburg (2019). 121
- [255] M. Weinberg, O. Jürgensen, C. Ölschläger, D.-S. Lühmann, K. Sengstock and J. Simonet: “Symmetry-broken momentum distributions induced by matter-wave diffraction during time-of-flight expansion of ultracold atoms”, *Phys. Rev. A* **93**, 033625 (2016). 122
- [256] C. K. Thomas, T. H. Barter, T.-H. Leung, S. Daiss and D. M. Stamper-Kurn: “Signatures of spatial inversion asymmetry of an optical lattice observed in matter-wave diffraction”, *Phys. Rev. A* **93**, 063613 (2016). 122
- [257] J. Heinze, S. Götze, J. S. Krauser, B. Hundt, N. Fläschner, D.-S. Lühmann, C. Becker and K. Sengstock: “Multiband Spectroscopy of Ultracold Fermions: Observation of Reduced Tunneling in Attractive Bose-Fermi Mixtures”, *Phys. Rev. Lett.* **107**, 135303 (2011). 127
- [258] N. Fläschner, M. Tarnowski, B. S. Rem, D. Vogel, K. Sengstock and C. Weitenberg: “High-precision multiband spectroscopy of ultracold fermions in a nonseparable optical lattice”, *Phys. Rev. A* **97**, 051601 (2018). 127
- [259] M. Weinberg, C. Ölschläger, C. Sträter, S. Prella, A. Eckardt, K. Sengstock and J. Simonet: “Multiphoton excitations of quantum gases in driven optical lattices”, *Phys. Rev. A* **92**, 043621 (2015). 127

- [260] S. V. Rajagopal, T. Shimasaki, P. Dotti, M. Račiūnas, R. Senaratne, E. Anisimovas, A. Eckardt and D. M. Weld: “Phasonic Spectroscopy of a Quantum Gas in a Quasicrystalline Lattice”, *Phys. Rev. Lett.* **123**, 223201 (2019). 127
- [261] A. Alberti, G. Ferrari, V. V. Ivanov, M. L. Chiofalo and G. M. Tino: “Atomic wave packets in amplitude-modulated vertical optical lattices”, *New Journal of Physics* **12** (6), 065037 (2010). 128
- [262] N. Goldman, J. Dalibard, M. Aidelsburger and N. R. Cooper: “Periodically driven quantum matter: The case of resonant modulations”, *Phys. Rev. A* **91**, 033632 (2015). 128
- [263] W. A. Benalcazar, B. A. Bernevig and T. L. Hughes: “Quantized electric multipole insulators”, *Science* **357** (6346), 61–66 (2017). 129
- [264] B. Yan and C. Felser: “Topological Materials: Weyl Semimetals”, *Annual Review of Condensed Matter Physics* **8** (1), 337–354 (2017). 129
- [265] Z.-Y. Wang, X.-C. Cheng, B.-Z. Wang, J.-Y. Zhang, Y.-H. Lu, C.-R. Yi, S. Niu, Y. Deng, X.-J. Liu, S. Chen and J.-W. Pan: “Realization of an ideal Weyl semimetal band in a quantum gas with 3D spin-orbit coupling”, *Science* **372** (6539), 271–276 (2021). 129
- [266] J. E. Sipe and A. I. Shkrebtii: “Second-order optical response in semiconductors”, *Phys. Rev. B* **61**, 5337–5352 (2000). 130
- [267] F. De Juan, A. G. Grushin, T. Morimoto and J. E. Moore: “Quantized circular photogalvanic effect in Weyl semimetals”, *Nature Comm.* **8**, 15995 (2017). 130
- [268] D. T. Tran, A. Dauphin, A. G. Grushin, P. Zoller and N. Goldman: “Probing topology by heating: Quantized circular dichroism in ultracold atoms”, *Science Advances* **3**, e1701207 (2017). 130
- [269] B. Xiong and U. R. Fischer: “Interaction-induced coherence among polar bosons stored in triple-well potentials”, *Phys. Rev. A* **88**, 063608 (2013). 139
- [270] E. J. Meier, F. A. An and B. Gadway: “Atom-optics simulator of lattice transport phenomena”, *Phys. Rev. A* **93**, 051602 (2016). 148
- [271] F. A. An, E. J. Meier and B. Gadway: “Direct observation of chiral currents and magnetic reflection in atomic flux lattices”, *Science Advances* **3** (4), e1602685 (2017). 148